Spectroscopic and Computational Studies of Morphology-Dependent Exciton Dynamics in TIPS-Pentacene Nanoparticles

Rohan J. Hudson

B.Sc. (Advanced), M.Phil. (Chemical Science)

A thesis submitted in fulfilment of the requirements for the degree of Doctor of Philosophy

March 2022

Department of Chemistry
The University of Adelaide
North Terrace Campus
Adelaide, South Australia 5005

Supervisors:
A/Prof. Tak W. Kee
A/Prof. David M. Huang

Contents

Abstract

Singlet fission (SF) is an exciton multiplication process whereby a singlet exciton converts into two lower-energy triplet excitons, which presents opportunities for bypassing the theoretical effficiency limit of single-junction photovoltaic devices. However, a deeper understanding of the photophysical processes underpinning SF must be developed in order to meaningfully improve photovoltaic efficiencies. 6,13-(triisopropyl silylethynyl)pentacene (TIPS-Pn) has been extensively studied as a model system for intermolecular SF, but the complex relationship between solid-state morphology and exciton dynamics in this material has previously complicated interpretation of results from such models. In particular, nanoparticle (NP) dispersions are a popular medium for spectroscopic study of solid-state excitonic processes, but significant quantitative discrepancies exist in the literature regarding exciton dynamics within TIPS-Pn NPs. This thesis presents a series of spectroscopic and computational investigations aimed at clarifying the relationship between intermolecular morphology, NP structure and exciton dynamics within TIPS-Pn NPs.

A novel mode of morphological control in these NP systems is investigated in Chapter 3, using poly(vinyl alcohol) as a chemical additive to convert the TIPS-Pn morphology from amorphous to crystalline. Experimental studies demonstrate that this transformation occurs rapidly and irreversibly through a surface-mediated interaction, and computational modelling suggests that a periodic dispersion interaction between hydroxyl- and TIPS-groups induces reorganization of the TIPS-Pn molecules. Characterization of this effect thus offers a reproducible and reliable strategy for accessing the crystalline phase of TIPS-Pn in NP models.

Chapter 4 uses ultrafast spectroscopy and electronic structure calculations to quantify triplet exciton mobility in crystalline TIPS-Pn NPs. Careful study of diffusion-limited triplet–triplet annihilation demonstrates that triplet mobility is highly anisotropic along different crystallographic axes, with diffusion coefficients varying by over seven orders of magnitude. Predicted exciton diffusion lengths range from almost 0.5 µm to less than 1 nm depending upon crystal orientation, with significant implications for the alignment of crystalline TIPS-Pn layers in device applications.

The effect of particle size on exciton dynamics in TIPS-Pn NPs is explored in Chapters 5 and 6. Chapter 5 studies a series of different-sized amorphous TIPS-Pn NPs, and shows that both the rate and yield of SF vary substantially with NP size. Upon decreasing particle size, SF slows, triplet decay accelerates and an additional, previously undiscovered non-radiative singlet quenching channel becomes significant. All of these effects are ascribed to increased morphological disorder within these NPs at smaller sizes, hence indicating that not all NP sizes are reasonable models of bulk amorphous TIPS-Pn and care must be taken when interpreting results from such systems. Contrasting with this, Chapter 6 observes negligible changes in NP morphology or exciton dynamics with particle size for crystalline TIPS-Pn NPs. Kinetic Monte Carlo modelling shows that while size-dependent triplet decay kinetics are possible due to exciton confinement in very small NPs, this will only occur at conditions that are experimentally unlikely. Small crystalline TIPS-Pn NPs are therefore expected to be excellent model systems for bulk crystalline TIPS-Pn.

Declaration

I certify that this work contains no material which has been accepted for the award of any other degree or diploma in my name, in any university or other tertiary institution and, to the best of my knowledge and belief, contains no material previously published or written by another person, except where due reference has been made in the text. In addition, I certify that no part of this work will, in the future, be used in a submission in my name, for any other degree or diploma in any university or other tertiary institution without the prior approval of the University of Adelaide and where applicable, any partner institution responsible for the joint-award of this degree.

The author acknowledges that copyright of published works contained within the thesis resides with the copyright holder(s) of those works. I also give permission for the digital version of my thesis to be made available on the web, via the University's digital research repository, the Library Search and also through web search engines, unless permission has been granted by the University to restrict access for a period of time.

I acknowledge the support I have received for my research through the provision of an Australian Government Research Training Program Scholarship.

Rohan J. Hudson
March 29th, 2022

Acknowledgements

It takes a village to raise a ~~child~~ PhD student, and there are many people to whom I am grateful for their help during my PhD candidature. My supervisors Assoc. Prof. Tak W. Kee and Assoc. Prof. David M. Huang have been incredibly supportive and encouraging of my work, and I am very appreciative of all their help. They have taught me new skills and concepts, provided opportunities for travel and networking (despite a global pandemic) and been immensely patient with my many, many questions. I am extremely grateful for their mentoring and willingness to share advice, both scientific and otherwise.

Many thanks also go to the rest of the Kee and Huang research groups. I am enormously thankful for all of the support provided by Dr. Patrick Tapping, from helping overcome experimental troubles to providing assistance with coding and data analysis. In particular, the LaTeX template used to write this thesis was developed by Patrick, as well as other pieces of code used to analyse and visualise some of the data presented herein. My fellow PhD students Alex Stuart and Jess de la Perrelle have been fantastic friends, colleagues and co-authors throughout my PhD, and I am very grateful for their friendship. Thankyou both for all of your emotional support over the last few years and for generally being excellent; I'm going to sincerely miss our office and lab conversations. And to all of the various members of our research group over the last three years, thankyou for helping to make such a welcoming and friendly research environment.

Much of the work undertaken during my PhD would not have been possible without the fantastic technical staff here at The University of Adelaide. Matthew Bull and Peter Apoefis have been invaluable in their support of our experimental apparatus, and I am incredibly grateful for their help in repairing or rebuilding countless pieces of equipment over the years, as well as their excellent technical advice for troubleshooting experiments. Thanks also go to Dr. Oliver Linder-Patton for his help with XRD experiments, Belinda Boehm and Dr. Andrew Tarzia for their assistance with computational resources, and Dr. Natasha Maddigan and Dr. Elizabeth Tran for their help in accessing DLS facilities.

I must also thank our research collaborators at Princeton University; the study on PVA-induced crystallinity in TIPS-Pn presented in Chapter 3 of this thesis would not have been possible without their input. Thanks go to Prof. Gregory Scholes, Dr. Ryan Pensack and Dr. Bryan Kudisch for their willingness to cooperate on this work.

To my friends and family, thankyou for helping me to keep sane over the last several years. Special mentions go to my gym partner Bowie, sister Gen and parents John and Karan, who have helped me to de-stress and unwind when I needed to. And to my wife Rosie - the last few years have been eventful, to say the least. Thankyou for supporting me unconditionally when I decided to go back to uni *again*, and for all of your love and encouragement.

Publications

This thesis is based on the following publications that detail some of the research undertaken during the period of candidature:

1. Hudson, R. J.; de la Perrelle, J. M.; Pensack, R. D.; Kudisch B.; Scholes, G. D.; Huang, D. M.; Kee, T. W. Organizing Crystalline Functionalized Pentacene Using Periodicity of Poly(Vinyl Alcohol). *J. Phys. Chem. Lett.* **2020**, *11*, 516–523.

2. Hudson, R. J.; Huang, D. M.; Kee, T. W. Anisotropic Triplet Exciton Diffusion in Crystalline Functionalized Pentacene. *J. Phys. Chem. C* **2020**, *124*, 23541–23550.

3. Hudson, R. J.; Stuart, A. N.; de la Perrelle, J. M.; Huang, D. M.; Kee, T. W. Nanoparticle Size–Dependent Singlet Fission and Exciton Dynamics in Amorphous TIPS-Pentacene. *J. Phys. Chem. C* **2021**, *125*, 21559–21570.

4. Hudson, R. J.; Huang, D. M.; Kee, T. W. Confinement Effects Upon Triplet Exciton Dynamics in Crystalline TIPS-Pentacene Nanoparticles. **2022**, manuscript in preparation.

In addition, contributions were also made to the following publication (not part of this thesis):

5. Hudson, R. J.; Stuart, A. N.; Huang, D. M.; Kee, T. W. What Next for Singlet Fission? The Fate of Triplet and Triplet-Pair Excitons. *J. Phys. Chem. C* **2022**, accepted for publication. DOI: 10.1021/acs.jpcc.2c00273.

Abbreviations

1D one-dimensional

2D two-dimensional

2DES two-dimensional electronic spectroscopy

3D three-dimensional

AFM atomic force microscopy

BBO β-barium borate

CB conduction band

CDFT constrained density functional theory

CDFT-CI constrained DFT configuration-interaction

CI configuration-interaction

CT charge-transfer

DET Dexter excitation transfer

DFT density functional theory

DLS dynamic light scattering

DPP diketopyrrolopyrrole

EEA exciton–exciton annihilation

EM electron microscopy

ESA excited-state absorption

FRET Förster resonance energy transfer

GGA generalized gradient approximation

GSB ground-state bleach

GTA global and target analysis

HF Hartree-Fock

IQE internal quantum efficiency

ISC intersystem crossing

KMC kinetic Monte Carlo

LDA local density approximation

MEG multiple exciton generation

NP nanoparticle

OPA optical parametric amplifier

PAA poly(acrylic acid)

PCE power conversion efficiency

PEG poly(ethylene glycol)

PMMA poly(methyl methacrylate)

PV photovoltaic

PVA poly(vinyl alcohol)

PXRD powder X-ray diffraction

SE stimulated emission

SF singlet fission

SFG sum-frequency generation

TA transient absorption

TCA triplet–charge annihilation

TES-Pn 6,13-(triethylsilylethynyl)pentacene

THF tetrahydrofuran

TIPS-Pn 6,13-(triisopropylsilylethynyl)pentacene

TIPS-Tn 5,12-(triisopropylsilylethynyl)tetracene

TMS-Pn 6,13-(trimethylsilylethynyl)pentacene

TTA triplet–triplet annihilation

UC upconversion

VB valence band

List of Figures

List of Tables

CHAPTER 1
Introduction

1.1 Solar Energy Harvesting and Photovoltaics

Global demand for energy is increasing rapidly, with worldwide energy consumption having approximately doubled since 1980.[6] At the same time, the impacts of greenhouse gas emissions from the combustion of fossil fuels upon the Earth's climate are becoming increasingly clear. Recent modelling suggests that an increase in mean global surface temperatures of 1.5°C relative to the year 1900 is likely by 2030, with a possible rise of up to 4.8°C by 2100.[7] Concerns regarding the climatological impacts of such warming, coupled with current growth in energy consumption, are currently driving an unprecedented transformation of global energy infrastructure towards renewable and non-fossil-fuel energy sources. In particular, electricity generation through harnessing solar energy with photovoltaic (PV) devices has seen significant growth, as incident solar radiation at the Earth's surface provides approximately $10^4\times$ current global energy needs.[8] This is exemplified by the recent uptake of PV in Australia, shown in Figure 1.1. Since 2010, electricity generation by PV has grown from negligible levels to account for approximately 8% of all electrical power generated nationwide, and almost twice this in the state of South Australia.[9] There is therefore significant current research interest in improving existing PV technologies, particularly in terms of bypassing fundamental efficiency limits of existing devices.

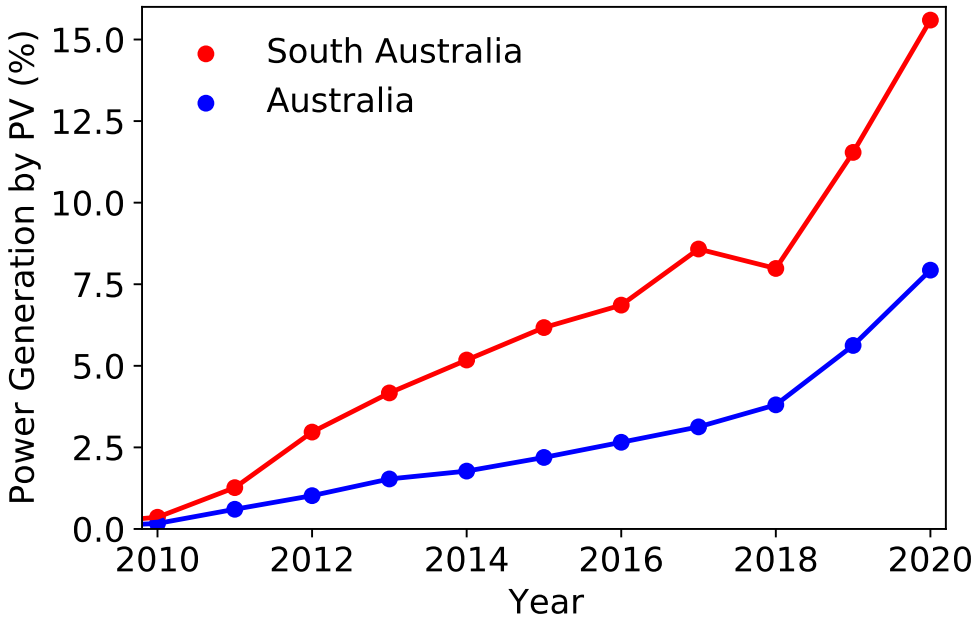

Figure 1.1: Percentage power generation by photovoltaics Australia-wide (blue) and in the state of South Australia (red), 2010–2020. Data is taken from ref. 9.

1.1.1 Efficiency Limits of Single-Junction Photovoltaics

Single-junction PV devices (constructed from a single p-n junction within the semiconducting layer) are limited to a maximum possible solar power conversion efficiency (PCE) of approximately 33%, termed the "detailed-balance limit".[10,11] This occurs for a hypothetical material with a band-gap of 1.3 eV; for doped silicon, the active material used in most existing PV technologies, this limit is closer to 29%.[12] There are several mechanisms which contribute to this efficiency limit, but the two largest energy-loss pathways are illustrated in Figure 1.2. The active layer of a single-junction PV device consists of a single semiconducting material, with band-gap of energy E_B separating the filled valence band (VB) and vacant conduction band (CB). Solar photons of energy lower than E_B cannot be absorbed by this material, reducing the overall energy efficiency of the device. Photons of energy $E_{photon} \geq E_B$ may be absorbed by the semiconductor, promoting an electron from the VB to the CB and leaving a positively-charged vacancy (termed an "electron-hole", or simply "hole") in the VB. In some materials these electrons and holes are able to move independently of one another as charge carriers, while in others they remain electrostatically bound as an electron–hole pair, often termed an "exciton".[13] However, high-energy electrons or excitons in the CB undergo ultrafast thermal relaxation ("thermalization") to the CB edge. Such thermalization comprises a significant PV energy loss pathway upon irradiation with high-energy photons, and is a major contributing factor to the detailed-balance limit for single-junction PV devices.

The highest reported PCE for a single-junction silicon PV device is 26.7%, which approaches the silicon detailed-balance limit of 29%.[14,15] Only minimal further efficiency improvements are therefore possible for such devices, and so significant study is now being devoted to developing alternative PV architectures which may bypass the detailed-balance limit. Coupling multiple cells in tandem[16] or photon upconversion[17] are both promising methods for harnessing low-energy photons below the silicon

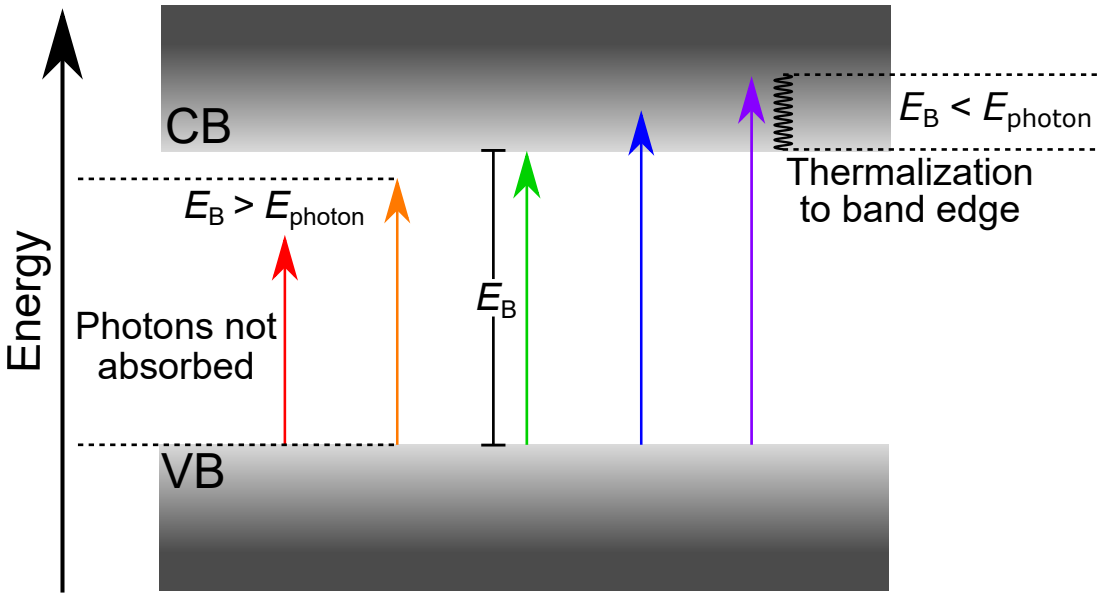

Figure 1.2: Illustration of the major loss pathways which contribute to the detailed-balance efficiency limit of single-junction photovoltaic devices. Coloured arrows represent visible photons with energies E_{photon}.

band-gap. Multiple exciton generation (MEG) is also topic of considerable interest at present, as conversion of one high-energy photon to multiple lower-energy excitons or charge carriers in the CB has potential to minimize energy losses through thermalization.[18] One method of MEG showing significant potential for use in PV devices is singlet fission (SF), which may improve the yield of excited states transferred to the semiconductor CB.

1.1.2 Singlet Fission Photovoltaics

SF is the photophysical process by which an excited-state chromophore with singlet multiplicity (S_1) couples to an adjacent ground-state chromophore (S_0) to yield two neighbouring excited-state chromophores with triplet multiplicity (T_1).[19] This process is spin-allowed as it proceeds via a correlated triplet pair intermediate state, $^1(TT)$:[20]

$$S_1 + S_0 \rightarrow {}^1(TT) \rightarrow T_1 + T_1. \tag{1.1}$$

SF is an energy-conserving process, as the energy of the initial singlet-state excitation is in general equal to or greater than the combined energy of the two triplets formed. Exceptions can occur for slightly endothermic SF, whereby thermal energy or entropic contributions make up this energy difference,[21] but even in such cases the triplet energy is still approximately half that of the singlet energy. SF hence converts one high-energy exciton into two lower-energy excitons, and has therefore been proposed as a potential MEG mechanism for PV devices.[18] High-energy photons which suffer significant energy losses through CB thermalization could instead be absorbed by a SF sensitizing layer, with the resulting singlet exciton subsequently converted into two low-energy triplet excitons via SF, as shown in Figure 1.3a–b. Upon exciton transport to the interface between sensitizer and semiconductor (Figure 1.3c), these triplet excitons may undergo either energy or electron transfer into the semiconductor CB (Figure 1.3d). The combined thermalization energy loss of these lower-energy triplet excitons would be less than that of the original high-energy singlet exciton. Hence, MEG by SF may minimize energy losses from CB thermalization in PV devices, and therefore improve PCEs beyond the detailed-balance limit. Assuming a SF yield of 200% (two triplet excitons formed from every photon absorbed; often termed "quantitative yield") and that no losses occur in triplet transport or transfer into the CB, the efficiency limit of a SF-sensitized PV device has been calculated as approximately 46%.[18,22,23] For silicon sensitized with tetracene (a SF chromophore with triplet energy favorable for transfer into the silicon CB), more recent studies have revised this limit to 32–36%, which remains a considerable improvement on the detailed-balance limit of 29% for silicon.[24,25]

However, such efficiency improvements have yet to be practically realized, with reported PCEs of SF-sensitized PV devices rarely exceeding 5%.[26–31] With reference to the tetracene-sensitized silicon design mentioned above, the highest PCE recorded from such a device is 5.1%,[32] significantly lower than the 32–36% PCE limit calculated for this system. Multiple studies have reported that despite achieving quantitative SF yields in the sensitizing layer, charge-carrier yields in such devices are generally significantly lower than 200%.[27–29] This therefore implies that while every singlet excitation is successfully converted into two triplet excitons within the SF-active layer, not every triplet exciton is then transferred into the semiconductor CB. Efficiency losses must hence arise during either exciton transport within the SF layer or transfer into

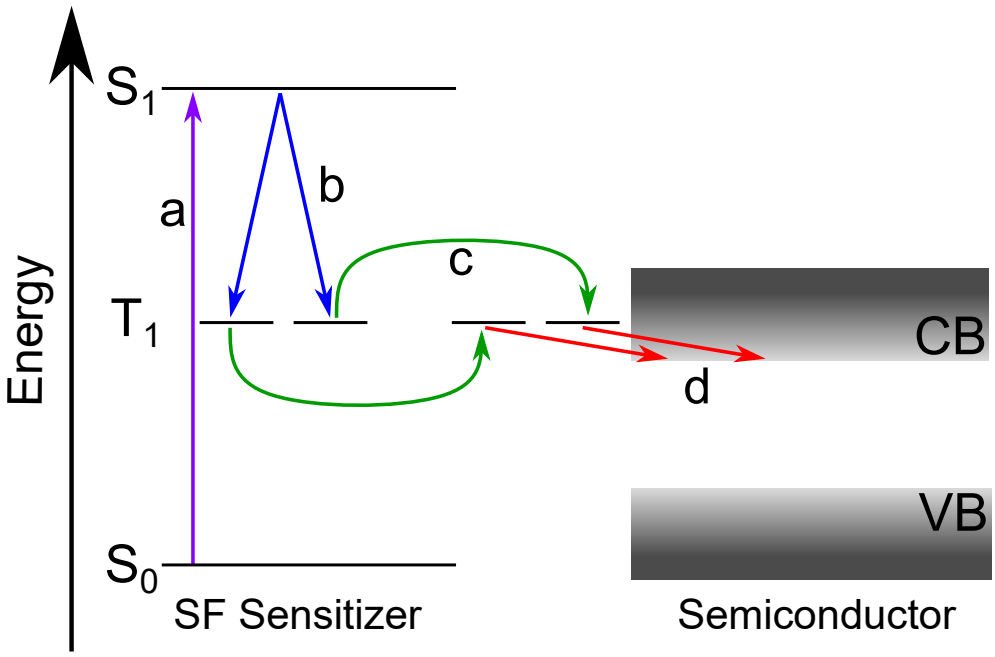

Figure 1.3: Schematic illustration of an ideal SF-sensitized PV device. Labelled processes correspond to (a) photo-excitation of the SF sensitizer by high-energy solar photons to form a singlet exciton, (b) rapid and irreversible SF of the singlet exciton to form two triplet excitons, (c) transport of both triplet excitons to the sensitizer:semiconductor interface, and (d) energy or electron transfer from both triplet excitons into the conduction band of the semiconductor.

the semiconductor, but the cause(s) of these reduced efficiencies are not currently well understood. A deeper understanding of the mechanisms governing these excitonic processes is therefore necessary, such that these loss processes can be minimized and the efficiencies of SF-sensitized PV devices improved.

1.2 Mechanisms of Excitonic Processes

1.2.1 Singlet Fission

Despite the relative simplicity of Equation 1.1, the mechanism underpinning SF is much more complex than this description suggests, as illustrated in Figure 1.4. Direct conversion of S_1 into ^{1}(TT) requires a concerted, effective two-electron transfer between adjacent chromophores (Figure 1.4b). For weakly-coupled chromophores this can be described by Marcus theory, with a rate strongly dependent upon the S_1–^{1}(TT) diabatic coupling.[33] However, while this direct mechanism may be relevant in some circumstances,[34,35] a growing body of evidence now suggests that charge-transfer (CT) states appear to play a significant role in the SF process.[36] CT states, in which a single electron is transferred between chromophores to yield a cation/anion pair, are thought to act as intermediate states in ^{1}(TT) formation.[37] CT states of energy comparable to the S_1 state have been proposed as being real intermediates in SF (Figure 1.4c),[38] while others have suggested that higher-energy CT states may act as virtual intermediates, indirectly coupling the S_1 and ^{1}(TT) states through an effective "superexchange" mechanism (Figure 1.4d).[39,40] Multiple experimental studies have observed accelerated SF

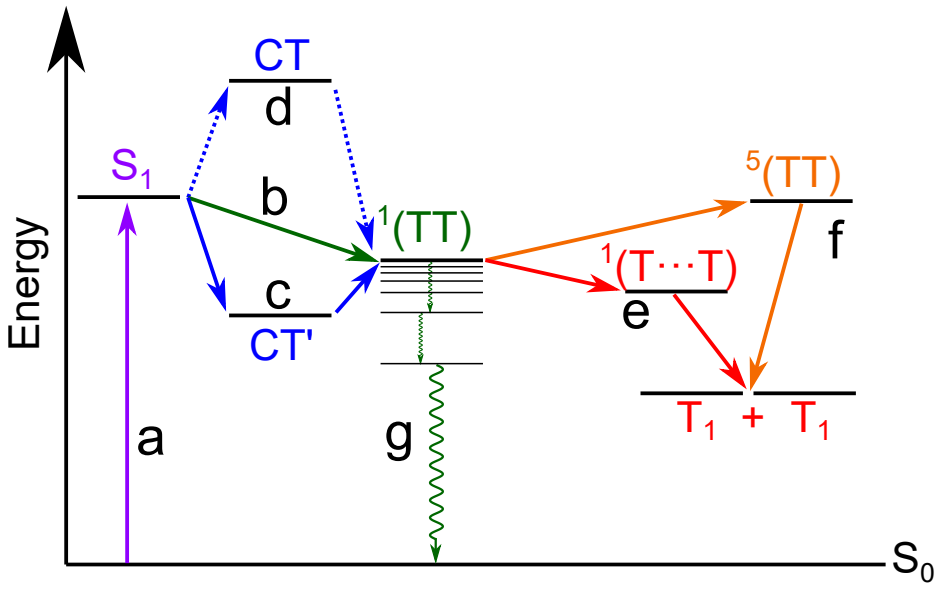

Figure 1.4: Jablonski diagram of the mechanistic processes associated with singlet fission: (a) photo-excitation from S_0 to S_1, (b) direct formation of ^{1}(TT), (c) direct and (d) virtual charge-transfer mediated formation of ^{1}(TT), (e) direct separation of ^{1}(TT), (f) quintet-mediated separation of ^{1}(TT), and (g) non-radiative relaxation of ^{1}(TT) to S_0 through vibrational or nuclear motions.

rates upon increasing solvent polarity, ascribed to polar solvents stabilizing these CT intermediate states.[41–45] For more strongly coupled chromophores, however, incoherent electron transfer theory cannot fully describe the SF mechanism. Recent work has demonstrated that a resonant superposition of S_1, ^{1}(TT) and CT states can be formed upon photoexcitation of strongly-coupled chromophores, coupled through either electronic[46–49] or vibrational[50–55] coherences. Subsequent dephasing of these coherences then results in the formation of ^{1}(TT) state on ultrafast timescales. Some studies have reported both coherent and incoherent SF mechanisms operating simultaneously within the same material,[48,56] thus highlighting the complex nature of ^{1}(TT) formation in SF-capable materials.

In order to effectively improve PV device efficiencies, the ^{1}(TT) state formed during SF must effectively separate into two independent triplet excitons. Some studies have suggested that the ^{1}(TT) state in some materials possesses a finite binding energy relative to free triplets, that must be overcome through thermal or entropic contributions in order to induce separation.[50,57,58] Several recent studies have demonstrated that ^{1}(TT) dissociation is limited by triplet exciton transfer away from the initial SF site.[59–61] Separation of the ^{1}(TT) state through this process is thought to involve a second triplet pair intermediate, comprising spatially-separated but spin-correlated triplet excitons, denoted ^{1}(T···T).[62,63] Subsequent loss of spin correlation in this weakly-interacting intermediate then yields two independent triplet excitons (Figure 1.4e).[64] An alternative mechanism proposed for the separation of the ^{1}(TT) state involves triplet pair states of higher multiplicities. Pair states of triplet (^{3}(TT)) or quintet (^{5}(TT)) multiplicity may also arise from triplet–triplet interactions,[20,65] which may mix with the ^{1}(TT) state in the limit of weak spin-orbit coupling.[66] Quantum beating in the delayed fluorescence of tetracene has previously been attributed to the formation of a coherent superposition of ^{1}(TT) and ^{3}(TT) states formed following SF.[58,67,68] Quintet pair states have been

identified by spin-resonance techniques intermediates in a number of SF-capable systems following ^{1}(TT) formation, but before separation into free triplets.[43,69–71] These ^{5}(TT) states have hence been proposed to act as intermediates in ^{1}(TT) separation to free triplet excitons (Figure 1.4f). Experimental evidence has been reported for both direct and quintet-mediated separation pathways, but never from the same study. It is therefore currently unclear how these two mechanisms of ^{1}(TT) separation relate to one another: they may be complementary aspects of the same mechanism, competing processes in the same material, or pathways exclusive to different chromophores.

Distinct from these mechanisms of ^{1}(TT) separation, other decay pathways have also been identified for the correlated triplet pair state. Several recent studies have demonstrated that a sub-population of ^{1}(TT) excitons formed through SF do not separate, but instead decay non-radiatively to the ground state.[58,72–75] The exact nature of this pathway has not yet been established, but it has been hypothesized that this non-radiative decay is facilitated by relaxation through vibrational modes or other nuclear motions within the material (Figure 1.4g).[74,75] Delayed fluorescence from tetracene, pentacene and other SF-capable chromophores has also been attributed to radiative decay of the ^{1}(TT) state, with coherent mixing of the "bright" S_1 state and "dark" ^{1}(TT) states proposed as enabling this transition.[58,67,68,76] Finally, direct charge transfer from the ^{1}(TT) state into electron-accepting materials has also been reported in some instances, effectively bypassing the formation of free triplet excitons.[46,58] The nature and behaviour of correlated triplet pair states is clearly highly complex, and is hence an active and rapidly evolving field of research.

1.2.2 Exciton Transport

Exciton transport may occur via a number of possible energy transfer processes. For weakly-coupled chromophores, two distinct mechanisms of incoherent excitation energy transfer may occur, both of which are described in Figure 1.5. Förster resonance energy transfer (FRET) allows for excitation energy transfer between spatially-separated chromophores through a coupling of transition dipole moments (Figure 1.5a).[77] This process involves no exchange of electrons or emission of radiation, as energy is transferred only via resonant de-excitation and excitation of the two chromophores. For an interchromophore separation r, the rate of FRET between two chromophores scales as r^{-6}, with relatively fast and efficient singlet exciton transfer generally occurring for separations of 10 nm or less.[77,78] However, the respective excitation and de-excitation transitions required for FRET must be spin-allowed. Therefore, triplet exciton transfer cannot occur through FRET, as de-excitation of a triplet excited state is spin-forbidden. Instead, triplet exciton migration occurs through Dexter excitation transfer (DET), shown schematically in Figure 1.5b. DET is an electron exchange mechanism, and so is highly dependent upon the electronic coupling and hence molecular orbital overlap between adjacent chromophores.[79] The interchromophore separations required for DET are therefore significantly smaller than for FRET; the DET rate scales as $\exp(-2r)$, and so is effectively negligible beyond $r = 1$ nm.[79,80] Triplet exciton migration is hence orders of magnitude slower than singlet migration within the same material.[80] Incoherent exciton transfer through FRET or DET can be described as "hopping", as each transfer event occurs independently of those preceding it. The collective motion of an ensemble of such excitons is therefore random and governed by Brownian motion, and so the migration of excitons in a weakly-coupled system is generally described as

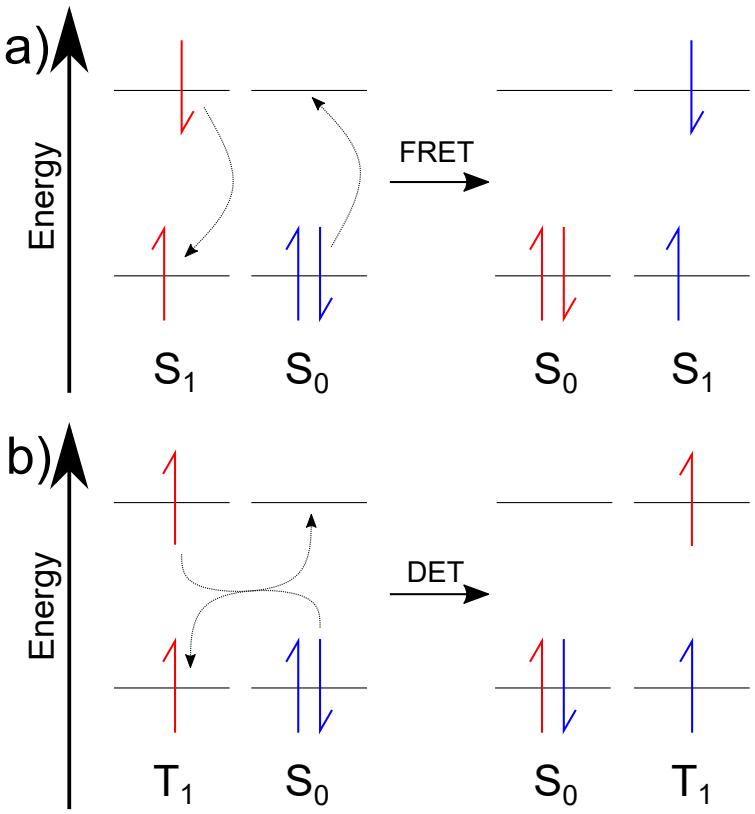

Figure 1.5: Orbital diagram depicting (a) singlet exciton transfer by Förster resonance energy transfer (FRET) and (b) triplet exciton transfer by Dexter excitation transfer (DET).

"exciton diffusion".[81]

For more strongly-coupled chromophores, however, DET and FRET are not the only possible means of exciton transport. Photo-excitation of a strongly-coupled system may form a coherent superposition of states (either vibrational or electronic) between separate chromophores.[82] Oscillations within this superposition can then facilitate rapid, long-range transfer of excitation energy between chromophores. Coherent transport of excitons has been observed in a variety of organic[83] and inorganic[84] materials, on timescales of up to hundreds of femtoseconds and length scales of several nanometers. Vibronic coherences have also been reported in a number of biological systems,[85–87] although whether these coherences contribute towards exciton transport is currently a topic of debate.[88–90]

1.2.3 Exciton–Exciton Annihilation

An encounter between two excitons may result in de-excitation of one or both excitons, through a process known as exciton–exciton annihilation (EEA). EEA is an energy-conserving process, whereby the combined energy of both excitons promotes one exciton to a higher energy state, while returning the other to the ground state. In the case of annihilation between singlet excitons, this typically forms a high-lying singlet excited state (denoted S_n) which generally rapidly relaxes back to the S_1 state:[91]

$$S_1 + S_1 \rightarrow S_n + S_0 \rightarrow S_1 + S_0. \tag{1.2}$$

EEA between singlets can only form high-energy excitons of singlet multiplicity, as the net spin of the system is zero. For annihilation of triplet excitons, however, a more

complex series of interactions occur, as the first step in triplet–triplet annihilation (TTA) involves the formation of a triplet-pair encounter state. As discussed in Section 1.2.1, (TT) pair states may have singlet, triplet or quintet multiplicity. TTA through the singlet channel results in mutual annihilation of both triplet excitons and formation of a singlet state. ^{3}(TT) encounter states may relax to a hot triplet state T_n, which then may further relax to T_1 such that one triplet is removed through this annihilation pathway. Localized quintet states in most materials are generally too high in energy to be accessible via TTA, and so formation of a ^{5}(TT) encounter state usually results in dissociation back to $T_1 + T_1$.[92,93] The process of TTA may hence be summarized as

$$T_1 + T_1 \rightarrow \begin{cases} {}^1(TT) \rightarrow S_1 + S_0 \\ {}^3(TT) \rightarrow T_n + S_0 \rightarrow T_1 + S_0 \\ {}^5(TT) \rightarrow T_1 + T_1. \end{cases} \tag{1.3}$$

An encounter between two triplet excitons results in a manifold of nine possible triplet–pair states. If these states remain spin-pure, this manifold consists of one singlet state, three triplet states and five quintet states.[65] In such circumstances, mutual annihilation may occur from only one state and annihilation of a single exciton from three, yielding respective probabilities of 1/9 and 3/9 for these processes. However, mixing between these pair states may occur in many chromophore materials, resulting in a manifold of mixed-character (TT) states. TTA through each channel may hence occur from any encounter state with some level of either singlet or triplet character, with rates proportional to the singlet or triplet projection onto the state of interest.[94,95] The relative energies of intermediate states involved in TTA also play a significant role in determining the pathway through which TTA occurs. Numerous experimental studies have observed singlet yields from TTA significantly higher than what would be expected through spin-statistics.[96–98] This has been attributed to high-lying T_n states possessing such high energies that the $^3(TT) \rightarrow T_n + S_0$ relaxation is highly endoergic, inhibiting TTA through this pathway.

For triplet excitons arising from SF, two distinct types of TTA can occur.[99] Annihilation of two triplet excitons formed from the same SF event is referred to as "geminate" TTA.[100] This is the reverse process of SF, and is often alternatively termed "triplet fusion" or "triplet recombination". Geminate TTA occurs with first-order kinetics, as each pair of triplet excitons decays independently of one another. Recent reports have observed that triplet excitons formed from SF may possess some level of long-term "spin memory", recombining with a faster rate than would be expected by spin-statistics.[101] This may arise from geminate recombination of the spin-correlated but spatially-separated $^1(T\cdots T)$ intermediate state. For encounters of triplet excitons formed from separate SF events, "bimolecular" TTA can occur. This process exhibits second–order kinetics with respect to triplet concentration:

$$\frac{d[T_1]}{dt} = -\gamma[T_1]^2, \tag{1.4}$$

for γ the bimolecular annihilation rate coefficient.[92] Triplet excitons are generally highly localized upon SF chromophores,[102] and so bimolecular TTA can only occur for two triplets brought into very close proximity through exciton hopping. In the limit of annihilation occurring much faster than diffusive exciton transport, exciton diffusion becomes the rate-limiting step for TTA. Bimolecular TTA may hence be described as a diffusion-limited process under these conditions, and γ may be expressed as function

of the exciton diffusion coefficient D.[92] The exact functional form of γ depends upon the dimensionality and nature of triplet exciton diffusion within the material.[100,103]

1.2.4 The Role of Morphology

Many of the excitonic processes discussed in the preceding sections depend strongly upon the relative spatial arrangement of chromophores, often collectively termed "morphology" or "microstructure". These terms are quite broad, and can be used to describe structural aspects on length scales ranging from the molecular level to the micrometer-scale. Within the context of SF, interchromophore couplings between S_1, ^{1}(TT) and CT states control both the mechanism and efficiency of $S_1 + S_0 \rightarrow {}^1$(TT) conversion. These couplings are governed by the effective overlap of molecular orbitals between chromophores of interest,[104] and so are highly dependent upon chromophore morphology. Multiple computational[105–107] and experimental[108,109] studies have demonstrated that angstrom-scale variations in intermolecular separations or orientations can cause order-of-magnitude changes in these couplings, hence resulting in substantial variations in SF yields and rates. Similarly, different polymorphs or phases of the same chromophore have been shown to exhibit radically different SF dynamics.[34,110–113]

Changes in local chromophore morphology also impact the behaviour and yield of ^{1}(TT) and T_1 excitons arising from SF. The exponential decay of the DET rate with interchromophore separation causes significant changes in triplet diffusion and transport properties from just slight alterations in intermolecular packing. Triplet diffusion in an amorpohously-packed pentacene derivative has been recorded as over an order of magnitude slower than in the crystalline phase of the same material.[110] Triplet pair dissociation in some materials is limited by triplet hopping away from the initial SF site, and Stuart et al. demonstrated that the triplet yield from SF decreased in more disordered environments of a pentacene derivative.[72] In the same material, Grieco and coworkers showed that subtle changes in crystal packing increased the rate of ^{1}(TT) separation by a factor of two.[63]

Even within a single crystal polymorph, triplet mobility has been shown to vary substantially between crystallographic axes for small-molecule SF chromophores.[114,115] Such materials typically exhibit significant structural anisotropy in their crystal packing, and so the strong distance dependence of DET-mediated triplet migration therefore yields anisotropic triplet exciton mobilities within these structures. Diffusion-limited TTA has been well characterized as a major decay pathway for triplet excitons in crystalline SF chromophores, and analysis of TTA kinetics is often used to quantify their triplet transport properties.[116–118] However, many of these studies assume isotropic triplet exciton mobility in three dimensions, and so neglect the effects of structural anisotropy upon triplet diffusion.[110,117,119] It is only recently that advanced spectroscopic techniques such as transient absorption microscopy have been used to unambiguously demonstrate the anisotropic nature of triplet exciton mobility in crystalline SF chromophores.[114,115]

In all of these examples, subtle changes in intermolecular packing or local morphology are responsible for these significant changes in exciton behavior. Given the wide variety of polymorphs and microstructures available to small-molecule SF chromophores,[120,121] there is hence an overwhelmingly large library of possible SF chromophore morphologies, each with their own unique SF dynamics. Rather than attempting to characterize each one of these, several materials have instead been intensively stud-

ied as "model systems" over the last decade, in order to elucidate fundamental aspects of SF and associated exciton dynamics.

1.3 Model Systems for Studying Singlet Fission

1.3.1 TIPS-Pentacene as a Model Chromophore

Pentacene is a widely-studied SF chromophore, as its crystalline phase exhibits sub-picosecond SF with approximately quantitative yield.[19,28,116] However, pentacene is relatively insoluble in most common solvents, limiting opportunities for its study or incorporation into devices.[122] Additionally, crystalline pentacene packs in a herringbone-like motif,[123] which has recently been suggested to limit triplet separation and accelerate ^{1}(TT) non-radiative decay.[71] To mitigate these issues, 6,13-(triisopropylsilylethynyl) pentacene (TIPS-Pn) was developed as a functionalized alternative to pentacene.[124] Functionalization with TIPS groups at the 6- and 13-positions (Figure 1.6a) significantly improves the chromophore solubility,[19] and constrains the crystalline packing of TIPS-Pn to a two-dimensional slip-stacked geometry (Figure 1.6b-c), with π–π stacking throughout the *ab*-crystallographic plane.[125] This slip-stacked orientation has been identified as facilitating ultrafast and efficient SF for multiple small-molecule SF chromophores,[19,126–128] and several experimental studies have reported sub-picosecond SF with approximately quantitative triplet yield in crystalline TIPS-Pn.[75,129,130]

The crystal packing shown in Figure 1.6 is not the only TIPS-Pn morphology known to exhibit SF. A wide variety of TIPS-Pn crystalline polymorphs have been identified, accessible through solvent–annealing,[110,131] thermal–annealing,[63,120,132] application of

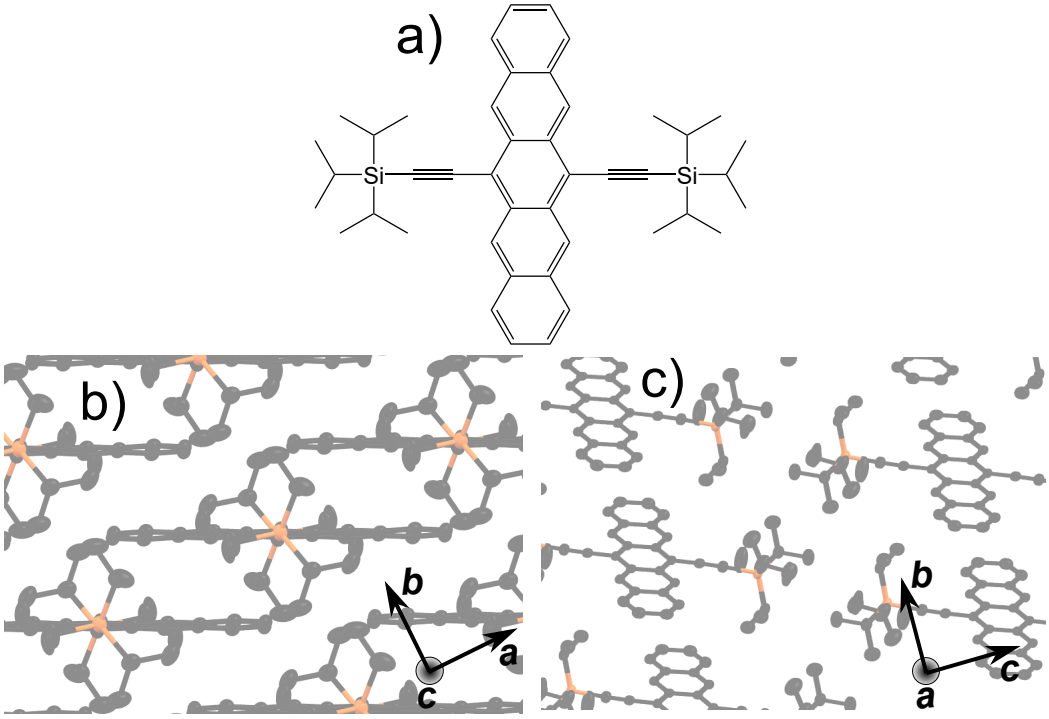

Figure 1.6: (a) Chemical structure of TIPS-Pn. (b-c) Crystal packing of the dominant TIPS-Pn crystalline polymorph, taken from ref. 125. Carbon atoms are shown in black and silicon atoms in orange. Hydrogen atoms are omitted for clarity.

external pressure[109] or deliberate introduction of impurities and defect sites.[127,128] All of these polymorphs have been reported as undergoing SF, with yields and rates highly dependent upon the mode of crystal packing. In addition, several studies have also identified a SF-capable amorphous phase of TIPS-Pn, despite this morphology possessing no long-range structural order.[72,75,110,133,134] SF has even been reported in concentrated solutions of TIPS-Pn,[135,136] with a recent study demonstrating that this occurs through diffusion-limited encounters of molecular dimers.[137] TIPS-Pn is therefore an excellent model chromophore for studying the impact of variations in local morphology upon the dynamics of SF and other related excitonic processes. As such, TIPS-Pn has attracted significant research interest in recent years, and is arguably now one of the most well-characterized chromophores in the SF field.

1.3.2 Colloidal Nanoparticle Dispersions

Colloidal suspensions of nanoparticles (NPs) are a popular medium for studying the photophysics of a variety of organic semiconducting materials, including conjugated polymers and small-molecule SF chromophores.[35,41,62,138–140] Use of NP dispersions allows for spectroscopic study of solid-state materials but with an overall liquid-phase sample, thus minimizing practical issues of sample opacity and localized heating or photo-bleaching generally associated with solid media. NP suspensions are hence convenient for spectroscopic investigations into SF exciton dynamics. Therefore, several recent studies have used aqueously-dispersed NPs to examine the ultrafast kinetics of SF in TIPS-Pn.[72,75,119,133,134,141]

However, quantitative discrepancies currently exist in the literature regarding exciton dynamics within TIPS-Pn NPs. While some authors have noted that these NP systems appear to closely resemble bulk TIPS-Pn,[119,134] other studies have reported exciton behavior in these NPs that is inconsistent with the bulk material. For example, SF in amorphous TIPS-Pn films has been quantified as occurring on a sub-picosecond timescale,[110,142] but studies of amorphous TIPS-Pn NPs have observed SF rates an order of magnitude slower than this.[72,141] The lifetime of triplet excitons arising from SF is also unclear; this has been reported as being on the order of microseconds in bulk amorphous TIPS-Pn, but triplet decay within 1–10 nanoseconds has been observed in amorphous NPs.[72,110,133] The cause of these discrepancies between NPs and bulk TIPS-Pn is currently unknown, but they likely arise from subtle morphological variations within these NPs that are not yet understood.

Confusion also exists within the literature regarding the mode of intermolecular packing within colloidal TIPS-Pn NPs. Tayebjee et al. reported that aqueously dispersed TIPS-Pn NPs initially formed with amorphous morphologies, but then slowly converted into a more strongly-coupled crystalline packing in the days–weeks following preparation.[133] Subsequent studies failed to reproduce this morphological transformation, however, showing that amorphous TIPS-Pn NPs were stable for weeks at a time.[72,134] Further work by other authors then demonstrated that this amorphous-to-crystalline transformation could only occur in the presence of a contaminant or chemical additive.[119] However, the exact nature of this additive and the mechanism by which it facilitated morphological conversion were not identified.

Additionally, the effect of particle size upon local morphology and hence exciton dynamics in TIPS-Pn NP systems is currently unclear. Size-dependent photophysical properties are well established for a variety of conjugated polymer NPs,[143,144] and both

the rate and yield of SF in diketopyrrolopyrrole (DPP) NPs have been shown to strongly depend upon particle size.[41] Size-dependent SF dynamics have also been reported for thin films of rubrene, attributed to variations in chromophore morphological with film thickness.[111] However, while reported particle sizes for TIPS-Pn NPs vary by almost an order of magnitude,[133,141] the potential for NP size to influence the dynamics of SF or other excitonic processes in these systems has not yet been explored.

1.4 Research Aims and the Scope of this Thesis

TIPS-Pn NPs hence represent a promising and convenient medium for spectroscopic study of SF, but the aforementioned sources of uncertainty regarding their exciton dynamics and morphology must be clarified before such NP dispersions can be considered as reliable model systems. This thesis presents a series of investigations into the ultrafast exciton dynamics of TIPS-Pn NPs, aiming to clarify these discrepancies and further elucidate the relationship between NP morphology and exciton behavior in these materials. Time-resolved spectroscopic techniques are used to observe and quantify exciton kinetics in a variety of TIPS-Pn NP systems, supported by computational modelling which provides molecular-level insight into how these dynamics are influenced by NP morphology.

Chapter 3 details an investigation into the mechanism by which chemical additives induce crystallinity in amorphous TIPS-Pn NPs, and demonstrates that a periodic interaction with poly(vinyl alcohol) (PVA) at the NP surface induces a phase transition to form crystalline TIPS-Pn. This novel interaction offers a convenient and reliable pathway for the preparation of crystalline TIPS-Pn NPs. Chapter 4 then uses time-resolved spectroscopy and quantum chemical modelling to quantify the mobility of triplet excitons within these crystalline TIPS-Pn NPs. This study highlights that triplet diffusion is highly anisotropic within crystalline TIPS-Pn, and that previous kinetic analyses using isotropic diffusion models give significantly misleading predictions regarding triplet mobility.

The influence of particle size upon the morphology and exciton dynamics in amorphous TIPS-Pn NPs is explored in Chapter 5. Significant variations in SF kinetics, SF yield and triplet lifetime are observed upon changing particle size, ascribed to an increase in morphological disorder at smaller particle sizes. Notably, this study identifies a previously-unknown (non-SF) non-radiative decay pathway of singlet excitons in amorphous TIPS-Pn NPs, which may constitute a substantial efficiency loss mechanism for SF at small particle sizes.

Chapter 6 then extends this consideration of particle-size effects to crystalline TIPS-Pn NPs. Time-resolved spectroscopic measurements demonstrate that negligible changes in morphology and hence exciton dynamics occur in these crystalline particles over a similar range of particle sizes to those studied in the previous chapter. Kinetic Monte Carlo simulations show that size-dependent triplet decay kinetics through exciton confinement effects are possible in crystalline TIPS-Pn NPs, but are only prevalent at very small particle sizes or low excitation densities and so are unlikely to be experimentally observable.

CHAPTER 2
Methods

This chapter summarizes the underlying theory of significant experimental and computational methods used throughout this work. The descriptions presented here are broad and generalized; specific experimental and computational details are given in the methods sections of Chapters 3–6.

2.1 Experimental Methods

2.1.1 Nanoparticle Preparation by Re-Precipitation

Nanoparticle (NP) dispersions of 6,13-(triisopropylsilylethynyl)pentacene (TIPS-Pn) and other chromophores studied in this work were prepared by the re-precipitation (also known as "flash precipitation") method first developed by Kasai and co-workers.[144,145] This technique induces NP nucleation by rapid chromophore aggregation following a sudden change in solvent environment. A solution of chromophore dissolved in a good solvent is rapidly injected into a large volume of poor solvent for the chromophore (often water for organic chromophores), under vigorous stirring or agitation. Rapid mixing of these solvents results in an abrupt decrease in chromophore solubility, causing the chromophore molecules to aggregate in order to minimize unfavorable interactions with the new solvent environment.[139] This process is illustrated in Figure 2.1. Subsequent growth of these NPs is believed to occur by addition of chromophore monomers from solution to these nuclei, and continues until all chromophore molecules have been removed from solution.[146,147]

NPs nucleated by re-precipitation into water are known to acquire a negative surface

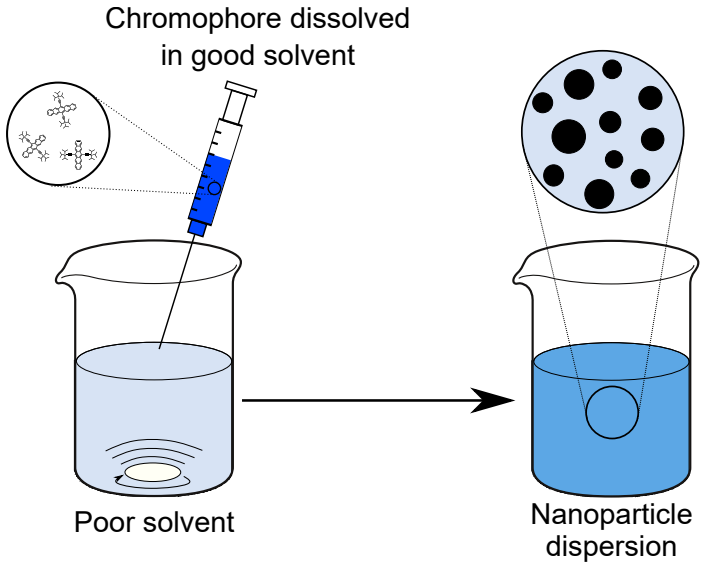

Figure 2.1: Illustration of nanoparticle preparation through re-precipitation.

charge,[148] which inhibits particle aggregation through repulsive electrostatic interactions. The origin of this surface charge is still under debate in the literature: some works have suggested that friction between the solvent and chromophores results in a static charge build-up at the NP surface,[149] while others have attributed this surface charge to an accumulation of hydroxide[150] or hydronium[151] ions at the NP surface, or even a partial charge transfer between water molecules at the interface.[152] Regardless of their cause, these negative surface charges impart significant colloidal stability to NPs prepared by the re-precipitation method, inhibiting NP aggregation.[153] TIPS-Pn NPs are also remarkably stable in the presence of oxygen: the TIPS-Pn triplet energy is too low to sensitize singlet oxygen and TIPS-Pn oxidation is both slow and reversible,[154] and so oxidative NP degradation occurs on a timescale of months.[72,134] Re-precipitation and subsequent handling of TIPS-Pn NPs may therefore occur under ambient atmospheric conditions, and as such these NPs represent a robust model system for experimental study of exciton dynamics.

TIPS-Pn NPs were prepared here by re-precipitation into water from tetrahydrofuran (THF) solution. Several previous studies have demonstrated that this solvent combination yields relatively monodisperse TIPS-Pn NPs suspensions, with reported particle sizes ranging from 30 nm up to 160 nm.[75,119,133,134,141] Specific experimental details of NP preparation are listed in the experimental methods sections of Chapters 3–6.

2.1.2 Dynamic Light Scattering

Size-dependent properties are well known to occur for NPs of both organic[145] and inorganic[155] materials. Therefore, accurate particle size quantification is crucial when reporting results of NP systems. In this work, NP particle sizes were characterized using dynamic light scattering (DLS). While methods such as electron microscopy (EM) or atomic force microscopy (AFM) are now commonly used for particle size determination, these approaches were unsuitable for use with the systems studied here as they generally require solid-phase samples for study. As discussed in Section 2.1.1, aggregation of NPs prepared by re-precipitation is inhibited by electrostatic repulsion between surface charges at the NP:water interface. These charges are unlikely to persist after removal of NPs from suspension, and hence particle aggregation becomes likely upon precipitation out of suspension. Therefore, the process of preparing solid samples for study with EM or AFM may alter the NP size. *In situ* particle size characterization was instead necessary, such that the NPs used here could be characterized while remaining in suspension. DLS allows for the study of liquid-phase particle dispersions, as it uses the light scattering correlation of particles undergoing Brownian motion to determine particle size. For relatively monodisperse particle distributions, DLS has been shown to yield particle sizes that agree closely with those determined by AFM.[156] DLS is capable of accurately measuring particle sizes as small as 1 nm,[157,158] and so this technique is well-suited for characterizing TIPS-Pn NPs prepared by re-precipitation, which typically have diameters on the order of tens of nanometers.[119,141]

As shown in Figure 2.2, DLS studies the scattering of a laser pulse from a particle dispersion at a scattering angle close to 180°. For non-interacting, monodisperse particles diffusing isotropically in suspension, the first-order autocorrelation function of scattered light as a function of time is given by[159]

$$g_1(t) = g_1(0)\exp(-Dq^2t), \tag{2.1}$$

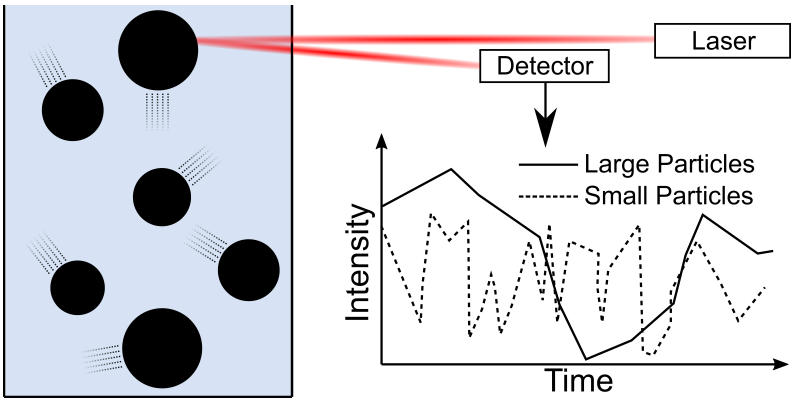

Figure 2.2: Schematic illustration of particle size determination by dynamic light scattering.

where D is the diffusion coefficient of the particles and q is the scattering vector, defined as

$$q = \frac{4\pi n_0}{\lambda} \sin\left(\frac{\theta}{2}\right). \tag{2.2}$$

Here n_0 is the solvent refractive index, λ is the wavelength of scattered light and θ is the angle of scattering.[156] Assuming spherical particles, the diffusion coefficient can be related to the hydrodynamic diameter d of the particles by the Stokes-Einstein equation:[160]

$$D = \frac{k_\mathrm{B} T}{3\pi\eta d}, \tag{2.3}$$

for η the viscosity of the liquid medium, T the temperature and k_B the Boltzmann constant. Combining Equations 2.1 and 2.3 therefore shows that $g_1(t) \propto \exp(-d^{-1})$, and so the scattering autocorrelation decay is highly sensitive to particle size. This dependence is illustrated in Figure 2.2: scattering patterns from smaller particles fluctuate more rapidly over time than those of larger particles. Equations 2.1–2.3 apply for perfectly monodisperse particle distributions, but in practice all NP suspensions exhibit some finite level of polydispersity. In this case, the overall autocorrelation function of the system is given by the sum of contributions from all particle sizes:

$$g_1(t) = \sum_i g_{1,i}(t) = \frac{1}{\sum_i n_i I_i} \sum_i n_i I_i \exp(-D_i {q_i}^2 t), \tag{2.4}$$

for n_i the number of particles present of size d_i and scattering intensity I_i.[161] Scattering data from such systems is generally analyzed using the method of cumulants, which calculates the mean scattering decay time and hence a mean particle size.[162] Specifically, this analysis yields what is known as a "Z-average particle diameter", defined as

$$d_\mathrm{Z} = \frac{\sum_i n_i I_i}{\sum_i {d_i}^{-1} n_i I_i}. \tag{2.5}$$

This finite polydispersity limits the dynamic range of particle sizes observable through DLS, as $I \propto d^{-6}$ in the limit of $d \ll \lambda$ and so weak signals from smaller particles may be masked by much stronger scattering from larger particles.[159] Particle size determination by DLS is therefore only quantitatively accurate for relatively monodisperse NP distributions.

Particle size characterization by DLS was undertaken here using a Malvern Zetasizer Nano ZSP, using a 633-nm laser at a backscattering angle of 173°. All particle sizes in this work are reported as Z-average diameters.

2.1.3 Transient Absorption Spectroscopy

Transient absorption (TA) spectroscopy, also commonly referred to as pump–probe spectroscopy, is a time-resolved spectroscopic technique used to study the kinetics of ultrafast photo-induced processes. A pump laser pulse resonant with a sample's absorbance is used to promote this sample to an excited state, and after some time interval a probe pulse is then used to determine the change in sample absorbance (ΔA) due to the initial pump. The probe pulse is typically broadband in nature, allowing for ΔA to be measured as a function of probe wavelength, λ. Modulation of the delay time between these two pulses also allows for study of ΔA as a function of time t. A two-dimensional dataset is hence built up by TA spectroscopy, with $\Delta A(\lambda, t)$ determined as

$$\Delta A(\lambda, t) = A(\lambda, t)_{\text{pump on}} - A(\lambda, t)_{\text{pump off}}. \tag{2.6}$$

$A(\lambda, t)_{\text{pump off}}$ simply corresponds to the sample's steady-state absorption spectrum. However, this is constantly monitored throughout the experiment by alternating pump-on and pump-off measurements, hence minimizing experimental noise due to laser intensity fluctuations. As $A(\lambda, t)_{\text{pump on}}$ contains signal contributions from excited-state species within the sample, Equation 2.6 may be rewritten as

$$\Delta A(\lambda, t) = A(\lambda, t)_{\text{es}} - A(\lambda, t)_{\text{gs}}, \tag{2.7}$$

where subscripts "es" and "gs" denote excited and ground states, respectively. Several photophysical phenomena may contribute to a TA signal, with the most common of these illustrated in Figure 2.3. Excited-state species formed by the pump pulse may be further excited to higher lying excited states, resulting in a probe absorption that is not present in the ground state. This generates a positive TA signal, and is referred to as an excited-state absorption (ESA). Sample excitation by the pump pulse reduces the ground-state population of the sample, thereby also decreasing the magnitude of

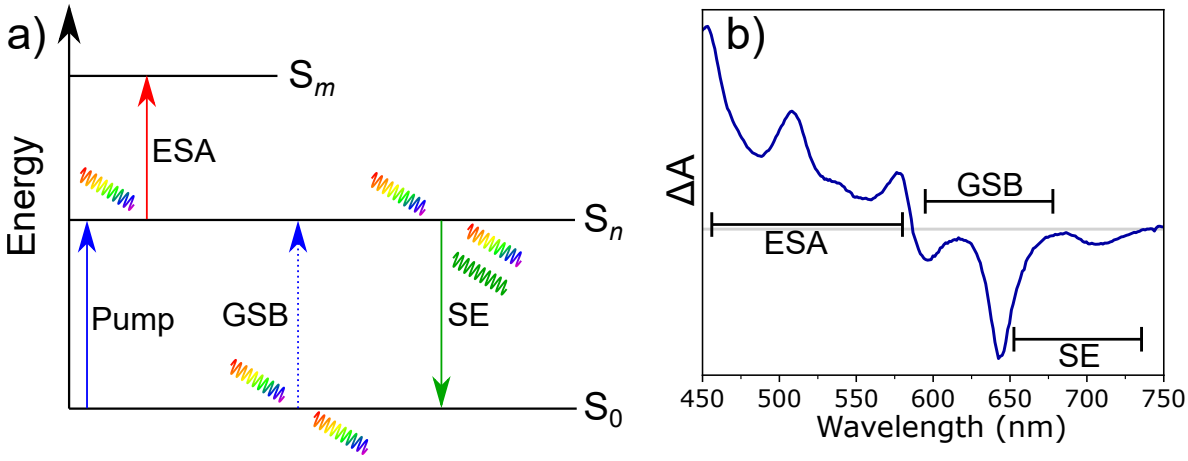

Figure 2.3: (a) Illustration of the photophysical processes contributing to a transient absorption (TA) spectrum: excited state absorption (ESA), ground-state bleach (GSB) and stimulated emission (SE). S_0 denotes the ground state, while S_n and S_m are excited electronic states of the system with $E_{S_n} < E_{S_m}$. Multicoloured pulses represent the broadband probe, and the dashed arrow represents an inhibited transition due to depopulation of the ground state. (b) Example of a typical TA spectrum, showing instances of all three signal types.

$A(\lambda, t)_{es}$ at wavelengths corresponding to the sample's steady-state absorbance. As per Equation 2.7, this hence manifests as a negative $\Delta A(\lambda, t)$ signal at these wavelengths, and is termed a ground-state bleach (GSB). Probe photons resonant with the energy gap between ground state and a populated excited state can also trigger radiative decay to the ground state through stimulated emission (SE). This increases the intensity of probe photons reaching the detector, producing an effect equivalent to increasing the sample transmittance and hence reducing the apparent magnitude of $A(\lambda, t)_{es}$ at these wavelengths. Therefore, SE also appears as a negative $\Delta A(\lambda, t)$ signal in TA spectra.

This work used a commercial transient absorption spectrometer with a 150-fs instrument response function (Ultrafast Systems, Helios), and a schematic diagram of this apparatus is shown in Figure 2.4a. Seed laser pulses at 800 nm were generated by a mode-locked Ti:sapphire oscillator (Spectra-Physics, Tsunami) pumped by a 532-nm continuous-wave Nd:YVO_4 laser operating at 8 W (Spectra-Physics, Millenia Prime). These pulses seeded a Ti:sapphire regenerative amplifier (Spectra-Physics, Spitfire Pro XP 100F), pumped by a 20-W, 1-kHz Q-switched Nd:YLF laser (Spectra-Physics, Empower), to produce 800-nm laser pulses with a 100-fs pulse width at a repetition rate of 1 kHz. Pump pulses at a variety of wavelengths were generated by an optical parametric amplifier (OPA) (Light Conversion, TOPAS-C), and were modulated by an optical chopper running at 500 Hz. Broadband visible probe pulses were obtained through focusing of the 800-nm fundamental output onto a 3.2-mm sapphire crystal. Probe delay timing was varied by a computer-controlled delay line, out to a maximum delay time of 3.2 ns. Probe pulses were split into signal and reference lines before reaching the sample, with each probe measured by a linear CMOS detector (Ultrafast Systems, CAM-VIS-2). Further experimental details regarding pump wavelengths, pulse energies, polarizations and spot-sizes are given in the experimental methods sections of Chapters 3–6.

2.1.4 Fluorescence Upconversion Spectroscopy

Time-resolved fluorescence data were collected here using fluorescence upconversion (UC) spectroscopy. Similarly to TA spectroscopy, fluorescence UC is a two-pulse ultrafast spectroscopic technique, in which an initial pump pulse is used to excite the sample of interest. Fluorescence from this sample arising from spontaneous emission following photoexcitation is then focused onto a β-barium borate (BBO) crystal. A second gate pulse is also focused onto this crystal, overlapping with the focused sample fluorescence. BBO is a birefringent material with nonlinear optical properties, and so at the correct rotation of the crystal (termed the "phase-matching condition") sum-frequency generation (SFG) between the gate pulse and the fluorescence can occur. This effectively "up-converts" the two pulses to form higher-energy photons, which are then detected by filtering out any residual light from the gate or pump pulse. Crucially, SFG can only occur when the gate pulse and fluoresence are overlapped in time at the BBO. Time resolution in fluorescence UC is hence obtained by delaying the timing of the gate pulse relative to the pump. This limits the time resolution of this data only by the width of the laser pulses, rather than by the significantly slower response times of the electronic detectors.

Fluorescence UC experiments were undertaken here using a commercial fluorescence spectrometer possessing a 450-fs instrument response function (Ultrafast Systems, Halcyone), and a schematic diagram of this apparatus is shown in Figure 2.4b. The same

Ti:sapphire regenerative amplifier used by the Helios TA spectrometer described in Section 2.1.3 was also used here as the fundamental laser source, generating 800-nm, 100-fs pulses at a 1-kHz repetition rate. Pump pulses at 590 nm were produced using an OPA (Light Conversion, TOPAS-C) from the second harmonic of the signal. Pulses from the amplifier output at 800 nm were used as the gate, focused onto an 0.4-mm BBO crystal for SFG with sample fluorescence. Delay timing of the gate pulse was achieved by a computer-controlled optical delay line, out to a maximum possible delay time of 3.2 ns. Upconverted fluorescence was passed through a monochromator to filter out residual pump and gate, and was subsequently detected by a photomultiplier tube.

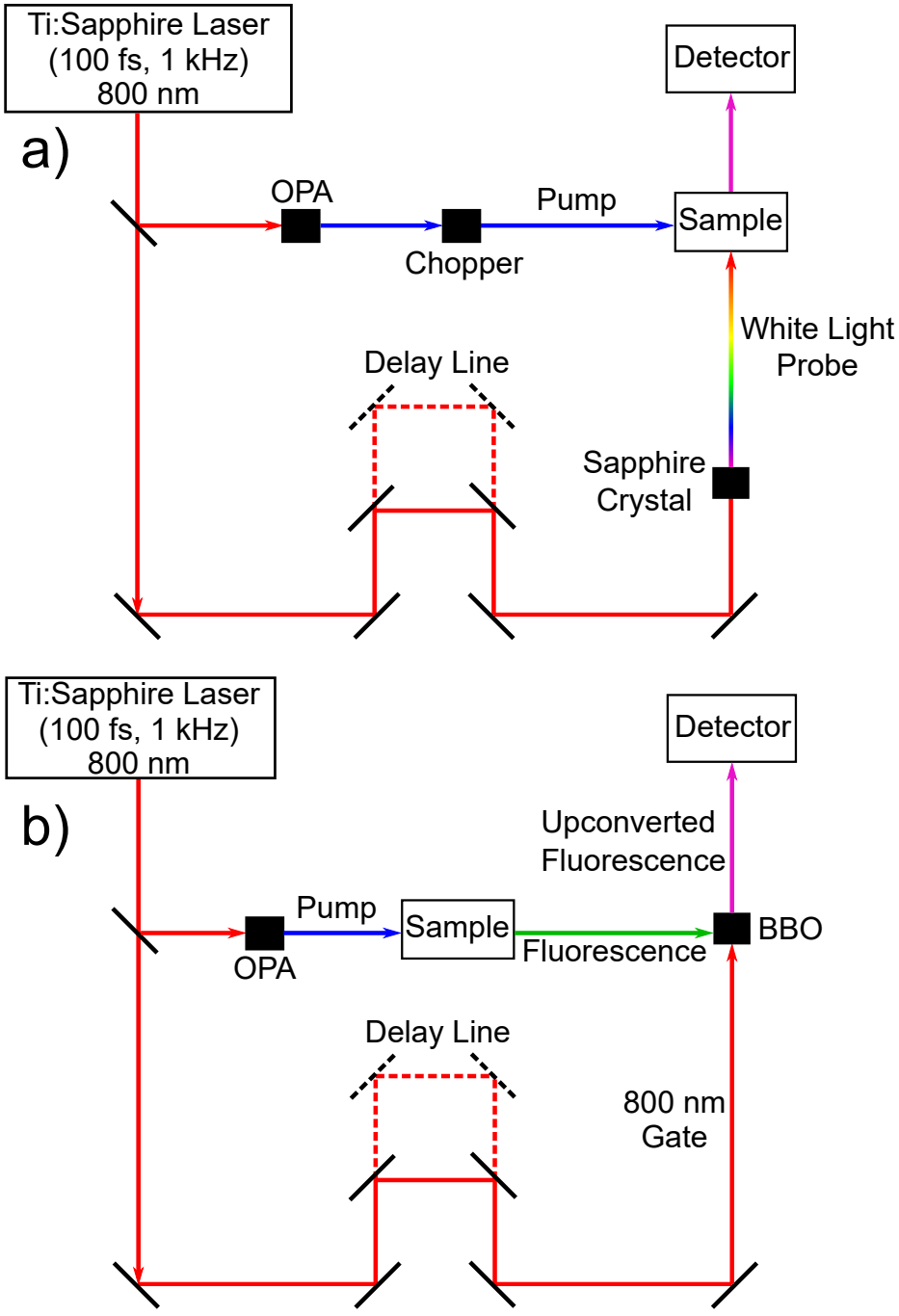

Figure 2.4: Schematic diagrams of (a) transient absorption and (b) fluorescence upconversion apparatus used in this work.

2.2 Theoretical and Computational Methods

2.2.1 Density Functional Theory

Density functional theory (DFT) is a computational technique used to compute the ground-state electronic structure and related properties of a molecular system. Wavefunction-based electronic structure solution methods such as Hartree-Fock (HF) attempt to solve the electronic Schrödinger equation:

$$\hat{H}^{\text{elec}}\Psi_0^{\text{elec}}(\mathbf{r}^n) = E_0^{\text{elec}}\Psi_0^{\text{elec}}(\mathbf{r}^n), \tag{2.8}$$

for $\hat{H}^{\text{elec}}$ the electronic Hamiltonian operator, E_0^{elec} the ground-state electronic energy of the system and $\Psi_0^{\text{elec}}(\mathbf{r}^n)$ the ground-state wavefunction of a system consisting of n electrons with spatial coordinates $\mathbf{r}^n$.[163,164] $\Psi_0^{\text{elec}}(\mathbf{r}^n)$ is hence a $3n$-dimensional function, which becomes highly complex and prohibitively difficult to solve computationally for large molecular systems. An alternative approach was developed by Hohenberg and Kohn, who showed that the energy of a molecular system is a unique functional of the electron density ρ, and that this energy is minimized if and only if ρ is equal to the ground-state electron density ρ_0.[165] ρ depends only upon the three Cartesian coordinates, and so calculating the system's electron density rather than electronic wavefunction significantly reduces the number of degrees of freedom to be considered. Additionally, the above "Hohenberg-Kohn theorem" also prescribes a method for determining the ground-state electronic density of a molecular system: the electron density which minimizes the system energy is the true ground-state density.

A practical approach to determining the energy of this ground-state electron density was subsequently developed by Kohn and Sham, who showed that the energy of a molecular system could be expressed in terms of an equivalent system containing the same electron density but with non-interacting electrons:[166]

$$E_0[\rho] = T[\rho] + E_{\text{EE}}[\rho] + E_{\text{NE}}[\rho] + E_{\text{XC}}[\rho]. \tag{2.9}$$

In Equation 2.9, $T[\rho]$ denotes the electron kinetic energy of this non-interacting system, and $E_{\text{EE}}[\rho]$ and $E_{\text{NE}}[\rho]$ the electron-electron and nuclear-electron coulombic interactions, respectively. These quantities have exact classical solutions, and so these three terms can be computed exactly. All remaining non-classical electron-electron interactions such as exchange and correlation combined into the final term, $E_{\text{XC}}[\rho]$. This so-called "exchange-correlation" functional is the only non-exact term in Equation 2.9, and is approximated by a number of different DFT methods. Local density approximation (LDA) and generalized gradient approximation (GGA) functionals estimate $E_{\text{XC}}[\rho]$ as the potential of a hypothetical uniform electron gas, while hybrid functionals combine LDA and GGA functionals with exact quantities of exchange from HF methods. From a given starting structure and density, a DFT calculation iterates over possible electron densities until $E_0[\rho]$ as per Equation 2.9 is minimized, obtaining the ground-state energy and electron density. "Single-point" calculations calculate this only for a specified input structure, while optimization calculations subsequently vary the molecular geometry until an energy-minimum molecular structure is found.

DFT calculations in this work were performed using both the Gaussian 16 and Q-Chem 5 software packages.[167,168] Specific details regarding functionals, basis sets and molecular systems are given in the computational methods sections of Chapters 3 and 4.

2.2.1.1 Constrained Density Functional Theory

DFT as presented in the preceding section allows for computational determination of the electron density and associated physical properties for the ground state of a molecular system. However, electronic states other than the global energy minimum are often of physical interest, but cannot be studied by conventional DFT techniques. In particular, spin- or charge-localized states are of interest for singlet fission (SF) chromophores and other organic semiconductors, but often do not correspond to global energy minima states and so are inaccessible by DFT. Therefore, alternative computational formulations are required to study these states. Constrained density functional theory (CDFT) is one such method, in which a constraint to the system's electron density or spin density is applied such that the minimum-energy state in the presence of this constraint differs from the ground state.[169] This constraint is applied as an external potential added to the $E_{\mathrm{XC}}[\rho]$ term in Equation 2.9, and is implemented as a Lagrange multiplier during the minimization procedure.[170]

CDFT was used in this work to study triplet excitons localized upon individual molecules within TIPS-Pn dimer pairs. Constraints were applied such that one molecule in each dimer pair possessed singlet multiplicity, but the overall molecular pair was of triplet multiplicity. These calculations were performed for triplet localization upon each molecule within the pair, with subsequent configuration-interaction (CI) calculations used to determine the electronic coupling between these diabatic states.[80,171] Further details of these calculations are presented in Chapter 4.

2.2.2 Kinetic Monte Carlo Simulations

Much of the research presented in this thesis considers the dynamic evolution of excited-state systems. Kinetic models are frequently used to understand the evolution of such systems over time; for examples of this, see Chapters 4 and 5. However, analytical solutions or simple kinetic schemes for this behavior are not always available, and so in some circumstances more advanced computational techniques are required to appropriately describe these dynamic processes. One method which has been extensively used to model the dynamics of excitons in condensed-phase materials is the kinetic Monte Carlo (KMC) technique.[172–176] KMC is a probability-based simulation method used to model stochastic processes for which the rates or probabilities of transitions between states are known. By Poisson statistics, the probability $P(t)$ of a process *not* occurring in time interval Δt is given by

$$P(t) = \exp(-k\Delta t), \tag{2.10}$$

where k is the probability per unit time of the process occurring. Therefore, the time taken for a stochastic process to occur can be expressed as

$$\Delta t = -\frac{\ln x}{k}, \tag{2.11}$$

for $x \in (0, 1]$ a random uniform variate.[175] In the KMC method, Δt for every possible process in the system is calculated as per Equation 2.11. The process with the smallest Δt is chosen and acted upon, and the time of the system is incremented by Δt. This is repeated until some cutoff or endpoint threshold for the simulation is met. KMC simulations were used here to model the kinetics of triplet exciton hopping and triplet–triplet annihilation (TTA) in crystalline TIPS-Pn NPs. Specific details of the model used are given in the computational methods section of Chapter 6.

CHAPTER 3
Organizing Crystalline Functionalized Pentacene Using Periodicity of Poly(Vinyl Alcohol)

Statement of Authorship

Title of Paper	Organizing Crystalline Functionalized Pentacene Using Periodicity of Poly(Vinyl Alcohol)
Publication Status	Published
Publication Details	Hudson, R. J.; de la Perrelle, J. M.; Pensack, R. D.; Kudisch B.; Scholes, G. D.; Huang, D. M.; Kee, T. W. Organizing Crystalline Functionalized Pentacene Using Periodicity of Poly(Vinyl Alcohol). *J. Phys. Chem. Lett.* **2020**, *11*, 516–523. DOI: 10.1021/acs.jpclett.9b03373

Principal Author

Principal Author	R.J. Hudson		
Contribution to the Paper	Experimental work, computational modelling, data analysis, construction of figures, writing of manuscript.		
Overall Percentage	85%		
Certification	This paper reports on original research I conducted during the period of my Higher Degree by Research candidature and is not subject to any obligations or contractual agreements with a third party that would constrain its inclusion in this thesis. I am the primary author of this paper.		
Signature		Date	25/11/21

Co-Author Contributions

By signing the Statement of Authorship, each author certifies that the stated contributions to the following publication are accurate and that permission is granted for the

publication to be included in this thesis.

Co-Author	J.M. de la Perrelle		
Contribution to the Paper	TIPS-tetracene:PVA and PEG/PAA/ethanol experiments, assistance with editing of manuscript.		
Signature		Date	23/11/21

Co-Author	R.D. Pensack		
Contribution to the Paper	Preliminary experiments contributing to the development of this work, assistance with editing of manuscript.		
Signature		Date	23/11/2021

Co-Author	B. Kudisch		
Contribution to the Paper	TES-pentacene:PVA experiments, assistance with editing of manuscript.		
Signature		Date	24/11/2021

Co-Author	G.D. Scholes		
Contribution to the Paper	Supervision of preliminary experiments contributing to the development of this work, assistance with editing of manuscript.		
Signature		Date	24/11/2021

Co-Author	D.M. Huang		
Contribution to the Paper	Supervision of computational work, assistance with writing and editing of manuscript.		
Signature		Date	22/11/21

Co-Author	T.W. Kee		
Contribution to the Paper	Supervision of project, assistance with writing and editing of manuscript, corresponding author.		
Signature		Date	22/11/2021

3.1 Abstract

Nanoparticles (NPs) of acenes exhibit highly efficient intermolecular singlet fission (SF). Recent reports indicate that altering the morphology of 6,13-(triisopropyl silylethynyl)pentacene (TIPS-Pn) NPs has a profound influence on their SF dynamics. Here, we show that poly(vinyl alcohol) (PVA) induces a phase transition in pre-formed TIPS-Pn NPs. These NPs are amorphous when initially formed, but crystalline after addition of PVA. Surface characterization indicates that a diffuse PVA layer surrounds the NPs. We propose that a periodic interaction between the hydroxyl groups of PVA and TIPS groups of TIPS-Pn on the NP surface induces a large-scale structural rearrangement to yield crystalline TIPS-Pn. Such reorganization in pre-formed organic NPs is unprecedented, and we believe that this is the first report of such an effect induced by polymer adsorption. Transient absorption spectroscopic results reveal that SF within these NPs is accelerated by an order of magnitude upon structural rearrangement.

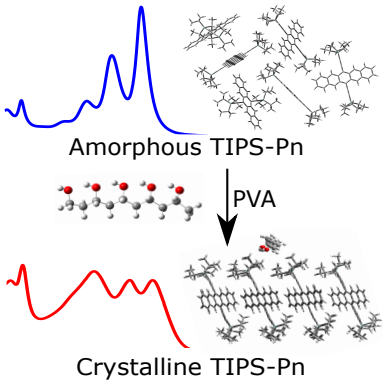

3.2 Introduction

Singlet fission (SF) is a spin-allowed exciton multiplication process, in which a singlet excited-state chromophore couples to an adjacent ground-state chromophore to form two triplet excited states. This process involves a spin-entangled correlated triplet pair state:[19]

$$S_1 + S_0 \rightarrow {}^1(TT) \rightarrow T_1 + T_1. \tag{3.1}$$

SF-capable chromophores have attracted intense interest in recent years, as their incorporation into photovoltaic (PV) devices may enable circumvention of the detailed balance limit.[10,22,23,177] However, to improve photovoltaic efficiencies, a SF quantum yield close to 200% (two triplet excitons produced per singlet exciton) is required, as well as the SF process being sufficiently fast to out-compete thermal relaxation of excitons. Therefore, significant effort is currently being invested into developing an improved understanding of the SF mechanism, such that chromophores that undergo high-yielding and rapid SF may be engineered for use in future photovoltaic devices.

Several different organic structural motifs have been identified as being favorable for SF, including carotenoids,[140] diimides[44,178] and pyrollo-thiophene structures.[179] However, the most widely-studied family of SF chromophores are the acenes.[34,51,180–186] In particular, 6,13-(triisopropylsilylethynyl)pentacene (TIPS-Pn) has been extensively studied,[57,59,72,75,101,110,119,131,133,134,187,188] as its SF is slightly exoergic ($E(S_1) > 2E(T_1)$), and has been shown to occur within 100 fs of excitation.[47,52] As SF is an intermolecular process, local molecular packing and overall structural morphologies influence SF kinetics significantly. Recently, we showed that a substantial population of the correlated triplet pair intermediate were unable to separate into free triplets in amorphous TIPS-Pn nanoparticles (NPs), and attributed this to the disordered molecular packing in these NPs preventing effective triplet hopping away from the SF site.[72] In another study, the rate of SF was observed to increase with the proportion of crystalline do-

mains in thin films of TIPS-Pn.[110] Similarly, by tuning intermolecular packing through altering the size of the side-chains on pentacene derivatives, SF rates in NP dispersions have been shown to vary by up to an order of magnitude.[134]

SF in TIPS-Pn is often studied as an aqueous NP dispersion, as this system allows for SF dynamics to be probed spectroscopically in a quasi-solid state without issues related to thin films including opacity and localized sample heating.[72,119,133,134] This approach has previously been applied to study a wide variety of other chromophores.[144,189–192] However, conflicting conclusions have been reached for the resulting morphologies of TIPS-Pn NPs. Tayebjee and co-workers reported that TIPS-Pn NPs re-precipitated from tetrahydrofuran (THF) into water initially formed amorphously packed structures, which then slowly reorganized into crystalline domains over days to weeks.[133] However, in other studies of TIPS-Pn NPs prepared under equivalent conditions, such crystallization was absent.[72,134] We then demonstrated that this transition of amorphous to crystalline morphologies could be replicated in the presence of a silicone-based syringe lubricant,[119] but the chemical species responsible for this phase transition was not identified. However, it was also observed that re-precipitation of TIPS-Pn into dilute aqueous poly(vinyl alcohol) (PVA) solutions induced an identical effect, and an additional study has since reported modulation of pyrene NP morphology using a similar method.[193] PVA is a common additive in the preparation of both organic[190–192,194–197] and inorganic[198–200] NP dispersions, although the rationale for this is often unclear. Some authors have noted that inclusion of PVA appears to stabilize NP dispersions through binding to the surface and acting as a capping agent,[201,202] while others have also suggested that it influences the nucleation stage through controlling factors such as viscosity and surface tension.[203] However, in the case of TIPS-Pn NPs, the nature of the interaction that stabilizes the crystalline phase has been unclear until now.

In this work, we examine how PVA induces morphological change in TIPS-Pn NPs. Addition of PVA to pre-formed NPs results in a phase transition of amorphous to crystalline morphologies. Characterization of these structures suggests that a PVA:TIPS-Pn interaction at the NP surface templates these crystalline domains. This effect is specific to TIPS-Pn and PVA, and likely stems from a favorable, periodic dispersion–dipole interaction of the polymer hydroxyl groups with TIPS groups of TIPS-pentacene. Transient absorption studies then reveal that altering the TIPS-Pn morphology through this method increases the rate of SF within the NPs by an order of magnitude, providing a straightforward and low-cost method of tuning both morphology and SF dynamics in TIPS-Pn.

3.3 Results and Discussion

The steady-state visible absorption spectra of TIPS-Pn in THF is shown in Figure 3.1(a). The most prominent absorption peaks are due to transitions within the $S_1 \leftarrow S_0$ vibronic manifold, with the 0–0 transition at 640 nm, the 0–1 transition at 590 nm and the 0–2 transition at 550 nm.[72] Two smaller peaks at 438 and 414 nm have previously been assigned to the $S_3 \leftarrow S_0$ and $S_4 \leftarrow S_0$ transitions, respectively.[204] On re-precipitation into water, a small amount of scattering occurs at shorter wavelengths (confirming the formation of nanoscale particles), and a slight change in relative vibronic peak intensities is observed, attributable to weak intermolecular couplings between the chromophores.[72,134] The absence of major spectral changes between solution

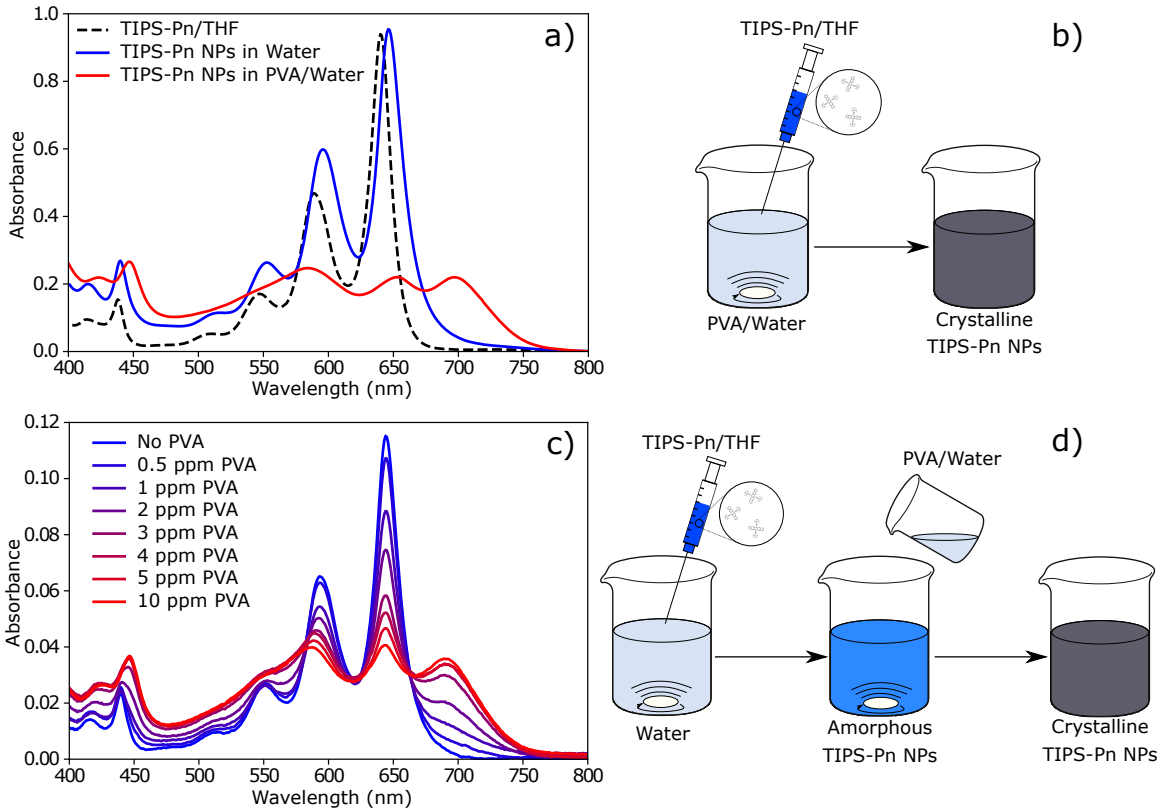

Figure 3.1: (a) Steady-state absorption spectra of TIPS-Pn NPs re-precipitated in either water or 100 ppm aqueous solution of PVA, with the spectrum of TIPS-Pn in THF solution shown for reference. (b) Schematic diagram of how the crystalline NPs with spectrum shown in (a) were prepared. (c) Steady-state absorption spectra of TIPS-Pn NPs re-precipitated in water with subsequent addition of PVA at various concentrations, collected 30 minutes after PVA addition. (d) Schematic diagram of how the crystalline NPs with spectra shown in (c) were prepared. TIPS-Pn concentrations are 200 ppm for the spectra presented in (a) and 25 ppm for (c). Spectra were collected in a 2-mm path length cuvette.

and re-precipitation (beyond small changes in relative vibronic peak intensities) indicates that any intermolecular interactions within the NPs are indeed weak. As such, these NPs are assigned as having amorphous morphologies with a lack of long-range structural order, agreeing with previous work.[72,75,119,133,134]

On re-precipitation in the presence of PVA, however, a significant change in the visible absorption spectrum is observed (Figure 3.1(a), red curve). The previously identified peaks broaden and red-shift considerably, resulting in a spectrum that has been previously assigned to crystalline TIPS-Pn.[59,119,131,133,188,205] Augmenting these findings, our results also show that this same conversion can be achieved by addition of PVA solution to pre-formed amorphous TIPS-Pn NPs (Figure 3.1(c)). Remarkably, this phase transition occurs at room temperature and on a timescale ranging from seconds to minutes, indicating that the PVA chains induce a large-scale reorganization of TIPS-Pn molecules under ambient conditions. Preliminary kinetic studies show that this process exhibits a sigmoidal behavior, suggesting that the initial PVA:TIPS-Pn interaction nucleates crystalline domains which then spread throughout the NP structure(s). These kinetics also show a strong dependence on PVA molecular weight, with crystallization occurring more rapidly with shorter polymer chains (Supporting

Information).

To support the morphological assignments of the NPs, powder X-ray diffraction (PXRD) was undertaken on samples evaporated to dryness, with the resulting diffraction patterns shown in Figure 3.2. For NPs precipitated in PVA, several diffraction peaks are observed, agreeing well with the patterns previously recorded for TIPS-Pn crystals and polycrystalline thin films.[110,132] This result supports the earlier assignment of a crystalline morphology to these NPs, as there is sufficient structural order within these NPs to give these characteristic X-ray reflections. Evaporation of amorphous TIPS-Pn NPs in aqueous suspension resulted in significant aggregation into macroscopic, needle-like crystals. This phenomenon demonstrates the metastable nature of amorphous TIPS-Pn, with the rapid flash-precipitation method kinetically trapping the NPs in this phase. To preserve the structure of these amorphous NPs on evaporation to dryness, a polymer that is inert towards TIPS-Pn reorganization, poly(acrylic acid) (PAA) or poly(ethylene glycol) (PEG) (see below), was added in order to isolate the NPs from one another. For NPs co-evaporated with either PAA or PEG, only diffraction peaks attributable to the polymer were observed (Figure 3.2 and Supporting Information). Therefore, these NPs lack long-range structural order, and hence the assignment of amorphous morphologies is valid.

NP characterization by dynamic light scattering (DLS) showed particle size distributions with an initial Z-average diameter of 75 nm for amorphous NPs (Table 3.1), which agrees with the sizes previously determined for TIPS-Pn NPs prepared by similar methods.[119,134] On addition of PVA (while keeping TIPS-Pn concentration constant), however, these size distributions broaden and shift to a larger diameter (Table 3.1 and Supporting Information). As the hydrodynamic diameter measured by DLS includes species adsorbed or coordinated to the NP surface, we propose that adsorption of PVA chains to the TIPS-Pn NP surfaces leads to these changes in size and size dispersity. Core-shell-like structures may form with increased apparent particle size, as has been previously observed for PVA adsorption to NPs of other organic materials.[201,202] Additionally, uneven PVA coatings on the NP surface or un-adsorbed chain segments may

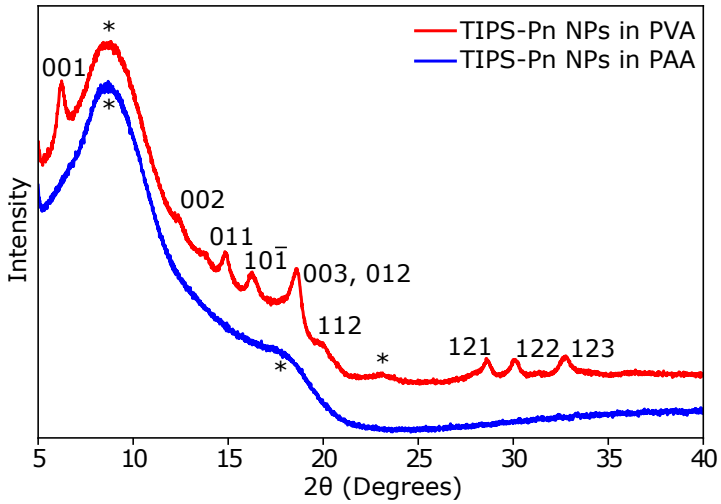

Figure 3.2: Powder X-ray diffraction patterns of TIPS-Pn NPs co-precipitated from suspension in either PVA or PAA. Reflection assignments are made based upon those by Chen and co-workers for TIPS-Pn crystals,[132] while the peaks corresponding to polymer matrices are indicated with asterisks. Patterns are offset for clarity.

Table 3.1: Zeta potentials and Z-average particle diameters of TIPS-Pn NPs before and after addition of PVA.

[PVA] (ppm)[a]	Z-Average Diameter (nm)[b]	Zeta Potential (mV)[b]
0	75.65 ± 0.06	-38.0 ± 0.4
100	107.9 ± 0.5	-15.5 ± 0.5

[a] TIPS-Pn concentration fixed at 20 ppm.

[b] Uncertainties are twice the standard error in the mean calculated from triplicate measurements of each sample.

yield a wider apparent particle size distribution. A similar phenomenon has previously been observed when modelling the adsorption of PVA chains to silver NPs,[206] for which diffuse multilayers were found on the NP surface as the number of PVA monomers in the system was increased. This effect is also supported by zeta-potential measurements, which show that this increase in particle Z-average diameter is concomitant with screening of the particle's surface charge (Table 3.1). However, when comparing these changes in particle size distributions to the spectral changes observed in Figure 3.1(c), the onset of crystalline absorption features corresponds to a minimal increase in Z-average diameter. Therefore, we conclude that the interaction between PVA and TIPS-Pn that induces crystallinity occurs upon the NP surface, and that only a minimal coating of PVA is required to initiate this morphological conversion.

Attempts to reproduce this phase transition with other water-soluble polymers (PEG and PAA) were unsuccessful. Addition of ethanol as a "monomer equivalent" of PVA also resulted in a negligible effect on TIPS-Pn NP morphology (Supporting Information). Therefore, of the materials tested here, only PVA, which contains hydroxyl groups regularly spaced upon a polymer backbone, is able to induce crystallinity in TIPS-Pn. Additionally, attempts to induce crystallinity in NPs of 5,12-(triisopropyl silylethynyl)tetracene (TIPS-Tn) with PVA were unsuccessful (Supporting Information). This result therefore implies that the interaction causing this phase transition is specific to PVA and TIPS-Pn; changing either the polymer or the acene inhibits this effect. However, TIPS-Pn contains very few structural motifs capable of specific intermolecular interactions. Indeed, the only non-hydrocarbon atoms within TIPS-Pn are the silicon atoms in the TIPS-groups, which are very sterically hindered and are unlikely to engage in any intermolecular interaction. Hence, this interaction is most likely to be governed by dispersion or dispersion-dipole forces between the OH groups of PVA and the isopropyl groups of TIPS-Pn.

For crystalline TIPS-Pn, the molecular displacement between adjacent, slip-stacked molecules along the crystal a-axis (7.565 Å)[125] is nearly three times the inter-hydroxyl spacing of PVA chains ($3 \times 2.520 = 7.560$ Å).[207] It is likely that a regular interaction between the periodicity of these structures promotes and stabilizes the crystalline morphology of TIPS-Pn. A structural templating effect may occur, in which the NP structure reorganizes in order to maximize this periodic interaction. To test this hypothesis, we used density functional theory (DFT) to model the adsorption of short PVA oligomers onto a "frozen", crystalline structure of twelve TIPS-Pn molecules, from a number of randomly chosen starting structures (see Supporting Information for further details). While the use of DFT for dispersion-based interactions is less common than for bonded interactions, functionals such as ωB97XD[208] contain an empirical dispersion correction and can better account for these interactions than most other DFT

functionals. Therefore, the use of DFT with ωB97XD can offer insight into the nature of the PVA:TIPS-Pn interaction.

Figure 3.3(a) shows the binding energies of short $(PVA)_n$ oligomers to the TIPS-facing side of the TIPS-Pn crystal structure. A relatively modest binding strength is observed for short oligomers ($n < 4$), with the chains oriented away from the surface, interacting with TIPS-Pn only through a single terminal methyl group. A significant increase in binding strength occurs for chains of four monomers or longer, corresponding to adsorption of the PVA oligomer upon the TIPS-Pn surface. In this binding mode, the hydroxyl groups on the PVA chains point towards the surface and interact with the TIPS groups, as demonstrated in Figure 3.3(b) for the PVA pentamer. The binding shows agreement with the repeat-unit matching suggested above. Figure 3.3(c) shows that for PVA_5:TIPS-Pn_{12}, every fourth hydroxyl group interacts with an equivalent position on adjacent TIPS-Pn molecules. Therefore, we postulate that

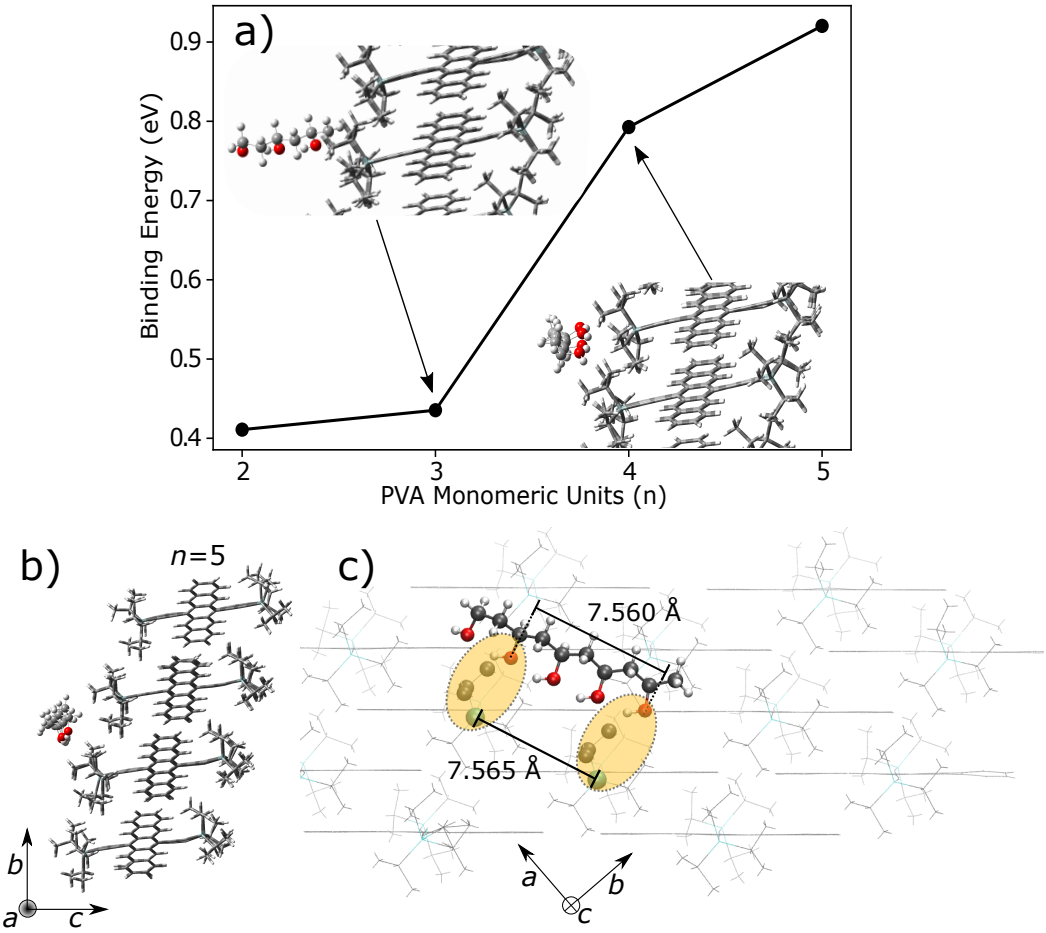

Figure 3.3: (a) Binding energies of PVA oligomers to the TIPS-Pn_{12} crystal structure, with insets showing the lowest energy binding modes of the PVA trimer and tetramer. (b) Side-on and (c) side-on views of the PVA_5:TIPS-Pn_{12} minimum-energy structure (binding energy of 0.92 eV). Highlighted regions represent locations of the periodic interaction between hydroxyl- and TIPS-groups. Crystallographic axes for TIPS-Pn are shown in (b) and (c), with the former looking down the a axis (out of the page) and the latter the c axis (into the page). Carbon atoms are shown in grey, hydrogen in white, oxygen in red and silicon in cyan. Energies were computed at the ωB97XD/cc-pVDZ level of theory. Further details on these calculations are presented in the Supporting Information.

the crystallization of amorphous TIPS-Pn NPs upon PVA adsorption occurs by this hydroxyl:TIPS interaction. This interaction promotes rearrangement of the TIPS-Pn molecules and organizes the molecular structure in order to maximize this favorable interaction. In the previous report of chemical additives causing phase instability in amorphous TIPS-Pn NPs, it was identified that oligomers of an alkyl siloxane or other silicone-based compound could also induce such phase transitions, but the exact identity of this species was undetermined.[119] We suggest that the oligomers in question may have a structure similar to PVA, containing hydroxyl groups spaced such that a regular interaction with the TIPS groups is possible.

DFT calculations were also performed on tetramers of PEG and PAA interacting with the TIPS-Pn surface (Supporting Information), but the minimum-energy structures for both show a lack of structural matching between polymer and TIPS-Pn. A higher-energy conformer with the PEG chain lying parallel to the TIPS-Pn stacking direction exists, but with a negligible binding energy of 0.1 eV and a mismatch in periodicity. Therefore, these calculations predict that any PEG:TIPS-Pn or PAA:TIPS-Pn surface interactions are unlikely to template the formation of crystalline domains, which agrees with the experimental results discussed above.

As mentioned above, use of ethanol in place of PVA is ineffective in inducing crystallinity in TIPS-Pn NPs, even though ethanol may also interact with TIPS-Pn through hydroxyl groups. It can therefore be inferred that the periodicity of this interaction is the essential factor in inducing morphological change within the NPs. The periodicity of the polymer chain must also match that of the TIPS-Pn crystal packing; PEG and PAA possess repeat units that show a mismatch with TIPS-Pn, hence an absence of periodic interaction between adjacent TIPS-Pn molecules. This periodic-matching criterion also explains the lack of crystallinity induced in TIPS-tetracene on PVA addition, as TIPS-Tn packs in a pairwise motif in the crystalline phase, rather than the two-dimensional "brickworks" pattern that TIPS-Pn adopts. Hence, there is a lack of long-range periodic matching between TIPS-Tn and PVA, as a polymer chain aligned with one pair of TIPS-Tn molecules in a crystalline structure is then misaligned with all other neighboring molecules.

However, even for chromophores that show long-range crystalline stacking similar to TIPS-Pn, the slip-stacked molecular displacement should match the polymer repeat unit in order to organize the crystal structure. For example, 6,13-(trimethylsilylethynyl) pentacene (TMS-Pn) and 6,13-(triethylsilylethynyl)pentacene (TES-Pn) are pentacene derivatives that differ from TIPS-Pn only by the length of the side-chains (methyl and ethyl *vs* isopropyl), with the latter having been previously studied alongside TIPS-Pn in the context of singlet fission kinetics.[75] Both of these molecules show extended π-stacking in their crystal structures, but their stacking displacements (5.83 & 7.20 Å for TMS-Pn[124] and TES-Pn,[209] respectively) exhibit a mismatch with multiples of the PVA repeat unit (5.04 or 7.56 Å for 2 or 3 repeat units, respectively). Therefore, a periodic interaction between PVA and these chromophores along the π-stacking direction is absent. PVA is therefore unlikely to induce crystallinity in amorphous systems of these molecules, which is supported by experimental results of TES-Pn NPs (Supporting Information). An absence of morphological change is observed in TES-Pn NPs on re-precipitation in the presence of PVA. While periodicity-induced morphological change is only observed in TIPS-Pn with PVA here, should a similar matching be found between other polymers and small molecules a similar structural reorganization could be induced.

Structural reorganization in bulk TIPS-Pn has previously been reported using either thermal[110,120] or solvent vapor annealing[110,210] methods. In the case of the latter, reorganization is achieved through the absorption of solvent vapor into a solid TIPS-Pn film, slightly solvating the molecules. This phenomenon increases the mobility of the TIPS-Pn molecules, allowing rearrangement into the thermodynamic minimum-energy structure (slip-stacked crystalline TIPS-Pn). The PVA-induced morphological change observed here in TIPS-Pn shares some similarities with solvent vapor annealing; both involve the introduction of an additional chemical species to induce reorganization of TIPS-Pn morphology. However, we emphasize that these processes are likely to be distinctly different. Solvent vapor annealing requires the absorption of small solvent molecules into the bulk material, followed by structural relaxation and then desorbtion of the solvent molecules. While the diffusion of short-chain PVA beyond the NP surface is possible, the high molecular weight of PVA chains used here (approx. 3000 repeat units) should significantly inhibit diffusion into the NP interior. Given the relatively large size of the NPs used here (Table 3.1) and the rapid crystallization observed on PVA addition (Supporting Information), it is very likely that crystallinity is induced through interactions with the NP surface rather than the interior. Additionally, any PVA that is absorbed into the NP interior is unlikely to then desorb; a previous study of polymer NPs found that any PVA incorporated into the NP was irreversibly bound in that position.[203] Therefore, any PVA inside the TIPS-Pn NPs would be expected to remain there, disordering the molecules and preventing the formation of crystalline domains. Clearly, that phenomenon is absent here, so this effect must be a distinctly different process to solvent vapor annealing. Rather than solvating the entire solid, this process likely occurs only on the NP surface, nucleating small crystalline domains that then spread throughout the structure. The exact mechanism by which the periodic TIPS-Pn:PVA interaction nucleates crystallinity is currently unclear. PVA binding may simply lower the energy barrier of reorganization from the metastable amorphous phase into the stable crystalline phase, or it may play a more active role in the molecular motions associated with this reorganization.

PVA is commonly used as a templating or emulsifying agent in the preparation of organic NP dispersions, typically acting as a capping agent to promote particle dispersity and minimize aggregation.[190,191,194,201,203] Previous studies have shown that inclusion of PVA in the re-precipitation step slows the growth of perylene NPs,[202] and favors the formation of the crystalline phase in pyrene NPs.[193] However, in all of these previous reports, PVA acts as a template to guide the formation of NPs to a desired size or morphology, and is considered only within the context of NP formation and growth. Here, it evident that PVA alters the morphology of TIPS-Pn NPs after the re-precipitation and growth stages, induced by a periodic, dispersion-based interaction on the NP surface. To the best of our knowledge, this is the first reported instance of such an interaction reorganizing the structure of pre-formed organic NPs in suspension. The importance of this distinction should not be overlooked; rather than acting as a stabilizing agent for the NPs, the PVA is *destabilizing* the amorphous morphology of TIPS-Pn NPs here. Therefore, we suggest that "stabilizing agents" such as PVA should be used with caution in NP preparation, to ensure that the structure being stabilized is in fact the desired structure.

To demonstrate the applicability of this novel mode of morphological control, transient absorption (TA) spectroscopy measurements of amorphous and crystalline TIPS-Pn NPs were collected. Representative spectra at early times after excitation are shown

in Figure 3.4. For amorphous NPs, excited-state absorption (ESA) bands at 456 nm and 570 nm are evident immediately after excitation, which decay concurrently with the growth of signals at 476 nm and 570 nm on a timescale of several picoseconds. These ESA features have been previously assigned to the decay of singlet and formation of triplet excited states of TIPS-Pn, respectively.[75,134] The interconversion between these signals is therefore indicative of SF occurring in these NPs on a timescale of picoseconds, agreeing with previous studies of amorphous TIPS-Pn.[72,119] In contrast, Figure 3.4(b) shows that SF in crystalline TIPS-Pn occurs much faster than in amorphous TIPS-Pn, such that a majority of the initially-formed singlet states have converted to triplet states within 0.5 ps after excitation. The two aforementioned triplet ESA bands are now slightly red-shifted to 488 nm and 523 nm, with negligible spectral evolution beyond 0.5 ps after excitation. A modest growth in these bands occurs between 0.2 ps and 0.5 ps, and corresponds to a decay at 620 nm, which has been previously assigned to an ESA of the singlet excited state in crystalline TIPS-Pn.[119] The rapid SF in crystalline TIPS-Pn NPs agrees with multiple previous studies, which have shown that the time constant of singlet fission in crystalline TIPS-Pn is on the order of 100 fs.[47,110,119] Hence, modifying the morphology of TIPS-Pn NPs by addition of PVA as described above accelerates the singlet fission rate in these systems by an order of magnitude. Given the wide availability and non-toxicity of PVA, this may therefore allow for straightforward tuning of singlet fission rates in TIPS-Pn containing materials.

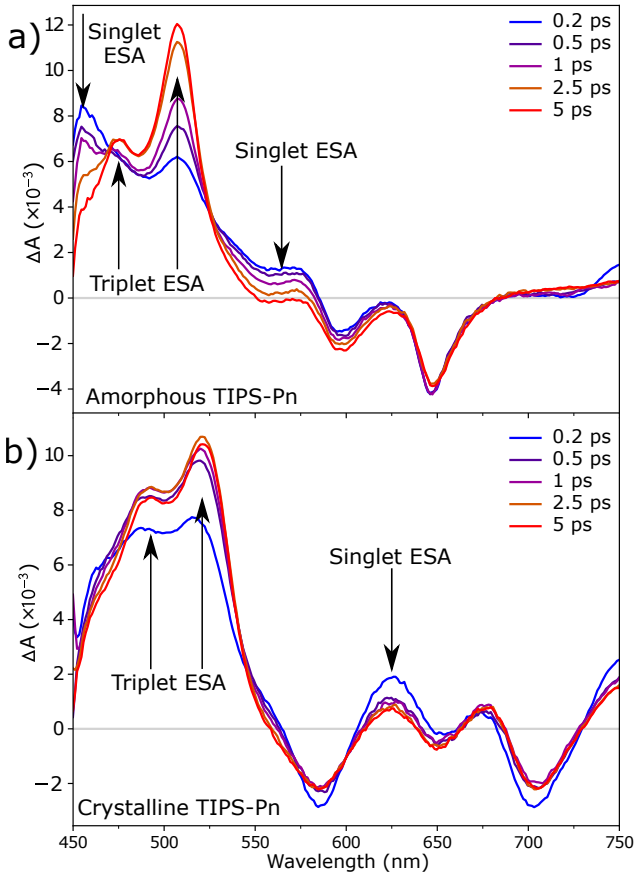

Figure 3.4: Transient absorption spectra of (a) amorphous and (b) crystalline TIPS-Pn NPs excited at 440 nm. Arrows highlight the growth or decay of spectral features associated with different excited states of TIPS-Pn.

3.4 Conclusions

In summary, we have shown that addition of PVA solution to aqueous dispersions of TIPS-Pn NPs induces a large-scale structural reorganization of amorphous packing to crystalline domains within the NPs. This effect is unique to PVA and TIPS-Pn; other water-soluble polymers or hydroxyl-containing monomers in place of PVA show a negligible change in NP morphology, as does PVA with other substituted acenes. Particle size distributions become broader and move towards larger sizes on PVA addition due to polymer adsorption to the NP surface, but the observed structural changes occur with only a thin coating of polymer. DFT calculations indicate that PVA organizes this crystal structure by promoting TIPS-Pn rearrangement to maximize favorable TIPS:hydroxyl interactions between the polymer and acene. Inducing this structural rearrangement with PVA allows for significant control over the SF kinetics of TIPS-Pn, potentially allowing for high-throughput tailoring of TIPS-Pn SF dynamics.

3.5 Experimental Methods

Materials

TIPS-pentacene (99.9%) was used as-purchased from Ossila. TIPS-tetracene (99.9%) was used as-purchased from Lumtec. TES-pentacene (99.9%) was used as-purchased from Sigma-Aldrich. All water used in this work was purified by an 18-MΩ Millipore Milli-Q Reagent Water System fitted with a 0.45-µm filter. THF of HPLC grade was purchased from RCI Labscan and freshly distilled before use. All polymers were sourced as solid powders from Sigma-Aldrich, with average molecular weights of 130, 14 and 1.5 kg/mol for PVA, PEG and PAA respectively. Polymer stock solutions were made up to concentrations of 10 mg/mL in water; for PEG and PVA, this required heating at 90 °C for 1–2 hours.

Nanoparticle Preparation

NPs were prepared here by the re-precipitation (or "flash-precipitation") method.[72,119,193] 400 µL of TIPS-Pn in THF (0.8 mM) was rapidly injected into 10 mL of vigorously stirred MilliQ water or aqueous PVA solution, and allowed to mix for 5 minutes. This procedure was repeated 3-5 times to prepare multiple independent samples of NPs with a TIPS-Pn concentration of 20 ppm. These samples were then combined and the THF removed under reduced pressure, and further concentrated to 200 ppm TIPS-Pn. Finally, the NP suspensions were filtered through a 0.2-µm hydrophilic syringe filter (Sartorius Minisart NML).

To convert pre-formed TIPS-Pn NPs from amorphous to crystalline morphologies, aqueous TIPS-Pn NP suspensions and PVA solutions were combined together to achieve TIPS-Pn concentrations of 20 ppm and PVA concentrations of 1-1000 ppm, to a final volume of 1 mL.

Nanoparticle Characterization

Steady-state UV–visible absorption spectra were collected using a Cary Varian 1E UV–visible spectrophotometer, with samples contained in a 2-mm path length quartz

cuvette (Starna Cells 21-Q-2).

Solid NP samples were prepared by addition of a polymer (PVAs, PAA or PEG) into a NP suspension at a polymer:TIPS-Pn mass ratio of 20:1, and then evaporation to dryness under reduced pressure. The resulting NP/polymer powders were mounted upon silicon plates, and PXRD patterns were collected using a Bruker D4 Endeavour Powder Diffractometer, using Co Kα radiation (1.79 Å) over a 5–52 ° 2θ range.

DLS and zeta potential characterization of NP suspensions were conducted using a Malvern Zetasizer Nano ZSP, employing a 633-nm laser at 10 mW output power. While TIPS-Pn exhibits significant absorption at this wavelength, recent work by Geißler and co-workers showed that particle sizes measured by DLS were independent of the particles' absorbance at the incident laser wavelength, provided that an insignificant level of fluorescence at that same wavelength is present.[211] As the NPs studied here are essentially non-fluorescent (Supporting Information), use of a laser at this wavelength was deemed appropriate. DLS measurements were taken at a backscattering angle of 173°, using a 1-cm disposable plastic cuvette. Particle zeta potentials were measured using a folded capillary cell (DTS1060).

Transient Absorption Spectroscopy

Ultrafast spectroscopic measurements were collected on a transient absorption (TA) spectrometer (Ultrafast Systems, Helios). The primary light source consisted of 800-nm laser pulses with a 100-fs pulse width from a Ti:sapphire regenerative amplifier (Spectra Physics, Spitfire Pr XP 100F) at a 1-kHz repetition rate. 440-nm pump pulses were generated using the fourth harmonic of the idler from an optical parametric amplifier (Light Conversion, TOPAS-C), with an energy of 1.0 µJ and spot size of 465 µm (pump fluence of 150 µJ cm^{-2}). Probe pulses were produced from focusing of the 800-nm amplifier pulses onto a 3.2-mm sapphire crystal. This yielded a white-light continuum with a spot-size of 122 µm FWHM, which was split into signal and reference beams. Pump and probe pulses were polarized at the magic angle (54.7 °) relative to one another to minimize anisotropic effects. NP dispersions were constantly stirred in a 2-mm path length quartz cuvette (Starna Cells 21-Q-2) throughout these experiments, and negligible photo-degradation was observed.

3.6 Computational Methods

All DFT calculations were performed using Gaussian 16, revision A.03.[167] The 12-molecule TIPS-Pn surface model was constructed from the crystal structure reported by Anthony et al.[125] Due to the large size of this crystal model (1200 atoms), geometry optimizations treating all atoms at a full DFT level were infeasible. Hence, the initial optimization step was undertaken as a multi-level calculation using the ONIOM algorithm,[212,213] with the polymer chain treated at the ωB97XD/cc-pVDZ[208,214–216] level of theory and the TIPS-Pn molecules (frozen in place) at the AM1 semiempirical level.[217] 3–10 initial geometries were used for all structures of interest, with polymer chains lying on different faces and at different orientations relative to the crystal structure. The resulting energy minima structures then had their energies re-calculated using the ωB97XD/cc-pVDZ theory level on the entire system. Binding energies were calculated using

$$E_{\mathrm{BE}} = (E_{\mathrm{Polymer}} + E_{\mathrm{TIPS\text{-}Pn}}) - E_{\mathrm{Polymer:TIPS\text{-}Pn}}, \tag{3.2}$$

where E_{Polymer} and $E_{\text{TIPS-Pn}}$ are the energies of the polymer chain and TIPS-Pn crystal computed in separate calculations at the equivalent level of theory.

Acknowledgements

The authors thank Dr. Elizabeth Tran for assistance with DLS measurements, Dr. Oliver Linder-Patton for his help with collecting XRD data, and Dr. Patrick Tapping and Alexandra Stuart for stimulating discussions. Computational aspects of this work were undertaken with resources provided by the Phoenix High Performance Computing service at the University of Adelaide and the National Computational Infrastructure (NCI Australia), an NCRIS-enabled capability supported by the Australian Government. This work was supported by an Australian Government Research Training Program (RTP) scholarship and funding from the Australian Research Council (DP160103797 and LE0989747). R.D.P., B.K. and G.D.S. acknowledge funding from the Princeton Center for Complex Materials, a MRSEC supported by NSF Grant DMR 1420541. B.K also acknowledges that this material is based on work supported by the National Science Foundation Graduate Research Fellowship under Grant Number DGE-1656466.

3.7 Supporting Information

Kinetics of TIPS-Pn Nanoparticle Crystallization

In order to characterize the rate of crystallization in TIPS-Pn NPs induced by PVA addition, visible absorption spectra of a TIPS-Pn:PVA mixture were collected over regular time intervals. In order to observe both the amorphous absorption peak at 645 nm and the crystalline peak at 695 nm, spectra were collected over a range of 620–720 nm. The width of this spectral window limited the time resolution to a single scan every 18 s. NP suspension and PVA solution were mixed in a 1-cm cuvette and then immediately placed into the spectrophotometer, in order to observe any changes that occur within the first few seconds of mixing. Figure 3.5 shows an example of the resulting kinetic scans for a high concentration of PVA with TIPS-Pn NPs. The conversion of amorphous to crystalline domains within the nanoparticles occurs with sigmoidal kinetics; after an initial induction period of minimal change, a rapid interconversion of peaks occurs, followed by further slow growth. This final rate is substantially slower than the initial step, with the process taking hours to complete; however it should be noted that this slow conversion continues until the spectrum resembles that of fully-crystalline TIPS-Pn.

Sigmoid-like kinetics are highly characteristic of auto-catalytic processes such as the well-established Finke-Watzky model,[218–222] in which for a simple first-order conversion of species A into species B, B then accelerates the conversion of A into B:

$$A \xrightarrow{k_1} B, \tag{3.3}$$

$$A + B \xrightarrow{k_2} 2B. \tag{3.4}$$

Within the context of TIPS-Pn crystallization, species A represents amorphous TIPS-Pn and B crystalline TIPS-Pn. Equation 3.4 implies that amorphous TIPS-Pn molecules add auto-catalytically to any crystalline domains formed to create larger crystalline

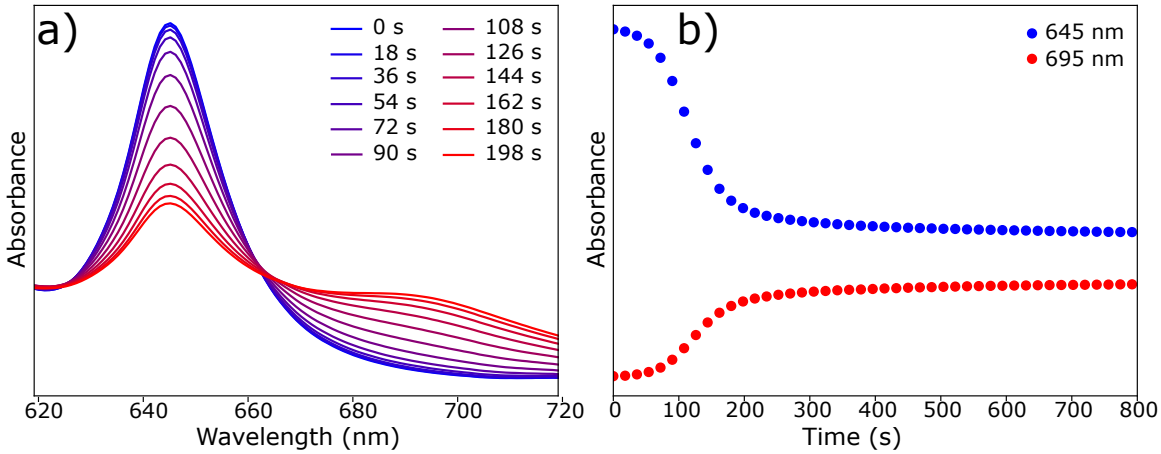

Figure 3.5: (a) Steady-state absorption spectra over time of TIPS-Pn NPs after PVA addition, and (b) intensities of the 'amorphous' (645 nm) and 'crystalline' (695 nm) absorption peaks as a function of time (500 ppm PVA, 35 ppm TIPS-Pn).

domains. Therefore, PVA adsorption at the nanoparticle surface may nucleate small crystalline domains which then spread throughout the entirety of the nanoparticle. The extent to which PVA is involved with this auto-catalytic step is unclear; however, the formation of fully-crystalline spectral features indicates that the interior of the NPs must also crystallize. Within the short timescale in which crystallization occurs, it is unlikely that the bulky PVA chains can penetrate to this depth inside the NPs through purely diffusive motion. Therefore, this crystallization likely occurs at least in part independently of PVA, and therefore at least some of this growth must be due to TIPS-Pn molecules spontaneously rearranging to add to existing crystalline domains.

The rates associated with these sigmoidal kinetics were highly dependent upon PVA concentration used, as demonstrated by the markedly different rates shown in Figure 3.6. In general, the rate of crystallization increased with PVA concentration at low concentrations (1–50 ppm), but then decreased when further increasing PVA concentration (100–1000 ppm). These decreased rates at higher concentrations may be due to some form of interaction between PVA chains slowing diffusion to the nanoparticles

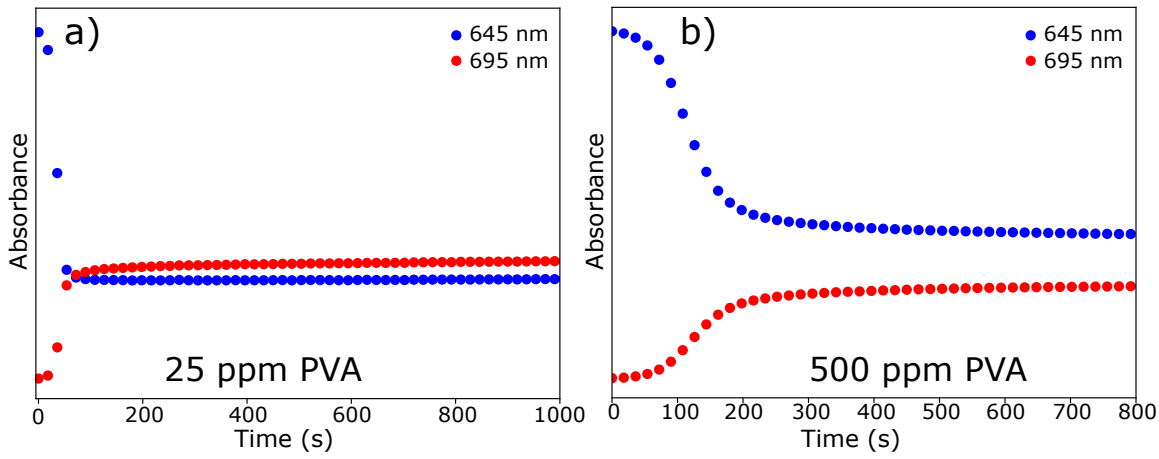

Figure 3.6: Kinetic profiles of 645 and 695 nm steady-state absorption peaks upon addition of (a) 25 ppm and (b) 500 ppm PVA (35 ppm TIPS-Pn).

or binding to the surface. However, it is worth noting that these kinetics were poorly reproduceable and hence difficult to quantify. Factors such as the rate of mixing in the cuvette may be at least partially responsible for this lack of reproducibility. Despite this, the shape of the kinetics remained sigmoidal in shape in every observed instance. Therefore, the above discussion regarding autocatalytic growth is relevant regardless of the actual rates of crystallization.

Figure 3.7 shows the growth of the crystalline TIPS-Pn absorption peak at 695 nm due to addition of PVA at equivalent mass concentrations but differing molecular weights. A trend is clearly evident, with 14 kg/mol PVA chains resulting in almost complete crystallinity in TIPS-Pn NPs within the first time point, while the larger-chain polymers induce this crystallinity much more slowly. While the 166 kg/mol chains appear to initiate crystallinity slightly faster than the 130 kg/mol chains, this discrepancy is likely well within the margin of error in these experiments, as uncertainties in the rates of mixing and time zero are likely significant here. Increasing molecular weight appears to affect this rate of crystallization in a similar manner to increasing PVA concentration, suggesting that some form of self-interaction or entanglement between PVA chains may be responsible for this decreased rate; either *inter*molecular at high concentrations, or *intra*molecular at high molecular weights. However, it should be noted that polymer molecular weight influences many physical properties such as solubility and viscosity, and it is unclear how all of these factors contribute to the rate of crystallization.

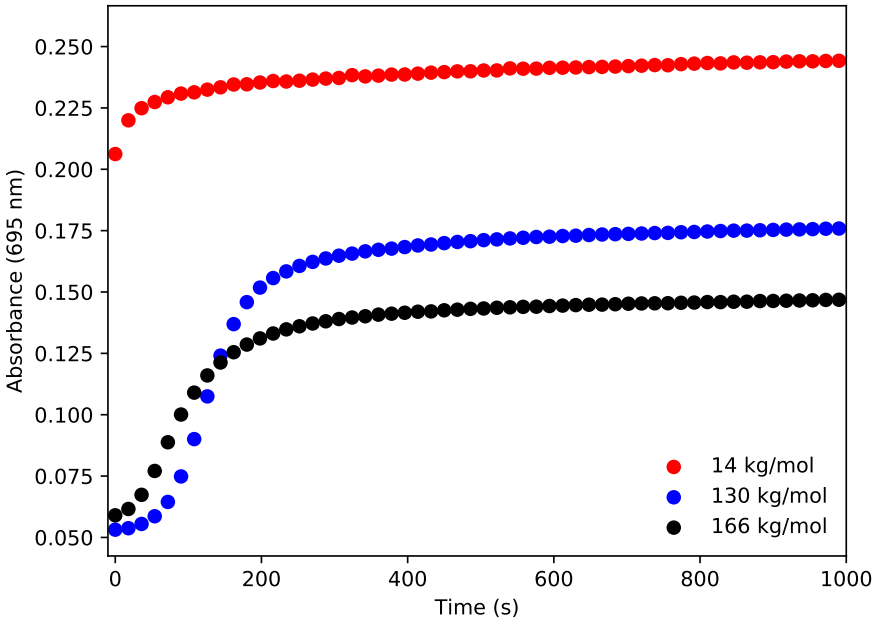

Figure 3.7: Kinetics of the crystalline steady-state absorption peak at 695 nm upon addition of 500 ppm PVA at different molecular weights (35 ppm TIPS-Pn).

PXRD Patterns of Pure-Polymer Films

To ensure that the PXRD pattern of TIPS-Pn NPs embedded in a PVA matrix (Figure 3.2) was representative of the NPs themselves and not the polymer matrix, patterns were also collected of pure polymer films drop-cast from aqueous solution (Figure 3.8,

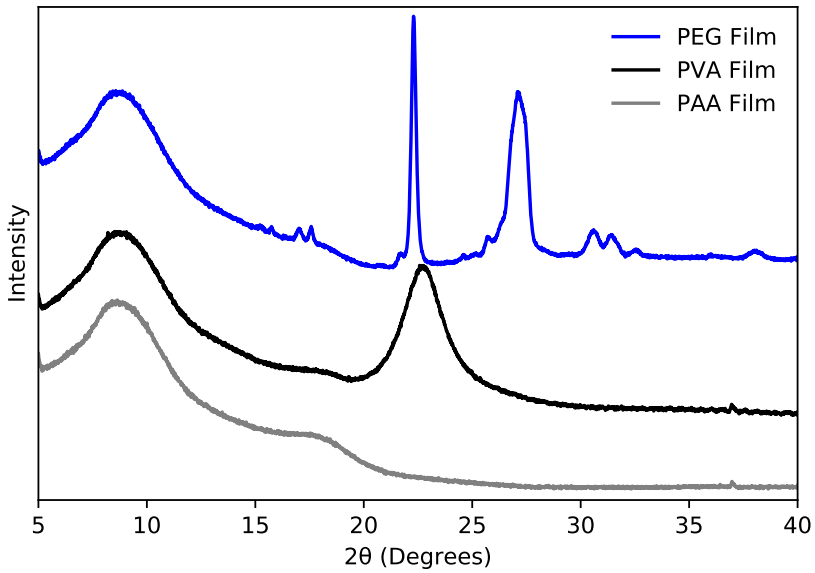

Figure 3.8: Powder X-ray diffraction patterns of PVA and PAA films, drop-cast from 10 mg/mL solutions at room temperature.

below). All three polymer films show broad, poorly-defined peaks at $2\theta = 8\,^\circ$ and $18\,^\circ$, attributable to amorphous packing of polymer chains within these films. The PVA film also shows a much sharper peak at $2\theta = 23\,^\circ$, which matches well with the (101) crystalline PVA peak previously assigned by Lue et al.[223] A significant peak pattern is observed in the PEG film, which also matches well with a previously-reported pattern for pure PEG.[224]

Figure 3.9 shows the resulting diffraction patterns from TIPS-Pn NPs evaporated to dryness in matrices of PVA, PEG or PAA. As is clearly evident, the characteristic crystalline TIPS-Pn diffraction peaks are only present in the TIPS-Pn:PVA pattern. The crystalline PEG and PVA peaks are also observed in the TIPS-Pn:PEG and TIPS-Pn:PVA patterns, but at much lower intensities. This discrepancy can be attributed to the difference in sample preparation techniques — the TIPS-Pn:polymer matrices were prepared by evaporation to solidity under reduced pressure and gentle heating, while the pure polymer films were evaporated under ambient temperature and pressure. Hence, the pure polymer films formed at a slower rate compared to the NP:polymer matrices, allowing for more polymer chains to rearrange into the lower-energy crystal structure, and hence achieving a higher degree of crystallinity in these samples.

It is worth noting that the polymer matrices used here are unlikely to fully isolate the nanoparticles from one another; indeed, some level of NP aggregation is likely to occur during the preparation of TIPS-Pn:polymer matrices. The purpose of embedding nanoparticles within these matrices is instead to minimize this aggregation, such that large-scale structural reorganzation of the TIPS-Pn molecules does not occur during precipitation. As Figure 3.9 shows, NPs shown to have amorphous absorption features showed no significant TIPS-Pn diffraction peaks on precipitation in PAA or PEG, while NPs with crystalline absorption features also showed a diffraction pattern characteristic to TIPS-Pn when co-precipitated with PVA. Therefore, we conclude that the use of these polymer matrices was successful, in that the molecular packing of the TIPS-Pn molecules within the nanoparticles was largely unperturbed during precipitation.

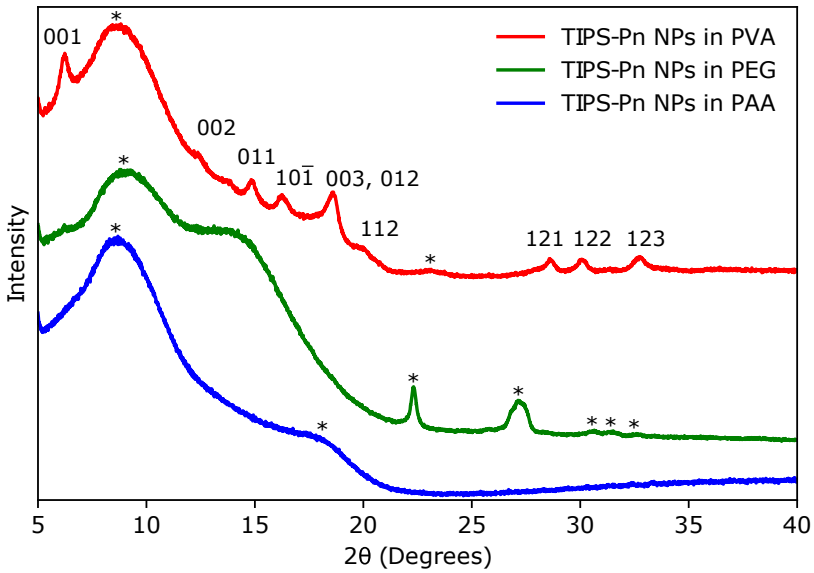

Figure 3.9: Powder X-ray diffraction patterns of TIPS-Pn NPs co-precipitated from suspension in PVA, PEG or PAA. Reflection assignments are made based upon those by Chen and co-workers for TIPS-Pn crystals,[132] while the peaks corresponding to polymer matrices are indicated with asterisks. Patterns are offset for clarity.

Dynamic Light Scattering of TIPS-Pn NP Suspensions

Figure 3.10 shows the intensity-weighted size distributions of TIPS-Pn NPs determined by DLS, with varying concentrations of PVA added. A clear shift to larger particle sizes is observed with increasing PVA concentration, which is concurrent with a broadening of the size distribution. As PVA is well-known to bind to the surface of organic nanoparticles in aqueous suspension,[201,203] we hypothesize that the added PVA forms a diffuse layer of polymer coating the surface of the nanoparticles. This layer is then

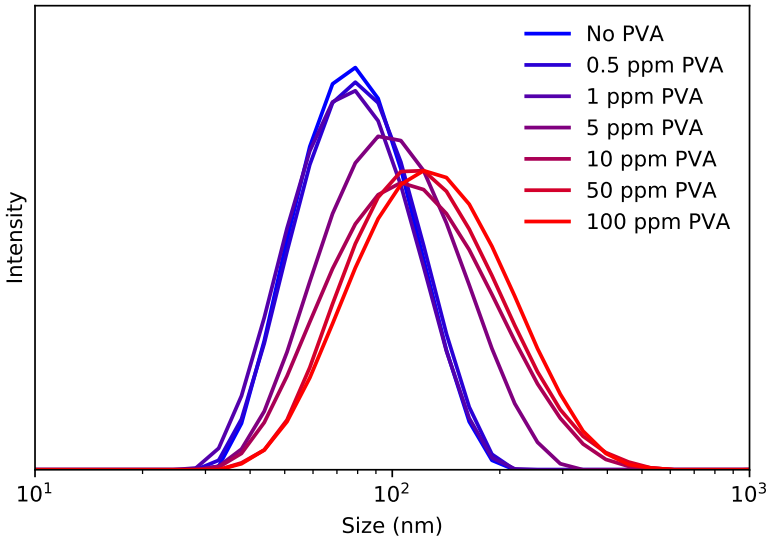

Figure 3.10: Intensity-weighted particle size distributions of TIPS-Pn NPs for varying PVA concentration. TIPS-Pn concentration is held constant at 20 ppm.

observed in DLS as an increase in the particles' hydrodynamic radii, increasing both the Z-average diameter and dispersity of these size distributions.

Attempts to Induce Phase Transitions in TIPS-Pn NPs With Other Water-Soluble Polymers and Ethanol

Aqueous solutions of poly(ethylene glycol) (PEG) and poly(acrylic acid) (PAA) were prepared in an analogous manner to PVA. While PEG required a similar level of heating as PVA to fully dissolve, PAA dissolved almost instantaneously upon stirring at room temperature. In an attempt to replicate the amorphous-to-crystalline conversion of TIPS-Pn NPs observed with PVA, spectra of these NPs were collected on addition of aliquots of PEG or PAA solution, or a solution of ethanol (EtOH) in water (Figure 3.11). While some intensity in the TIPS-Pn amorphous absorption peaks is lost on addition of these solutions, growth of the crystalline TIPS-Pn peak at 695 nm is absent at any concentration tested. Therefore, crystallinity is absent in these nanoparticles with PEG, PAA or ethanol. The decrease in intensity may be due to a change in the suspension refractive indices at higher polymer/ethanol concentrations, or perhaps a minor level of aggregation induced between nanoparticles. Only low concentrations of ethanol could be tested here, as at concentrations higher than 100 ppm the solvent polarity was significantly changed such that the EtOH/water mixture began to re-dissolve the TIPS-Pn.

Attempts to Induce Phase Transitions in TIPS-Tetracene NPs with PVA

NPs of TIPS-tetracene were prepared in an analogous manner to the TIPS-Pn NPs used throughout this work, and PVA solution was added in an attempt to crystallize them. The resulting visible absorption spectra (Figure 3.12) show negligible changes on addition of PVA to any concentration, apart from a slight loss in absorption intensity. As discussed in the preceding section, this loss in intensity may be due to changes in the suspension refractive index, or minor aggregation induced by the introduction of the polymer. Alternatively, this loss in intensity may be due to photo-degradation of TIPS-tetracene from exposure to ambient light. Previous work by Friend and co-workers showed that for TIPS-tetracene, no further peaks are introduced to the visible absorption spectrum on converting from amorphous to polycrystalline packing, but a broadening of the existing peaks occurs.[51] The absence of any such broadening in the spectra collected here suggests a lack of significant morphological changes within the TIPS-tetracene NPs, and as such demonstrates an inability of PVA to induce crystallinity in TIPS-tetracene the same way that it does in TIPS-Pn.

Optimized Structures of PVA Oligomers on TIPS-Pn_{12} Crystal Model

Figure 3.13 shows the 12-molecule TIPS-Pn crystal model constructed for computational studies, as well as the optimized geometries of the PVA oligomers considered for this study. The TIPS-Pn model (hereafter referred to as TIPS-Pn_{12}) consists of a single sheet of slip-stacked molecules, 2–3 molecules wide and 5 molecules high. This was considered sufficiently large such that an oligomer interacting with the center of

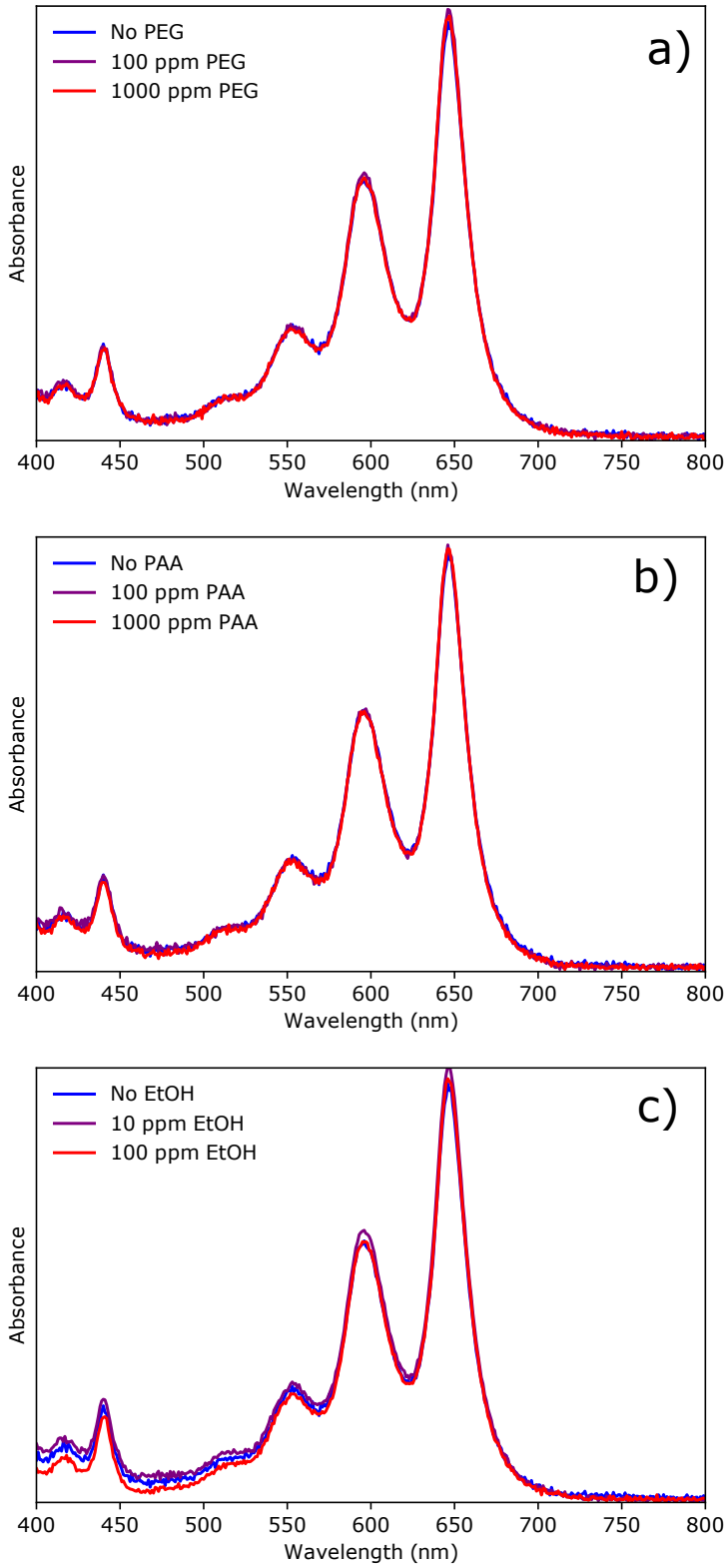

Figure 3.11: Steady-state absorption spectra of TIPS-Pn nanoparticles with (a) PEG, (b) PAA and (c) ethanol added in place of PVA.

the model on the TIPS-facing side experiences negligible unphysical edge-binding effects. Structures containing the oligomer bound to the edge or top of this crystal were investigated, but were not considered in the subsequent analysis as the oligomer fre-

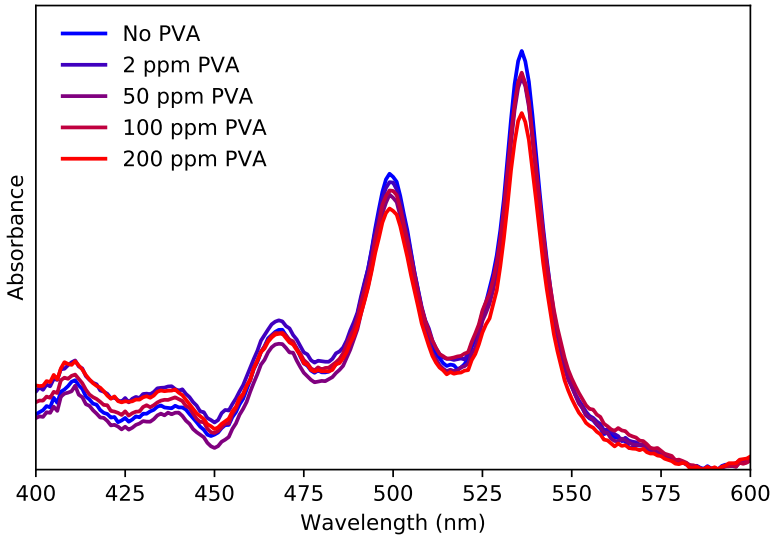

Figure 3.12: Steady-state absorption spectra of TIPS-tetracene nanoparticles re-precipitated in water with subsequent addition of PVA to different concentrations.

quently wrapped around multiple facets of the model, which is absent in the larger nanoparticles that this model represents.

Figures 3.14 and 3.15 show the minimum-energy structures of the PVA dimer and trimer bound to the TIPS-Pn_{12} model, respectively. In both structures, the PVA oligomer interacts with the crystal model only through a terminal methyl group, rather

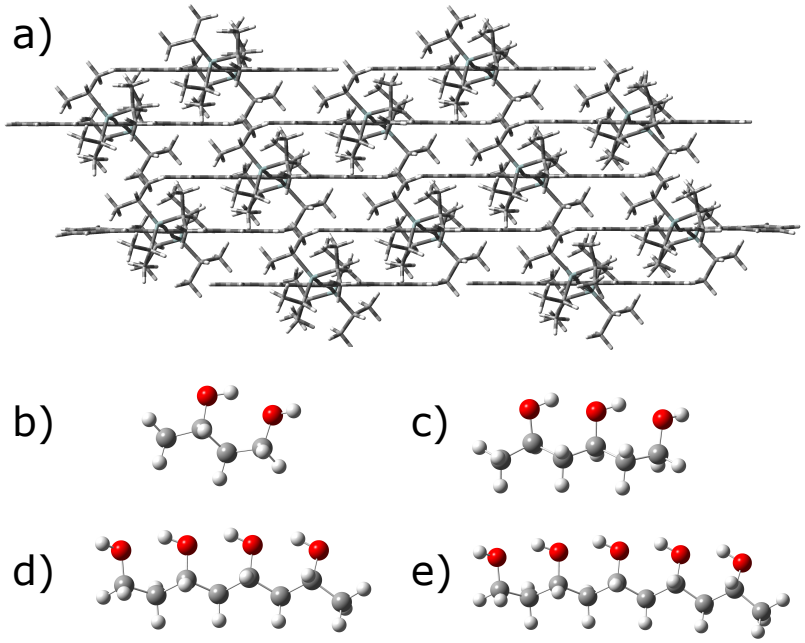

Figure 3.13: Structures of (a) the TIPS-Pn_{12} model surface built from the crystal structure reported by Anthony et al.,[125] and (b) PVA dimer, (c) trimer, (d) tetramer and (e) pentamer structures optimized at the ωB97XD/cc-pVDZ level of theory.

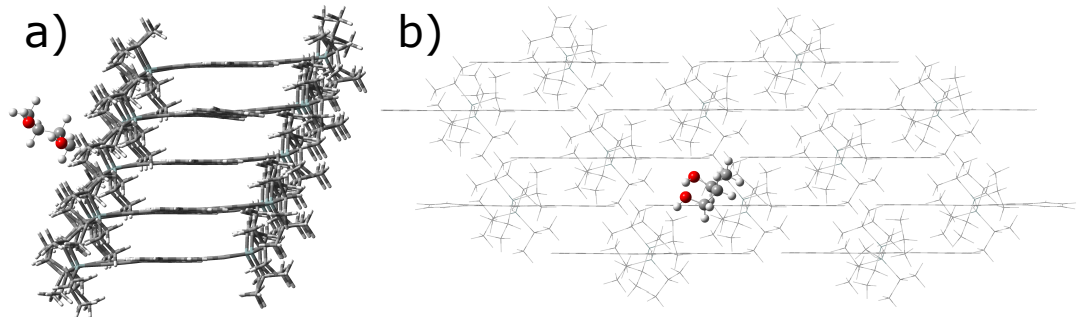

Figure 3.14: (a) Edge-on and (b) side-on views of the PVA_2:TIPS-Pn_{12} minimum-energy structure (PVA binding energy of 0.41 eV).

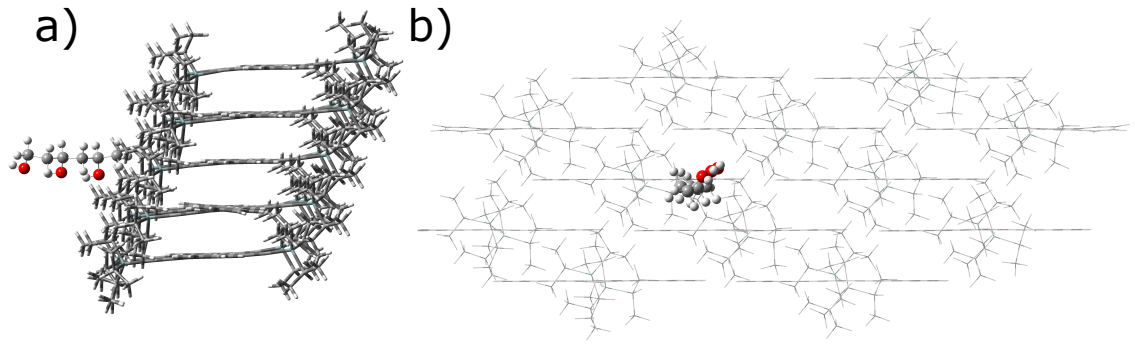

Figure 3.15: (a) Edge-on and (b) side-on views of the PVA_3:TIPS-Pn_{12} minimum-energy structure (PVA binding energy of 0.44 eV).

than lying flat on the surface like longer oligomers (see above). It should be acknowledged that only a single trial structure was optimized for each of these stoichiometries due to limitations on computational resources. However, these trial structures began with the oligomer lying flat upon the surface, so these results indicate that these short oligomers indeed have a preference for being terminally-bound over lying flat on the surface.

The minimum-energy geometries of the PVA tetramer (Figure 3.16) and pentamer (Figure 3.3), however, show the oligomers lying flat upon the TIPS-Pn model, with the hydroxyl groups directed towards the closest TIPS groups. In the case of the tetramer, two conformers are observed that are nearly equivalent in energy (a difference of < 0.1 eV), with the PVA oligomer aligned with different crystal facets of the TIPS-Pn. The minimum-energy structure (Figure 3.16a,b) has the PVA aligned in the direction of stacking between 2nd-nearest-neighbor TIPS-Pn molecules, whereas for the low-lying conformer (Figure 3.16c,d) it aligns in the nearest-neighbor direction. Both of these stacking directions have TIPS-Pn repeat distances that are approximately integer multiples of the PVA repeat unit (10.21 and 7.57 Å *vs* 2.52 Å), so both of these binding configurations could plausibly template crystallinity in TIPS-Pn.

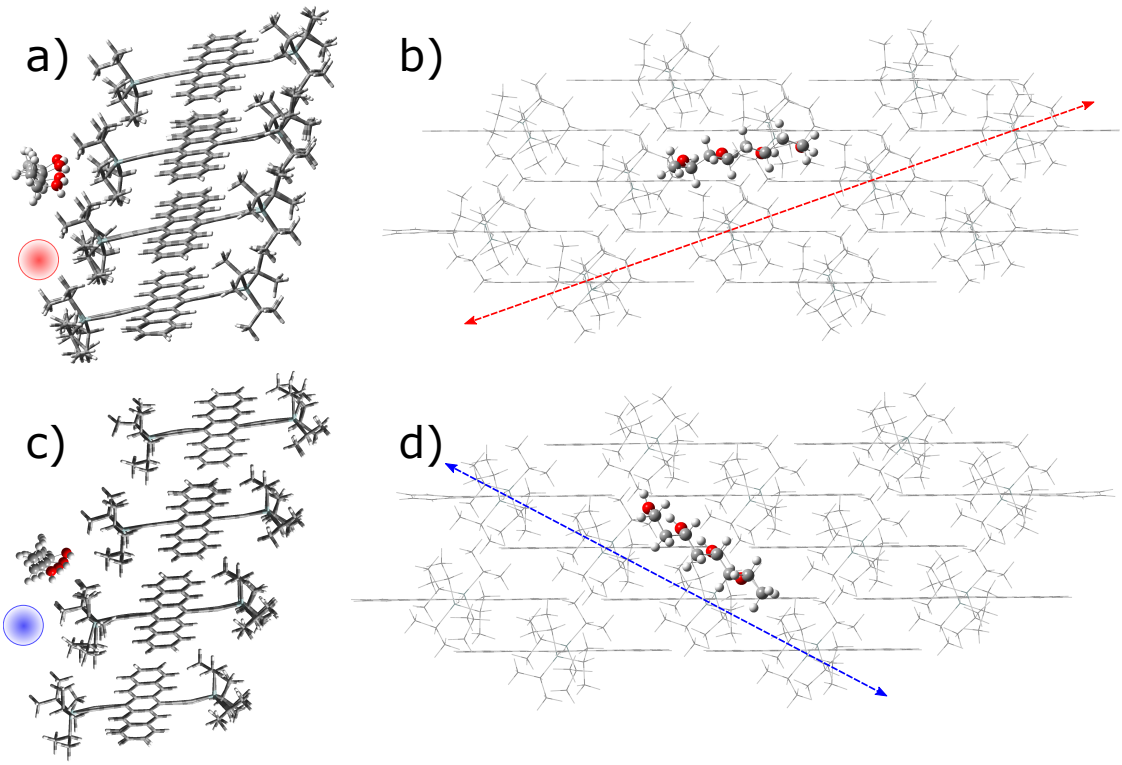

Figure 3.16: a) Crystal-facet-aligned and (b) side-on views of the PVA_4:TIPS-Pn_{12} minimum-energy structure (PVA binding energy of 0.79 eV). (c) Crystal-facet-aligned and (d) side-on views of the PVA_4:TIPS-Pn_{12} low-lying energy conformer (PVA binding energy of 0.74 eV). Blue and red lines show the TIPS-Pn nearest-neighbor and second-nearest-neighbor stacking directions (respectively), corresponding to the crystal alignment directions shown in (a) and (c) (red and blue circles).

Optimized Structures of PEG and PAA Oligomers on TIPS-Pn_{12} Crystal Model

For calculations involving PEG or PAA, more than ten different starting geometries were used, to ensure a thorough search of these potential energy surfaces. Figure 3.17 shows the minimum-energy and a relevant high-lying energy conformer of the PEG tetramer bound to the TIPS-Pn_{12} model. The minimum-energy geometry, while lying flat upon the TIPS-Pn surface, shows a lack of alignment with the TIPS-Pn stacking directions. The higher-energy conformer does show alignment with the nearest-neighbor stacking direction of TIPS-Pn, but is much higher in energy with a negligible binding energy.

Figure 3.18 shows the minimum-energy structure of the PAA tetramer adsorbed to the TIPS-Pn_{12} model. While there is some level of alignment of the oligomer with the TIPS-Pn 2nd-nearest-neighbor stacking direction, the acid groups upon the PAA chain are significantly disordered such that no periodic interaction between oligomer and surface occurs. This disorder appears to be largely due to the size of the oligomer side-chains; the acid groups are sufficiently bulky that they adopt a staggered conformation about the chain to minimize steric interactions. No other optimized geometries of PAA_4:TIPS-Pn_{12} showed any significant alignment or periodic matching between oligomer and surface.

In addition to this lack of aligment between oligomer chains and TIPS-Pn stacking

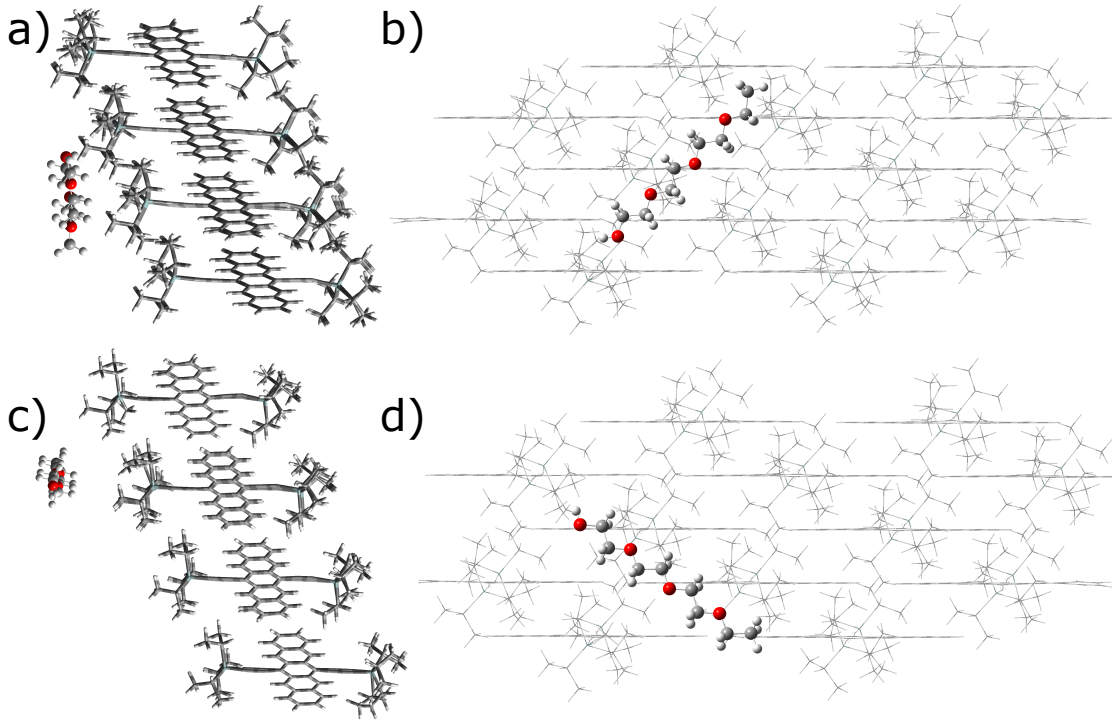

Figure 3.17: (a) Crystal-facet-aligned and (b) side-on views of the PEG_4:TIPS-Pn_{12} minimum-energy structure (PEG binding energy of 0.81 eV). (c) Crystal-facet-aligned and (d) side-on views of the PEG_4:TIPS-Pn_{12} higher-energy conformer (PEG binding energy of 0.1 eV).

directions for both PEG and PAA, it is worth noting that the repeat units of these polymers do not match the periodicity of TIPS-Pn in the same way that PVA does. PEG has a repeat unit of 3.57 Å, and PAA's repeat unit between non-staggered acid groups is approximately 5.50 Å. Neither of these allow for periodic matching with either of the TIPS-Pn stacking directions (10.21 and 7.57 Å), and so a periodic, dispersion based interaction as is observed between PVA and TIPS-Pn would not be expected for either PAA or PEG.

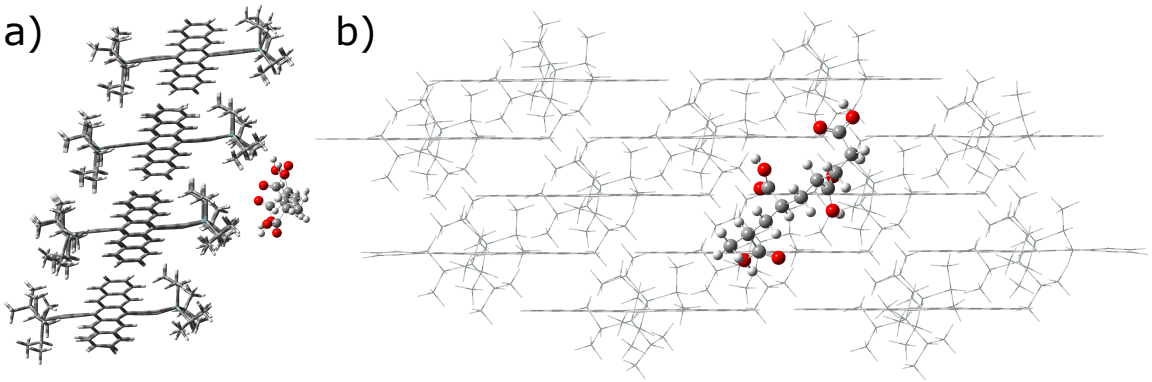

Figure 3.18: (a) Crystal-facet-aligned and (b) side-on views of the PAA_4:TIPS-Pn_{12} minimum-energy structure (PAA binding energy of 0.78 eV).

Attempts to Induce Phase Transitions in TES-Pentacene NPs with PVA

Nanoparticles of TES-pentacene were prepared in an analogous manner to the TIPS-Pn NPs used throughout this work. Re-precipitation was attempted into a 10 ppm solution of PVA, in an attempt to induce crystallinity in a similar manner to TIPS-Pn. Figure 3.19 shows the steady-state absorption spectra of the resulting nanoparticle suspensions. On re-precipitation into PVA, the only observable change is a small increase in absorption at lower wavelengths, however this could be attributed to an increased level of scattering arising from the PVA in solution. Critically, no change in absorption at either 645 or 695 nm is observed, and so no amorphous-to-crystalline conversion is evident upon re-precipitation into a PVA/water solution. Therefore, it can be concluded that PVA does not induce morphological change in TES-Pn in the same manner as TIPS-Pn, as predicted above.

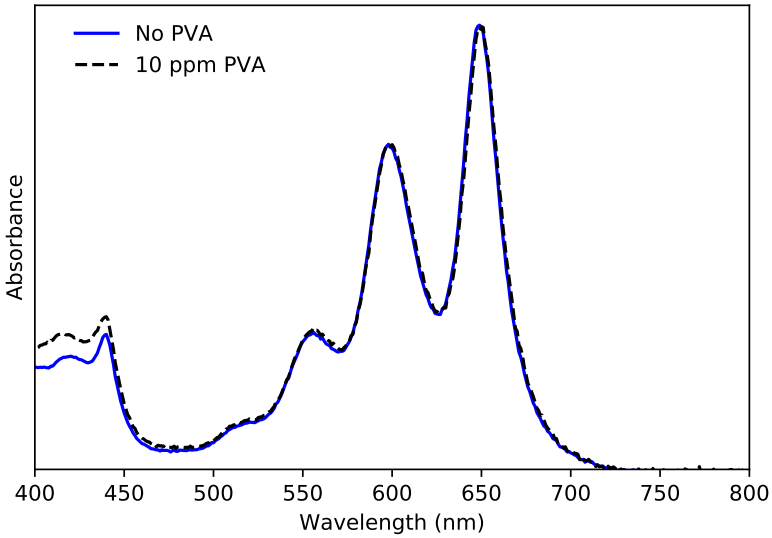

Figure 3.19: Steady-state absorption spectra of TES-pentacene nanoparticles re-precipitated into either water or 10 ppm PVA in water.

Steady-State Fluorescence of TIPS-Pn NPs

Steady-state fluorescence spectra were recorded using a PerkinElmer LS 55 fluorescence spectrophotometer with a 1-cm path length quartz cuvette (Starna Cells 3-Q). Emission and excitation slit bandwidths of 5 nm each were used, and the sample absorbance at the excitation wavelength was always kept below 0.1. Figure 3.20 shows the resulting emission spectra of amorphous and crystalline TIPS-Pn NP suspensions at three relevant excitation wavelengths, with the absorption and emission spectra of a TIPS-Pn/THF solution shown for reference. As can clearly be seen, while the TIPS-Pn/THF solution shows a significant amount of emission, negligible fluorescence is observed for both amorphous and crystalline TIPS-Pn nanoparticles. A previous study has reported low-intensity emission from neat TIPS-Pn amorphous nanoparticles, but with an I/A ratio of 5 or less, which is approaching the detection limit here.[72] This fluorescence quenching can be attributed to ultrafast singlet fission occurring in these nanoparticles, such that any emissive singlet states have been converted to non-emissive triplets

within 10-20 ps of excitation. As singlet fission is expected to occur approximately an order of magnitude faster in crystalline TIPS-Pn when compared to amorphous TIPS-Pn,[47,119] it is therefore unsurprising that negligible fluorescence is also observed from the crystalline NPs.

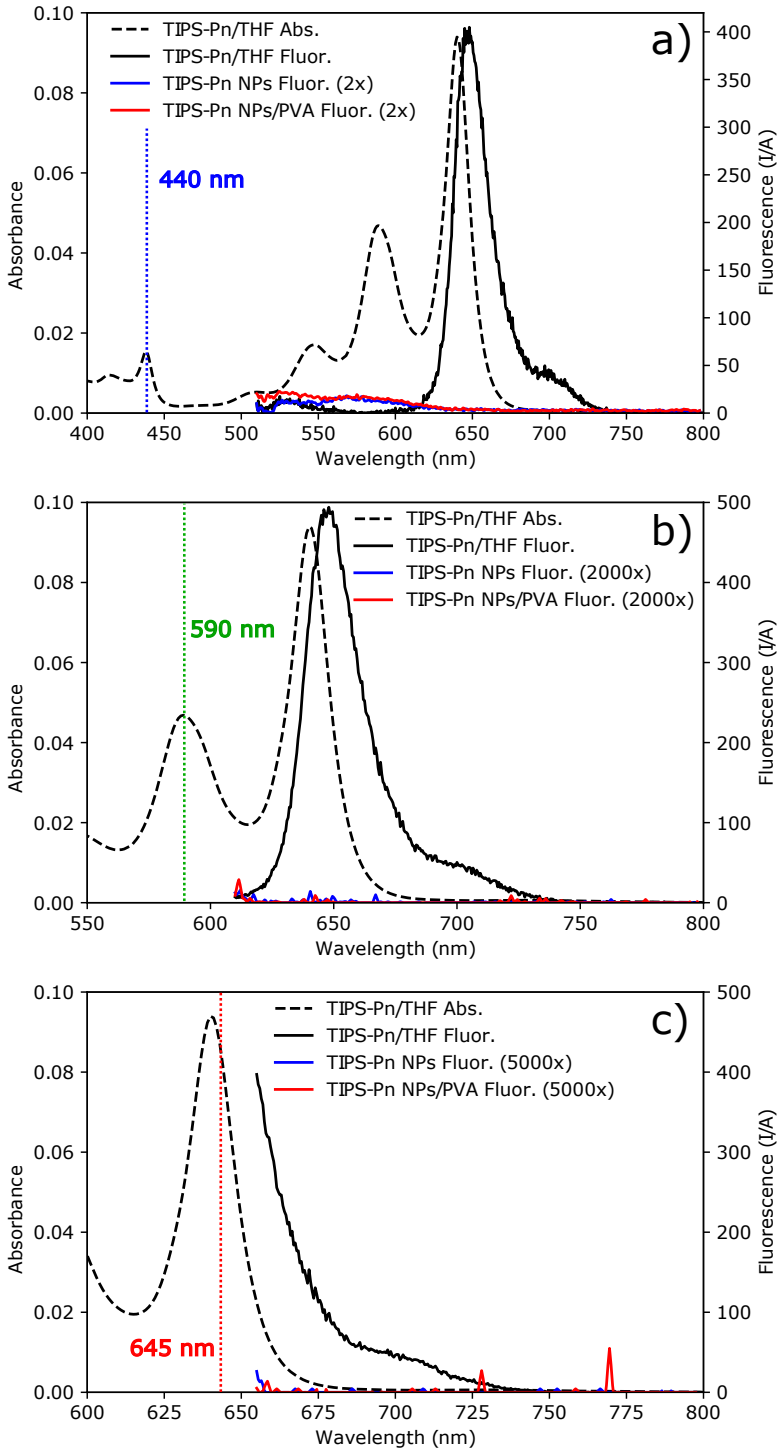

Figure 3.20: Steady-state fluorescence spectra of TIPS-Pn solution in THF, amorphous and crystalline TIPS-Pn nanoparticles in water, exciting at (a) 440 nm, (b) 590 nm and (c) 645 nm. The steady-state absorption spectrum of TIPS-Pn in THF (2.5 ppm) is shown for reference. Dotted lines show positions of excitation wavelengths.

CHAPTER 4
Anisotropic Triplet Exciton Diffusion in Crystalline Functionalized Pentacene

Statement of Authorship

Title of Paper	Anisotropic Triplet Exciton Diffusion in Crystalline Functionalized Pentacene
Publication Status	Published
Publication Details	Hudson, R. J.; Huang, D. M.; Kee, T. W. Anisotropic Triplet Exciton Diffusion in Crystalline Functionalized Pentacene. *J. Phys. Chem. C* **2020**, *124*, 23541–23550. DOI: 10.1021/acs.jpcc.0c07608

Principal Author

Principal Author	R.J. Hudson		
Contribution to the Paper	Experimental work, computational modelling, data analysis, construction of figures, writing of manuscript.		
Overall Percentage	85%		
Certification	This paper reports on original research I conducted during the period of my Higher Degree by Research candidature and is not subject to any obligations or contractual agreements with a third party that would constrain its inclusion in this thesis. I am the primary author of this paper.		
Signature		Date	25/11/21

Co-Author Contributions

By signing the Statement of Authorship, each author certifies that the stated contributions to the following publication are accurate and that permission is granted for the publication to be included in this thesis.

Co-Author	D.M. Huang		
Contribution to the Paper	Supervision of computational work, development of triplet–charge annihilation model, assistance with data analysis and writing and editing of manuscript.		
Signature		Date	22/11/21

Co-Author	T.W. Kee		
Contribution to the Paper	Supervision of project, assistance with writing and editing of manuscript, corresponding author.		
Signature		Date	22/11/2021

4.1 Abstract

Exciton multiplication through singlet fission (SF) offers scope for next-generation photovoltaic devices to exceed the detailed balance limit. Organic SF chromophores typically exhibit significant structural anisotropy in their crystal packing, which can impact exciton transport and influence the design of SF-enhanced devices. An improved understanding of the link between structural anisotropy and exciton diffusion is therefore crucial for developing SF-based photovoltaics. Here, we use femtosecond transient absorption spectroscopy to quantify the anisotropic triplet mobility in 6,13-(triisopropylsilylethynyl)pentacene (TIPS-Pn), a prototypical SF chromophore. Bimolecular triplet–triplet annihilation in crystalline TIPS-Pn is well-described by a kinetic model that assumes isotropic, three-dimensional triplet exciton diffusion, but with best-fit parameters that do not correspond to any physical parameters of the material. Kinetic models that assume either one-dimensional or anisotropic three-dimensional exciton diffusion describe the annihilation equally well but yield more physically realistic fit parameters, suggesting that triplet diffusion on the sub-nanosecond timescale occurs mostly along a single axis of the material. These findings highlight the need to treat parameters obtained from fits of experimental data with models of isotropic diffusion with caution for systems with anisotropic packing such as TIPS-Pn. Diffusion coefficients calculated by density functional theory predict that triplet exciton diffusion occurs predominantly along the crystallographic *a*-axis, with migration in any other direction through the crystal slower by over an order of magnitude. This anisotropic diffusion suggests that fast, directional exciton transport in layers or films of TIPS-Pn may be achieved by control of the chromophore morphology.

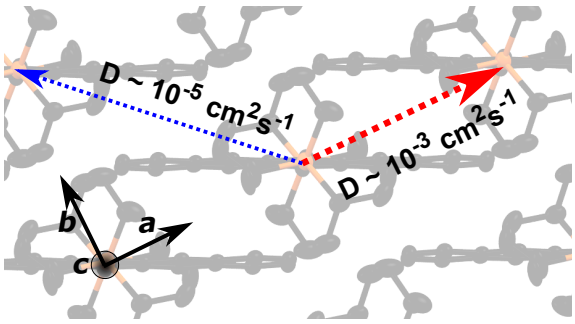

4.2 Introduction

Singlet exciton fission (SF) is the photophysical process in which a chromophore in a singlet excited state couples to an adjacent ground state chromophore to yield two triplet excited state chromophores.[37] SF has garnered significant interest in recent years, as it may help to surpass the detailed balance limit of single-junction photovoltaic (PV) devices.[22,23] However, practical implementations of SF-sensitized PV devices have shown only minor efficiency improvements thus far, despite using highly efficient SF chromophores.[29,177,181] Design of such devices must therefore also consider the processes involved in harvesting triplet excitons produced by SF. The migration of these excitons to interfaces or junctions at which either energy or charge transfer can occur plays a significant role, and hence must be well understood in order to design PV devices in which SF yields an appreciable efficiency increase.

Triplet exciton transfer is generally understood as a short-range, incoherent process that may be described as 'hopping' of excitons between chromophore sites.[80] As such, triplet mobility is often considered in terms of a diffusive random walk, with an effective diffusion coefficient describing the rate of triplet migration throughout the

material.[63,117,225] Models used to describe this behavior are generally derived from the seminal work of Smoluchowski, who developed an analytical solution for the three-dimensional coagulation of equivalent particles controlled by diffusive motion.[226,227] However, such models usually assume an isotropic medium in which these particles (or quasi-particles in the case of excitons) may diffuse, while the library of known SF-capable chromophores primarily consists of π-conjugated organic molecules with significant structural anisotropy in two or three dimensions.[19] Substantial anisotropy may therefore exist in triplet exciton diffusion rates along different crystallographic axes of organic SF chromophores. As a case in point, preferential triplet migration along a single axis was observed by transient absorption microscopy in a series of SF-capable acenes.[114] More recently, the rates of diffusion-controlled triplet–triplet annihilation (TTA) along different crystallographic axes in hexacene were shown to vary by a factor of four, attributed to different modes of crystal packing along these axes.[115] It is hence becoming clear that such anisotropic diffusion plays a significant role in triplet exciton migration through crystalline organic systems, and must be accounted for when designing PV devices containing these materials as SF chromophores.

6,13-(triisopropylsilylethynyl)pentacene (TIPS-Pn) is an intensely studied model SF chromophore, in which the SF process is slightly exoergic.[19] In its crystalline phase, SF has been shown to occur on sub-picosecond timescales[1,47] and with effectively quantitative yield of triplets.[119] The dominant crystal polymorph of TIPS-Pn consists of an extended slip-stacked structure with significant π–π stacking in two dimensions, but contact only through insulating TIPS groups along the third crystallographic axis.[120,125] This π-stacking is unequal in both slip-stacked directions; a recent computational study predicted electron and hole transfer integrals to differ by up to a factor of 8 between the different slip-stacked pairs on this plane.[63] Despite this significant structural anisotropy between all three crystallographic axes, previous studies of triplet diffusion in crystalline TIPS-Pn have assumed purely isotropic migration.[63,110] Such treatments are unlikely to accurately describe triplet exciton diffusion within TIPS-Pn, and may therefore give incorrect or misleading predictions when designing systems that depend upon triplet diffusion through TIPS-Pn. This issue is especially relevant given recent advancements in solution-coating methods, as solution-sheared layers of TIPS-Pn with single-crystal alignment on the order of millimeters have been recently reported.[120,228,229] On such a large length scale, even small inaccuracies in describing exciton diffusion rates would manifest in substantial errors in predicted exciton diffusion distances along different crystallographic axes. As such, it is necessary to develop a deeper understanding of the anisotropic nature of exciton diffusion in crystalline TIPS-Pn.

In this work, we study triplet diffusion through crystalline nanoparticles (NPs) of TIPS-Pn using femtosecond transient absorption (TA) spectroscopy. The decay kinetics of triplet excitons arising from SF are shown to depend strongly on excitation density, indicative of bimolecular exciton–exciton annihilation. These kinetics are well fit by a model that assumes isotropic three-dimensional triplet exciton diffusion, but yield best-fit parameters that are physically unreasonable when considering the intermolecular packing of crystalline TIPS-Pn. However, this annihilation is also well-modeled by considering diffusion mostly along a single axis and yields physically reasonable fit parameters, suggesting that diffusion through TIPS-Pn is highly anisotropic on the timescale considered here. This result agrees with diffusion coefficients predicted by density functional theory (DFT), which indicate that diffusion along the a-axis of crystalline TIPS-Pn is faster than diffusion through next-nearest-neighbor stacking within

the crystal by a factor of 25. This anisotropy highlights the importance of controlling chromophore morphology in the fabrication of SF-sensitized organic PV devices, as it may enable rapid and directional triplet exciton transport in single-crystal TIPS-Pn films.

4.3 Experimental Methods

Materials

TIPS-Pn was used as-purchased from Ossila. Poly(vinyl alcohol) (PVA; Merck, average molecular weight 130 kg/mol) was sourced as a solid powder, and dissolved to a stock concentration of 10 mg/mL by heating at 90 °C in water for 1 hour. Water was purified by an 18 MΩ Millipore Milli-Q Reagent Water System fitted with a 0.45-µm filter. HPLC-grade tetrahydrofuran (THF; RCI Labscan) was freshly distilled before use.

Nanoparticle Preparation

Crystalline TIPS-Pn nanoparticles were prepared using a previously described procedure.[1] Briefly, TIPS-Pn in THF (200 µL, 800 µM) was flash-precipitated into rapidly-stirred water (10 mL), yielding an aqueous suspension of amorphous-phase TIPS-Pn nanoparticles. This process was repeated twice, and the resulting suspensions combined and concentrated under reduced pressure to a final TIPS-Pn concentration of 100 ppm. The suspension of nanoparticles was filtered through a 0.2-µm syringe filter (Sartorius Minisart NML). A 20-µL portion of PVA solution (10 mg/mL) was then added to 1.98 mL of NP suspension, and the nanoparticles allowed to crystallize for 16 hours. Dynamic light scattering (DLS) characterization of nanoparticle size was conducted with a Malvern Zetasizer Nano ZSP, using a 633-nm laser at a backscattering angle of 173°.

Spectroscopic Measurements

All spectroscopic measurements were collected in a 2-mm path length quartz cuvette (Starna Cells 21-Q-2). Steady-state absorption spectra were collected using a Cary Varian 1E UV-visible spectrophotometer. Time-resolved spectroscopic measurements were collected on a transient absorption spectrometer (Ultrafast Systems, Helios). Laser pulses at 800 nm with a 100-fs pulse width and 1-kHz repetition rate were generated as the primary light source using a Ti:sapphire regenerative amplifier (Spectra Physics, Spitfire Pro XP 100F). An optical parametric amplifier (Light Conversion, TOPAS-C) was used to produce 440-nm pump pulses from the fourth harmonic of the idler, with a spot-size of 465 µm at the sample position. Pump fluences were varied from 20 µJ cm^{-2} to approximately 1 mJ cm^{-2}. Focusing of the 800-nm pulses onto a 3.2-mm sapphire crystal generated white-light continuum probe pulses with a spectral coverage of 450–750 nm and a spot-size of 122 µm at the sample position. Pump and probe were polarized at the magic angle of 54.7° relative to one anther in order to minimize polarization biases in the measurements. NP suspensions were constantly stirred during experiments, with negligible photo-bleaching observed.

4.4 Computational Methods

DFT calculations were performed using the Q-Chem computational chemistry software package, version 5.2.2.[168] All calculations were run at the PBE/6-31G* level of theory,[230,231] as it has been previously used to give reasonable predictions of triplet diffusion rates in other polyaromatic hydrocarbons.[80] Electronic couplings were computed by constrained DFT configuration-interaction (CDFT-CI) calculations of TIPS-Pn dimer pairs taken from the crystal structure reported by Anthony and co-workers.[125,171] Given that the solubilizing isopropylsilyl groups in TIPS-Pn have a minimal influence on triplet energetics, these were replaced by methyl groups in these calculations to reduce computational expense. In each state, one monomer was constrained to triplet spin and the other to singlet spin. Further details of these calculations are given in the Supporting Information.

4.5 Results and Discussion

Size characterization by DLS (Supporting Information) shows that a monodisperse size distribution of nanoparticles (Z-average diameter of 72 nm) results from the preparation method employed here. This is in close agreement with other size distributions previously reported for TIPS-Pn NPs prepared through this method.[1,119] Additionally, steady-state absorption (Supporting Information) and femtosecond TA spectra (Figure 4.1) of these NPs are identical to those reported in our previous study of crystalline TIPS-Pn NPs, in which X-ray diffraction was used to confirm that the chromophores adopted the slip-stacked morphology characteristic of crystalline TIPS-Pn.[1] Therefore, we conclude that the TIPS-Pn NPs studied here possess a crystalline morphology with the slip-stacked packing motif first reported by Anthony and co-workers.[125]

Figure 4.1a shows representative TA spectra of crystalline TIPS-Pn NPs at delay times ranging from 200 fs to 3 ns. Excited-state absorption (ESA) features at 488 nm, 523 nm and 750 nm are observed to rise within 1 ps, concomitant with the decay of other ESA bands at 460 nm and 620 nm. These bands have been previously assigned to the triplet state (T_1) and singlet state (S_1) of TIPS-Pn, respectively.[47,110] This rapid interconversion is indicative of singlet fission occurring on a sub-picosecond timescale in crystalline TIPS-Pn, agreeing with multiple previous studies.[1,63,134] Subtle restructuring of the triplet ESA bands at 488 nm and 523 nm then occurs over several picoseconds, with these features slightly red-shifting and the longer-wavelength band becoming more intense. This has previously been attributed to spatial separation of the correlated triplet pair state, and so we assign this spectral change to the formation of free triplet excitons from correlated triplet pairs.[119] The transient spectra then decay, with negligible further spectral evolution beyond 50 ps (Figure 4.1b), indicating minimal further relaxation within the triplet excited-state manifold, with these triplet states only decaying to the ground state. Therefore, we assign these TA spectra from 50 ps onwards as being predominantly due to free triplet excitons within crystalline TIPS-Pn, with negligible contributions from singlet excitons and no further separation of any correlated triplet pair excitons.

The ESA at 680 nm and the ground-state bleach (GSB) at 700 nm red-shift slightly at delay times beyond 50 ps, which becomes increasingly evident at high pump fluences (Supporting Information). This spectral shift may be due to a change in the nature

of the GSB itself. A recent study by Jones and co-workers identified a lower energy shoulder in the main absorption band of crystalline TIPS-Pn, which they assigned to excitations of non-equilibrium crystal packings induced by grain boundaries or defect sites.[127] Should such lower energy sites exist in the nanoparticles studied here, they may

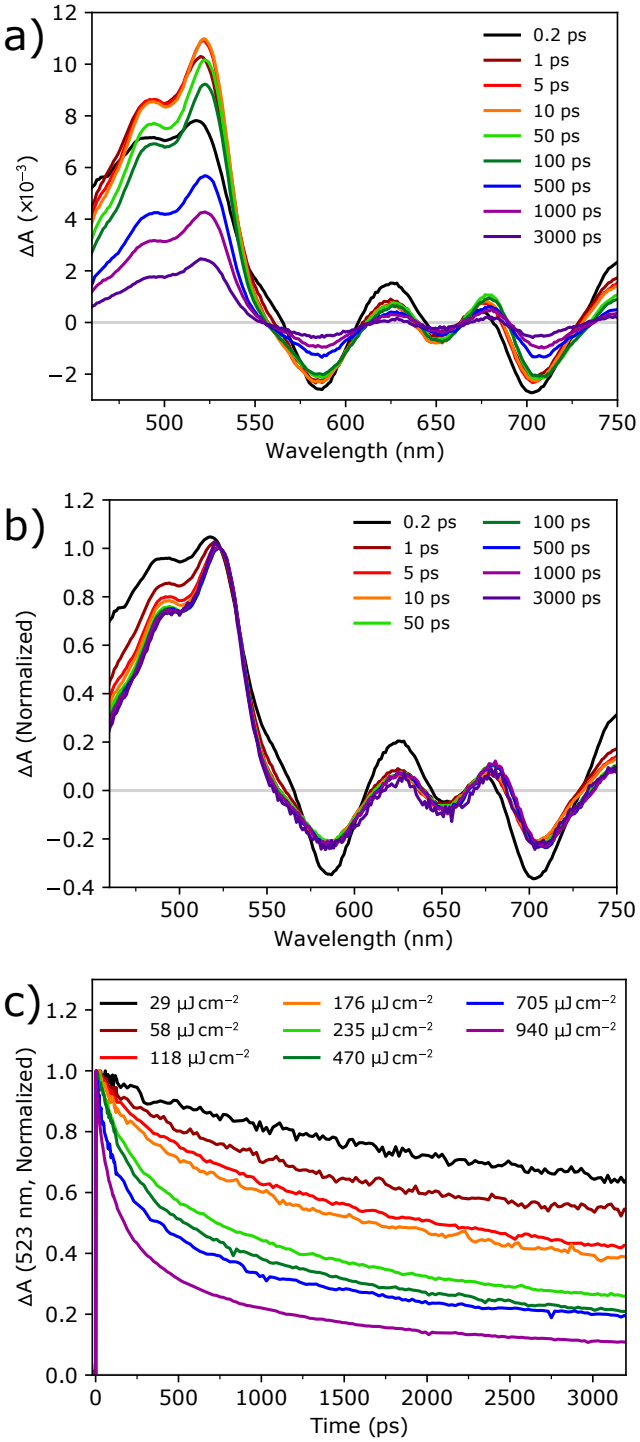

Figure 4.1: TA spectra of crystalline TIPS-Pn NPs after excitation at 440 nm at a pump fluence of 470 µJ cm^{-2}, as (a) measured ΔA and (b) ΔA normalized to the 523 nm triplet ESA feature. (c) Normalized decay kinetics of the 523 nm triplet ESA under a range of pump fluences.

act as trap sites, with triplet excitons funneled to these sites due to the surrounding energy gradient. This process would result in a shift in the relative exciton populations at equilibrium and non-equilibrium TIPS-Pn sites over time, yielding a corresponding shift in the GSB due to the spectral differences of these sites in their ground states.

The decay of the 523 nm ESA signal depends strongly upon pump fluence: as demonstrated in Figure 4.1c, this decay accelerates at higher pump fluences. This behavior is indicative of bimolecular exciton–exciton annihilation (EEA) interactions dominating the triplet decay at the excitation densities used here.[63,110,119] To quantify these annihilation interactions, we consider a number of bimolecular annihilation kinetic models fit to the collected data. All models considered have the general form

$$\frac{\mathrm{d[T]}}{\mathrm{d}t} = -k_1[\mathrm{T}] - k_2[\mathrm{T}]^2, \tag{4.1}$$

where k_1 is the unimolecular rate coefficient associated with first-order triplet decay and k_2 is the bimolecular annihilation rate coefficient. Assuming isotropic diffusion of triplet excitons and that annihilation is effectively instantaneous upon contact, k_2 may be related to the diffusion constant D and annihilation radius R of triplet excitons by[226,227]

$$k_2 = 8\pi RD\left(1 + \frac{R}{\sqrt{2\pi Dt}}\right). \tag{4.2}$$

At long times for which $\sqrt{2\pi Dt} \gg R$, Equation 4.2 reduces to

$$k_2 = 8\pi RD. \tag{4.3}$$

The approximation in Equation 4.3 has been widely used to describe bimolecular annihilation for excitons encountering one another through a three-dimensional (3D) random walk.[92,232] Several previous studies have applied Equation 4.3 to model the bimolecular annihilation kinetics of pentacene[117] and TIPS-Pn.[63,110] While both equations stem from the same model, they are qualitatively different: one treats the exciton annihilation rate coefficient as time-independent, while the other also includes a time-dependent component on short timescales. We consider both forms of this model when attempting to fit the TA data here, and refer to them below as the "constant k_2" and "time-dependent k_2" isotropic 3D diffusion models, respectively.

Triplet concentrations within the nanoparticles were extracted from the TA data (see Supporting Information for details), and both isotropic 3D models presented above were fit to the data over a range of excitation densities. Figure 4.2 shows a sample of the fits at a pump fluence of $470\,\mu\mathrm{J\,cm^{-2}}$, while the remaining fits are shown in the Supporting Information. When considering the isotropic 3D diffusion models, the time-dependent k_2 model (solid curve, coincident with the dashed curve) fits the data significantly better than the constant k_2 model (dotted curve), with the latter underestimating the decay rate at early times and overestimating at later times. Clearly, the time-dependent nature of the triplet annihilation rate coefficient due to diffusion must be accounted for on the sub-nanosecond timescale when describing excitonic migration within crystalline TIPS-Pn. As such, the isotropic 3D diffusion model with constant k_2 is excluded from the following discussion, and the time-dependent k_2 model is hereafter referred to as the "isotropic 3D diffusion model" for simplicity.

The best-fit parameter values for the isotropic 3D diffusion model are shown in Table 4.1. Using the best-fit R and D values in the long-time limiting case (Equation 4.3), a bimolecular annihilation constant of $(1.2 \pm 0.2) \times 10^{10}\ \mathrm{M^{-1}\,s^{-1}}$ is obtained,

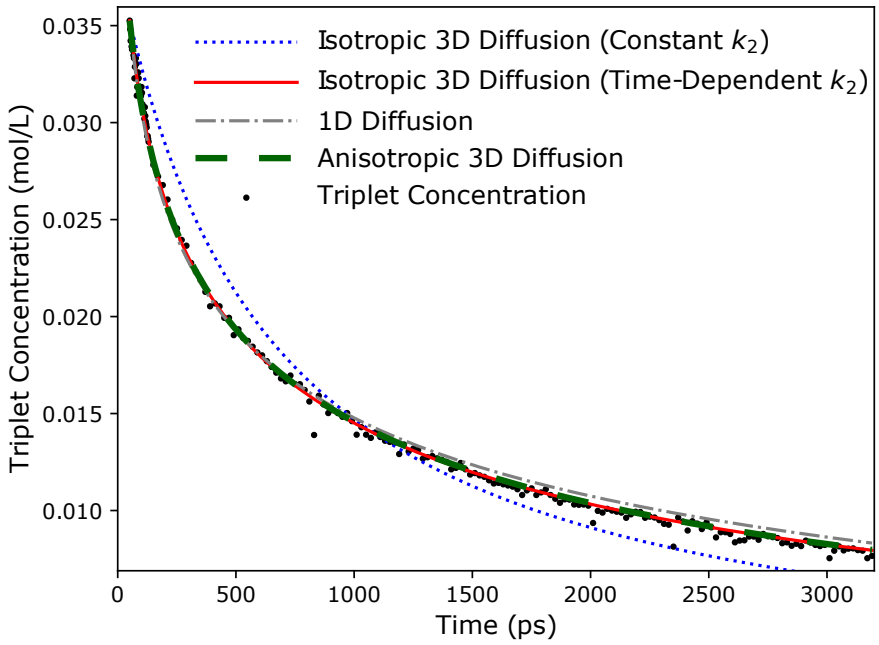

Figure 4.2: Triplet concentrations in crystalline TIPS-Pn NPs from 50 ps after excitation with pump fluence of 470 µJ cm^{-2}, with fits from all bimolecular annihilation models considered here. Best-fit parameters from models of interest are shown in Table 4.1. Note that the fits from the isotropic 3D (time-dependent k_2) and anisotropic 3D models are coincident, and that the concentrations shown here refer to exciton concentrations within the TIPS-Pn NPs (see Supporting Information for further details).

which agrees closely with a previous measurement for polycrystalline TIPS-Pn thin-films.[110] Additionally, with these values of R and D, Equation 4.3 is expected to be valid on timescales much longer than 10^{-9} s. Therefore, the short-time behavior of Equation 4.2 is irrelevant on timescales longer than nanoseconds. This result may help to reconcile the apparent discrepancy between the fitting of time-dependent spectral data on triplet populations here and in other reports; previous studies of TTA in TIPS-Pn have generally focused upon timescales of 10^{-8}–10^{-6} s,[63,110,114] in which Equation 4.3 is a good approximation of Equation 4.2. This study, however, considers diffusion on a significantly shorter timescale, for which the time-dependent form of k_2 is necessary to adequately describe bimolecular TTA in TIPS-Pn.

The first-order rate constants (k_1) obtained from all diffusion models considered here (Table 4.1) correspond to intrinsic triplet lifetimes on the order of tens to hundreds of nanoseconds, which are significantly shorter than the timescale of microseconds previously reported for TIPS-Pn.[110,114] While accurate fitting of such a slow process from the 3-ns time window observed here is not expected, these rapid decays are unusual. This first-order term is necessary to adequately fit the data, as using only the bimolecular term is insufficient to capture all of the triplet decay (Supporting Information). Several other studies using ps–ns TA have also reported first-order triplet decays on similar timescales for TIPS-Pn.[59,72,133] One possible explanation for this behavior is geminate TTA or first-order ^{1}(TT) decay. While the triplet ESA signals observed here show negligible spectral evolution beyond 50 ps after excitation, it is possible that some triplet pair states may still be present, as correlated triplet pairs and free triplets in crystalline TIPS-Pn are spectrally similar in the visible region.[59,119] It has recently

Table 4.1: Best-fit parameters for 1D and 3D diffusion models fit to triplet exciton concentrations in crystalline TIPS-Pn NPs. [a]

Diffusion Model	D ($\mathrm{cm^2\,s^{-1}}$)	R (nm)	k_1 (10^7 $\mathrm{s^{-1}}$)	χ^2 (10^{-4} $\mathrm{M^2}$)[b]
Isotropic 3D	$(3.5 \pm 0.5) \times 10^{-6}$	2.3 ± 0.1	0.6 ± 0.5	1.87
1D	$(3.52 \pm 0.06) \times 10^{-3}$ [c]	0.7565[c]	7.9 ± 0.4	2.52
Anisotropic 3D	$(2.5 \pm 0.1) \times 10^{-3}$ [c,d]	0.7565[c]	2.3 ± 0.6	1.88

[a] Uncertainties are 95 % confidence intervals estimated from the fitting process.
[b] χ^2 denotes the sum of squared residuals between the model and experimental triplet concentrations.
[c] Assumes R_{1D} to be equal to the a-axis lattice spacing of 7.565 Å.
[d] Diffusion coefficient along the fast axis (D_z); a separate coefficient of $D_\rho = (1.1 \pm 0.3) \times 10^{-7}$ $\mathrm{cm^2\,s^{-1}}$ is fit in the slower direction.

been demonstrated that the SF kinetics in amorphous TIPS-Pn could only be fully described when including a population of triplet pair states that underwent fast non-radiative decay.[62,72] It was suggested that this may be due to certain TIPS-Pn pair geometries being unsuitable for triplet pair separation, with diffusion away from these sites inhibited. We hypothesize that a similar phenomenon may occur in the crystalline TIPS-Pn NPs studied here, with a relatively small population of triplet pair states unable to separate into free triplets. These triplet pairs would therefore be unable to undergo bimolecular annihilation in the crystal bulk, and would instead recombine or relax with first-order kinetics.

An alternative cause of this rapid first-order decay in triplet concentration could be triplet–charge annihilation (TCA). We have previously demonstrated that TIPS-Pn NPs re-precipitated into water acquire a negative surface charge, which improves the colloidal stability of these suspensions.[1] Encounters between these charges and triplet excitons could result in exciton annihilation that is pseudo first-order with respect to triplet concentration, as has previously been reported in other organic semiconductors.[233,234] By considering the rate at which triplets diffuse to charged sites at the NP surface, whose density was estimated from experimental zeta potential measurements, we estimate that TCA in the TIPS-Pn NPs studied here could occur on a time scale of 10^{-8}–10^{-5} s, based on the diffusion coefficients in Table 4.1 and the conservative assumption that every triplet-charge encounter leads to exciton annihilation (Supporting Information). These values are consistent with the best-fit first-order decay coefficients from the experimental data. However, there is a significant level of uncertainty in these estimates, which precludes us from assigning the extent to which TCA contributes to this first-order decay. Scattering of the laser pulse was also considered as an alternative process that could result in this rapid first-order triplet decay (Supporting Information), but was discounted as a major contributor as it could only occur on a time scale much slower than the first-order rate coefficients fit here.

The best-fit value of D determined from the isotropic 3D model is of a similar order of magnitude to that previously determined for polycrystalline TIPS-Pn.[63,110] However, the annihilation radius R is much larger than what has been previously considered physically reasonable for TIPS-Pn. Triplet excitons are generally understood to be highly localized upon single chromophores, with hopping limited to nearest-neighbors by Dexter excitation transfer (DET).[80,102] Given the close intermolecular

contacts within slip-stacked TIPS-Pn, an annihilation radius on the order of 1 nm or less has been previously predicted for triplet excitons in TIPS-Pn.[110,114] However, these previous studies were unable to independently determine both R and D as they used Equation 4.3 to model the long-time triplet diffusion in crystalline TIPS-Pn. In contrast, the fitting of Equation 4.2 to early-time data here allows for independent extraction of these two parameters, but yields a best-fit value of R as 2.3 nm, which is clearly incongruent with these previous estimates. We considered the possibility that this large value may have arisen due to poor sensitivity of the fitting process to variations in the value of R, and attempted to fit this model with R constrained to more physically reasonable values. However, reduction of R below 1.8 nm reduced the quality of the fit to the experimental data and yielded unreasonably low values of the rate coefficient k_1 for first-order triplet decay (Supporting Information). Therefore, we discount this factor as a source of error for the large value of R determined here.

However, both of the diffusion models considered so far assume that triplet excitons diffuse isotropically in three dimensions through TIPS-Pn, which is highly unlikely given the significant anisotropy within the crystal packing. As shown in Figure 4.3a, preferential exciton migration through the *ab* plane of the material would be expected, as the slip-stacked morphology provides π-stacking interactions and hence relatively large electronic couplings between chromophores in these directions.[125] Conversely, hopping in the *c*-direction should be significantly slower, as the TIPS-Pn molecules contact one another only through insulating TIPS-groups in this direction (Figure 4.3b). The good fit of the isotropic 3D diffusion model to the experimental data in Figure 4.2 despite the 3D anisotropy of TIPS-Pn can be rationalized as follows. The rate coefficients for bimolecular reactions limited by anisotropic 3D diffusion have been shown for various cases of anisotropy in either the diffusion tensor or reaction volume to obey an equation of the general form[100,103]

$$k_2 = B + \frac{C}{\sqrt{t}}, \tag{4.4}$$

for some constants B and C. However, the relationship between these constants and physical parameters depends on the anisotropy of the diffusion tensor or reaction (annihilation) volume. As Equation 4.2 for isotropic 3D diffusion is equivalent in form to Equation 4.4, the isotropic 3D diffusion model may therefore fit the data well even if diffusion is highly anisotropic in the measured system, but with best-fit parameters that may not be physically meaningful. This consideration may hence explain the unreasonably large best-fit value of R determined from the fitting here. We therefore offer a cautionary note: while 3D isotropic diffusion models similar to those used here are commonly used to explain exciton migration in organic materials,[63,72,110,117,225] the diffusion coefficients and annihilation radii resulting from this fitting may not correspond to the material's true, physical properties, and should be interpreted with care.

Given the significant anisotropic packing of crystalline TIPS-Pn, it is reasonable to question whether a full 3D treatment of diffusion is necessary to describe bimolecular TTA. Due to the exponential decrease of the DET rate constant with interchromophore distance,[79,235] long-distance hopping along the *c*-axis should contribute negligibly to overall exciton diffusion. Additionally, π–π stacking is most significant along the *a*-axis, so triplet energy transfer is expected to be fastest along this axis. This directional triplet transfer is supported by a previous transient absorption microscopy study of triplet migration in single-crystal TIPS-Pn, which found that triplet diffusion was

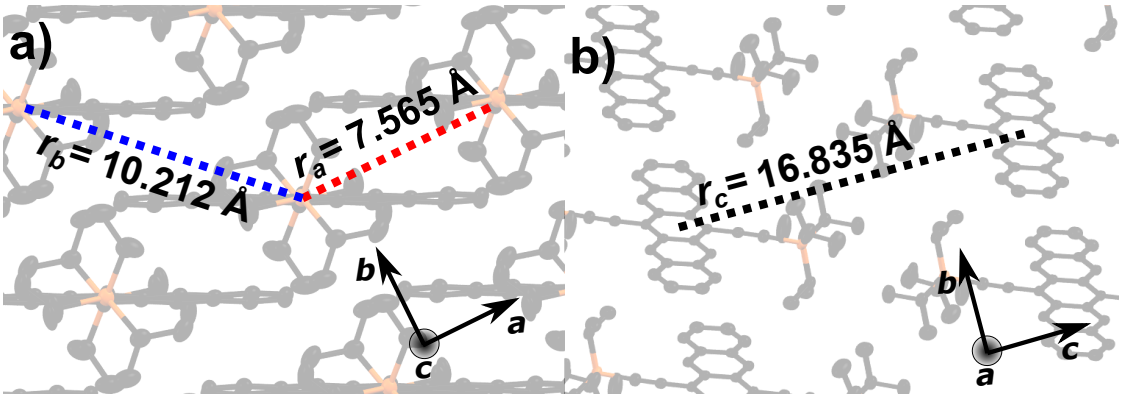

Figure 4.3: Crystal packing of the primary polymorph of crystalline TIPS-Pn in the (a) *ab*-plane and (b) *bc*-plane. Dashed lines represent intermolecular packing distances, with unit cell axes shown from each perspective for reference. Carbon atoms are shown in black and silicon atoms in orange; hydrogen atoms are omitted for clarity. The crystal structure is taken from ref. 125.

anisotropic on the *ab*-plane and fastest along the *a*-axis.[114] Therefore, we hypothesized that triplet diffusion in TIPS-Pn on the sub-nanosecond timescale could be approximated by one-dimensional (1D) diffusion along the *a*-axis. To test this hypothesis, we considered a model in which diffusion is only allowed in a single dimension,[236]

$$k_2 = \frac{1}{R_{1D} N_0} \sqrt{\frac{8 D_{1D}}{\pi t}}, \tag{4.5}$$

where N_0 is the average molecular density throughout the system (calculated from the density and molecular weight of TIPS-Pn; Supporting Information), and R_{1D} and D_{1D} are 1D analogues of the parameters discussed above. When applying this model to the experimental data here (Figure 4.2, dot-dashed curve and Supporting Information), a relatively good fit to the data is observed. The 1D model captures much of the triplet decay kinetics, and fits the data almost as well as the isotropic 3D diffusion model at early times (< 1 ns). Therefore, the TTA kinetics studied here may be reasonably approximated by diffusive motion in only a single dimension on the sub-nanosecond timescale. Like Equation 4.2 for isotropic 3D diffusion, Equation 4.5 for 1D diffusion is equivalent in form to Equation 4.4, but has a different relationship between the constants B and C and physical parameters (notably $B = 0$ for 1D diffusion). Therefore, this fit yields very different values for these parameters compared with the analogous parameters in the isotopic 3D model. Due to the nature of Equation 4.5, R_{1D} and D_{1D} are not separable when fitting this model, but the term ${D_{1D}}^{1/2}\,{R_{1D}}^{-1}$ fits as a single parameter. However, if it is assumed that R_{1D} corresponds to the nearest-neighbor stacking distance along the *a*-axis of 7.565 Å, fitting this model to the data yields $D_{1D} = 3.52 \times 10^{-3}\,\mathrm{cm^2 s^{-1}}$, which agrees closely with the 1D diffusion coefficient determined by Zhu and co-workers' study of single-crystal TIPS-Pn.[114] This relatively good fit to the data and agreement with another study suggests that exciton diffusion along the *a*-axis dominates the bimolecular TTA in crystalline TIPS-Pn on the sub-nanosecond timescale.

However, the 1D diffusion model does not fit the experimental data as well the isotropic 3D model over the entire time window observed here; at later times (> 1 ns) it begins to underestimate the rate of triplet decay. This discrepancy suggests that

slow but non-negligible diffusion may occur along other crystallographic axes of TIPS-Pn, which is not included in the 1D model. To account for this, we considered an expanded model in which diffusion is still fastest along a single axis, but a slower rate of diffusion in the directions perpendicular to this is permitted. For simplicity, this model assumes that the rates of diffusion along both axes perpendicular to the direction of fast diffusion are equivalent. In this "anisotropic 3D diffusion model", the bimolecular rate constant is given by[103]

$$k_2 = 16\sqrt{\frac{D_z D_\rho}{\pi R_z N_0}} + \frac{1}{R_z N_0}\sqrt{\frac{8D_z}{\pi t}}, \tag{4.6}$$

where D_z and D_ρ represent the diffusion coefficients in the fast and slow directions, respectively, and R_z is the annihilation radius along the direction of fast motion (the correspondence to equations in ref. 103 is obtained by noting that $(R_z N_0)^{-1} = \pi {R_\rho}^2$, where R_ρ is the average annihilation radius in the directions perpendicular to the fast direction, assuming annihilation between excitons on nearest-neighbor molecules). Again, this model has the same general form as Equation 4.4, and as D_ρ approaches zero Equation 4.6 reduces to the 1D diffusion model. Fits of the anisotropic 3D diffusion model to the experimental data are shown in Figure 4.2 (dashed curve) and the Supporting Information, with best-fit parameters in Table 4.1. As with the 1D model, the annihilation radius R_z is constrained to the *a*-axis molecular displacement during the fitting process. The anisotropic 3D diffusion model shows an improved fit over the 1D model, fitting the experimental data equally as well as the isotropic 3D diffusion model. The similarity in the fits of the isotropic and anisotropic 3D diffusion models to the data is again due to the equivalence of their functional forms (Equation 4.4), but these models have significantly differing relationships between coefficients B and C and physical parameters. This result again highlights the issue identified above with using isotropic diffusion models to describe anisotropic diffusion: the model may fit the data well, but the best-fit parameters may not have the expected relationship to the material's physical properties.

The two diffusion coefficients fit to the anisotropic 3D diffusion model differ by four orders of magnitude. The fast diffusion coefficient D_z is comparable to D_{1D} fit from the 1D diffusion model, while D_ρ is four orders of magnitude smaller. This result supports the earlier hypothesis that triplet exciton diffusion in crystalline TIPS-Pn is fastest along the *a*-axis, with significantly slower diffusion occurring in the directions perpendicular to this. However, the anisotropic 3D diffusion model assumes that diffusion both of these perpendicular directions are equivalent, which is likely not the case in crystalline TIPS-Pn. As demonstrated in Figure 4.3, molecular packing modes along the *b*- and *c*-axes are substantially different from one another, and so the rates of diffusion in each of these directions are likely also inequivalent. D_ρ should therefore be considered some form of averaged diffusion coefficient along these two axes, but the exact contributions from each of these directions cannot be determined from this model.

To verify our measurements of anisotropic diffusion in TIPS-Pn, DFT and Marcus theory were used in combination to estimate triplet hopping rates and diffusion coefficients along different packing directions of crystalline TIPS-Pn, as per the method reported by Yost et al.[80] Triplet energy transfer requires an effective transfer of two electrons between donor and acceptor sites, and so is commonly approximated by Marcus electron-transfer theory.[80] In Marcus theory, the rate coefficient for electron transfer

between a donor site and an acceptor site is given by

$$k_{\mathrm{da}} = \frac{2\pi}{\hbar}|V_{\mathrm{da}}|^2\sqrt{\frac{1}{4\pi k_{\mathrm{B}}T\lambda}}\exp\left[-\frac{(\Delta G^{\circ}+\lambda)^2}{4\lambda k_{\mathrm{B}}T}\right], \tag{4.7}$$

where V_{da} is the electronic coupling between donor and acceptor diabatic states, T is temperature, λ is the reorganization energy, ΔG° is the free energy change upon transfer and k_{B} is the Boltzmann constant.[237] ΔG° is zero for triplet excitons hopping through an infinite crystalline lattice, as adjacent lattice sites are equivalent in crystalline TIPS-Pn. λ was calculated at the PBE/6-31G* theory level using the four-point method on a single molecule of TIPS-Pn,[80,230,231] and V_{da} was determined by CDFT-CI calculations between each unique dimer pair at the same level of theory.[171] Further details of these calculations are shown in the Supporting Information. The hopping rate coefficient can then be related to the one-dimensional diffusion coefficient along each axis by[238]

$$D_{\mathrm{1D}} = \frac{a^2}{2}k_{\mathrm{da}}, \tag{4.8}$$

where a is the lattice parameter along this axis.

Predicted hopping rate coefficients and diffusion coefficients along the a, b and c stacking directions (denoted as r_{a}, r_{b} and r_{c}, respectively, in Figure 4.3) are shown in Table 4.2. While r_{a} and r_{c} correspond to the crystallographic a and c axes of crystalline TIPS-Pn, respectively, r_{b} does not fully align with the b-axis. Therefore, we hereafter refer to the "b slip-stacking direction" or "b molecular pair" to avoid confusion with the crystallographic b-axis. Triplet hopping and diffusion is predicted to be faster along the a-axis relative to the b-stacking direction by over an order of magnitude, with diffusion along the c-axis slower again by at least five orders of magnitude. The predicted diffusion coefficient along the a-axis agrees relatively well with the best-fit values of D_{1D} and D_z from the experimental data (given the low level of computational theory used), differing by only a factor of 2–3. Additionally, the best-fit value of D_ρ from the anisotropic 3D diffusion model is on the same order of magnitude as the geometric mean of the predicted diffusion coefficients along the b and c packing directions ($6.4 \times 10^{-7}\,\mathrm{cm^2\,s^{-1}}$). These results therefore support the above conclusions from fitting to the experimental data, indicating that triplet exciton diffusion occurs predominantly along the a-axis on short timescales, with significantly slower diffusion in the b-direction and negligible diffusion along the c-axis.

Such anisotropy in the diffusion of triplet excitons through crystalline TIPS-Pn has significant implications when considering the design and fabrication of any device using TIPS-Pn as an excitonic down-converter. The triplet diffusion length through crystalline TIPS-Pn is defined as

$$L_{\mathrm{D}} \equiv \sqrt{D\tau}, \tag{4.9}$$

Table 4.2: Predicted electronic couplings, hopping coefficients and diffusion coefficients for triplet excitons between different molecular pairs within the TIPS-Pn crystal structure.

TIPS-Pn Pair	V_{da} (meV)	k_{da} ($\mathrm{ps^{-1}}$)	D_{1D} ($\mathrm{cm^2\,s^{-1}}$)
a	7.92	3.70×10^{-1}	1.06×10^{-3}
b	1.16	7.94×10^{-3}	4.14×10^{-5}
c	$< 1 \times 10^{-3}$	$< 7 \times 10^{-9}$	$< 1 \times 10^{-10}$

where τ is the intrinsic lifetime of the triplet excitons. Under conditions of solar flux, bimolecular TTA is expected to be negligible (Supporting Information), so we consider τ to correspond to the previously reported natural triplet lifetime of 2.1 µs.[110] Using the 1D diffusion coefficients derived computationally here, Equation 4.9 yields diffusion lengths of 470 nm, 93 nm and < 1 nm along the *a*-axis, *b*-stacking direction and *c*-axis of TIPS-Pn, respectively. That is, triplet excitons in crystalline TIPS-Pn may diffuse over 5× further along the *a*-axis than the *b*-stacking direction throughout the exciton lifetime. The predicted diffusion length along the *c*-axis is smaller than the intermolecular separation in this direction, highlighting that diffusion in the *c*-direction of crystalline TIPS-Pn is negligible within the triplet lifetime.

The predicted triplet diffusion lengths for the *a* and *b* stacking directions are both exceptionally large given the poor mobilities of triplet excitons in organic materials.[80,239] However, these values assume diffusion through single-crystal TIPS-Pn, with no polycrystallinity or grain boundaries between crystalline domains. As demonstrated by the significant disparity between hopping rate coefficients along different directions in Table 4.2, any disruption of the TIPS-Pn slip-stacking will substantially slow triplet mobility through the material. We therefore suggest that the triplet diffusion length in crystalline TIPS-Pn is largely limited by grain boundaries between crystalline domains, and that triplet excitons will accumulate at such boundaries over time. This suggestion agrees with the assignment of the spectral red shifts observed here (Supporting Information) as an accumulation of excitons at low-energy defect sites such as those at grain boundaries. A significant proportion of TIPS-Pn thin-film systems reported in the literature are polycrystalline in nature,[57,59,63,101,110,131,136,184,188,205,210,240] and may therefore experience this phenomenon. Additionally, even for films that achieve large-scale crystalline alignment, the relative orientation of these slip-stacking directions to the device architecture must also be considered. To achieve optimal exciton transfer to an electron accepting layer, the film should be oriented with the *a*-axis perpendicular to the interface with this layer. Recently, multiple reports have emerged of solution-sheared layers of TIPS-Pn that have large-scale single-crystal alignment with the *a*-axis oriented perpendicular to the substrate surface.[120,228,229] Such alignment would allow for fast, directional diffusion of triplet excitons to interfaces with acceptor materials at early times, and would therefore be optimal for SF down-conversion layers in PV devices.

Finally, we note that our analysis until this point has neglected the spin statistics of TTA in TIPS-Pn. For two encountering triplet excitons, a manifold of nine encounter states are possible; one singlet, three triplets and five quintets (assuming degeneracy of encounter states).[232] Previous treatments of TTA in organic crystals have attempted to account for this by including a pre-factor of 1/9 in Equation 4.2, as only one out of the possible nine resulting encounter states results in the removal of two triplet excitons.[241] In practice, contributions from quintet encounter states are generally neglected, as they are usually so high in energy that they are effectively inaccessible,[242] thus revising this factor to 1/4 (three triplet states and one singlet state). However, recent studies have shown quantum yields of fluorescence from TTA in rubrene and anthracene surpassing this limit.[96,97] These findings were ascribed to the energy of the T_2 state in these systems being significantly higher than twice the T_1 energy and thus minimizing annihilation occurring through the triplet manifold, as annihilation through the triplet channel requires the formation of one high-energy triplet state from two lower-energy triplets. Indeed, upon observing similar results, Auckett and co-workers suggested

that no such spin-statistical limit exists for TTA in rubrene.[98] To assess whether such a spin-statistical limit of TTA should be considered here, we examined the energies of the low-lying singlet and triplet excitons in crystalline TIPS-Pn (energy level diagram shown in the Supporting Information). While the S_1 state of crystalline TIPS-Pn is approximately isoergic with twice the energy of the T_1 state, the T_2 energy is almost 0.4 eV higher in energy than $2 \times T_1$. This energy difference is greater than $k_B T$ by over an order of magnitude at room temperature, indicating that high-lying triplet states should be effectively inaccessible from TTA under ambient conditions. Therefore, crystalline TIPS-Pn is likely to behave similarly to anthracene and rubrene, with singlet encounter states contributing more to TTA than the prediction from the spin-statistical limit. Annihilation via triplet encounter states may still occur, however the relative contributions of singlet and triplet encounter states cannot be accurately predicted for TIPS-Pn purely from the statistics of encounter state spins. Therefore, the best-fit parameters presented in Table 4.1 represent the limiting case in which all triplet-triplet encounters result in mutual annihilation of both excitons.

4.6 Conclusions

In summary, by studying TTA in crystalline TIPS-Pn using femtosecond transient absorption spectroscopy, we have demonstrated that the mobility of triplet excitons is well-described by diffusion that is spatially anisotropic. While the results show a good fit to an isotropic, 3D Smoluchowski-type diffusion model, the resulting fit parameters are not physically representative of crystalline TIPS-Pn, due to the inherent anisotropy of this structure and the similar functional form of the time dependence of isotropic and anisotropic diffusion. The results are also well described by a 1D diffusion model, indicating that early-time bimolecular TTA in crystalline TIPS-Pn is dominated by exciton diffusion along a single axis. Fits to an anisotropic 3D diffusion model and computationally predicted diffusion coefficients support this finding, suggesting that diffusion along the crystallographic a-axis is at least one order of magnitude faster than any other direction in crystalline TIPS-Pn. Diffusion lengths of 470 nm and 93 nm are predicted for triplet excitons diffusing along the a and b packing directions, respectively, in single crystal TIPS-Pn. This work therefore demonstrates that triplet diffusion along is highly anisotropic in crystalline TIPS-Pn, highlighting the importance of single crystal alignment in promoting efficient exciton transport through TIPS-Pn films.

Acknowledgements

This work was supported by an Australian Government Research Training Program (RTP) scholarship and funding from the Australian Research Council (DP190102100, DP160103797 and LE0989747). The authors also thank Dr. Patrick Tapping, Alexandra Stuart and Jessica de la Perrelle for stimulating conversations that contributed to this work.

4.7 Supporting Information

Particle-Size Characterization by Dynamic Light Scattering

Figure 4.4 shows the intensity-weighted particle size distributions determined by DLS of TIPS-Pn NPs prepared by the same method as those studied by TA here. A relatively monodisperse particle distribution is observed for the as-prepared NPs, with a Z-average diameter of 72 nm. This closely resembles other size distributions reported previously (by our group and others) for TIPS-Pn NPs prepared by this method,[1,119] indicating that this NP preparation method is highly reproducible. A shift to larger particle sizes (115 nm Z-average diameter) and slight increase in polydispersity is evident upon NP crystallization with PVA. As discussed in our previous work,[1] this change likely corresponds to the formation of a PVA layer at the NP surface, increasing the apparent hydrodynamic diameter. Therefore, we consider the size of the TIPS-Pn interior of these NPs to remain unchanged upon PVA addition, with a diameter of 70–80 nm.

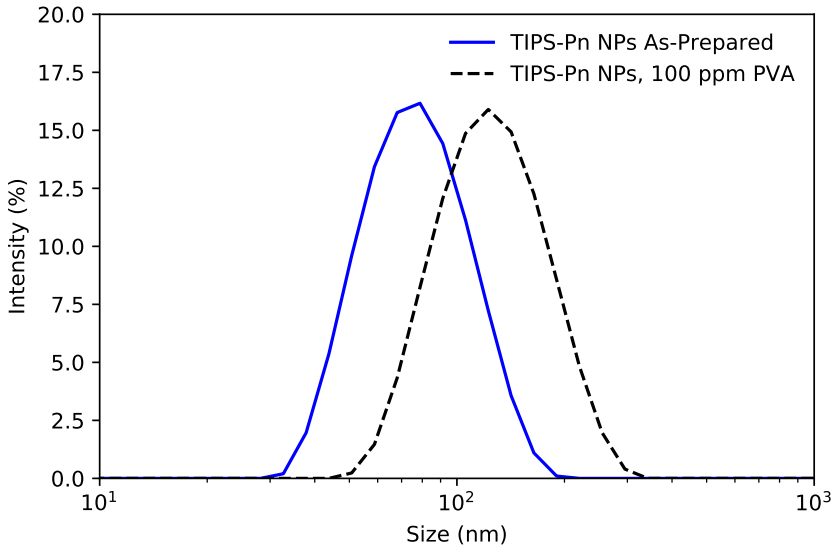

Figure 4.4: Intensity-weighted particle size distribution of TIPS-Pn NPs. TIPS-Pn concentration is 20 ppm.

Normalized Transient Absorption Spectra

Figure 4.5 shows TA spectra of crystalline TIPS-Pn NPs normalized to the triplet ESA at 523 nm, at four different pump fluences. The overall shape of the triplet ESA between 450–550 nm changes negligibly beyond 50 ps at all fluences, indicating that there is minimal singlet fission or triplet pair separation occurring after this time within the measured time window. However, a red-shift is apparent in the longer wavelength transient features, which becomes more pronounced at higher pump fluences. This is most easily observed in Figure 4.5d, with all ESA and GSB signals in the range 600–750 nm shifting to longer wavelengths with increasing time.

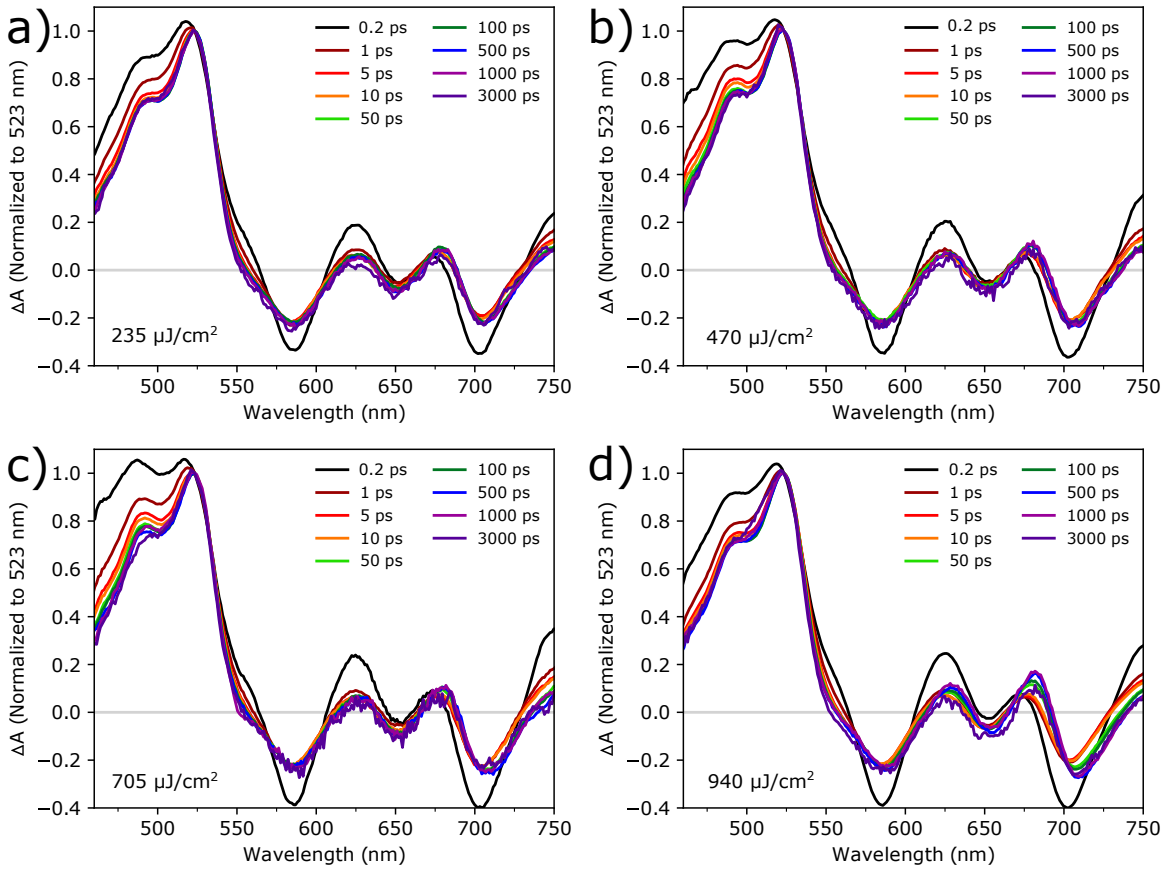

Figure 4.5: TA spectra of crystalline TIPS-Pn NPs (normalized to the triplet ESA at 523 nm) at excitation densities of (a) 235, (b) 470, (c) 705 and (d) 940 $\mu J\,cm^{-2}$.

Determination of Triplet Concentrations from Transient Absorption Data

The method used here for determining triplet exciton concentrations in TIPS-Pn NPs is similar to that used in our recent study of singlet fission kinetics in amorphous TIPS-Pn/poly(methyl methacrylate) (PMMA) composite NPs.[72] While this procedure involves assumptions that may introduce uncertainties into the absolute exciton concentrations determined, it minimally influences the evolution of the relative triplet concentrations over time, as the conversion is a largely scalar transformation of the data. Therefore, the arguments made in the main text regarding the functional form of the bimolecular annihilation rate constant (k_2) versus time will remain valid regardless of any potential errors introduced by this concentration fitting process.

Given the lack of spectral evolution in the triplet ESA beyond 50 ps noted above, at a sufficiently long delay time t we assume that the TA observed are entirely due to free triplets, with negligible contributions from singlet or triplet-pair states. As these crystalline NPs are negligibly fluorescent,[1] the negative signals observed cannot be attributed to stimulated emission and hence must be solely due to bleaching of ground-state molecules. Therefore, the magnitude of the GSB signal at 699 nm ($\Delta A(699\,nm, t)$) must correspond to the number of TIPS-Pn molecules that have been bleached from the ground state and now occupy triplet states. The concentration of triplet excitons

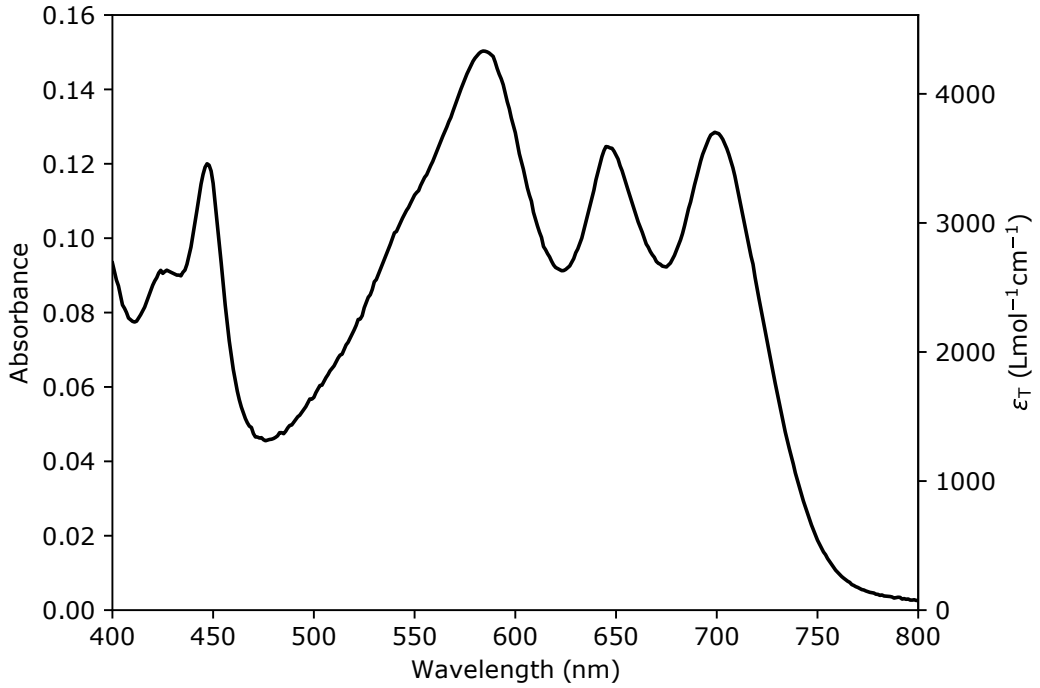

Figure 4.6: Steady-state absorption spectrum of crystalline TIPS-Pn nanoparticles in aqueous suspension, recorded at a TIPS-Pn concentration of 34.7 µM in a 1-cm path length quartz cuvette on a Cary Varian 1E UV-Visible spectrophotometer.

at delay time t can therefore be determined by

$$[\mathrm{T}](t) = \frac{\Delta\mathrm{A}(699\,\mathrm{nm}, t)}{-\epsilon_{\mathrm{ss}}(699\,\mathrm{nm})l} \tag{4.10}$$

where l is the sample path length, $\epsilon_{\mathrm{ss}}(699\,\mathrm{nm})$ is the molar extinction coefficient of crystalline TIPS-Pn at this wavelength (determined from the steady-state absorption spectrum of crystalline TIPS-Pn NPs, Figure 4.6), and we consider spectra at $t = 3\,\mathrm{ns}$. Knowing that the entire TA at this time corresponds only to free triplets, the molar extinction coefficient $\epsilon_{\mathrm{T}}(\lambda)$ at each wavelength λ for triplets in crystalline TIPS-Pn is hence determined by

$$\epsilon_{\mathrm{T}}(\lambda) = \frac{\Delta\mathrm{A}(699\,\mathrm{nm}, 3\,\mathrm{ns})}{[\mathrm{T}](3\,\mathrm{ns})l}. \tag{4.11}$$

This procedure was undertaken independently for TA spectra collected at pump fluences in the range of 115–600 µJ cm^{-2}. Lower fluences were excluded due to poor signal-to-noise in the 699 nm GSB signal, and higher excitation densities were not considered to minimize any influence of the spectral red-shifts noted in Figure 4.5.

The resulting molar extinction coefficients were averaged across these pump fluences, to yield the triplet basis spectrum shown in Figure 4.7a. Then, triplet concentrations $[\mathrm{T}](t)$ were solved for by fitting

$$\Delta\mathrm{A}(\lambda, t) = [\mathrm{T}](t)l\epsilon_{\mathrm{T}}(\lambda), \tag{4.12}$$

to the experimental data across all wavelengths, in the time range of 50–3200 ps. An example of the resulting fits are shown in Figure 4.7b. Finally, a correction was applied to account for the excitons not being isotropically distributed throughout the entire

suspension, but rather localized within the TIPS-Pn nanoparticles. The ratio between the triplet concentration throughout the suspension ($[\mathrm{T}]_{\mathrm{sus}}$) and within the TIPS-Pn NPs ($[\mathrm{T}]_{\mathrm{NP}}$) is given by

$$\frac{[\mathrm{T}]_{\mathrm{NP}}}{[\mathrm{T}]_{\mathrm{sus}}} = \left(\frac{n_{\mathrm{T,NP}}}{V_{\mathrm{NP}}}\right)\left(\frac{n_{\mathrm{T,NP}}}{V_{\mathrm{sus}}}\right)^{-1} = \frac{V_{\mathrm{sus}}}{V_{\mathrm{NP}}}, \tag{4.13}$$

where V_{sus} and V_{NP} denote the volumes of the total suspension and the NPs in suspen-

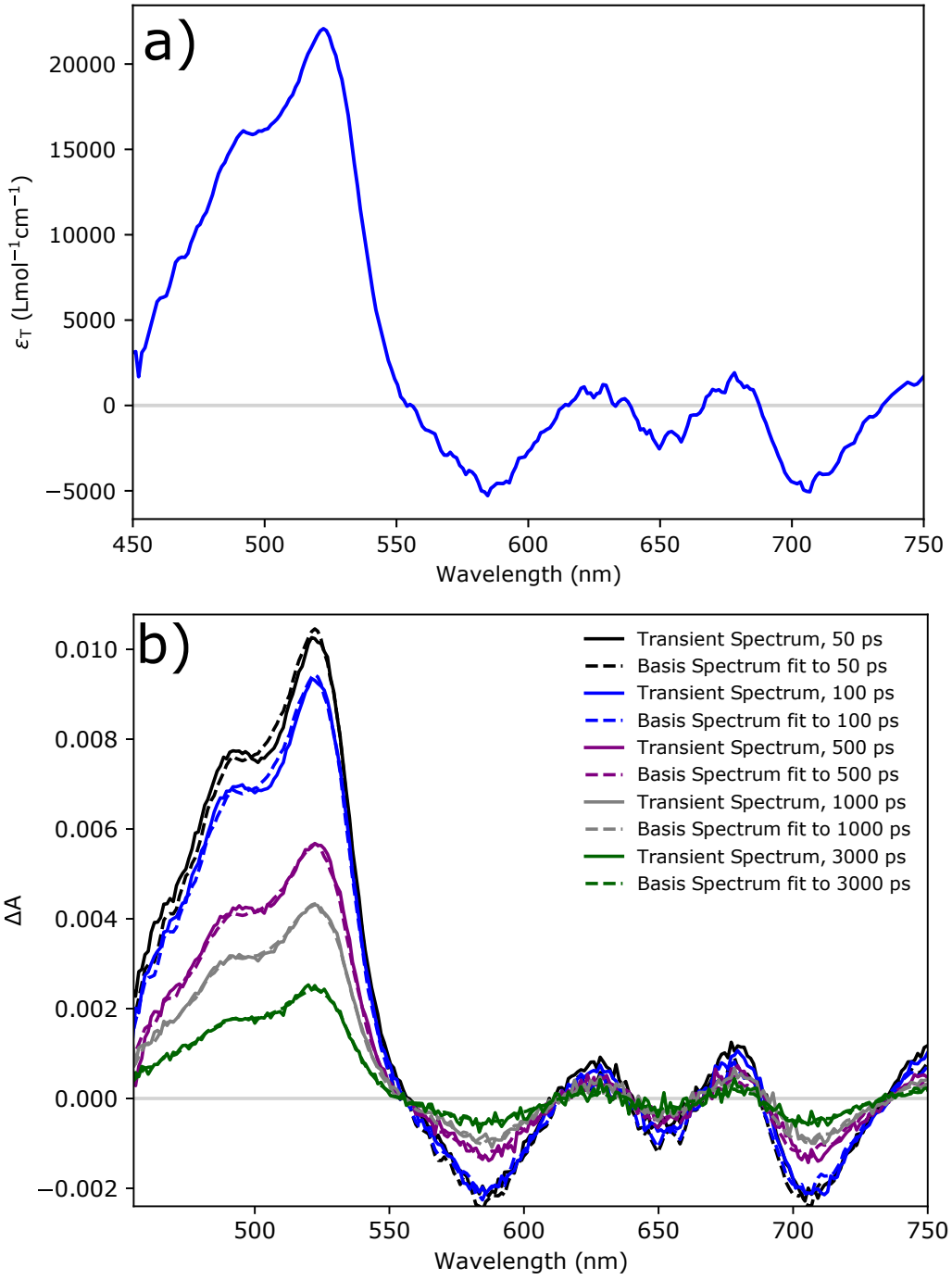

Figure 4.7: (a) Triplet basis spectrum extracted from 3 ns TA data as per Equation 4.11. (b) Example fits of the triplet basis spectrum to TA data collected at a pump fluence of 470 µJ cm^{-2}.

sion, respectively. V_{NP} may be expressed in terms of the nanoparticles' mass m_{NP} and density ρ_{NP}, yielding

$$\frac{[\mathrm{T}]_{\mathrm{NP}}}{[\mathrm{T}]_{\mathrm{sus}}} = \frac{V_{\mathrm{sus}}\rho_{\mathrm{NP}}}{m_{\mathrm{NP}}} = \frac{\rho_{\mathrm{NP}}}{c_{\mathrm{NP}}}, \tag{4.14}$$

where c_{NP} is the mass concentration of TIPS-Pn NPs in suspension. We take the TIPS-Pn density as $\rho_{\mathrm{NP}} = 1.104\,\mathrm{g\,cm^{-3}}$ here, assuming the crystalline NPs to have the same density as bulk crystalline TIPS-Pn. As crystalline TIPS-Pn NPs prepared through this method have been previously shown to closely resemble thin films of crystalline TIPS-Pn,[119] we consider this a reasonable assumption. Knowing the NP concentration used in these experiments to be 74.2 ppm (116 µM), Equation 4.14 becomes

$$[\mathrm{T}]_{\mathrm{NP}} = 14900[\mathrm{T}]_{\mathrm{sus}}. \tag{4.15}$$

Equation 4.15 was therefore applied to all concentrations determined through fitting of the triplet basis spectrum, yielding average triplet concentrations within the TIPS-Pn NPs.

Fit of Diffusion Models to Transient Absorption Data

Four different diffusive triplet–triplet annihilation models (Equations 4.1–4.3 and 4.5–4.6) were fit to the exciton concentrations determined by the method outlined in Equations 4.12–4.15. Resulting fits are shown in Figure 4.8, with global best-fit parameters (where appropriate) displayed in Table 4.1. Only data with pump fluences in the range of 100–600 $\mu\mathrm{J\,cm^{-2}}$ were considered for fitting; fluences below this range had poor signal-to-noise ratios and only showed limited bimolecular kinetics, while those above showed significant spectral shifts over time (Figure 4.5) not accounted for in the triplet basis spectrum used here. Model fitting was undertaken using a least-squares method and applied globally to all different pump fluences considered.

At all fluences considered, the isotropic 3D diffusion model (time-dependent k_2) fits the data considerably better than the constant k_2 form of this model, highlighting the need to consider the time-dependent nature of the exciton annihilation rate coefficient on the picosecond timescale. The one-dimensional model also fits the data relatively well, indicating that triplet diffusion in crystalline TIPS-Pn may be reasonably well approximated by diffusion only along a single crystallographic axis on the timescale studied here. The anisotropic 3D model improves this fit relative to the 1D model, fitting the experimental data equally as well as the isotropic 3D model (time-dependent k_2). This highlights that while triplet exciton diffusion is largely one-dimensional on the timescales considered here, slower diffusion in other directions cannot be entirely neglected.

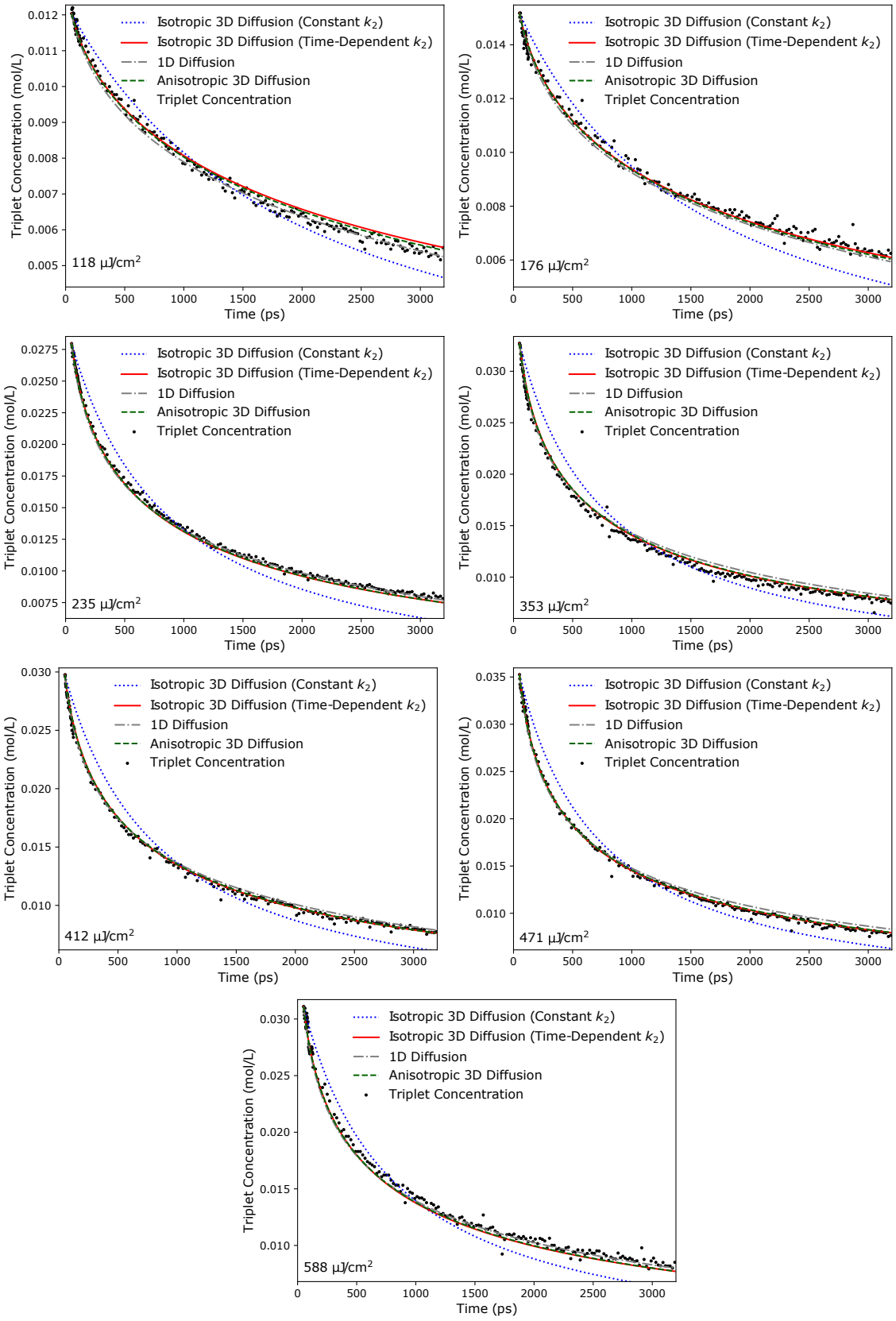

Figure 4.8: Fits of all exciton diffusion models considered here to the triplet concentrations in crystalline TIPS-Pn NPs. Note that triplet concentrations here refer to concentration within the TIPS-Pn NPs (not within the entire suspension) as per Equation 4.15.

Fit of the Isotropic Three-Dimensional Diffusion Model Without a First-Order Decay Term

To assess the importance of the first-order decay term in the models used here, a modified diffusion model was used to fit the data, in which this first-order term was neglected:

$$\frac{\mathrm{d[T]}}{\mathrm{d}t} = -k_2[\mathrm{T}]^2, \tag{4.16}$$

$$k_2 = 8\pi RD\left(1 + \frac{R}{\sqrt{2\pi Dt}}\right). \tag{4.17}$$

Fits of this model to the triplet decay data are shown in Figure 4.9. As is clear, the model fails to fully account for all triplet decay within the 3.2 ns window without a first-order decay term, underestimating the amount of exciton decay at every fluence considered. Clearly, this first-order decay term is important in accurately describing triplet exciton behavior in crystalline TIPS-Pn, even on the picosecond timescale studied here.

Other Possible First-Order Decay Processes

Dynamic Light Scattering

Here we consider the possibility that the first-order decay triplet observed in the TA experiments may be influenced by signal fluctuations due to dynamic light scattering from the nanoparticles. Assuming a monodisperse distribution of particle sizes, the first-order correlation function $g_1(t)$ of scattered light reaching a detector can be described by a single exponential,[159]

$$g_1(t) = g_1(0)\exp(-\Gamma t). \tag{4.18}$$

Γ is the inverse correlation time, given by

$$\Gamma = Dq^2, \tag{4.19}$$

where D is the diffusion coefficient of the suspended particles and q is the momentum transfer vector (also called the wave vector). q is found by

$$q = \frac{4\pi n_0}{\lambda}\sin\left(\frac{\theta}{2}\right), \tag{4.20}$$

where λ is the wavelength of light being scattered, n_0 is the refractive index of the dispersant and θ is the scattering angle.[159] We approximate the refractive index of the suspension by that of water (1.33), and consider scattering at 530 nm, where the major TIPS-Pn triplet ESA is located. We also use the extreme case of $\theta = 180°$ at which scattering will be most intense, acknowledging that the scattering angles in the TA apparatus used here will likely be significantly lower. Using these values, Equation 4.20 predicts a wave vector of $3.15 \times 10^7\ \mathrm{m}^{-1}$ for this system. The diffusion coefficient D of the nanoparticles can be determined from the Stokes–Einstein equation,[160]

$$D = \frac{k_\mathrm{B}T}{6\pi\eta r}. \tag{4.21}$$

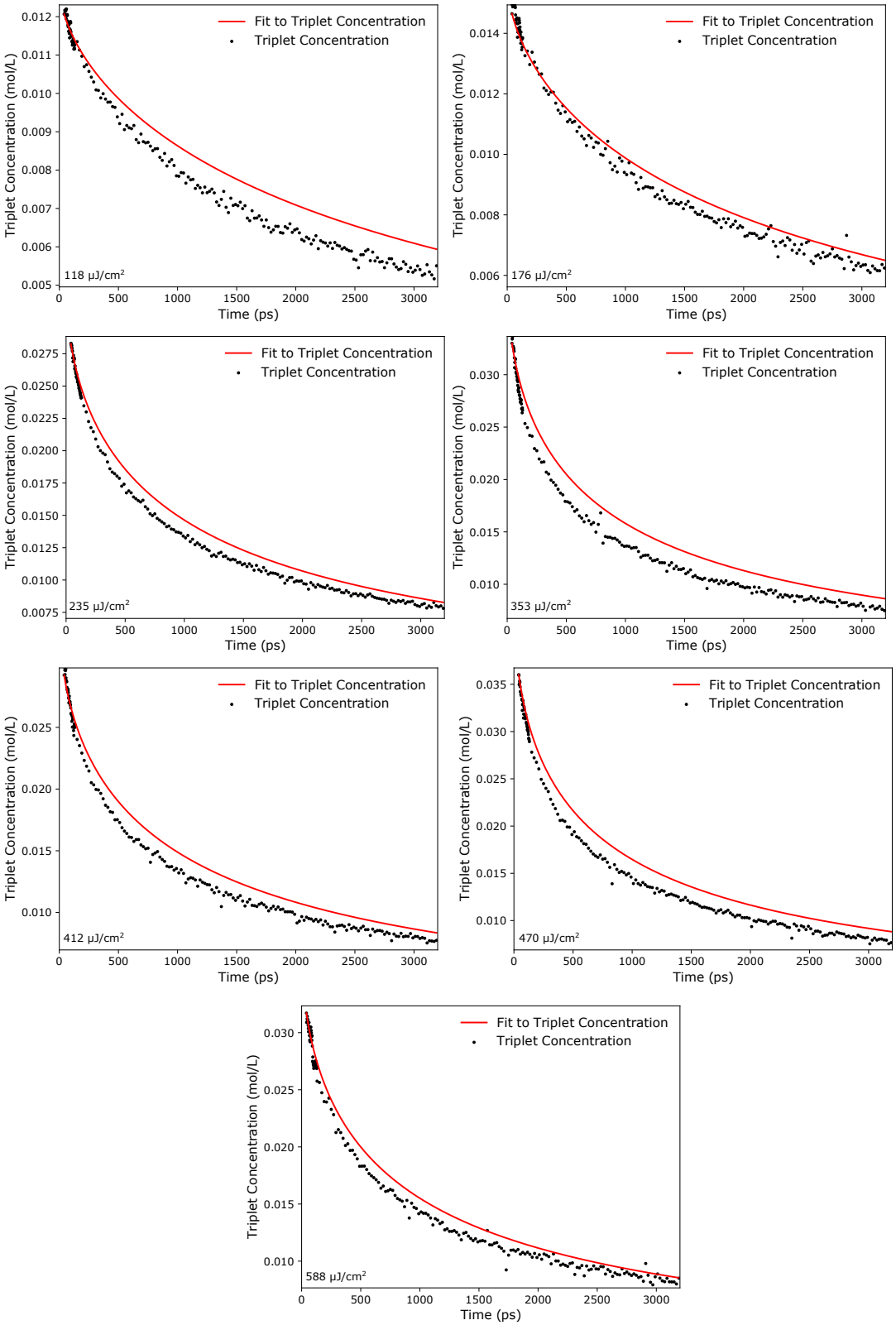

Figure 4.9: Fits of the isotropic 3D diffusion model to triplet concentrations without a first-order decay term. Best-fit parameters for this model are $R = 1.83 \pm 0.02\,\mathrm{nm}$ and $D = (5.8 \pm 0.2) \times 10^{-5}\,\mathrm{cm^2\,s^{-1}}$.

Here, r is the nanoparticle radius, η is the dynamic viscosity of the dispersant, $T = 298\,\mathrm{K}$ is the temperature and k_B is the Boltzmann constant. Knowing the dynamic viscosity of water to be 0.89 mPa s and using the Z-average radius of 36 nm established for these NPs as r (Figure 4.4), Equation 4.21 gives a diffusion coefficient of $3.4 \times 10^{-12}\,\mathrm{m^2\,s^{-1}}$ for these nanoparticles. Using these values of q and D in Equation 4.19 yields an inverse correlation time of $3.4 \times 10^4\,\mathrm{s^{-1}}$. This is 2–3 orders of magnitude slower than the first-order decay fit to the TA data in this work; indeed, it is slower than the expected natural triplet decay in crystalline TIPS-Pn.[110] Therefore, signal fluctuations due to dynamic light scattering from the NPs can be ruled out as a cause of the rapid first-order triplet decay observed in the TA experiments.

Triplet–Charge Annihilation

Another alternative first-order decay process that may occur within the TIPS-Pn NPs studied here is triplet–charge annihilation (TCA). We recently demonstrated that TIPS-Pn NPs in aqueous suspension acquire a slight negative surface charge upon re-precipitation,[1] as has been previously reported for aqueous nanoparticle suspensions of other organic chromophores.[143,243] These charges may undergo annihilation reactions with triplet excitons within the nanoparticles, resulting in a triplet decay process that is pseudo-first-order with respect to triplet concentration. TCA occurs over very short separations within other organic semiconductors.[233,234] Therefore, if it is assumed that these surface charges remain stationary, TCA can only occur at the NP surface. Assuming that every triplet–charge encounter results in triplet annihilation, the rate of triplet decay is given by the rate at which triplets diffuse to charged sites at the NP surface, where the fraction of charged surface molecules is given by N_C. To estimate this rate, we assume for simplicity that the NP is a perfect sphere with radius R, that exciton diffusion within the nanoparticle is isotropic with diffusion coefficient D, and that the initial exciton concentration distribution is uniform such that the concentration distribution of triplets $C(r,t)$ has only spatial dependence upon a radial coordinate r. The time dependence of $C(r,t)$ is given by the diffusion equation,

$$\frac{\mathrm{d}C}{\mathrm{d}t} = D\nabla^2 C = \nabla \cdot (D\nabla C), \tag{4.22}$$

with the reactive (Robin) boundary condition

$$-D\left(\frac{\mathrm{d}C}{\mathrm{d}r}\right)_{r=R} = \alpha C(R,t), \tag{4.23}$$

where α is the TCA rate at the NP surface. α can be related to the reaction probability P,[244] with $\alpha \approx DP/a$, where a is the exciton hopping distance, which we take to be the nearest-neighbor spacing in TIPS-Pn, i.e. $a = 7.565\,\text{Å}$. From the assumption that triplet–charge encounters always lead to annihilation, $P = N_\mathrm{C}$. Integrating Equation 4.22 over the entire nanoparticle volume V gives

$$\iiint \mathrm{d}V \frac{\mathrm{d}C}{\mathrm{d}t} = \iiint \mathrm{d}V \nabla \cdot (D\nabla C), \tag{4.24}$$

which by the divergence theorem results in

$$\frac{\mathrm{d}}{\mathrm{d}t}\iiint \mathrm{d}V C = \iint \mathrm{d}S \hat{\mathbf{n}} \cdot (D\nabla C), \tag{4.25}$$

with $\hat{\mathbf{n}}$ the vector normal to the NP surface $\mathrm{d}S$. Evaluation of the right-hand side of this equation at the surface ($r = R$) and identifying $\iiint \mathrm{d}VC/V$ with the spatial average of the triplet concentration within the nanoparticle, [T](t), then gives

$$V\frac{\mathrm{d[T]}}{\mathrm{d}t} = 4\pi R^2 D\left(\frac{\mathrm{d}C}{\mathrm{d}r}\right)_{r=R}. \tag{4.26}$$

Solving Equation 4.22 with boundary condition Equation 4.23, the concentration distribution $C(r,t)$ can be shown to be[245]

$$C(r,t) = \frac{2LRC_0}{r}\sum_{n=1}^{\infty}\frac{\exp(-D\beta_n^2 t/R^2)}{\{\beta_n^2 + L(L-1)\}}\frac{\sin(\beta_n r/R)}{\sin\beta_n} \tag{4.27}$$

where C_0 is the initial uniform concentration at $t = 0$, β_n are the roots of $\beta_n\cot\beta_n + L - 1 = 0$, and $L = \frac{\alpha R}{D} \approx \frac{RP}{a} \approx \frac{N_C R}{a}$. Evaluating the derivative of Equation 4.27 at $r = R$ gives

$$\left(\frac{\mathrm{d}C}{\mathrm{d}r}\right)_{r=R} = -\frac{2L^2C_0}{R}\sum_{n=1}^{\infty}\frac{\exp(-D\beta_n^2 t/R^2)}{\{\beta_n^2 + L(L-1)\}} \tag{4.28}$$

Substitution of Equation 4.28 into 4.26 with $V = 4\pi R^3/3$ and approximating [T] $\approx C_0$ (which is reasonable since the rate of change in [T] due to TCA that we estimate below is small compared with that due to TTA) gives

$$\frac{\mathrm{d[T]}}{\mathrm{d}t} = -\frac{6DL^2}{R^2}\sum_{n=1}^{\infty}\frac{\exp(-D\beta_n^2 t/R^2)}{\{\beta_n^2 + L(L-1)\}}\mathrm{[T]} \equiv -k_{\mathrm{TCA}}\mathrm{[T]}, \tag{4.29}$$

where k_{TCA} is the pseudo-first-order rate coefficient for triplet decay due to TCA given by

$$k_{\mathrm{TCA}} = \frac{6DL^2}{R^2}\sum_{n=1}^{\infty}\frac{\exp(-D\beta_n^2 t/R^2)}{\{\beta_n^2 + L(L-1)\}}. \tag{4.30}$$

N_C can be estimated from the charge density at the nanoparticle surface. We previously measured the zeta potential ζ of TIPS-Pn NPs in aqueous suspension as $-38\,\mathrm{mV}$.[1] Although not strictly valid for $|\zeta| > k_B T/e \approx 26\,\mathrm{mV}$, the Debye-Hückel model may be used to estimate the NP surface charge density σ by[246]

$$\sigma = \frac{\zeta\epsilon_r\epsilon_0(1 + R/\lambda_D)}{R}, \tag{4.31}$$

where ϵ_0 is the permittivity of vacuum, ϵ_r is the dielectric constant of the aqueous solution (80.2 for pure water was used here), k_B is the Bolzmann constant, $T = 298\,\mathrm{K}$ is the system temperature, e is the elementary charge and

$$\lambda_D = \left(\frac{\epsilon_0\epsilon_r k_B T}{e^2 c_{\mathrm{ion}}}\right)^{1/2} \tag{4.32}$$

is the Debye screening length for a total monovalent ion concentration c_{ion}. As the NPs studied here were suspended in MilliQ-grade water, the concentration of most ions was effectively negligible, and so c_{ion} corresponds to the intrinsic concentration of hydronium and hydroxide ions. Ultrapure water has pH 6.998, which therefore corresponds to $c_{\mathrm{ion}} = 2\times10^{-7}\,\mathrm{mol\,L^{-1}}$. Using this concentration, Equation 4.31 yields $\sigma = 7.8\times10^{-4}\,\mathrm{C\,m^{-2}}$. Assuming these charges to come from individual charges at

the NP surface, and estimating the thickness of this surface layer as 7.565 Å (nearest-neighbor separation in crystalline TIPS-Pn) gives a density of charges at the NP surface of $6.5 \times 10^{-3}\,\mathrm{nm}^{-3}$. Knowing the density of crystalline TIPS-Pn to be $1.04\,\mathrm{nm}^{-3}$, N_C can be simply determined by the ratio of these two densities, and is found to be 6.3×10^{-3}.
With $L \approx \frac{N_\mathrm{C} R}{a} = 0.30$, β_n can be obtained as described above, from which it can be shown that only the $n = 1$ term in Equation 4.30 contributes significantly to k_TCA. Using $\beta_1 \approx 0.92$, taking the nanoparticle radius R to be 36 nm (Figure 4.4) and using D_1D from the one-dimensional diffusion model as the diffusion coefficient D, an upper bound for k_TCA can be obtained by Equation 4.30 as $k_\mathrm{TCA} = (9.3 \times 10^7\,\mathrm{s}^{-1})\exp\left(-\frac{t}{4.3 \times 10^{-9}\,\mathrm{s}}\right)$, which is approximately constant and equal to $9.3 \times 10^7\,\mathrm{s}^{-1}$ over the time scale of our experiments. This value is of similar magnitude to the first-order triplet decay constant from the fits to the experimental data. On the other hand, using the diffusion coefficient from the isotropic 3D model as D in Equation 4.30, a lower estimate of $k_\mathrm{TCA} = (9.3 \times 10^4\,\mathrm{s}^{-1})\exp\left(-\frac{t}{4.3 \times 10^{-6}\,\mathrm{s}}\right) \approx 9.3 \times 10^4\,\mathrm{s}^{-1}$ is obtained, which is at least an order of magnitude slower than the first-order triplet decay coefficient from the experimental fits. The actual value of k_TCA is likely between these two extremes. Therefore, our calculations indicate that TCA could account for the fast first-order triplet decay fit to the experimental data. It is worth noting that while both estimates of k_TCA are time-dependent, the contribution of this time dependence to triplet decay will only be significant on time scales substantially longer than those studied here experimentally. This is because only a small fraction of triplets undergo first-order decay on the time scale of our experiments, and from the above estimates k_TCA only changes significantly on longer time scales. Therefore, the time dependence of TCA should not influence the fitting of bimolecular TTA kinetics.

Fit of the Isotropic Three-Dimensional Diffusion Model with Constrained Annihilation Radius

As the best-fit value of R for the isotropic 3D diffusion model used here was significantly larger than what has been previously considered physically reasonably for crystalline TIPS-Pn,[110] we considered the possibility that this large value was due to poor sensitivity of the fitting process to variations in R. To test for this, we attempted to fit the same model to the data with R constrained to several different values within the range of 0.6–2.3 nm, with both k_1 and D allowed to fit freely. A selection of the resulting fits are shown in Figure 4.10, with best-fit parameters for all constrained values of R listed in Table 4.3.

The parameter χ^2, the sum of the squared residuals between the model and the data, can be used to assess how well the model fits to the experimental data. As this is a sum of squares, an increase in χ^2 by a factor of four approximately corresponds to a doubling of the residuals between the model and the data. A relatively good fit to the experimental data is obtained upon decreasing R to 1.5 nm, with χ^2 increasing by less than a factor of 2. This may indicate that there is likely some level of variability the best-fit value of R in this model. However, 1.5 nm is still significantly larger than what would be expected for triplet–triplet annihilation in the closely slip-stacked packing of crystalline TIPS-Pn. Further decreasing R results in a significantly poorer fit of the model to the data, which is visible in Figure 4.10: the model underestimates the triplet decay at early times and over-estimates at later times. The second term of Equation

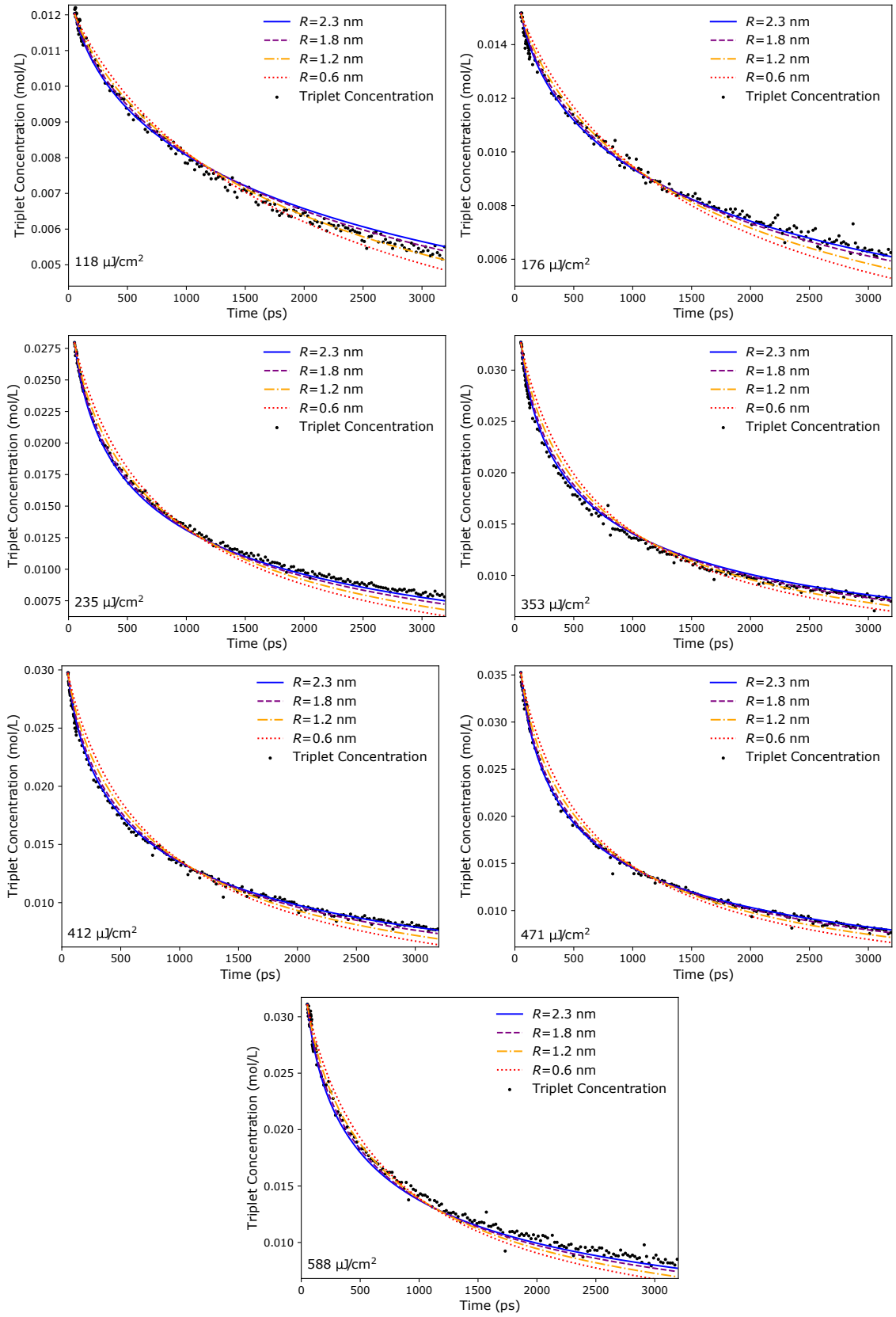

Figure 4.10: Fits of the isotropic 3D diffusion model to triplet concentrations with annihilation radius R constrained to different values.

Table 4.3: Best-fit parameters to the isotropic 3D diffusion model with constrained annihilation radii.

R (nm)	D (10^{-6} cm^2 s^{-1})	k_1 (s^{-1})	χ^2 (10^{-4} M^2)[a]
0.60	39	440	13.0
1.0	19	80	7.52
1.2	14	2100	5.74
1.5	8.7	6.0	3.34
1.8	6.5	120	2.46
2.1	4.2	1200	1.91
2.3	3.5	6×10^6	1.87

[a] χ^2 denotes the sum of squared residuals between the model and experimental triplet concentrations.

4.2, which describes the early-time behavior of k_2, has the form $R^2D^{1/2}$. As R is decreased, D must therefore increase quadratically to maintain the same early-time behavior. However, this then quadratically increases the first term of Equation 4.2 (which governs the late-time bimolecular decay), causing the model to fit more poorly at later times. The model attempts to minimize residuals from both of these regions simultaneously, hence resulting in the observed under- and over-estimations at early and later times, respectively.

However, reduction of R below 2.3 nm also results in unreasonably small values of the first-order rate constant k_1. As was shown in Figure 4.9, a first-order decay on the order of tens of nanoseconds is necessary to fully account for the triplet decay observed here. The best-fit values of k_1 for R constrained below 2.3 nm correspond to first-order decays on the order of 10^{-2}–10^{-4} s, which should not be observable in the 3-ns time window studied here, and are at least two orders of magnitude longer than the 2.1 µs triplet lifetime reported by Grieco and co-workers for crystalline TIPS-Pn.[110] Therefore, these extremely slow first-order rate constants must be an artefact of the model attempting to compensate for the increasing bimolecular rate coefficient at long times with decreased R, as identified above. Hence, while the isotropic 3D diffusion model appears to fit the experimental data well for $2.3 > R > 1.5$ nm, it gives unreasonably small best-fit values for the first-order rate coefficient k_1. Clearly then, variability in the best-fit value of R cannot explain the large annihilation radius fit by the isotropic 3D diffusion model to crystalline TIPS-Pn.

Calculation of the TIPS-Pn Average Molecular Density

The one-dimensional diffusion model uses a second-order annihilation constant given by

$$k_2 = \frac{1}{N_0 R_{1D}} \sqrt{\frac{8D_{1D}}{\pi t}}, \tag{4.33}$$

where N_0 is the average molecular density of the system.[236] N_0 can be determined simply from the molecular weight M_W and mass density ρ of TIPS-Pn:

$$N_0 = \frac{\rho}{M_W} \tag{4.34}$$

Using a molecular weight of 639.07 $\mathrm{g\,mol^{-1}}$ and density of 1.104 $\mathrm{g\,cm^{-3}}$, this yields an average molecular density of $N_0 = 1.73\ \mathrm{mol\,L^{-1}}$ for crystalline TIPS-Pn.

Prediction of Triplet Hopping Rates in Crystalline TIPS-Pn

As per the method reported by Yost and co-workers,[80] triplet hopping rates along different slip-stacking directions of crystalline TIPS-Pn were determined using the classical Marcus equation,

$$k_{\mathrm{da}} = \frac{2\pi}{\hbar}|V_{\mathrm{da}}|^2\sqrt{\frac{1}{4\pi k_{\mathrm{B}}T\lambda}}\exp\left[-\frac{(\Delta G^\circ + \lambda)^2}{4\lambda k_{\mathrm{B}}T}\right], \tag{4.35}$$

where V_{da} is the electronic coupling between donor and acceptor, T is the temperature, λ is the reorganization energy, ΔG° is the free energy change upon transfer and k_{B} is the Boltzmann constant.[237] ΔG° was set to zero here, as adjacent molecules in a TIPS-Pn crystal should be energetically equivalent.[125] The PBE/6-31G* theory level was used for all DFT and CDFT calculations here, as Yost et al. found that this showed the best agreement with experimental data for polyaromatic hydrocarbons similar to TIPS-Pn.[80]

The reorganization energy due to triplet hopping (λ) was calculated by the four-point method, assuming that all molecular reorganization outside of the donor and acceptor sites is negligible. The reorganization energy λ is therefore given by

$$\lambda = \lambda_{\mathrm{donor}} + \lambda_{\mathrm{acceptor}} = (E_{\mathrm{T,S}} - E_{\mathrm{T,T}}) + (E_{\mathrm{S,T}} - E_{\mathrm{S,S}}), \tag{4.36}$$

where $E_{i,j}$ denotes the energy of a monomer in electronic state i and geometry of electronic state j.[80] Geometry optimizations of the TIPS-Pn monomer (with the TIPS group replaced by methyl groups; see below) as singlet and triplet states were used to determine $E_{i,i}$, with $E_{i,i\neq j}$ then found by single-point calculations from these geometries. The energies of these calculations are shown in Table 4.4, and gave a reorganization energy of $\lambda = 0.19\,\mathrm{eV}$.

V_{da} was determined by CDFT-configuration interaction (CDFT-CI) calculations on pairs of TIPS-Pn molecules in the crystallographic stacking directions of interest. For each calculation, one molecule was constrained to an overall neutral singlet and the other a neutral triplet. Three molecular stacking directions were considered: nearest-neighbor stacking along the a-axis of the crystal, next-nearest-neighbor stacking (not directed along any single crystallographic axis, but closest to the b-axis), and packing along the c-axis. TIPS-Pn dimer structures were taken from the crystal structure of TIPS-Pn published by Anthony and co-workers,[125] and are shown in Figure 4.11. Tri(isopropylsilyl) (TIPS) groups were replaced by methyl groups in the a and b pair

Table 4.4: Energies of a TIPS-Pn monomer in singlet and triplet states used in determining the reorganization energy of TIPS-Pn.

State	Geometry	Energy Relative to $E_{\mathrm{S,S}}$ (eV)
Singlet	Singlet	0
Triplet	Singlet	0.71
Triplet	Triplet	0.61
Singlet	Triplet	0.09

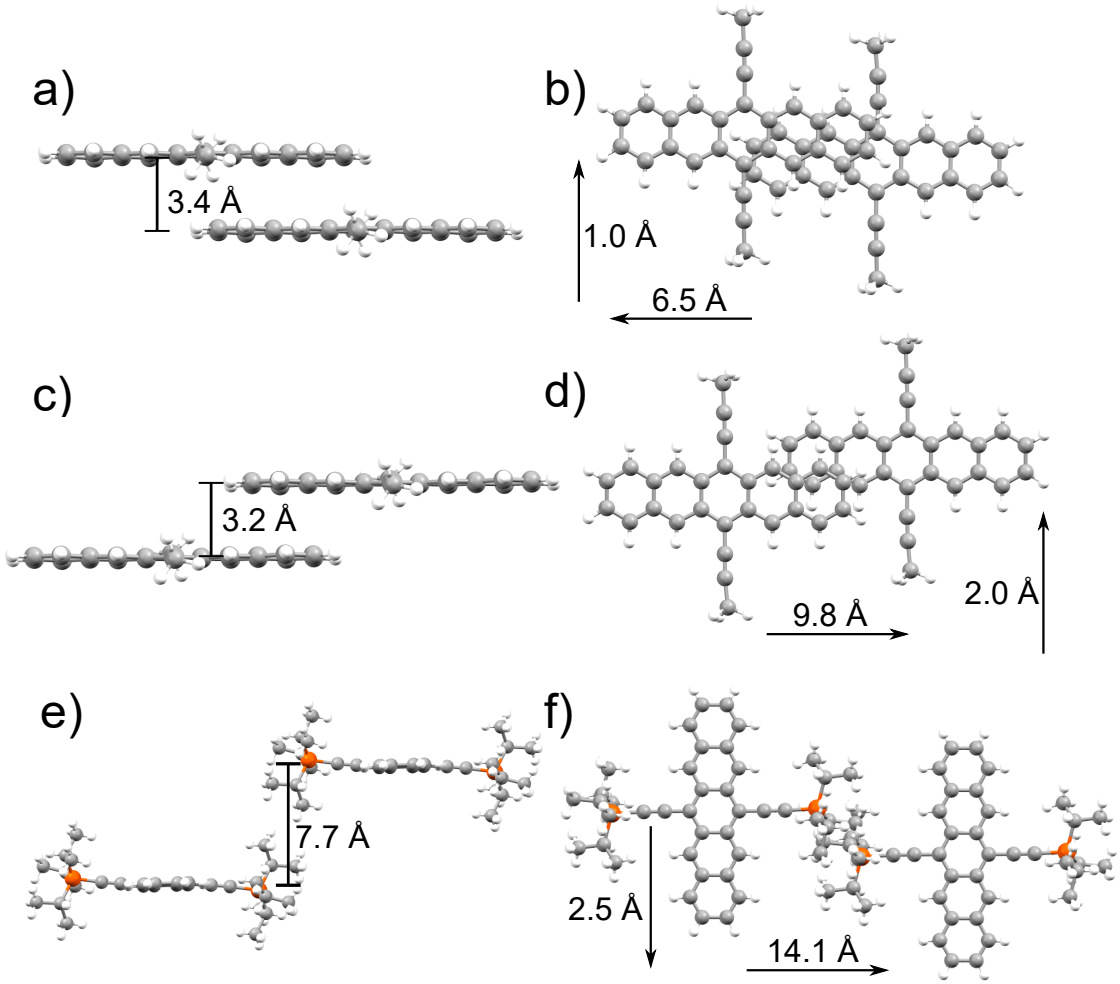

Figure 4.11: (a,b) Side-on and top-down views of the TIPS-Pn nearest-neighbor (crystallographic *a*-axis) slip-stacked pair. (c,d) Side-on and top-down views of the TIPS-Pn next-nearest-neighbor (pseudo *b*-axis) slip-stacked pair. (e,f) Side-on and top-down views of the TIPS-Pn crystallographic *c*-axis pair. Arrows denote horizontal displacements of the top molecule relative to the lower molecule. Carbon atoms are shown in grey, silicon atoms in orange and hydrogen atoms in white.

calculations to reduce computational expense, as the TIPS groups account for more than half of the atoms in TIPS-Pn but are highly insulating and should contribute negligibly to intermolecular electronic couplings. CDFT-CI calculations on the *c* pair structure could not be converged without including full TIPS groups upon both molecules. However, this inclusion of TIPS groups should not significantly bias the computed electronic coupling in this pair for the reasons outlined above. As will be shown below, this coupling is also several orders of magnitude lower than those of the other molecular pairs, and so any inconsistencies introduced by using TIPS groups in this calculation but not others are expected to be negligible.

Table 4.5 shows the resulting triplet electronic couplings between these crystallographic molecular pairs. The coupling is much stronger between the *a* pair than the *b* pair, differing by a factor of 7, while coupling between the *c* pair is at least three orders of magnitude lower. The *c* pair coupling was lower than the Q-Chem output threshold, so only an upper bound of this quantity can be estimated. These differences in cou-

Table 4.5: Triplet electronic couplings and hopping rate constants between different molecular pairs within the TIPS-Pn crystal structure.

Molecular Pair	V_{da} (meV)	k_{da} (ps^{-1})
a	7.92	3.70×10^{-1}
b	1.16	7.94×10^{-3}
c	$< 1 \times 10^{-3}$	$< 7 \times 10^{-9}$

plings can be rationalized when considering the relative geometries of these pairs. As shown in Figure 4.11, the a pair shows significantly more overlap between the pentacene cores than the b pair, while the c pair has no overlap between pentacene cores. The π–π overlap between the chromophores is therefore strongest along the a-axis, and so a larger electronic coupling between triplet states results on this geometry relative to the others. This difference in couplings between the a and b molecular pairs in crystalline TIPS-Pn is consistent with recent work on charge transfer in crystalline TIPS-Pn by Grieco et al., who found that the hole and electron transfer integrals across these dimer structures differed by factors of 6 and 8, respectively.[63]

Resulting triplet transfer rate constants between these two molecular pairs are also shown in Table 4.5. Due to the quadratic dependence of k_{da} on the coupling as per Equation 4.35, the difference in electronic couplings between chromophore pairs is magnified, such that triplet transfer between the a pair is predicted to be almost $50\times$ faster than between the b pair. Again, the contribution from the c-axis is effectively negligible, with a triplet transfer rate constant at least 8 orders of magnitude lower than that along the a-axis.

Triplet–Triplet Annihilation Kinetics Under Solar Irradiation

Under conditions of solar flux, the concentration of triplet excitons in a sample of crystalline TIPS-Pn would evolve over time according to the differential equation

$$\frac{\mathrm{d[T]}}{\mathrm{d}t} = G(t) - k_1[\mathrm{T}] - k_2[\mathrm{T}]^2, \tag{4.37}$$

where k_1 and k_2 are the first- and second-order decay rate coefficients as described above, and $G(t)$ is the generation rate of excitons from solar irradiation. To estimate $G(t)$, the product of the AM1.5 solar spectrum with the crystalline TIPS-Pn NPs' visible absorption spectrum (Figure 4.12) was integrated over the visible region, giving a rate of photon absorption by crystalline TIPS-Pn of $4.70 \times 10^3\,\mathrm{cm}^{-2}\mathrm{ps}^{-1}$. Using the suspension-to-nanoparticle concentration correction factor derived in Equation 4.15, and assuming that every photoexcitation yields two triplet excitons through singlet fission (as has recently been demonstrated for crystalline TIPS-Pn[119]), an exciton generation rate $G(t)$ of $1.16 \times 10^{-13}\,\mathrm{mol\,L}^{-1}\mathrm{ps}^{-1}$ results for the NPs used in this study. While the best-fit parameters of the isotropic 3D diffusion model have been established as not physically representative of crystalline TIPS-Pn, this model yields the best fit to the experimental data of all the models considered here. Therefore, we use this model to describe the decay of triplet excitons in TIPS-Pn on the longer timescales representative of solar irradiation. Using the values R, D and k_1 from this model with the estimate of $G(t)$ shown above, we solved Equation 4.37 numerically for the NP triplet population over the first microsecond of solar irradiation. As shown in Figure

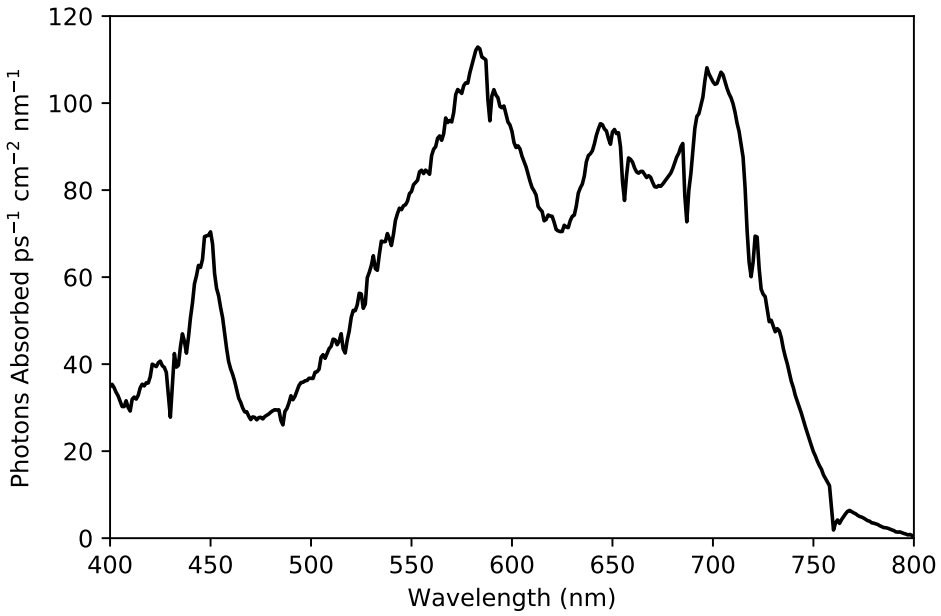

Figure 4.12: Product of the AM1.5 solar spectrum with the visible absorption spectrum of the crystalline TIPS-Pn NPs used in this study.

4.13, a steady-state concentration of less than 60 µmol L^{-1} is reached after approximately 800 ns. This is three orders of magnitude lower than the triplet concentrations achieved with the pump fluences used here, and as such the natural triplet decay would be expected to dominate over bimolecular annihilation. Therefore, under solar irradiation the lifetime of triplet excitons in crystalline TIPS-Pn should correspond to the intrinsic triplet lifetime, recently estimated as 2.1 µs.[110] Note that although these

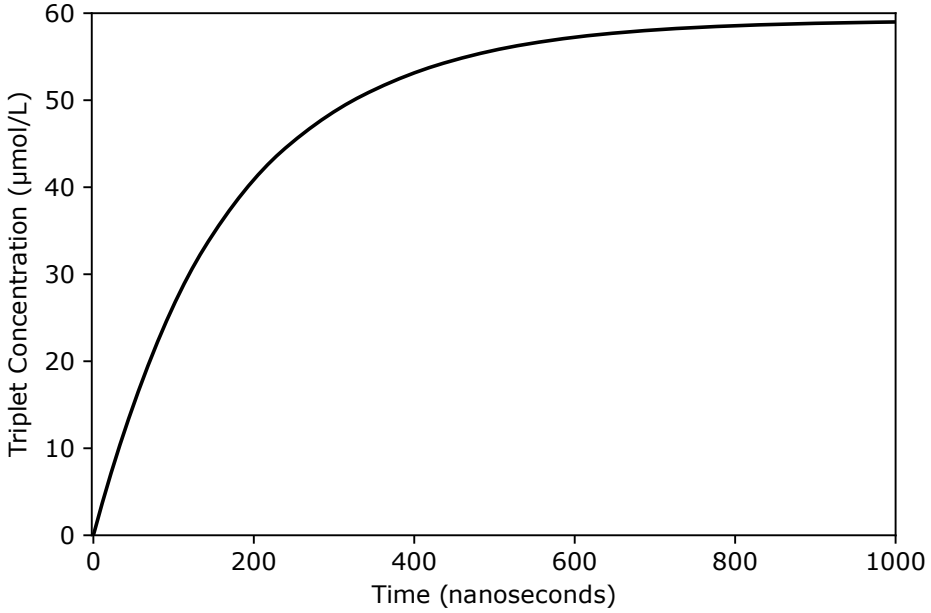

Figure 4.13: Simulated triplet exciton concentrations in crystalline TIPS-Pn NPs under solar irradiation (AM1.5 solar spectrum).

calculations indicate that bimolecular annihilation in crystalline TIPS-Pn is negligible under solar irradiation, the purpose of the current study is not to emulate solar irradiation conditions, but rather to use these bimolecular annihilation kinetics to study the diffusion of triplet excitons in crystalline TIPS-Pn.

TIPS-Pn Excited-State Energies

Figure 4.14 shows an approximate energy-level diagram of the excited states of crystalline TIPS-Pn, including both singlet and triplet manifolds. A number of studies — using both experimental and computational methodologies — have estimated the S_1 state energy in crystalline TIPS-Pn to lie between 1.7–1.8 eV relative to the ground state.[47,57,127,188] This agrees with the position of the lowest energy absorption of crystalline TIPS-Pn at 699 nm here, corresponding to an energy of approximately 1.77 eV. We therefore assign this state to an energy of 1.75 eV, acknowledging a possible error in this value of ±0.05 eV. Similarly, there is widespread agreement within the literature that the T_1 state energy of TIPS-Pn lies between 0.85–0.87 eV,[47,57,184,188] and so we list this energy as 0.86 eV. Comparatively less information is available on the energy of the T_2 state, however. Grieco et al. have estimated this energy as 2.04 eV, using the sum of the T_1 energy and that of the lowest-energy triplet ESA.[101] However, the value of the T_1 energy used in those estimations was in fact that of a pentacene dimer in solution, which does not agree with the T_1 energy observed by Bakulin et al. in solid-state crystalline TIPS-Pn.[47] Therefore, we re-estimated the energy of the T_2 state in crystalline TIPS-Pn as 2.11 eV, using the T_1 energy listed above and the $T_2 \leftarrow T_1$ transition energy of 1.25 eV listed by Pensack and co-workers.[119]

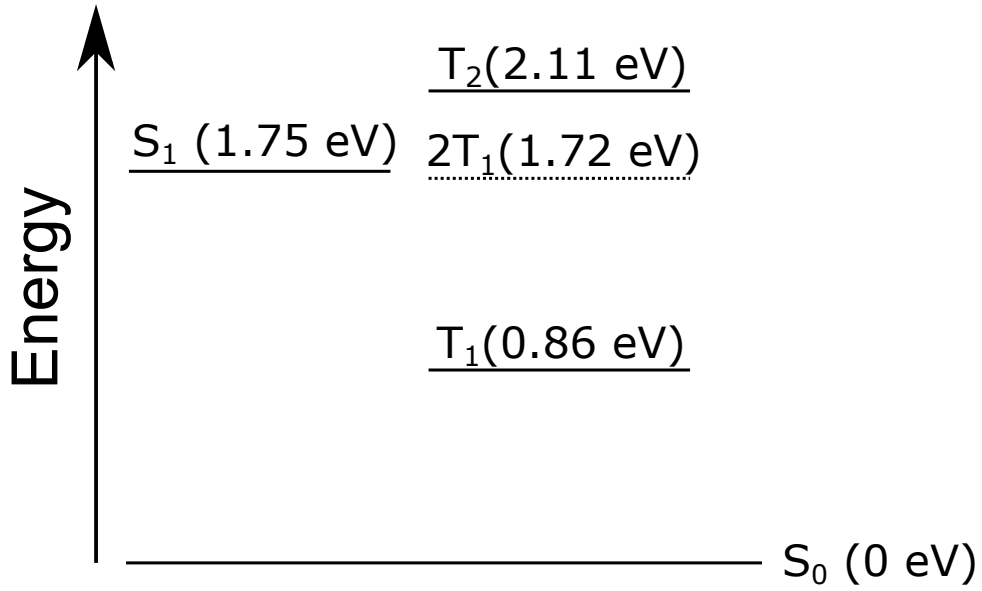

Figure 4.14: Energy level diagram of crystalline TIPS-Pn.

CHAPTER 5
Nanoparticle–Size–Dependent Singlet Fission and Exciton Dynamics in Amorphous TIPS-Pentacene

Statement of Authorship

Title of Paper	Nanoparticle Size–Dependent Singlet Fission and Exciton Dynamics in Amorphous TIPS-Pentacene
Publication Status	Published
Publication Details	Hudson, R. J.; Stuart, A. N.; de la Perrelle, J. M.; Huang, D. M.; Kee, T. W. Nanoparticle Size–Dependent Singlet Fission and Exciton Dynamics in Amorphous TIPS-Pentacene. *J. Phys. Chem. C* **2021**, *125*, 21559–21570. DOI: 10.1021/acs.jpcc.1c07048

Principal Author

Principal Author	R.J. Hudson		
Contribution to the Paper	Experimental work, data analysis and kinetic modelling, construction of figures, writing of manuscript.		
Overall Percentage	85%		
Certification	This paper reports on original research I conducted during the period of my Higher Degree by Research candidature and is not subject to any obligations or contractual agreements with a third party that would constrain its inclusion in this thesis. I am the primary author of this paper.		
Signature		Date	25/11/21

Co-Author Contributions

By signing the Statement of Authorship, each author certifies that the stated contributions to the following publication are accurate and that permission is granted for the publication to be included in this thesis.

Co-Author	A.N. Stuart		
Contribution to the Paper	1:90 TIPS-Pn:PMMA nanoparticle experiments, assistance with data analysis and editing of manuscript.		
Signature		Date	23/11/21

Co-Author	J.M. de la Perrelle		
Contribution to the Paper	Preliminary experiments contributing to the development of this work, assistance with editing of manuscript.		
Signature		Date	23/11/21

Co-Author	D.M. Huang		
Contribution to the Paper	Assistance with data analysis and writing and editing of manuscript.		
Signature		Date	22/11/21

Co-Author	T.W. Kee		
Contribution to the Paper	Supervision of project, assistance with data analysis and writing and editing of manuscript, corresponding author.		
Signature		Date	22/11/2021

5.1 Abstract

Aqueous nanoparticle (NP) dispersions are commonly used as model systems for spectroscopic study of singlet fission (SF) in acenes such as 6,13-(triisopropyl silylethynyl)pentacene (TIPS-Pn). However, the potential for particle size effects to complicate interpretation of results in such model systems is generally ignored. In this work, we study amorphous TIPS-Pn NP dispersions prepared by the re-precipitation method over a range of particle sizes. Time-resolved fluorescence and femtosecond transient absorption spectroscopy show that exciton dynamics in these systems depend significantly upon particle size. Kinetic analysis reveals that SF becomes slower at smaller NP sizes, while triplet exciton decay (through both correlated triplet pair relaxation and geminate triplet-triplet annihilation) accelerates. These significant size-dependent effects are ascribed to increased morphological disorder within smaller NPs, weakening the intermolecular couplings which control SF and triplet migration. A non-radiative singlet quenching channel separate from SF is also identified, which has not been previously reported for NPs of SF-capable chromophores. This non-radiative singlet decay becomes a significant relaxation pathway at small particle sizes, substantially reducing SF yields. Interestingly, exciton kinetics in the largest NPs considered here (81 nm diameter) approach those of bulk amorphous TIPS-Pn, suggesting that NPs of this size or larger are likely good models for bulk TIPS-Pn. This work demonstrates that particle-size effects are significant for small NPs of SF chromophores, and must be accounted for in order to accurately model bulk materials with such NP dispersions.

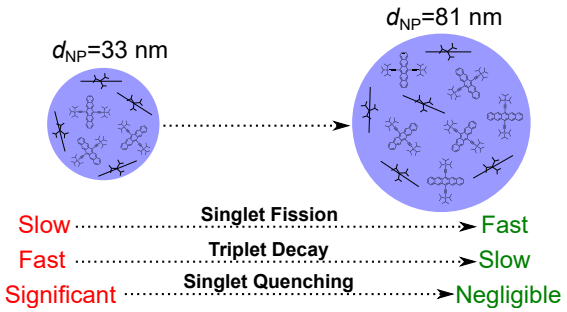

5.2 Introduction

Singlet exciton fission (SF) is an exciton multiplication process in which a chromophore in a singlet excited state (S_1) couples to a nearby ground-state chromophore to yield two lower-energy triplet excited state (T_1) chromophores.[19] This process is spin-allowed as it proceeds via a spin-0 correlated triplet pair intermediate ($^1(TT)$):[20,66]

$$S_1 + S_0 \rightarrow {}^1(TT) \rightarrow T_1 + T_1. \tag{5.1}$$

Interest in SF has risen dramatically in the last decade, as it has been recognized as a potential mechanism for improving photovoltaic (PV) device efficiencies beyond the theoretical efficiency limit for single-junction PV devices.[22,23,247] By forming two triplet excitons from every singlet exciton within the SF layer and subsequently harvesting these excitons, theoretical internal quantum efficiencies (IQEs) of 200% are possible for SF-sensitized PV devices. However, while SF-sensitized PV devices have been reported with IQEs surpassing 100%,[28,248] these devices remain much less efficient than conventional single-junction, inorganic PV architectures.[177,249] Significant effort is therefore being invested into improving understandings of how triplet excitons form and migrate in SF chromophores.

The known library of SF-capable compounds is highly diverse and has broadened substantially in recent years.[33,37] However, by far the most well-characterized class of SF chromophores are the acenes, especially pentacene and its derivatives, for which SF is exoergic and hence occurs quickly and irreversibly.[19,180] 6,13-(triisopropylsilyl ethynyl)pentacene (TIPS-Pn) in particular has attracted intensive study, as its bulky TIPS substituents improve solubility relative to unfunctionalized pentacene and facilitate an extended π-stacked motif in its predominant crystal polymorph.[125] Many different intermolecular packings for TIPS-Pn have since been reported: some studies have identified other crystal polymorphs,[109,120,127] while others have identified an amorphous phase.[72,75,110,119,134] TIPS-Pn is therefore widely considered a model system for intermolecular SF, as its wide variety of available morphologies allows for study of the relationship between intermolecular packing and exciton dynamics.

Aqueous dispersions of TIPS-Pn nanoparticles (NPs) are commonly used for spectroscopic characterization of SF and associated exciton dynamics.[1,2,72,133,134] Study of NP dispersions allows solid-state photophysical processes to be probed while using liquid-phase samples, which minimizes experimental issues associated with the study of thin films and other solid-phase media such as photo-bleaching or sample opacity. Such dispersions are generally prepared through the "re-precipitation" or "flash precipitation" method first reported by Matsuda and co-workers.[144] In this technique a solution of chromophore in a good solvent is rapidly mixed with a (miscible) poor solvent, inducing fast chromophore aggregation and hence NP nucleation. TIPS-Pn NPs prepared by the re-precipitation method have been shown to form with amorphous morphologies,[72,134] although more recent studies have since demonstrated methods of converting these to crystalline structures through use of chemical additives.[1,119] Particle sizes can be readily tuned by control of re-precipitation conditions such as chromophore concentration or solvent combination,[146,147] and TIPS-Pn NPs have been reported with diameters in the range of 30–160 nm.[133,141] However, despite this wide range of NP sizes used to study SF dynamics in TIPS-Pn, the potential influence of NP size upon exciton dynamics in this system has not yet been considered.

Size-dependent properties of NPs prepared by the re-precipitation method are known to occur for a variety of chromophore types. Conjugated polymer NPs have been demonstrated to exhibit strongly size-dependent absorption and emission profiles, attributed to molecules at the NP surface adopting a more disordered morphology than those in the particle interior.[143,250] More recently, SF in aqueously dispersed diketopyrrolopyrrole (DPP) NPs was shown to become substantially faster at smaller particle sizes.[41] This acceleration of SF was ascribed to polar water molecules at the NP surface stabilizing charge-transfer states, which are thought to act as intermediates in the SF process for DPP. Therefore, a precedent exists for surface effects and morphological changes as a function of particle size in NP dispersions of SF chromophores, which may influence SF and other exciton dynamics. However, the dependence of SF and related excitonic processes upon particle size within TIPS-Pn is currently unknown. As NP dispersions are often used to model SF and other exciton dynamics for TIPS-Pn thin films or other bulk media, it is hence crucial to understand and quantify any such particle-size effects which may occur in TIPS-Pn NPs.

In this work, we use transient absorption (TA) and time-resolved fluorescence spectroscopy to study amorphous TIPS-Pn NPs prepared by the re-precipitation method, with diameters ranging from 30 nm to 80 nm. Ultrafast exciton kinetics in these systems are found to vary significantly with NP diameter: smaller particle sizes yield

slower SF, faster ^{1}(TT) non-radiative decay and faster T_1 decay through geminate triplet–triplet annihilation (TTA). These results are consistent with the NPs adopting an increasingly disordered morphology at smaller NP sizes, highlighting that not all amorphous structures of TIPS-Pn can be considered equivalent. SF yields are also found to decrease substantially at smaller particle sizes, which we attribute to an additional non-radiative singlet decay channel. These results demonstrate that NP size must be explicitly considered when using TIPS-Pn NP dispersions to study exciton dynamics, as morphological constraints and additional decay pathways become significant at small particle sizes.

5.3 Experimental Methods

Materials

TIPS-Pn was used as received from Ossila. Water was purified by an 18.2-MΩ cm Millipak Milli-Q IQ-7000 Water Purification System fitted with a 0.22-µm filter. HPLC-grade tetrahydrofuran (THF; RCI Labscan) was freshly distilled before use.

Nanoparticle Preparation and Size Characterization

Aqueous suspensions of amorphous-phase TIPS-Pn NPs were prepared by re-precipitation from THF solution into water, as has been previously reported by our group and others.[1,2,72,119,133,134] Multiple parameters in the preparation procedure were carefully tuned to achieve the broad range of NP sizes studied in this work. However, the overall procedure remained similar for the preparation of each NP sample, and so here we describe this procedure in general terms, with Table 5.1 listing exact quantitative details of the procedure used for each NP size. A volume V_{THF} of TIPS-Pn dissolved in THF at concentration [TIPS-Pn] was rapidly injected into a volume of water $V_{\mathrm{H_2O}}$ upon vigorous stirring, using a syringe needle of diameter d_{S}. This procedure was repeated n times, with each fraction stirred for 5 minutes. The n fractions were then combined and concentrated under reduced pressure to a final TIPS-Pn concentration of 100 ppm. Each NP suspension was then filtered through a 0.2-µm syringe filter (Sartorius Minisart NML).

NP sizes were characterized by dynamic light scattering (DLS), using a Malvern Zetasizer Nano ZSP with a 633-nm laser source and a backscattering angle of 173 °. Resulting intensity-weighted size distributions of each NP suspension are shown in the Supporting Information. To differentiate between NP samples, we hereafter refer to each sample by its Z-average diameter (d_{NP}) measured by DLS, shown in the final column of Table 5.1.

Steady-State Spectrophotometric Characterization

Steady-state absorption spectra were collected in a 1-cm path length quartz cuvette (Starna Cells 21-Q-2), using a Cary Varian 1E UV-visible spectrophotometer. Steady-state fluorescence spectra were collected in a 1-cm path length quartz cuvette (Starna Cells 3-Q) on a Shimadzu RF-6000 fluorescence spectrofluorometer, using an excitation wavelength of 590 nm and excitation/emission slit bandwidths of 5 nm. All NP samples

Table 5.1: Preparation conditions for different-sized TIPS-Pn NPs by re-precipitation of THF solution into water, with NP Z-average diameters as measured by DLS.

[TIPS-Pn] (ppm)	V_{THF} (mL)	V_{H_2O} (mL)	d_S (mm)[a]	Fractions (n)	d_{NP} (nm)[b]
20	3	15	0.55	5	32.5 ± 0.1
50	3	15	0.55	2	45.1 ± 0.6
510	0.2	10	0.90	3	63.1 ± 0.3
1020	0.2	10	0.90	1	81.2 ± 0.4

[a] Exterior diameter of syringe needle.
[b] Uncertainties are twice the standard error in the mean calculated from triplicate measurements of each sample.

were diluted to a TIPS-Pn concentration of 2 ppm for fluorescence measurements, such that sample absorbance across the wavelength range studied was less than 0.1.

Time-Resolved Spectrophotometric Characterization

Time-resolved spectroscopic measurements were made using the output of a Ti:sapphire regenerative amplifier (Spectra Physics, Spitfire Pro XP 100F), generating laser pulses centered at 800 nm and 100 fs in duration at a 1 kHz repetition rate. An optical parametric amplifier (Light Conversion, TOPAS-C) was used to produce 590 nm light from the second harmonic of the signal. Time-resolved fluorescence measurements were performed using a fluorescence spectrometer (Ultrafast Systems, Halcyone) configured in upconversion (UC) mode with an estimated instrument response function of 450 fs. A small fraction of the 800-nm amplifier output was used to generate the UC gate, by focusing onto a 0.4-mm β-barium borate (BBO) crystal for sum-frequency generation. The 590-nm pump pulses were focused to a full width at half-maximum of 561 µm at the sample position, with a pulse energy of 0.1 µJ.

TA measurements were collected using a transient absorption spectrometer (Ultrafast Systems, Helios) with an instrument response function of 150 fs. 590-nm pump pulses had a spot size of 560 µm at the sample position, with pump fluences varying from 20 µJ cm^{-2} to 80 µJ cm^{-2}. White-light continuum probe pulses were generated by focusing the 800 nm amplifier output onto a 3.2-mm sapphire crystal, with a spectral coverage of 440–750 nm and spot size of 130 µm at the sample position. For both time-resolved fluorescence and absorption experiments, pump and gate/probe pulses were polarized at 54.7° (magic angle) relative to one another, in order to minimize polarization biases in the measurements. NP suspensions were constantly stirred while under irradiation, with negligible photo-degradation or morphological evolution observed throughout the course of these experiments.

5.4 Results and Discussion

5.4.1 Steady-State Spectrophotometric Characterization

Figure 5.1 shows the steady-state absorption spectra of all TIPS-Pn NP sizes studied here, with the absorption spectrum of TIPS-Pn in THF solution shown for reference. All NP samples exhibit spectral features closely resembling those of the solution spec-

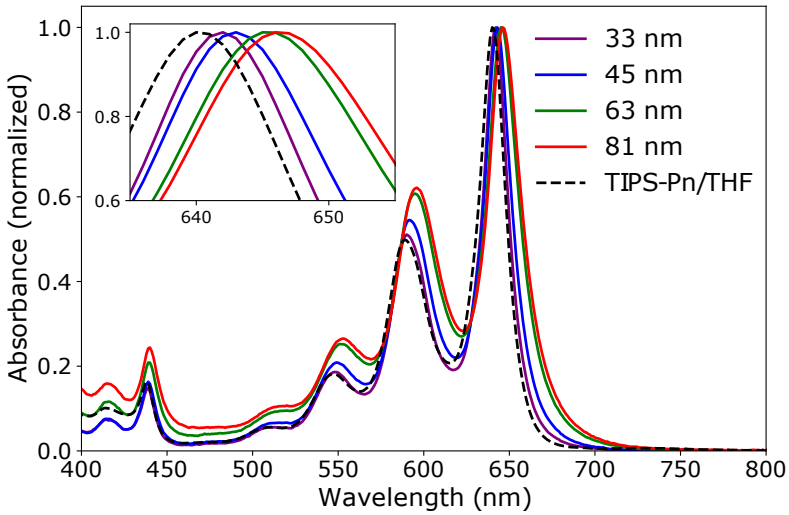

Figure 5.1: Steady-state absorption spectra of different-sized amorphous TIPS-Pn NPs, normalized to the $S_1 \leftarrow S_0$ 0–0 absorption peak around 645 nm. NP samples are labelled by diameter, and the steady-state absorption spectrum of TIPS-Pn in THF solution (dashed line) is shown for reference. Inset shows the shift in the position of the $S_1 \leftarrow S_0$ 0–0 absorption peak.

trum, displaying a clear series of vibronic transitions within the $S_1 \leftarrow S_0$ manifold from 500 nm to 650 nm and $S_3 \leftarrow S_0$ and $S_4 \leftarrow S_0$ electronic transitions at 440 nm and 420 nm, respectively.[204] The NP absorption spectra differ from the solution spectrum by only a slight red shift, indicating that only weak inter-chromophore coupling occurs in these NPs. We therefore assign these NPs as possessing amorphous morphologies, agreeing with multiple other studies of similar systems.[1,72,134] A raised baseline is apparent at shorter wavelengths for increasing NP size, consistent with increased Rayleigh scattering for these larger particles. However, a slight red shift is also observed for all absorption peaks upon increasing NP diameter (inset of Figure 5.1). This minor spectral shift suggests that the average chemical environment experienced by TIPS-Pn molecules within the NPs changes subtly with NP size.

Steady-state fluorescence spectra of these NPs upon excitation at 590 nm are shown in Figure 5.2a, with pronounced 0–0 and 0–1 vibronic peaks evident at 650 nm and 710 nm, respectively. In contrast to the relatively similar absorption spectra displayed above, significant differences in the fluorescence spectra are observed upon changing NP size. Smaller TIPS-Pn NPs are much more fluorescent than larger NPs, with fluorescence intensity varying by over an order of magnitude across the particle sizes considered here. The 81-nm NPs exhibit a slightly increased emission intensity relative to the 63-nm NPs, breaking the trend observed across smaller particle sizes. However, the absolute fluorescence intensity is very low for both of these NP sizes, and so this apparent change in intensity may be attributable to increased light scattering at larger particle sizes rather than any increase in NP emission intensity. Negligible changes in the overall spectral shape are observed upon varying NP size (Supporting Information). Therefore, decreased emission intensity at larger particle sizes due to self-absorption within the NPs can be discounted, as self-absorption would result in a change in the intensity ratio of the 0–0 and 0–1 vibronic emission peaks. Time-resolved fluorescence can offer insight into the cause of this effective fluorescence quenching at larger NP sizes.

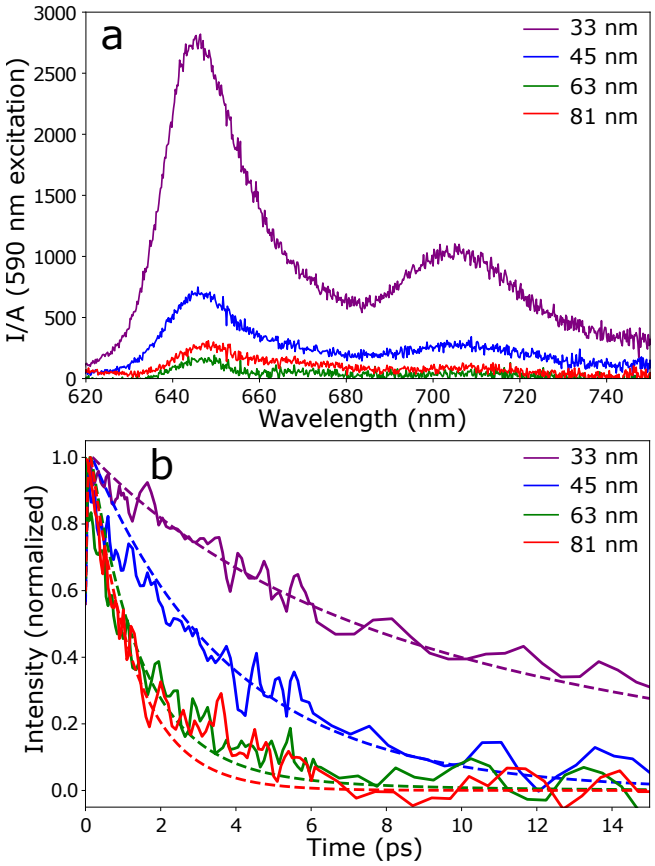

Figure 5.2: (a) Steady-state fluorescence spectra of amorphous TIPS-Pn nanoparticles upon excitation at 590 nm, normalized to sample absorbance at this wavelength. (b) Time-resolved fluorescence of TIPS-Pn NPs recorded at 700 nm, upon excitation at 590 nm. Dashed lines show fits of the S_1 population to the kinetic model described in Figure 5.6. NP samples are labelled by diameter. Time-resolved fluorescence traces have been smoothed by a Savitzky-Golay filter, using a 3rd-order polynomial and a 5-datapoint moving window.

5.4.2 Time-Resolved Spectrophotometric Characterization

Time-resolved fluorescence UC, detecting at 700 nm, was used to study the decay of the 0–1 emission band on the picosecond timescale. As is evident in Figure 5.2b, smaller TIPS-Pn NPs display much longer lived fluorescence at 700 nm than larger particles, thus accounting for the disparity in steady-state emission intensities. Fluorescence of larger NPs decays to baseline levels within 10 ps of excitation, whereas for smaller NPs some fluorescence intensity persists out to 50 ps (Supporting Information). Radiative decay of singlet excitons in TIPS-Pn is known to occur on the order of tens of nanoseconds,[72] which is several orders of magnitude too slow to account for the very rapid decays observed here. Therefore, non-radiative decay of singlet excitons must be responsible for this variation in emission lifetime.

However, fluorescence detects only emissive singlet excitons here, and gives no information regarding the nature of the species formed by singlet decay. Therefore, to determine the cause of the observed rapid singlet exciton decay, a method capable of detecting non-emissive excitonic species must be used. To this end, we characterized our NP samples using TA spectroscopy, exciting at 590 nm and detecting over the range 440–750 nm. Figure 5.3a shows representative TA spectra from each NP size at a probe delay time of 1 ps. Negative signals in the range of 600–650 nm mirror the steady-state

absorption peaks shown in Figure 5.1, and are hence assigned as ground-state bleach (GSB) signals. The GSB at 650 nm overlaps with a stimulated emission (SE) signal at 650 nm, with another SE feature evident at 710 nm. These SE signals persist for longer times upon decreasing NP size, consistent with the above observation that singlet exci-

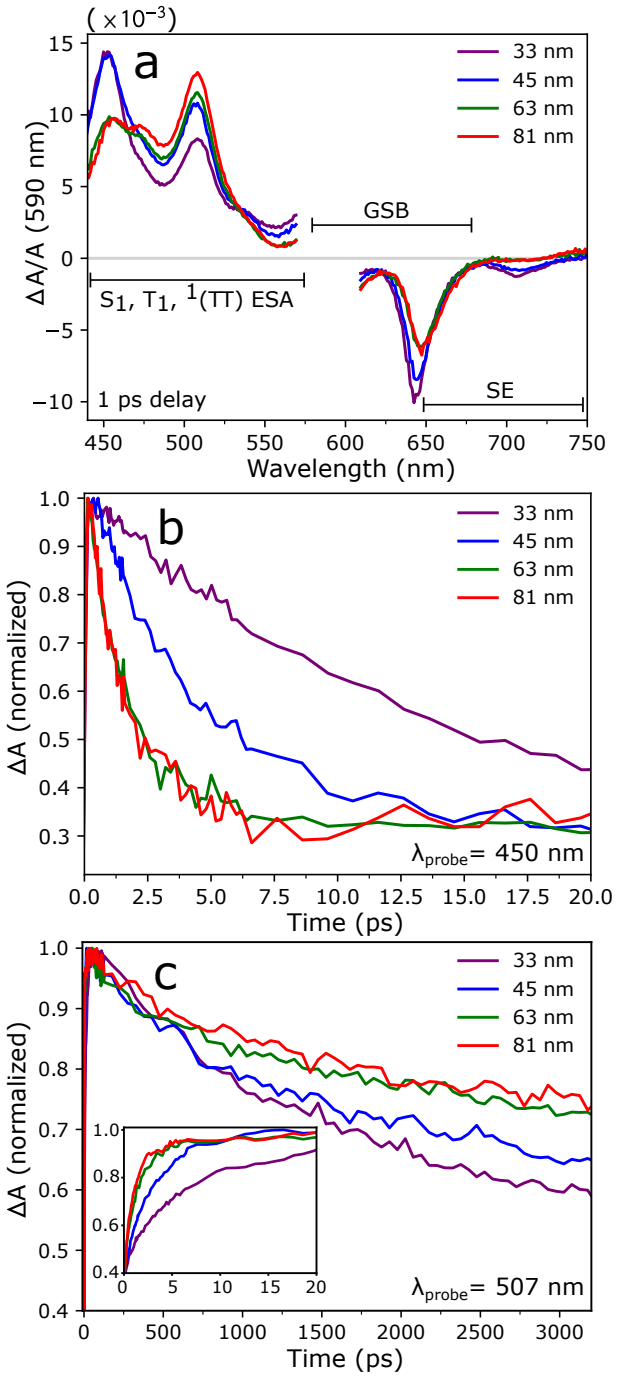

Figure 5.3: (a) Transient absorption spectra at 1 ps delay of amorphous TIPS-Pn NPs. Excited-state absorption (ESA), ground-state bleach (GSB) and stimulated emission (SE) features are labelled for clarity. (b) Early-time normalized kinetic traces of the 450-nm ESA, known to arise from singlet excitons in TIPS-Pn. (c) Normalized kinetic traces of the 507-nm ESA, attributed to triplet and triplet-pair excitons. Inset in (c) shows the 507-nm ESA kinetics over the first 20 ps after excitation. NP samples are labelled by diameter.

tons survive longer in smaller NPs. An excited-state absorption (ESA) signal at 450 nm appears at early times for all NP samples, which decays with kinetics very similar to the time-resolved fluorescence for these NPs (Figure 5.3b). This peak therefore appears to arise from a singlet excited state in amorphous TIPS-Pn, which is consistent with assignments of this peak to an $S_n \leftarrow S_1$ transition in other studies.[72,119,134] Concurrent with the decay of the 450-nm peak is the rise of an additional ESA at 507 nm, which grows on the order of 5–20 ps and decays over the 3.2-ns experimental time window (Figure 5.3c). This signal is well known to correspond to a $T_n \leftarrow T_1$ transition in disordered TIPS-Pn,[129,142] and hence indicates the formation of triplet excitons in these NPs. Intersystem crossing (ISC) occurs in TIPS-Pn on a timescale of 10^4–10^6 ps,[136] which is several orders of magnitude slower than the picosecond-scale rise of the triplet ESA signal observed here. Such rapid formation of triplet excitons therefore confirms that SF is responsible for some of the fast non-radiative decay of singlet excitons in these NPs. This assignment agrees with several previous studies which have reported SF occurring on timescales of 1–5 ps in amorphous TIPS-Pn.[1,72,110,119,134,142]

Upon decreasing NP diameter, the slower decay of singlet excitons noted above (Figures 5.2b and 5.3b) is coincident with a slower formation of the triplet ESA at 507 nm (inset of Figure 5.3c). This trend indicates that the overall rate of SF in these amorphous TIPS-Pn NPs depends upon NP size, with slower SF in smaller NPs. The decay of the triplet ESA signal also appears to vary significantly with NP size, as shown in Figure 5.3c. Within the observable 3.2-ns window, this ESA decays by only 22% for the 81-nm NPs but almost 40% for the smaller 33-nm sample. Clearly, NP size has a profound impact upon a number of excitonic processes within amorphous TIPS-Pn. However, it is difficult to precisely quantify these changes from the raw TA data shown here, as there is significant spectral overlap between the different exciton species in the visible region. The ESA at 450 nm also contains a contribution from the triplet state, as evidenced by this signal not decaying to zero but plateauing at 30% of its initial intensity (Figure 5.3b). Additionally, several previous studies of amorphous TIPS-Pn have reported the correlated triplet-pair intermediate ^{1}(TT) to have a spectral signature distinct to that of free triplets in TIPS-Pn, with broad absorption features in the range of 400–600 nm and 700–800 nm.[59,72,73,119] Such absorption would overlap with the identified ESA signals of both singlet and triplet excitons, as well as the 0–1 SE signal from the singlet state. As identified above, the 0–0 SE signal overlaps with the GSB at 650 nm, and the 0–1 GSB signal at 590 nm may be biased due to scattering of the 590-nm pump pulse and therefore unsuitable for analysis. As such, all TA spectral features identified here have contributions from either multiple exciton species or signals, and so use of single-wavelength kinetic traces to quantify the dynamics of SF and other processes in these NPs would be misleading. In order to more accurately quantify the impact of particle size upon the exciton dynamics in these NPs, the TA spectra presented above were decomposed into single-component contributions through the identification of exciton basis spectra.

5.4.3 Spectral Deconvolution of Transient Absorption Data

TA spectra are commonly deconvoluted using global and target analysis (GTA),[73,119,134] in which species-associated basis spectra may be extracted from a specified kinetic scheme. While GTA is a powerful analysis technique, the species-associated spectra generated through this method depend intrinsically upon the input kinetic model.[251]

As the cause of the particle-size dependence upon singlet and triplet kinetics here is unclear, we deemed it necessary to deconvolute the TA spectra using a different method, in which minimal assumptions are made regarding exciton kinetics. Instead of GTA, we used a method that we recently reported in a study of TIPS-Pn:poly(methyl methacrylate) (PMMA) composite NPs.[72] This method assumes only a basic kinetic evolution of the system as per Equation 5.1: S_1 excitons are present at early times, T_1 excitons are present at late times, and ^{1}(TT) excitons exist at some intermediate time. The S_1 basis spectrum was extracted from TA spectra of a 1:90 TIPS-Pn:PMMA NP sample, for which singlet excitons dominate the spectra at early times, as the TIPS-Pn molecules are sufficiently dilute that SF is slow. The T_1 spectrum was determined from the 63-nm NP TA spectra at a long delay time of 3 ns, at which all S_1 excitons have undergone complete decay. Resulting basis spectra for the various exciton species present are shown in Figure 5.4a, and further details on the determination of each basis spectrum are given in the Supporting Information.

Many previous TA studies of pentacene derivatives have demonstrated that the intermediate ^{1}(TT) state has a spectral signature in the visible region distinct from free triplets, which must be accounted for in order to accurately describe the shape of TA spectra on the picosecond timescale.[58,59,72,75,119] We also calculated a ^{1}(TT) basis spectrum to be used in the spectral deconvolution here. Determination of this basis spectrum is more complex than for the S_1 and T_1 basis spectra, as ^{1}(TT) is an intermediate species and therefore always coexists with either singlet or triplet excitons in our NP samples. Triplet pair states in pentacene derivatives have been

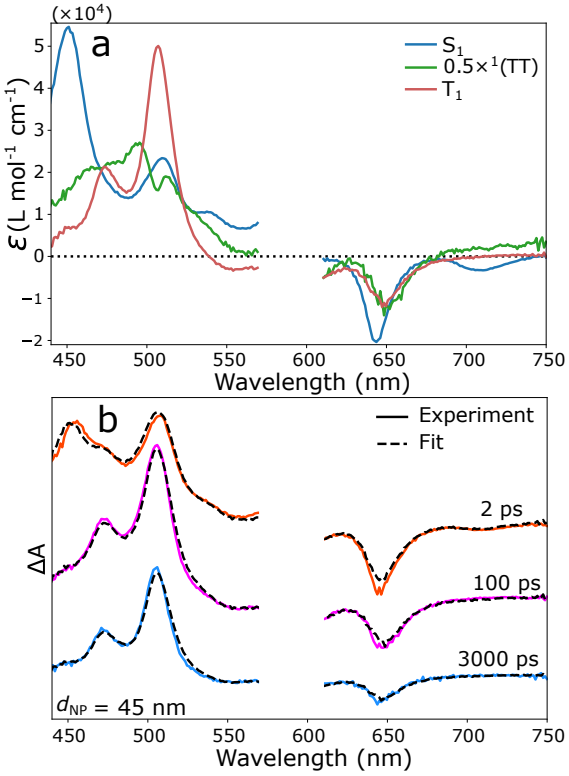

Figure 5.4: (a) Basis spectra of S_1, T_1 and ^{1}(TT) excitons in amorphous TIPS-Pn used to deconvolute the TA spectra here. (b) Fits to the TA spectra of the 45-nm diameter TIPS-Pn NPs using these basis spectra, at three representative delay times. The ^{1}(TT) basis spectrum shown in (a) uses $p = 0.1$, which was used in the deconvolution shown in (b).

shown to form on timescales of 0.1–10 ps, and persist for up to nanoseconds in some circumstances.[58,72,119] Therefore, the ^{1}(TT) basis spectrum was determined here from the 63-nm NP TA spectra at a delay time of 10 ps, at which all S_1 excitons have decayed (Figure 5.2b) but both ^{1}(TT) and T_1 excitons are present. This extraction requires the assumption of a proportion of T_1 decay over the experimental time window, which is denoted p. The 507 nm ESA for the 63 nm NP sample decays by 25% over the 3.2-ns window observed here, giving an upper bound of $p \approx 0.25$. Spectral deconvolution shown in Figure 5.4 uses an intermediate value of $p = 0.1$, but fits at $p = 0$ and $p = 0.25$ were used as upper and lower bounds for subsequent quantification of SF yields and kinetic modelling.

TA data for each NP sample were deconvoluted by a linear combination fit of the three basis spectra $\epsilon_i(\lambda)$ to the data $\Delta A(\lambda, t)$ according to the Beer-Lambert law,

$$\Delta A(\lambda, t) = l \left([S_1](t)\epsilon_{S_1}(\lambda) + [^1(TT)](t)\epsilon_{^1(TT)}(\lambda) + [T_1](t)\epsilon_{T_1}(\lambda) \right), \tag{5.2}$$

where l is the path length and square brackets denote concentrations. Figure 5.4b shows representative spectral fits for the 45-nm NP sample, with fits for all other NP sizes shown in the Supporting Information. This three-component fit results in excellent reconstruction of the TA data across the entire time window and range of NP sizes, capturing all of the GSB, SE and ESA signals identified above. Exciton concentrations extracted from this deconvolution for 33-nm and 81-nm NPs are shown in Figure 5.5, with concentrations for all NP samples shown in the Supporting Information. The trends identified from the TA data are reproduced in these extracted concentrations: larger NP sizes show faster SF and slower free triplet decay. Additionally, decay of ^{1}(TT) excitons appears to occur more rapidly in smaller NPs; as shown in Figure 5.5, the triplet pair population decays almost to zero after 500 ps for the 33-nm NPs, but a significant population of ^{1}(TT) still exists at this time for the larger 81-nm NPs. Clearly, NP size has a considerable influence upon the dynamics of S_1, T_1 and ^{1}(TT) excitons in amorphous TIPS-Pn.

In addition to the exciton kinetics identified above, another feature of considerable interest is the yield of the SF process. A SF yield close to 2 (often termed "quantitative SF") is frequently identified as one of the most necessary aspects for SF-capable PV devices to circumvent the detailed-balance limit.[19,23] However, the precise definition of the SF yield is not consistent in the literature. Some studies consider only the yield of the initial $S_1 + S_0 \rightarrow {}^1$(TT) step,[133,134] while others define the SF yield as the total yield of free triplet excitons.[19] We consider both definitions here, defining the overall SF quantum yield ϕ_{SF} as

$$\phi_{SF} = \frac{\max([T_1])}{\max([S_1])}, \tag{5.3}$$

while the yield including the first SF step ϕ'_{SF} is given by

$$\phi'_{SF} = \frac{\max([T_1] + 2 \times [^1(TT)])}{\max([S_1])}. \tag{5.4}$$

Table 5.2 shows ϕ_{SF} and ϕ'_{SF} for all NP sizes considered here, determined from exciton concentrations extracted from spectral deconvolution. ϕ'_{SF} is consistently larger than ϕ_{SF} for all NP sizes, indicating that not all ^{1}(TT) states formed during SF separate into free triplets. Other studies of various pentacene derivatives have demonstrated that triplet-pair states formed from SF can undergo non-radiative decay to the ground

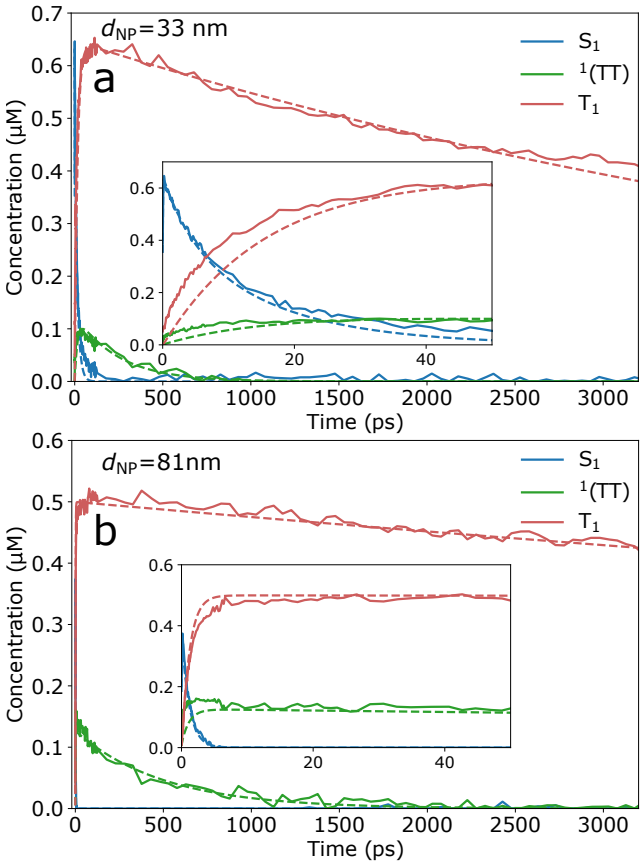

Figure 5.5: Extracted exciton concentrations from spectral deconvolution (solid lines) and kinetic fits to the model described in Figure 5.6 (dashed lines) for (a) 33-nm and (b) 81-nm TIPS-Pn NPs. Insets show the same data on a shorter timescale of 100 ps after excitation. Spectral deconvolution shown here used a ^{1}(TT) basis spectrum taken using $p = 0.1$.

state.[58,72,75] A slow decay of the ^{1}(TT) population over hundreds of picoseconds is observed here for all NP sizes, as shown in Figure 5.5 and the Supporting Information. Therefore, it is likely that such non-radiative ^{1}(TT) decay also occurs here, reducing the total yield of T_1 excitons from SF. This ^{1}(TT) decay cannot be explained by recombination of triplet pairs into singlet excitons, as the singlet population fit by spectral deconvolution remains at zero during the slow decay of correlated triplet pairs. The ^{1}(TT) basis spectrum identified here closely resembles a species-associated-spectrum previously assigned to short-lived triplet pair excitons in amorphous pentacene derivatives.[75] This prior study also recorded non-radiative decay of the triplet pair state on a timescale of ∼100 ps, and attributed this to an efficient internal conversion process. The non-radiative decay of ^{1}(TT) excitons identified here may therefore occur through a similar mechanism, with vibrational or nuclear motions facilitating relaxation to the ground state.

Interestingly, a clear trend can be discerned for both ϕ'_{SF} and ϕ_{SF}, with both yields increasing as a function of NP size. ϕ'_{SF} is approximately 2 for the 81-nm NPs, indicating that the first step of SF is quantitative for these larger particles. This result agrees with previous work that estimated unity yield from the $S_1 + S_0 \rightarrow {}^1$(TT) step in 70-nm diameter amorphous TIPS-Pn NPs.[119] Lower ϕ'_{SF} are observed at smaller particle sizes, however, indicating that some singlet excitons decay without forming triplet pairs. Rapid decay of triplet and triplet pair excitons cannot account for such

Table 5.2: Overall SF quantum yields (ϕ_{SF}) and yields of the first SF step (ϕ'_{SF}) determined from spectral deconvolution of TA data. [a]

d_{NP} (nm)	ϕ_{SF}	ϕ'_{SF}
33	1.03±0.05	1.26±0.03
45	1.2±0.1	1.65±0.01
63	1.3±0.1	1.85±0.01
81	1.5±0.1	2.05±0.01 [b]

[a] Values are averages for fits at $p = 0$ and $p = 0.25$. Uncertainties represent the range of fit values between $p = 0$ and $p = 0.25$.

[b] SF is sufficiently fast in this sample that the singlet population decays appreciably within the TA instrument response function of 150 fs. This results in an underestimate of max([S_1]) from spectral deconvolution and hence yields ϕ'_{SF} slightly greater than 2.

significant reductions in yield; estimation of the ^{1}(TT) decay rate indicates that fast non-radiative triplet pair decay could reduce ϕ'_{SF} to a minimum value of 1.64 for the 33-nm NPs (Supporting Information), which is significantly higher than the measured value of 1.26. Therefore, these results suggest that an additional singlet decay pathway may exist in parallel to SF, which becomes significant at smaller NP sizes. This pathway would result in an additional reduction of the singlet population without forming T_1 or ^{1}(TT) excitons, hence decreasing both ϕ'_{SF} and ϕ_{SF} (*vide infra*).

5.4.4 Kinetic Analysis of Transient Absorption Data

5.4.4.1 Kinetic Model

In order to explain the complex dependence of exciton dynamics upon NP size observed here, we used a kinetic model to fit the extracted exciton concentrations, described schematically in Figure 5.6. This model consists of two populations of singlet excitons, two populations of triplet pair excitons, and one population of triplet excitons. One population of singlet excitons ($S_{1,SF}$) undergoes SF through two competing pathways, forming triplet pair populations $^1(TT)_A$ and $^1(TT)_B$. This split population of triplet pairs is necessary to describe the non-radiative ^{1}(TT) decay identified above, as a single ^{1}(TT) population cannot accommodate both fast separation into T_1 excitons and long-lived ^{1}(TT) excitons over hundreds of picoseconds. Therefore, the model used here splits the population of triplet pairs into $^1(TT)_A$, which do not separate but decay non-radiatively with rate coefficient k_{pair}; and $^1(TT)_B$, which separate into free triplet excitons with rate constant k_{sep}. These triplet pair populations are formed from $S_{1,SF}$ with rate coefficients $k_{SF,A}$ and $k_{SF,B}$, respectively. T_1 excitons decay to the ground state with coefficient k_T. All of these aspects are consistent with the model used in our previous study of TIPS-Pn:PMMA composite NPs.[72] However, to account for the low ϕ'_{SF} and ϕ_{SF} at small NP sizes shown in Table 5.2 we have also included an additional singlet population, termed $S_{1,NR}$. As mentioned above, this singlet population undergoes non-radiative decay directly to the ground state, with rate coefficient k_{NR} in the model. The fraction of singlet excitons in this $S_{1,NR}$ population is given by the parameter f_{NR}, which was fit for each NP size. As discussed below, including this additional singlet population is necessary to obtain a good fit the data.

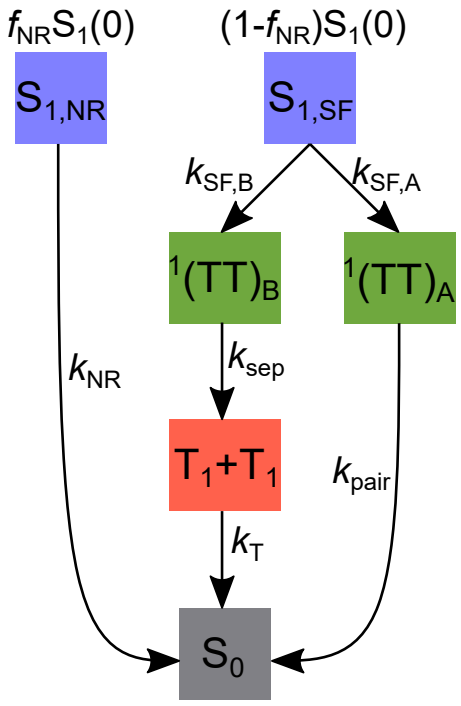

Figure 5.6: Schematic diagram of the kinetic model used to fit the TA data.

Radiative decay of the singlet state is ignored in this model; as mentioned above this process is known to occur on a timescale on the order of 10 ns and should therefore be negligible on the timescale considered here.[72] We have also disregarded diffusive transport between singlet populations, as estimated singlet diffusion lengths indicate that minimal diffusion occurs before the S_1 state is fully depopulated (Supporting Information). It should be noted that excitonic processes in the NPs studied here likely occur with a distribution of rate coefficients, due to the distribution of intermolecular packing geometries within their disordered morphologies. The rate coefficients used in this kinetic model therefore represent the averages of each of these distributions. The resulting kinetic model can be described by a series of coupled differential equations:

$$\begin{aligned}
\frac{\mathrm{d}[\mathrm{S}_{1,\mathrm{SF}}]}{\mathrm{d}t} &= -(k_{\mathrm{SF,A}} + k_{\mathrm{SF,B}})[\mathrm{S}_{1,\mathrm{SF}}];\\
\frac{\mathrm{d}[\mathrm{S}_{1,\mathrm{NR}}]}{\mathrm{d}t} &= -k_{\mathrm{NR}}[\mathrm{S}_{1,\mathrm{NR}}];\\
\frac{\mathrm{d}[^1(\mathrm{TT})_\mathrm{A}]}{\mathrm{d}t} &= k_{\mathrm{SF,A}}[\mathrm{S}_{1,\mathrm{SF}}] - k_{\mathrm{pair}}[^1(\mathrm{TT})_\mathrm{A}];\\
\frac{\mathrm{d}[^1(\mathrm{TT})_\mathrm{B}]}{\mathrm{d}t} &= k_{\mathrm{SF,B}}[\mathrm{S}_{1,\mathrm{SF}}] - k_{\mathrm{sep}}[^1(\mathrm{TT})_\mathrm{B}];\\
\frac{\mathrm{d}[\mathrm{T}_1]}{\mathrm{d}t} &= 2k_{\mathrm{sep}}[^1(\mathrm{TT})_\mathrm{B}] - k_\mathrm{T}[\mathrm{T}_1].
\end{aligned} \tag{5.5}$$

The system described by Equation 5.5 and Figure 5.6 was solved numerically and fit to the extracted exciton concentrations by an iterative least-squares method. $k_{\mathrm{SF,A}}$, $k_{\mathrm{SF,B}}$, f_{NR}, k_{pair} and k_T were allowed to vary with NP size. In fitting the data to the kinetic model, k_{sep} and k_{NR} were found to be effectively independent of NP diameter, and so were fit to constant values across all NP sizes. This invariance of k_{sep} with NP size is discussed further below. Best-fit parameters to this model are shown in Figure

5.7, with fits to the 33-nm and 81-nm NP data shown in Figure 5.5. Fits to all NP sizes are shown in the Supporting Information. A relatively good fit to the data is observed for all NP sizes, suggesting that this model provides a reasonable description of the underlying physical processes occurring in these systems. The only discrepancy in this fit is an over-estimation of the singlet decay at later times in the 33-nm NPs, as evident in the inset of Figure 5.5a. This discrepancy may be due to the presence of trap sites in this system (sites at which excitons cannot move or decay), which have previously been reported for both pentacene and TIPS-Pn but are not taken into account in the kinetic model used here.[72,116,133] However, this model still adequately describes the majority of singlet decay in the 33-nm NPs, and so this minor disagreement likely has an insignificant impact on the conclusions drawn from this analysis.

5.4.4.2 Size-Dependent Exciton Dynamics

Several trends are immediately evident from the fit parameters shown in Figure 5.7, which agree with the qualitative trends observed in the TA data mentioned above. On increasing NP diameter, rate coefficients of SF ($k_{SF,A}$ and $k_{SF,B}$) increase by over an order of magnitude, f_{NR} decreases to zero, k_{pair} decreases by half, and k_T also decreases substantially. f_{NR} decreases from almost one-third to effectively zero across the NP sizes studied here, consistent with the increase in ϕ'_{SF} with NP size shown in Table 5.2 and the quantitative yield noted for the 81-nm NPs. SF time constants, $\tau_{SF} = (k_{SF,A} + k_{SF,B})^{-1}$, range from 15 ps for the smallest NPs to 1.3 ps for the 81-nm

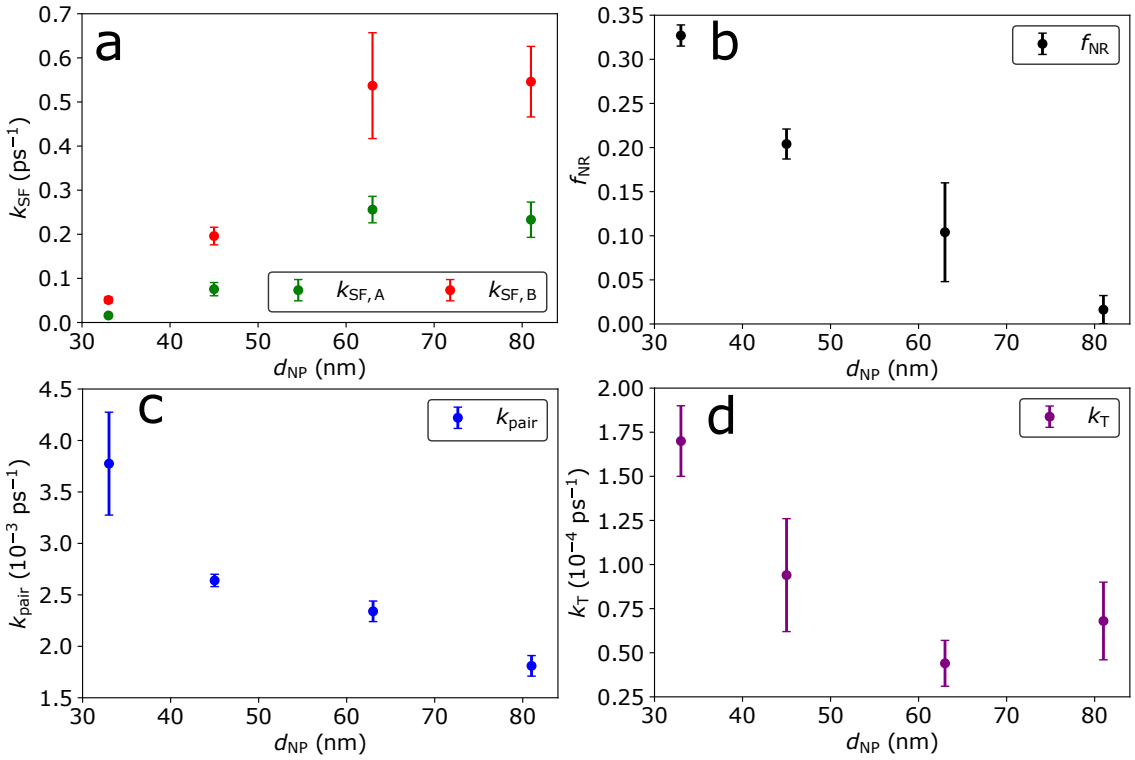

Figure 5.7: Best-fit values of (a) $k_{SF,A}$ and $k_{SF,B}$, (b) f_{NR}, (c) k_{pair} and (d) k_T from the kinetic model described in Figure 5.6 for all NP sizes. k_{sep} and k_{NR} fit to constant values across all NP sizes of $20.0 \pm 0.5\,ps^{-1}$ and $0.17 \pm 0.03\,ps^{-1}$, respectively. Values are averages for fits at $p = 0$ and $p = 0.25$, and uncertainties represent the range of fit values between $p = 0$ and $p = 0.25$.

NPs. The latter value agrees closely with SF time constants previously reported for amorphous TIPS-Pn films,[110,142] suggesting that these larger NPs exhibit SF kinetics similar to those of bulk TIPS-Pn. Best-fit values of k_{pair} are also of a similar order of magnitude to rate coefficients of ^{1}(TT) decay reported for TIPS-Pn[72,119] and other acene materials.[58,75]

The best-fit values of k_{T} correspond to triplet exciton lifetimes appreciably longer than the 3.2 ns experimental time window accessible here. Precise quantification of these rate coefficients is therefore difficult from the data collected here, and hence a significant degree of uncertainty is associated with these values of k_{T}. However, the best-fit parameters presented in Figure 5.7d clearly exhibit a trend of accelerated T_1 decay at smaller particle sizes even when these uncertainties are taken into account, consistent with the clear trend in the decay of T_1 concentrations (Supporting Information). The best-fit values of k_{T} determined here are 2–3 orders of magnitude larger than the rate coefficient for natural first-order decay of T_1 excitons, which has been demonstrated to be on the order of $10^{-7}\,\text{ps}^{-1}$.[110] Therefore, it is unlikely that the change in k_{T} with NP size here arises from natural triplet decay. Neither bimolecular TTA nor triplet-charge annihilation at the NP surface is consistent with this relatively fast T_1 decay, as varying either the excitation density or NP surface charge have negligible effects upon the observed triplet decay kinetics (Supporting Information). Therefore, the likely cause of this fast triplet decay is geminate TTA, in which pairs of triplet excitons generated from the same SF event annihilate with pseudo-first-order kinetics. We stress that is an annihilation process rather than recombination to the S_1 state, as neither re-formation of the singlet state in the TA spectra or delayed fluorescence occur in the results presented here. This lack of singlet re-formation is unsurprising, given that the $T_1 + T_1 \rightarrow S_1 + S_0$ process is endoergic in TIPS-Pn and therefore unfavorable.[19] For geminate annihilation to be the dominant triplet decay pathway here, separated triplet excitons must remain trapped in relatively close proximity to one another. A poor triplet exciton mobility is hence expected for these NPs, which is supported by a previous study of amorphous TIPS-Pn films.[110] Estimated triplet diffusion coefficients from this previous study correspond to diffusion lengths of less than 1 nm on the timescale of this experiment (Supporting Information). This diffusion length equates to an intermolecular separation of only 1–2 TIPS-Pn molecules, depending upon relative molecular orientations.[125] Several recent studies of both amorphous and crystalline TIPS-Pn have included a spin-correlated but spatially-separated (T$\cdots$T) state as an intermediate between ^{1}(TT) and $T_1 + T_1$ in their description of triplet pair separation, which is assigned as being spectrally indistinguishable from free triplet excitons.[62,75,109,142] Given the poor triplet mobility and significant geminate TTA observed here, a significant population of T_1 excitons here may hence exist as (T$\cdots$T) exciton pairs, separated only by 1–2 molecules. However, geminate annihilation of either free triplet excitons or (T$\cdots$T) pairs would result in first-order decay with respect to triplet concentration,[75,115,252] and so the results presented here cannot distinguish between these processes. Despite this, these data clearly show that geminate annihilation of triplet excitons accelerates at smaller particle sizes, concurrent with slower SF and faster ^{1}(TT) relaxation.

5.4.4.3 Changes in Nanoparticle Morphology

Overall, the results of this kinetic modelling show that SF becomes slower while non-radiative ^{1}(TT) decay and geminate TTA become faster as the diameter of amorphous

TIPS-Pn NPs decreases. As all of these processes involve intermolecular exciton interactions, it is reasonable to infer that these changes likely arise from variations in NP morphology with particle size. Previous studies have demonstrated that polymers such as PMMA, poly(ethylene glycol) (PEG) or poly(vinyl alcohol) (PVA) can disrupt or alter the morphology of TIPS-Pn NPs,[1,72,253] while the use of other additives as surfactants or emulsifying agents has been shown to alter the intermolecular packing of other organic nanoaggregates.[243,254] However, as the preparation of the TIPS-Pn NPs studied here uses only water, THF and TIPS-Pn, these changes in dynamics are unrelated to other chemical species disrupting or changing the NP morphology. Therefore, any change in morphology with NP size can only be due to a variation of the inherent TIPS-Pn intermolecular packing. While all NP sizes show spectral characteristics consistent with an amorphous morphology, Figure 5.1 shows a slight shift in the 0–0 $S_1 \leftarrow S_0$ steady-state absorption peak upon changing NP size. Similar peak shifts in TIPS-Pn and other functionalized pentacene derivatives have been previously attributed to changes in intermolecular packing, with more blue-shifted spectral features ascribed to a less dense and more disordered or "monomer-like" intermolecular packing in the solid state.[72,75] The peak shift observed here may hence indicate that smaller TIPS-Pn NPs may have more disordered solid-state packings than larger NPs, which is consistent with the changes in exciton dynamics noted here. Therefore, while all NP sizes studied here possess morphologies that can be classed as amorphous, these morphologies contain differing levels of disorder and cannot be considered as equivalent. The first step of SF, $S_1 + S_0 \rightarrow {}^1(TT)$, depends strongly upon the electronic coupling strength between adjacent chromophores,[19] and so an increase in molecular disorder would reduce the coupling between neighboring molecules, slowing the average rate of SF. Greater disorder would also inhibit long-range separation of triplet excitons, as triplet hopping through Dexter energy transfer depends strongly upon interchromophore distance.[80,235] This restriction of exciton mobility would increase the probability of triplet excitons formed from the same SF event remaining in close proximity to one another, thereby increasing the rate of geminate TTA.

Separation of the triplet pair state into free triplets has been shown to be limited by triplet hopping away from the initial SF site in crystalline[59] and amorphous[72] TIPS-Pn. As mentioned above, an increase in molecular disorder would significantly slow triplet mobility in these NPs. Hence, a more disordered intermolecular packing in these NPs could potentially slow the overall rate of $^1(TT)$ separation. However, the kinetic analysis undertaken here indicates that the rate coefficient of triplet pair separation is independent of NP size, fitting to a constant value of $k_{sep} = 20\,ps^{-1}$. This value corresponds to $^1(TT)$ separation occurring on a timescale of $< 100\,fs$, which is over an order of magnitude faster than $^1(TT)_B$ formation ($\tau_{SF,B} \approx 2 - 20\,ps$). The model used here is hence relatively insensitive to the value of k_{sep}, as the rate-limiting step for T_1 formation is the $S_1 + S_0 \rightarrow {}^1(TT)$ step. Therefore, it is difficult to fit k_{sep} to a high level of accuracy with the kinetic model used here. Contrasting with this behavior for k_{sep}, k_{pair} shows a strong dependence upon NP size, becoming significantly larger at smaller NP sizes. The exact mechanism by which the triplet pair state decays non-radiatively is still unclear, and so it is difficult to justify this accelerated decay at smaller NP sizes. However, increased morphological disorder at smaller particle sizes likely corresponds to less rigidity in the intermolecular packing within the NPs. The corresponding greater degrees of freedom in molecular vibrations and other nuclear motions may increase mixing of electronic states responsible for this non-radiative

decay.[13] The faster non-radiative ^{1}(TT) decay observed here at smaller particle sizes is therefore likely due to increased morphological disorder allowing greater degrees of freedom to the nuclear motions which facilitate this decay.

The large value of $k_{sep} = 20\,ps^{-1}$ fit here implies that the $^1(TT)_B$ population is not experimentally observable, as these pair states separate effectively immediately after formation. The ^{1}(TT) excitons observed in TA experiments here must therefore consist solely of $^1(TT)_A$ excitons, which cannot separate. The fraction of total ^{1}(TT) excitons formed through the SF_A pathway (given by $k_{SF,A}/(k_{SF,A} + k_{SF,B})$) remains relatively constant at 0.25–0.3 across all NP sizes studied here, thus indicating that approximately 25–30% of all ^{1}(TT) excitons formed in these amorphous NPs are unable to separate. Subsequent non-radiative decay of this $^1(TT)_A$ population hence reduces the SF yield ϕ'_{SF} relative to ϕ_{SF}, as shown in Table 5.2. The $^1(TT)_A$ population may therefore be better described as a "trap" species rather than SF intermediates, as instead of separating to $T_1 + T_1$ they provide an additional pathway for relaxation to the ground state. A similar loss mechanism was recently identified in TIPS-tetracene, whereby an emissive excimer state was found to form not as an intermediate in the SF process but through a competing process detrimental to SF yield.[183]

5.4.4.4 Singlet Exciton Quenching

The inclusion of a singlet population undergoing non-radiative decay in the kinetic model used here is intriguing. Kinetic fits to the TA data without this non-radiative decay pathway resulted in poor fits for the 33- and 45-nm NP samples (Supporting Information), with the fitted triplet/triplet pair concentrations overly high for these smaller NPs. Inclusion of this additional non-radiative S_1 decay mechanism is hence necessary to adequately describe the T_1 and ^{1}(TT) kinetics for these smaller NPs. This result is consistent with the SF yields shown in Table 5.2, as the low values of ϕ'_{SF} reported here for smaller NPs suggest that a singlet decay pathway independent of SF must also be present in these systems. SF in amorphous TIPS-Pn has been extensively studied,[72,75,110,119,133,134,142] but this non-radiative, non-SF related pathway appears to have been identified here for the first time. However, all of these previous studies considered either thin films or relatively large NPs ($d_{NP} > 70\,nm$). As shown in Figure 5.7b, f_{NR} decreases to nearly zero for the 81-nm NPs, indicating that this non-radiative decay pathway is effectively negligible for NPs of this size or larger. Therefore, this singlet quenching mechanism has likely not been reported before because it is only significant for relatively small NPs ($d_{NP} \leq 60\,nm$), and was hence absent in the larger particles or bulk films used in previous studies.

Aqueous colloidal dispersions of acenes and other organic semiconductors are known to acquire a negative surface charge during the re-precipitation process,[1,143,243] and so we considered the possibility that this singlet quenching effect arises from singlet–charge annihilation at the NP surface. However, varying the NP surface charge density resulted in negligible changes to singlet decay kinetics in these NPs (Supporting Information). Hence, it is unlikely that exciton–charge annihilation is the primary cause of this non-radiative decay. As the TA experiments conducted here were undertaken under standard atmospheric conditions, it is also possible that dissolved oxygen may contribute to exciton quenching at the NP surface. However, previous studies of acene quenching by triplet oxygen have measured rate coefficients on the order of 10^9–$10^{10}\,s^{-1}$, which is 1–2 orders of magnitude lower than the picosecond-scale S_1 deactivation observed here.[255,256] Therefore, singlet quenching by triplet oxygen is also unlikely to

be the main cause of the non-radiative singlet decay observed here. Picosecond-scale non-radiative singlet decay in aqueously-dispersed fullerene NPs has previously been attributed to exciton quenching by water.[257] However, the authors of this prior work assigned this exciton decay as arising from water–exciton interactions without offering comment on the underlying mechanism by which this might occur. Relatively strong exciton–water couplings would be required for water molecules to quench singlet excitons on such a fast timescale, presumably through interactions with the dipole moment of water molecules. Other studies have previously suggested that increased intermolecular coupling in pentacene derivatives is concurrent with increased charge-transfer (CT) nature of singlet excitons.[134] Such CT character in S_1 excitons could result in strong dipolar coupling to water molecules at the NP surface. However, the results presented here indicate that average TIPS-Pn intermolecular couplings become stronger with increasing NP size, which would therefore increase the CT character of singlet excitons in larger NPs. If singlet–water interactions were responsible for this non-radiative quenching, then larger particle sizes would hence be expected to yield stronger water–exciton couplings and therefore more singlet quenching at larger particle sizes. This is the opposite of the trend observed here for f_{NR}, and so quenching by water molecules is unlikely to be the physical cause of this non-radiative singlet exciton decay. The variation in intermolecular couplings across different-sized NPs here may be too small to yield any significant changes in the CT character of singlet excitons. Alternatively, any increase in exciton–water interaction strength may be offset by decreased surface area:volume ratios at larger particle sizes.

As the non-radiative singlet decay recorded here is unlikely to arise from exciton quenching by SF, surface charges, dissolved oxygen or water molecules, it is logical to consider that this process may be due to the inherent morphology of small TIPS-Pn NPs. The inverse scaling of f_{NR} with particle size could suggest that this morphology resides at the NP surface, as the NP surface area:volume ratio also scales inversely with d_{NP} (Supporting Information). Surface morphologies that differ from those of the NP interior or the bulk material have been previously reported for conjugated polymer NPs, attributed to the curvature of the NP surface restricting intermolecular packing.[143,250] The non-radiative singlet decay observed here could hence be due to morphologies formed at the NP surface which are conducive to fast non-radiative exciton quenching. We considered a model in which singlet quenching may occur within a finite depth of the NP surface (Supporting Information), which may explain the decrease of f_{NR} with particle size recorded here. However, the good fit of this model is not definitive evidence of this singlet quenching occurring solely at the NP surface; changes in morphology throughout the entire NP volume could also explain the scaling of f_{NR}. Therefore, the exact physical cause of this non-radiative singlet quenching is unclear from the results presented here.

5.4.4.5 TIPS-Pn Nanoparticles as Models for Bulk Systems

Three pathways of exciton decay to the ground state in amorphous TIPS-Pn NPs have been identified here: non-radiative quenching of singlet excitons, relaxation of ^{1}(TT) intermediates unable to separate, and geminate annihilation of separated triplet excitons. All of these processes (illustrated in Figure 5.8) depend strongly on NP size, with rate coefficients or population fractions that vary by up to an order of magnitude across the sizes considered here. This apparent dependence upon NP size is likely due to variations in morphological disorder within the NPs, which becomes more significant

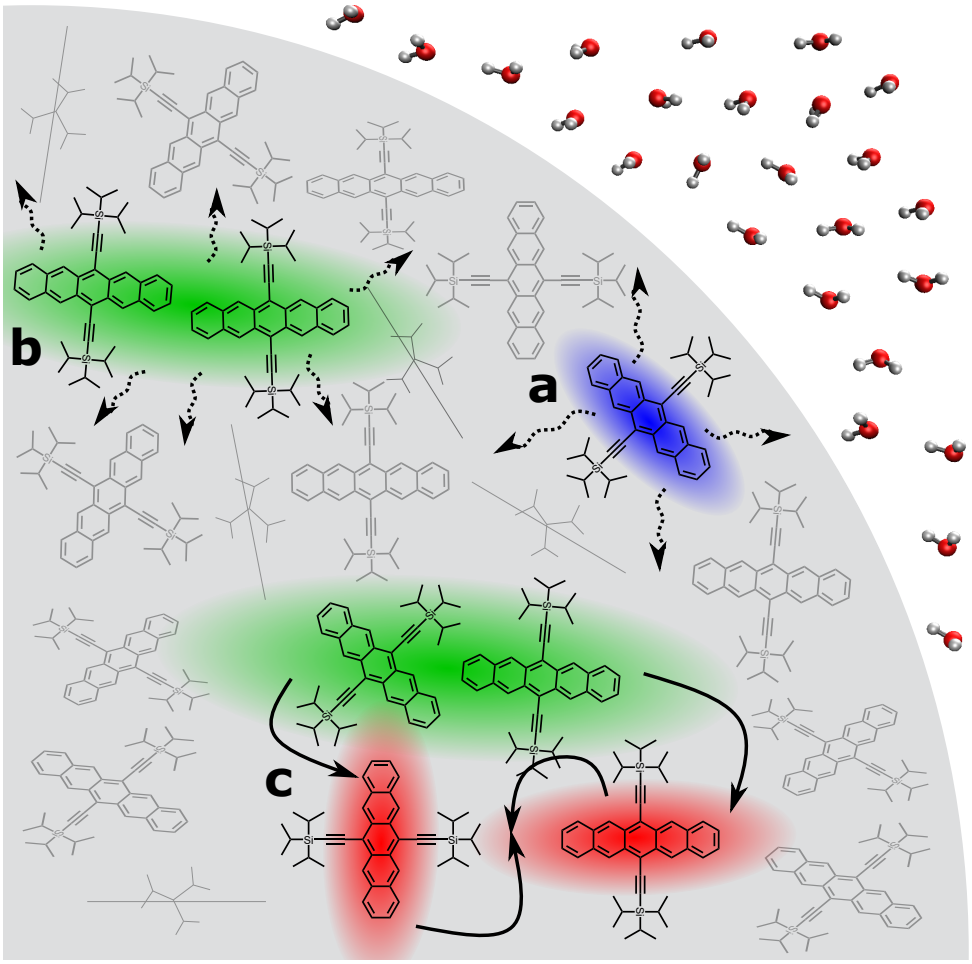

Figure 5.8: Illustration of the three different exciton decay pathways identified for amorphous TIPS-Pn NPs in this work: a) non-radiative singlet decay, b) non-radiative triplet pair decay, and c) triplet pair separation and subsequent geminate annihilation. Singlet excitons are shown in blue, triplet pair excitons in green and triplet excitons in red. Solid arrows denote exciton hopping and annihilation processes, while dashed arrows indicate non-radiative decay.

at smaller particle sizes. This behavior may be due to geometric constraints; increased curvature at the NP surface at smaller sizes may restrict intermolecular packing within the particle, thus increasing disorder. Growth of NPs to larger sizes may allow for more reorganization within the NP, hence decreasing disorder in the overall intermolecular packing.

The strong size dependence of excitonic processes in amorphous TIPS-Pn NPs uncovered here may help to resolve some discrepancies in the literature. Munson and co-workers demonstrated that SF in amorphous TIPS-Pn films occurred on a subpicosecond timescale,[142] but a recent study of small (d_{NP} = 30 nm) amorphous NPs showed no detectable SF within a 500-fs window.[141] Recognizing that the NPs in the latter study were of comparable size to the smallest NPs used here, these NPs likely possessed significant morphological disorder due to their small size, causing SF to occur much more slowly than in the bulk film. Such varying degrees of disorder with NP size likely also accounts for the wide variety of SF rate coefficients for amorphous TIPS-Pn NPs in other studies, which vary by up to an order of magnitude.[72,119,133,134,141,142] Additionally, while the natural triplet lifetime in bulk TIPS-Pn is known to be on the order

of µs,[110] other studies of amorphous TIPS-Pn NPs have reported first-order triplet decay orders of magnitude faster than this.[72,133] Again, this disagreement is likely due to higher disorder in NPs relative to bulk films, inhibiting triplet mobility and hence resulting in fast geminate TTA. The results of the present study therefore demonstrate the need for caution when using NP dispersions as models for bulk systems. Particle size effects, exciton quenching or other NP-specific processes that are irrelevant in the bulk may be important in such systems. Although use of NPs as model systems can yield useful information regarding SF, particle size should be explicitly considered when designing studies using NP models. For the case of amorphous TIPS-Pn considered here, singlet exciton quenching and size-dependent exciton dynamics are most prevalent at smaller NP sizes. As shown in Figure 5.7, rate coefficients of all excitonic processes begin to converge for d_{NP} = 63–81 nm, and f_{NR} reduces to effectively zero for the 81-nm NPs. Therefore, it can be reasonably concluded that particle-size-effects for amorphous TIPS-Pn NPs become negligible in the region of d_{NP} = 63–81 nm, and hence NPs of this size or larger should be reasonable models for bulk amorphous TIPS-Pn.

5.5 Conclusions

This work has demonstrated that exciton dynamics in amorphous TIPS-Pn NPs depend significantly upon particle size. While steady-state spectral characteristics indicate that all NPs possess amorphous morphologies, transient absorption and time-resolved fluorescence results show substantial variation in the dynamics of both singlet and triplet excitons with particle size. Spectral deconvolution and kinetic analysis show that larger NPs exhibit faster SF, slower ^{1}(TT) non-radiative decay and slower free triplet decay through geminate annihilation. These results are consistent with the intermolecular packing in these NPs becoming more disordered at smaller particle sizes, slowing SF and triplet exciton hopping. An additional non-radiative decay pathway of singlet excitons was identified, in which the S_1 state forgoes SF and decays directly to the ground state. This quenching process becomes significant at small particle sizes, greatly reducing triplet yields from SF. To the best of our knowledge, this is the first report of such a non-SF singlet quenching mechanism in acene NPs. These significant variations of exciton dynamics with particle size account for quantitative discrepancies in the literature for amorphous TIPS-Pn, hence indicating the importance of considering particle size in interpreting results of NP models for SF-capable chromophores such as TIPS-Pn.

Acknowledgements

This work was supported by an Australian Government Research Training Program (RTP) scholarship and funding from the Australian Research Council (DP160103797 and LE0989747). The authors also thank Dr. Patrick Tapping for discussions that contributed to this work.

5.6 Supporting Information

Particle Size Characterization by Dynamic Light Scattering

Intensity-weighted size distributions of all NP samples as determined by DLS are shown in Figure 5.9. Each NP sample exhibits a relatively monodisperse size distribution, but centred at distinctly different sizes. While several variables relating to the re-precipitation process were varied to achieve these sizes (Table 5.1, main text), the primary parameter used to adjust NP size was the concentration of the TIPS-Pn injection stock. Re-precipitation with relatively concentrated stock solutions (500–1000 ppm) yielded Z-average particle sizes on the order of 60–80 nm diameter, agreeing with several previous studies.[1,2,119] Conversely, re-precipitation with a very dilute concentration (20 ppm) resulted in relatively small NPs with $d_{NP} \approx 30$ nm in diameter, consistent with recent work by de la Perrelle.[141]

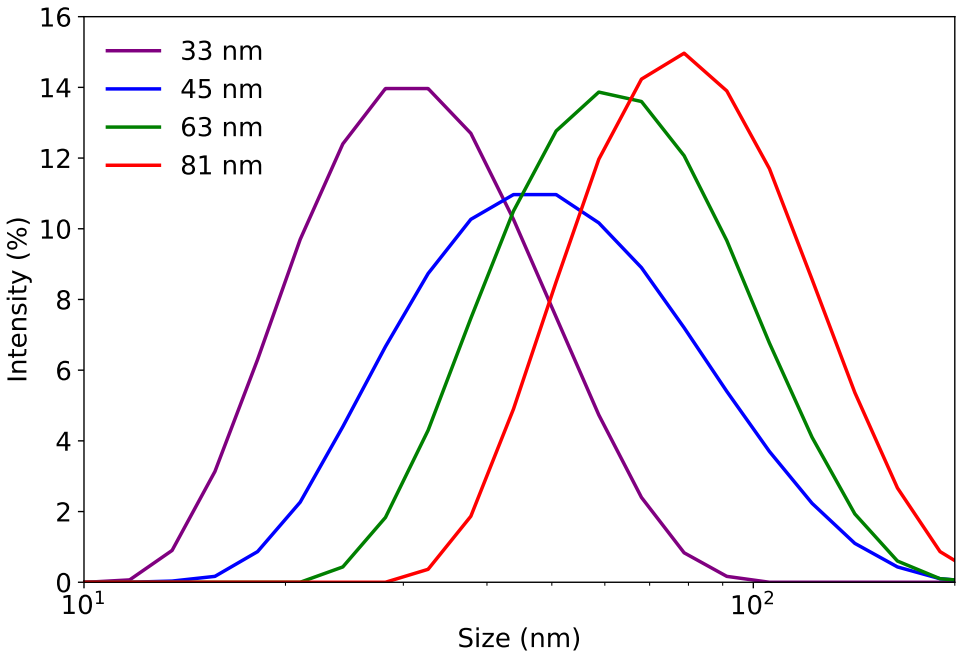

Figure 5.9: Intensity-weighted particle size distributions of TIPS-Pn NPs prepared by re-precipitation with varying injection concentrations. NP samples are labelled by diameter.

Additional Steady-State and Time-Resolved Fluorescence Data

Figure 5.10 shows normalized steady-state emission spectra for all NP samples considered here, upon excitation at 590 nm. The spectral shapes of emission from the two smallest NP samples are clearly the same, with the traces effectively coincident. Comparison is less straightforward for the larger NP samples, as low signal and increased scattering due to larger particle sizes result in significantly poorer quality spectra. However, the overall shape of the spectra do not appear to change dramatically for these larger NPs, with the ratio of 0–0 and 0–1 peak intensities appearing to be approximately the same. A slight red shift in the 0–0 peak at 650 nm is evident upon increasing particle size, concurrent with the red shifts in steady-state absorption shown in Figure 5.1 of the main text.

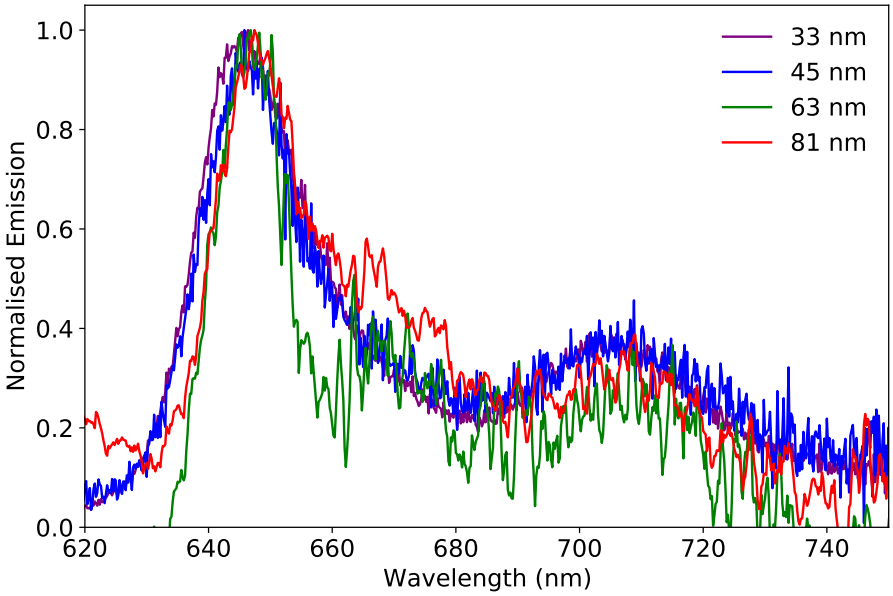

Figure 5.10: Steady-state emission spectra of all NP sizes upon excitation at 590 nm, normalized to the 0–0 emission peak. 63 nm and 81 nm NP spectra have been smoothed by a Savitzky-Golay filter of polynomial order 3 over a 1-nm window. NP samples are labelled by diameter.

Time-resolved fluorescence spectra of NP samples are shown only over a 15 ps window in Figure 5.2b of the main text, in order to highlight the rapid fluorescence decay for larger NP sizes. However, this small time window does not capture the majority of fluorescence decay for the smaller NPs, and so Figure 5.11 shows this same data for the 33 nm and 45 nm NPs over a longer time window of 45 ps. Emission from the 45-nm

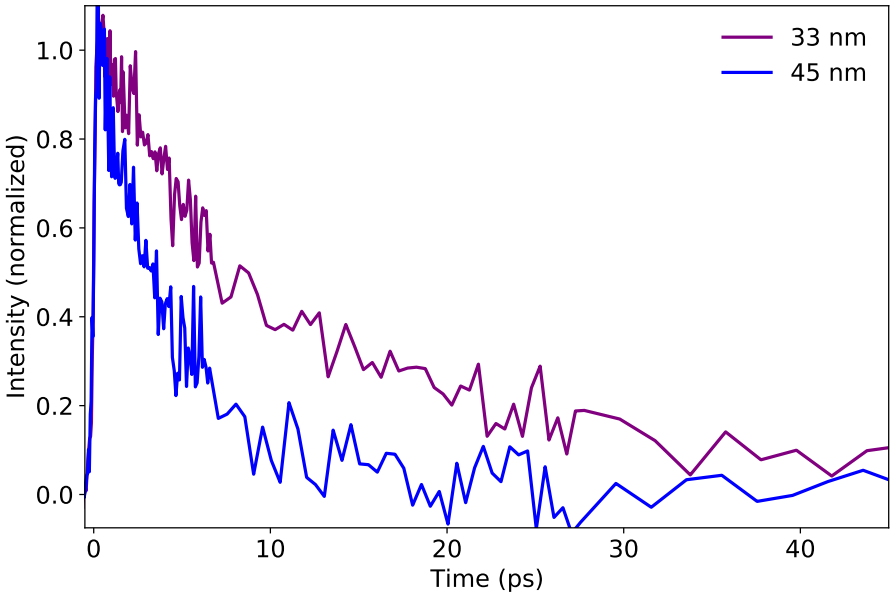

Figure 5.11: Long-time fluorescence upconversion of TIPS-Pn NP samples (excitation at 590 nm, detecting at 700 nm). Data is shown only for NP samples in which fluorescence persisted longer the 15 ps window shown in Figure 2b of the main text. NP samples are labelled by diameter.

NPs decays to baseline levels after approximately 20–25 ps, while around 10% of the initial intensity remains after 45 ps for the 33-nm NPs.

Extraction of Exciton Basis Spectra

T_1 Basis Spectrum

The basis spectrum for T_1 excitons was extracted using the method recently published by Stuart et al.[72] Assuming that only free triplet excitons are present at a sufficiently long delay time t, and assuming that there are no SE or ESA features overlapping with the GSB, the magnitude of the bleach at 645 nm ($\Delta A(t, 645\,\text{nm})$) can be used to determine the concentration of excitons in the sample by

$$[T_1](t) = \frac{\Delta A(645\,\text{nm}, t)}{\epsilon_{SS}(645\,\text{nm})l}, \quad t \gg \tau_{S_1}, \tau_{1(TT)}, \tag{5.6}$$

where $l = 2$ mm is the sample path length, τ_{S_1} and $\tau_{1(TT)}$ are lifetimes of the singlet and triplet-pair states, respectively, and $\epsilon_{SS}(645\,\text{nm})$ is the steady-state molar extinction coefficient at the 645 nm absorption peak, known to be $10\,400\,\text{L mol}^{-1}\,\text{cm}^{-1}$ for amorphous TIPS-Pn NPs as per our previous work.[1] From this concentration, the molar extinction coefficient of triplet excitons at each wavelength ($\epsilon_{T_1}(\lambda)$) can be calculated from the TA spectrum at time t by

$$\epsilon_{T_1}(\lambda) = \frac{\Delta A(\lambda, t)}{[T](t)l}, \quad t \gg \tau_{S_1}, \tau_{1(TT)}. \tag{5.7}$$

To extract the T_1 basis spectrum, we consider TA spectra of the 63-nm NPs at a delay time of $t = 3.0$ ns. The singlet population has entirely decayed away at such a late delay time, as evidenced by the fast time-resolved fluorescence decay in Figure 5.2b. We assumed that no other species such as correlated triplet pair excitons persist out to 3 ns. This is a reasonable assumption, as the ^{1}(TT) state in amorphous TIPS-Pn has previously been shown to separate on a timescale of 1–10 ps or decay on the order of 100 ps.[72,110,119,142] The population of this intermediate after 3 ns should be effectively negligible, and therefore we applied Equations 5.6 and 5.7 to determine the triplet basis spectrum shown in Figure 5.4a of the main text.

S_1 Basis Spectrum

The method used to determine the singlet exciton basis spectrum is similar to that outlined above for calculation of the triplet basis spectrum. However, as SF occurs on the picosecond timescale for all NP samples studied here, no early time TA data from these samples can be confidently assigned as arising purely from S_1 excitons. Therefore, we prepared a 1:90 TIPS-Pn:PMMA blend NP sample, in which TIPS-Pn was highly dilute. As reported in our recent work, this dilution causes large intermolecular separations between TIPS-Pn molecules, and hence results in extremely slow SF.[72] TA spectra over the first 50 ps after excitation (Figure 5.12) show a spectral shape that corresponds well to the identified S_1 spectral features in the main text and is invariant over the first 50 ps after excitation . Therefore, TA spectra from this sample at a 20-ps delay time were used to calculate the S_1 basis spectrum.

However, for singlet excitons in TIPS-Pn the negative signal at 645 nm arises not just from a GSB, but from an overlap of GSB and SE signals. Therefore, in order

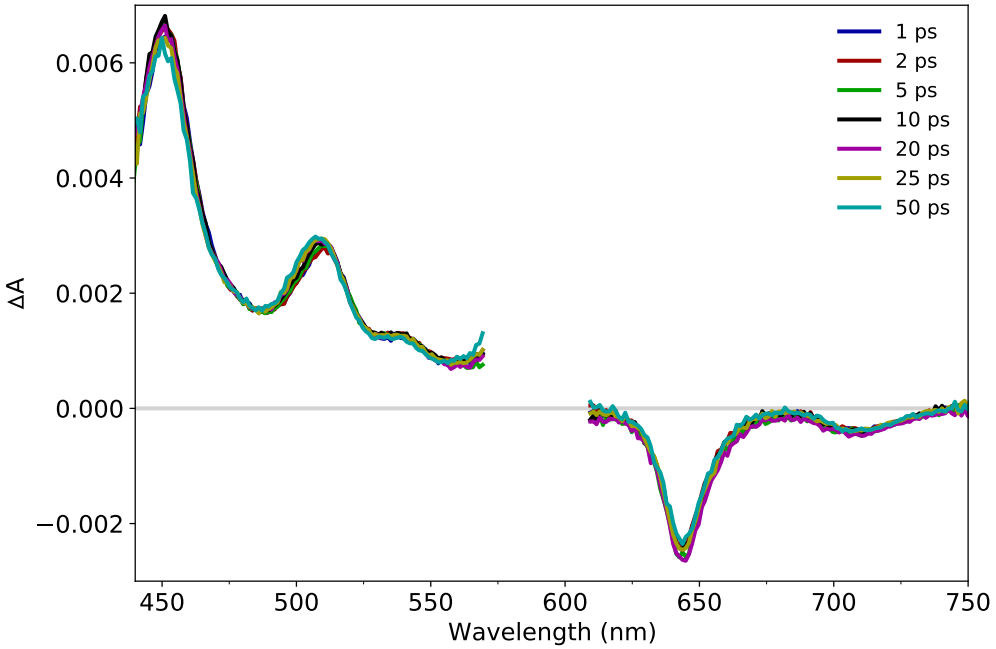

Figure 5.12: TA spectra of a 1:90 TIPS-Pn:PMMA blend NP sample at early times after excitation at 590 nm.

to determine the singlet exciton concentration from the GSB magnitude, the relative contributions of the GSB and SE to this signal in the TIPS-Pn:PMMA blend NP must be estimated. The relative intensities of the 645 nm and 710 nm signals in Figure 5.12 do not change over 50 ps. This is the timescale on which the S_1 state decays in the neat TIPS-Pn NPs (Figure 5.11), and so it is reasonable to assume that this intensity ratio is effectively invariant over time for all neat TIPS-Pn samples studied here. Hence, we estimated the ratio of 0–0 and 0–1 SE intensities in the TA spectra as the ratio of peak intensities in the steady-state emission spectra ($I_{SS}(\lambda)$). From Figure 5.10, we calculated this ratio as

$$\frac{\Delta A_{SE}(645\,\text{nm}, t)}{\Delta A_{SE}(710\,\text{nm}, t)} \approx \frac{I_{SS}(645\,\text{nm})}{I_{SS}(710\,\text{nm})} = 2.56. \tag{5.8}$$

The magnitude of the GSB signal at this wavelength can therefore be estimated as

$$\begin{aligned} \Delta A_{GSB}(645\,\text{nm}, t) &= \Delta A(645\,\text{nm}, t) - \Delta A_{SE}(645\,\text{nm}, t) \\ &= \Delta A(645\,\text{nm}, t) - 2.56\Delta A(710\,\text{nm}, t). \end{aligned} \tag{5.9}$$

Using the GSB magnitude determined from Equation 5.9, the S_1 concentration at an early time t can be determined by

$$[S_1](t) = \frac{\Delta A_{GSB}(645\,\text{nm}, t)}{\epsilon_{SS}(645\,\text{nm})l}, \quad t < 50\,\text{ps}, \tag{5.10}$$

analogously to the determination of $[T_1]$ as per Equation 5.6. Using $t = 20$ ps in Equation 5.10 with the 1:90 TIPS-Pn:PMMA TA data, the S_1 basis spectrum was hence determined as

$$\epsilon_{S_1}(\lambda) = \frac{\Delta A(\lambda, t)}{[S](t)l}, \quad t = 20\,\text{ps}, \tag{5.11}$$

Given the somewhat approximate nature of the [S_1] calculation above, the accuracy of this method was tested by comparing exciton concentrations fit by this basis spectrum to initial exciton densities expected from experimental conditions. At sufficiently early times after excitation ($t > 0.5\,\text{ps}$) most excitons will remain as singlets, and so the singlet exciton concentration is expected to match the experimental excitation density, given by

$$C_{\text{exp}} = (1 - T_\lambda)\rho_e, \tag{5.12}$$

where T_λ is the sample transmittance at the excitation wavelength and ρ_e is the excitation density of the laser pulse. Table 5.3 compares C_{exp} with [S_1]($t = 0.2\,\text{ps}$) – determined by fits of a preliminary basis spectrum calculated as per Equation 5.11 – for all NP sizes. [S_1](0.2 ps) is consistently higher than C_{exp} for all NP sizes, suggesting that a systematic error may have occurred in the determination of singlet concentration here, likely due to the estimation of GSB magnitude in Equation 5.9. This discrepancy becomes smaller for larger NP sizes, which may be due to faster SF in these larger particles resulting in some conversion into ^{1}(TT) and T_1 even at $t = 0.2\,\text{ps}$. However, fluctuations in the pump pulse intensity of ±10% are also possible with the experimental system employed here, which may introduce random errors into C_{exp} and hence also contribute to differences between C_{exp} and [S_1](0.2 ps). Therefore, to correct for this error in [S_1](t) we considered only the average difference between C_{exp} and [S_1](0.2 ps) across all NP sizes, in order to minimize the influence of fluctuations in laser power. As [S_1](0.2 ps) is on average 14.2% higher than C_{exp} for all NP sizes, we scaled [S_1](t) to 85.6% of the value determined by Equation 5.10. This adjusted concentration was then used in Equation 5.11, yielding the S_1 basis spectrum shown in Figure 5.4a of the main text.

While the approximations made here in determining [S_1](t) may introduce some uncertainty in the magnitude of the resulting singlet basis spectrum, this will have a minimal impact upon the analysis and interpretation of results presented in this work. As per Equation 5.11, the value of [S_1](t) affects only the magnitude of the S_1 basis spectrum, not its spectral shape. Any uncertainty in this value would therefore vary the absolute concentrations of singlet excitons fit during deconvolution, but would not change the quality of the fit to the TA data. This could in turn result introduce a scalar offset in the absolute values of ϕ_{SF} and ϕ'_{SF}, but would not change the trends observed in these parameters. Additionally, due to the split-singlet population nature of the kinetic model used to analyse this data (Figure 5.6, main text), any variation in the absolute singlet concentration would simply shift the magnitude of f_{NR} fit to the data – without affecting the trend of f_{NR} with d_{NP} – and would have no effect upon the other parameters in this model.

Table 5.3: Initial exciton concentrations estimated from excitation density (C_{exp}) and spectral analysis ([S_1]).

d_{NP} (nm)	C_{exp} (10^{-7} mol/L)	[S_1](0.2 ps) (10^{-7} mol/L)	% Difference
33	6.26	7.89	26.1
45	5.59	6.49	16.1
63	6.28	7.11	13.2
81	5.41	5.49	1.57
		Average	14.2

^{1}(TT) Basis Spectrum

As mentioned above, the singlet population has decayed entirely to zero after only 10 ps in the 63-nm NP sample. Therefore, the only species that can contribute to the TA spectra at this time are free triplet excitons or correlated triplet pairs. As with our previous study,[72] we estimated the concentration of ^{1}(TT) excitons at this time by assuming some proportion p of T_1 exciton decay over the 3.2-ns experimental time window. The triplet pair population at this time is hence given by

$$[^1(\mathrm{TT})](10\,\mathrm{ps}) = \frac{\Delta A(645\,\mathrm{nm}, 10\,\mathrm{ps}) - \frac{\Delta A(645\,\mathrm{nm}, 3200\,\mathrm{ps})}{1-p}}{-2\epsilon_{SS}(645\,\mathrm{nm})l}, \tag{5.13}$$

where the factor of 2 accounts for a triplet-pair state bleaching two TIPS-Pn molecules. From this concentration, the ^{1}(TT) basis spectrum can be determined by

$$\epsilon_{^1(\mathrm{TT})}(\lambda) = \frac{\Delta A(\lambda, 10\,\mathrm{ps}) - \frac{\Delta A(\lambda, 3200\,\mathrm{ps})}{1-p}}{[^1(\mathrm{TT})](10\,\mathrm{ps})l}. \tag{5.14}$$

In the 63-nm TIPS-Pn NP sample, the $T_1/^1$(TT) ESA at 507 nm decays by 25 % over the 3.2 ns TA window. Therefore, $p \leq 0.25$ can be applied as a reasonable upper bound. We used $p \geq 0$ as a lower bound, as it is unlikely that the T_1 concentration increases from 10 ps to 3.2 ns, given recent reports of ^{1}(TT) separation occurring on the order of picoseconds.[119,142] Figure 5.13 shows a series of possible ^{1}(TT) basis spectra determined over the range $0 \leq p \leq 0.25$. The ^{1}(TT) basis spectrum and subsequent spectral deconvolution shown in Figure 5.4a of the main text uses $p = 0.1$; however, all quantitative results in this work that arise from spectral deconvolution (SF yields, kinetic fits etc.) consider the full range of possible p values, reporting uncertainties as the range of possible best-fit parameters for $0 \leq p \leq 0.25$.

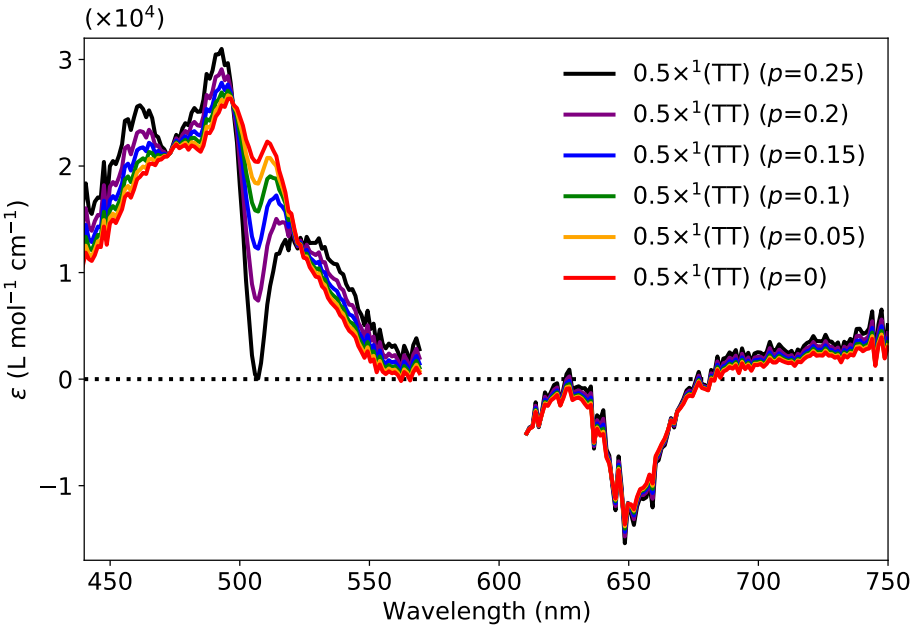

Figure 5.13: ^{1}(TT) basis spectra for representative values of $0 \leq p \leq 0.25$.

Spectral Deconvolution of Transient Absorption Spectra

TA spectra of all NP samples were deconvoluted by linear combination fits of the basis spectra identified above, as per Equation 5.2 in the main text. Fits to the TA data for all NP samples are shown in Figure 5.14, at three representative delay times. The three-component deconvolution fits the experimental data well, with all GSB, SE and ESA features in the data well described by these fits. Figure 5.14 shows fits using a ^{1}(TT) basis spectrum extracted using $p = 0.1$, but it should be noted that deconvolution using basis spectra across the entire range of possible p values result in identical fits to the data. We hence only display one set of spectral fits here for brevity.

Figure 5.15 shows extracted exciton concentrations for all NP samples arising from the spectral deconvolution described in Figure 5.14. Figures 5.16 and 5.17 then show sample exciton concentrations extracted using basis spectra determined with $p = 0$ and $p = 0.25$. While varying the value of p changes the kinetics and concentration profiles of T_1 and ^{1}(TT) excitons extracted from the spectral deconvolution process, it does not influence the overall trend in exciton kinetics with NP size. For all values of p considered, singlet decay is slower and triplet decay is faster for the 33-nm NPs than for the 81-nm NPs. Therefore, choice of p does not impact the interpretation of results arising from deconvolution and subsequent kinetic analysis, but instead provides bounds and uncertainties for quantitative results of these processes.

Estimated SF Yield Losses due to Triplet Pair Decay

Spectral deconvolution of the TA spectra reveals that ^{1}(TT) populations in all NP samples decay on the order of 10^2–10^3 ps (Figures 5.15–5.17). This is consistent with previous studies of amorphous TIPS-Pn which identified a sub-population of correlated triplet pairs that cannot separate and instead decay to the ground state non-radiatively.[58,72,119] In order to estimate the possible losses in ϕ'_{SF} due to this decay, we approximated this decay as a first-order exponential decay with a lifetime of $\tau_{pair} \approx 250$–500 ps. This estimation is made only from observation of the ^{1}(TT) decay kinetics in Figures 5.15–5.17, but it is worth noting that these lifetimes agree with fits to values of k_{pair} from the subsequent kinetic analysis (Table 5.4). Assuming first-order decay kinetics, this non-radiative decay of the correlated triplet pairs can be described by

$$[^1(\mathrm{TT})](t) = [^1(\mathrm{TT})](0)\exp\left(-\frac{t}{\tau_{pair}}\right), \tag{5.15}$$

where $[^1(\mathrm{TT})](0)$ is the ^{1}(TT) concentration at $t = 0$. Singlet exciton decay is slowest in the 33-nm NPs, for which the S_1 population decays to zero over approximately 50 ps. Within this time, Equation 5.15 shows that triplet pair decay can reduce the ^{1}(TT) concentration to 82–91% of its maximum value, for $\tau_{pair} = 250$ ps and 500 ps respectively. Therefore, the correlated triplet pair population can decay by only 9–18% before SF reaches completion in the 33-nm NPs. As $\phi'_{SF} \propto (2 \times [^1(\mathrm{TT})])$, (Equation 5.4, main text) non-radiative triplet pair decay may account for a reduction in ϕ'_{SF} of up to 0.36. This gives a minimum bound of $\phi_{SF} \geq 1.64$ for the 33-nm NPs, assuming that all S_1 excitons undergo SF. This is still significantly larger than the value of $\phi'_{SF} = 1.26$ determined by spectral deconvolution, indicating that non-radiative triplet pair decay cannot be the only mechanism contributing to reduced SF yields.

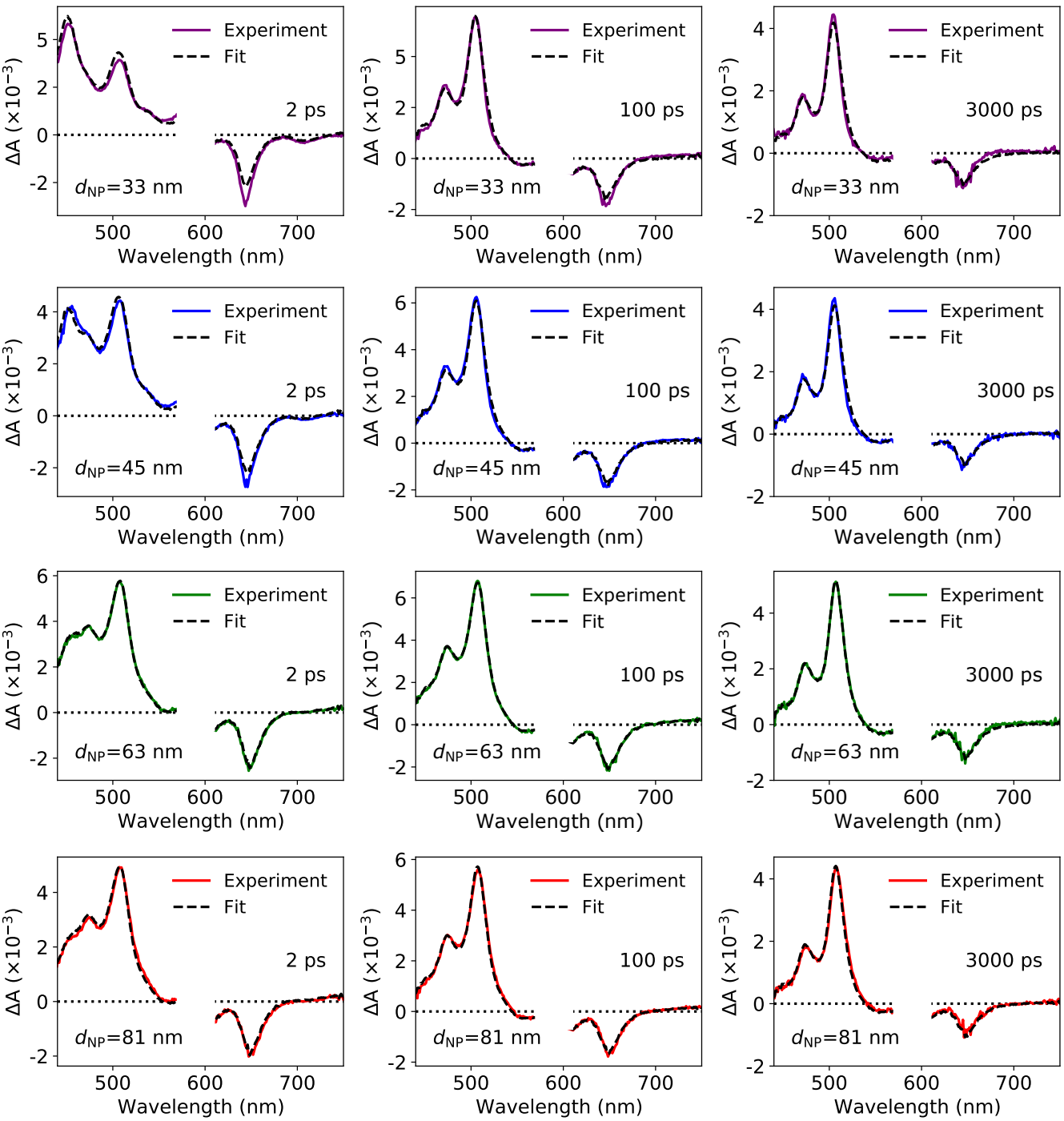

Figure 5.14: Fits to the TA spectra of all TIPS-Pn NP samples considered here by linear combinations of the exciton basis spectra shown in Figure 5.4a (main text), at representative delay times of 2 ps, 100 ps and 3000 ps. Spectral deconvolution here used a ^{1}(TT) basis spectrum extracted using $p = 0.1$.

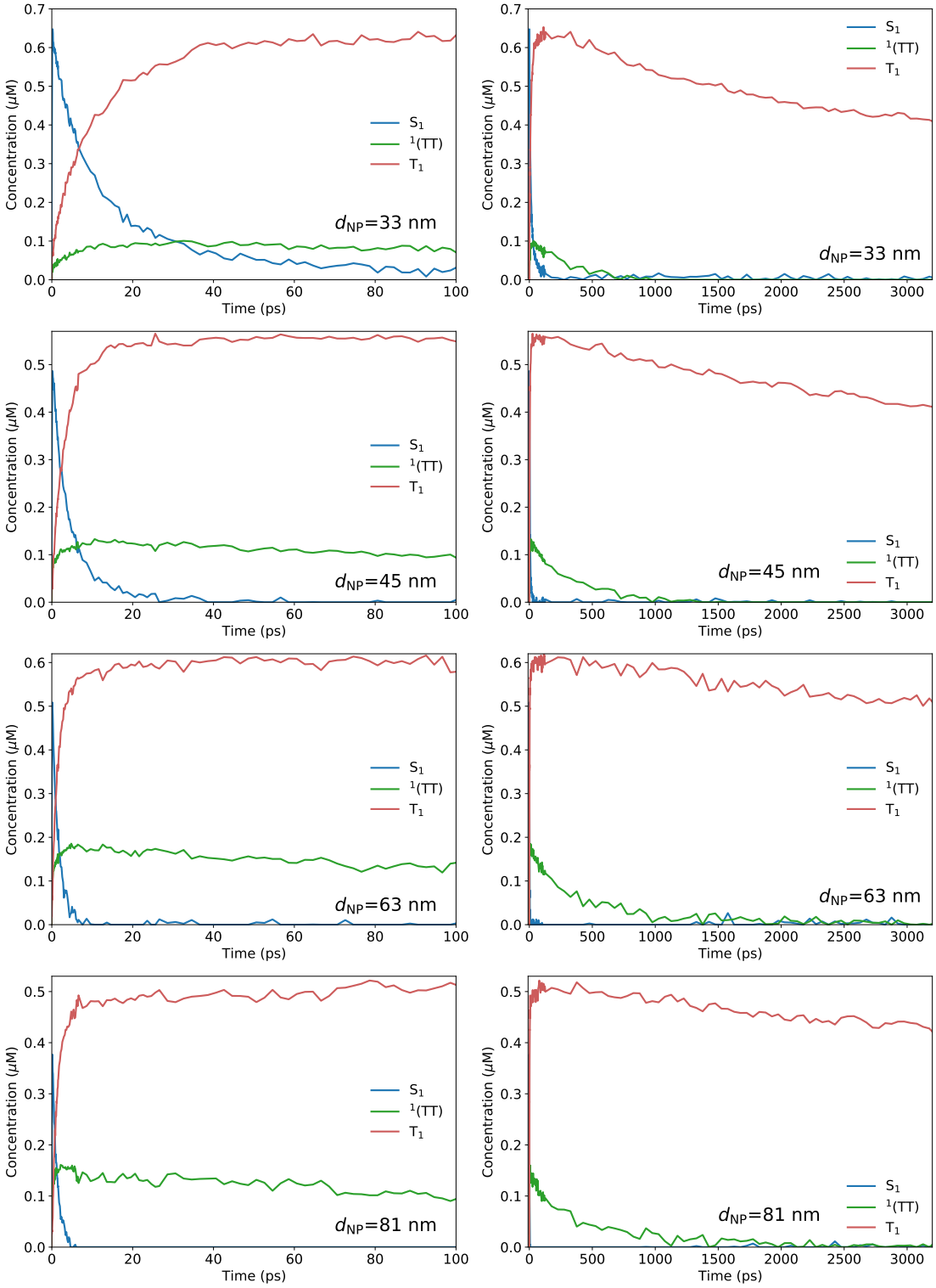

Figure 5.15: Spectrally extracted concentrations of S_1, ^{1}(TT) and T_1 excitons for all NP sizes studied here, (left) over the first 100 ps after excitation and (right) over the entire 3.2-ns TA window. Spectral deconvolution for these concentrations used a ^{1}(TT) basis spectrum extracted using $p = 0.1$.

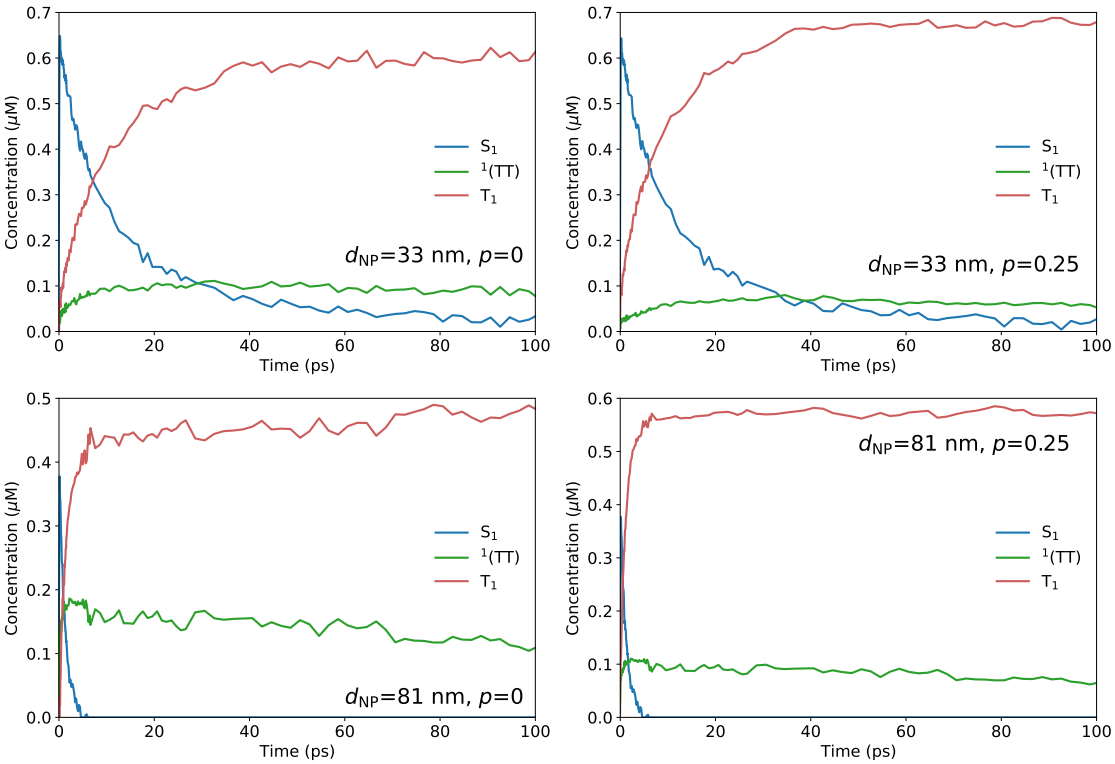

Figure 5.16: Spectrally extracted concentrations of S_1, ^{1}(TT) and T_1 excitons for the 33-nm and 81-nm NP samples over the first 100 ps after excitation, using ^{1}(TT) basis spectra extracted using (left) $p = 0$ and (right) $p = 0.25$.

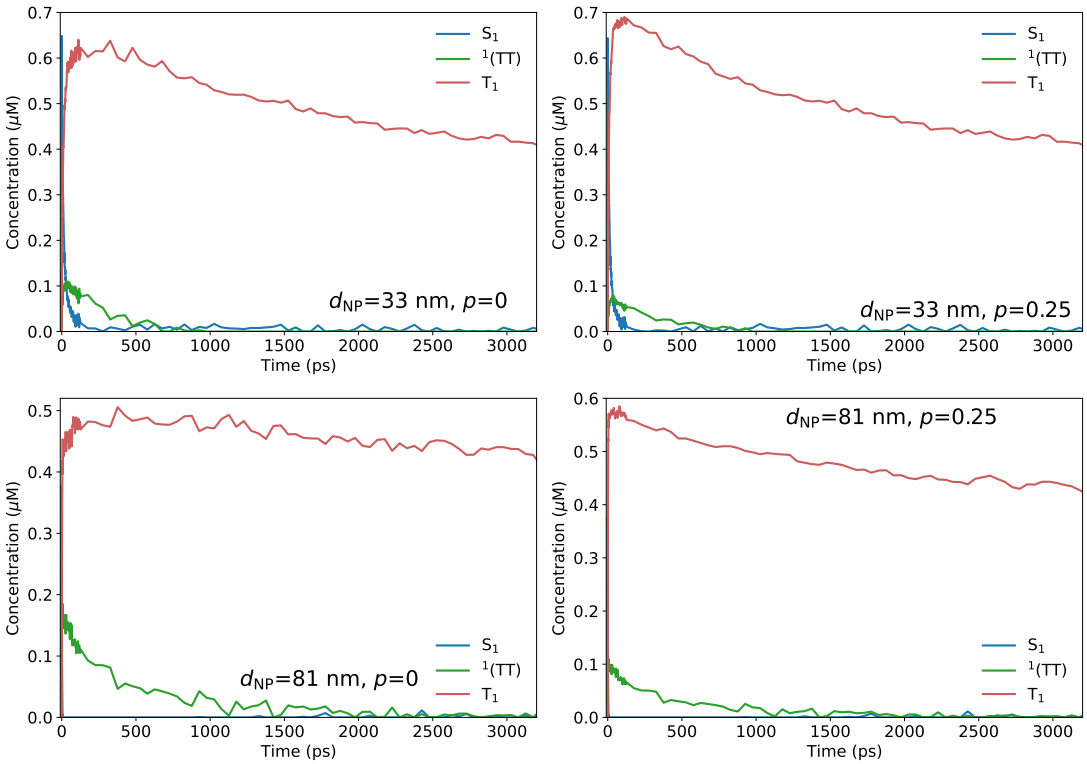

Figure 5.17: Spectrally extracted concentrations of S_1, ^{1}(TT) and T_1 excitons for the 33-nm and 81-nm NP samples over the entire 3.2-ns TA time window, using ^{1}(TT) basis spectra extracted using (left) $p = 0$ and (right) $p = 0.25$.

Estimation of Exciton Diffusion Lengths

The diffusion length L_D of a diffusing species is defined as

$$L_D \equiv \sqrt{D\tau}, \tag{5.16}$$

where D is the diffusion coefficient of the species in question and τ is the species' lifetime or time over which diffusion is relevant.[80]

Singlet Exciton Diffusion

Previous TA studies of disordered acenes have estimated singlet exciton diffusion coefficients to be on the order of 10^{-4}–$10^{-5}\,cm^2\,s^{-1}$.[72,258] Here we take the upper limit of this range, $D = 10^{-4}\,cm^2\,s^{-1}$. We approximate the TIPS-Pn singlet exciton lifetime in the presence of SF as $\tau = 50\,ps$, noting that this is significantly longer than the SF timescale for most NP sizes considered here. Using these values of D and τ, Equation 5.16 yields a singlet diffusion length of 0.7 nm. This is hence an upper bound on the possible diffusion length of singlet excitons within the NP systems studied here, which corresponds to less than one intermolecular separation between TIPS-Pn molecules.

Triplet Exciton Diffusion

The triplet exciton diffusion coefficient in amorphous TIPS-Pn films has been estimated from nanosecond TA measurements to be in the range of $1.33\text{–}10 \times 10^{-7}\,cm^2\,s^{-1}$.[110] Using these possible diffusion coefficients, Equation 5.16 yields possible triplet exciton diffusion lengths in the range of 0.21–0.57 Å for amorphous TIPS-Pn over the $\tau = 3.2\,ns$ window accessible experimentally here. Again, these exciton diffusion lengths are significantly less than one intermolecular separation within TIPS-Pn.

Kinetic Fits to all Nanoparticle Sizes

Table 5.4 lists best-fit parameter values for the kinetic model described by Figure 5.6 and Equation 5.5 of the main text to exciton concentrations for all NP sizes. Figure 5.18 shows fits of this kinetic model to concentrations extracted using a ^{1}(TT) basis spectrum determined with $p = 0.1$. Figures 5.19 and 5.20 then show fits to exciton concentrations extracted using basis spectra determined with $p = 0$ and $p = 0.25$.

Table 5.4: Best-fit parameters of the kinetic model described in Figure 5.6. [a,b]

d_{NP} (nm)	f_{NR}	$k_{SF,A}$ (ps^{-1})	$k_{SF,B}$ (ps^{-1})	k_{pair} (10^{-3} ps^{-1})	k_T (10^{-4} ps^{-1})
33	0.33±0.01	0.016±0.002	0.051±0.006	3.8±0.5	1.7±0.2
45	0.20±0.02	0.08±0.01	0.20±0.02	2.64±0.06	0.9±0.3
63	0.10±0.06	0.26±0.03	0.5±0.1	2.3±0.1	0.4±0.1
81	0.02±0.02	0.23±0.04	0.55±0.08	1.8±0.1	0.7±0.2

[a] k_{sep} and k_{NR} fit to constant values across all samples of $20.0 \pm 0.5\,ps^{-1}$ and $0.17 \pm 0.03\,ps^{-1}$, respectively.

[b] Values are averages for fits at $p = 0$ and $p = 0.25$. Uncertainties represent the range of fit values between $p = 0$ and $p = 0.25$.

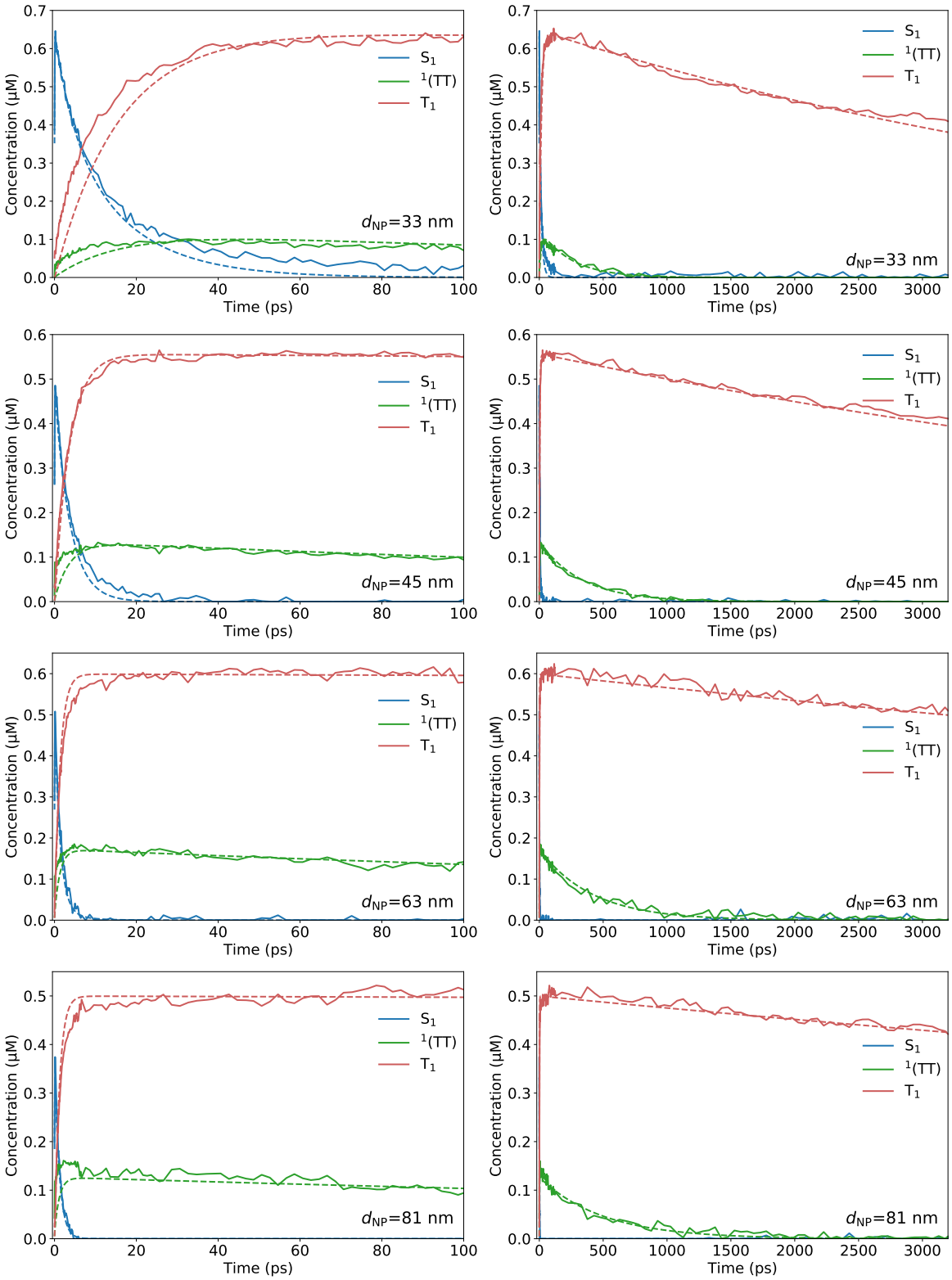

Figure 5.18: Fits of the kinetic model described in Figure 5.6 (dashed lines) to spectrally extracted exciton concentrations (solid lines) for all NP sizes considered here, (left) over the initial 100 ps after excitation and (right) over the entire 3.2-ns TA time window. Concentrations were extracted from spectral deconvolution using a ^{1}(TT) basis spectrum determined with $p = 0.1$.

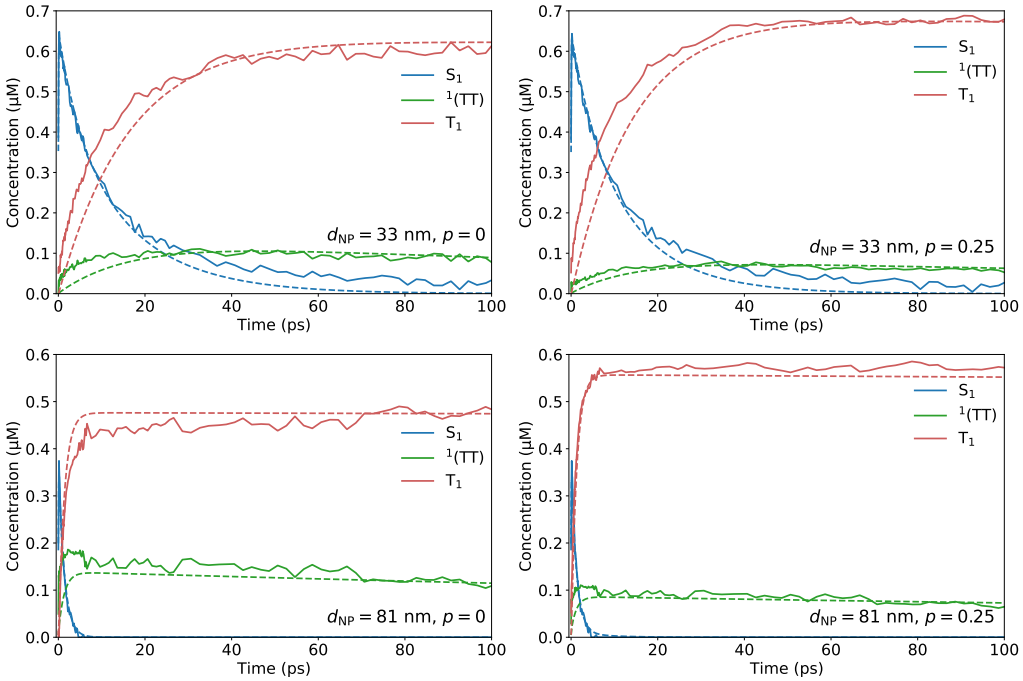

Figure 5.19: Fits of the kinetic model described in Figure 5.6 (dashed lines) to spectrally extracted exciton concentrations (solid lines) for the 33-nm and 81-nm NP samples over the first 100 ps after excitation, using ^{1}(TT) basis spectra extracted using (left) $p = 0$ and (right) $p = 0.25$.

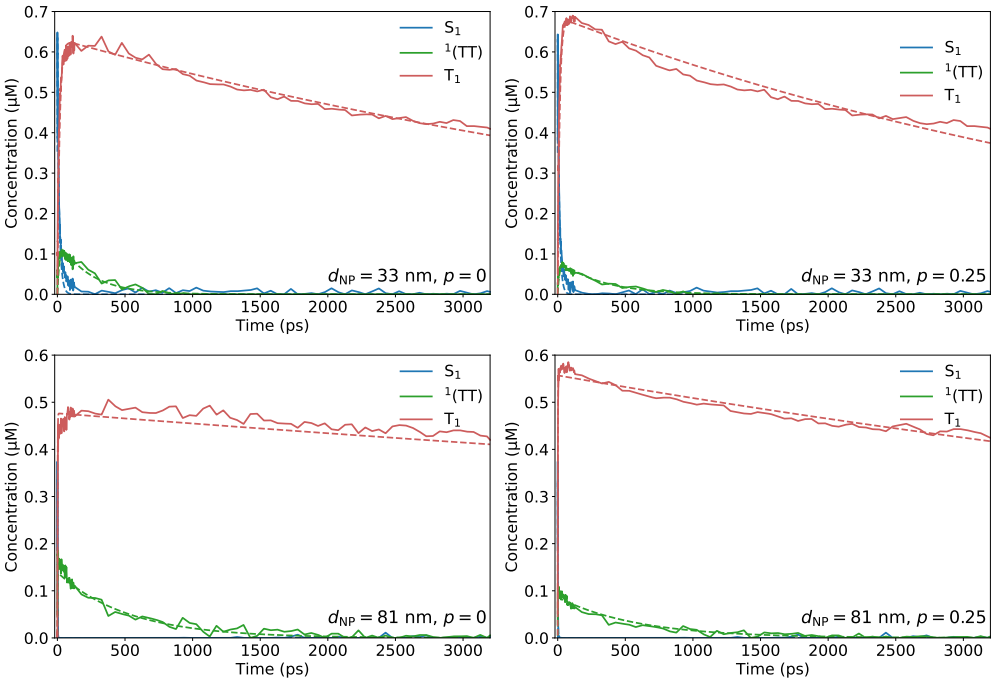

Figure 5.20: Fits of the kinetic model described in Figure 5.6 (dashed lines) to spectrally extracted exciton concentrations (solid lines) for the 33-nm and 81-nm NP samples over the entire 3.2-ns TA time window, using ^{1}(TT) basis spectra extracted using (left) $p = 0$ and (right) $p = 0.25$.

Excitation Density- and Surface Charge Density-Dependent Transient Absorption Experiments

Excitation Density-Dependent Experiments

As shown in Figure 5.21, the decay kinetics of both the singlet and triplet/triplet-pair ESA signals (at 450 nm and 507 nm, respectively) are invariant upon changing excitation density. While this is shown only for the 33-nm NPs here, all NP sizes exhibited kinetics that were similarly independent of excitation density. This observation therefore rules out bimolecular exciton-exciton annihilation pathways as significant contributors to these decays, as bimolecular processes are second-order with respect to exciton concentration, and would therefore be expected to occur more quickly upon increasing pump fluence and hence exciton concentration.

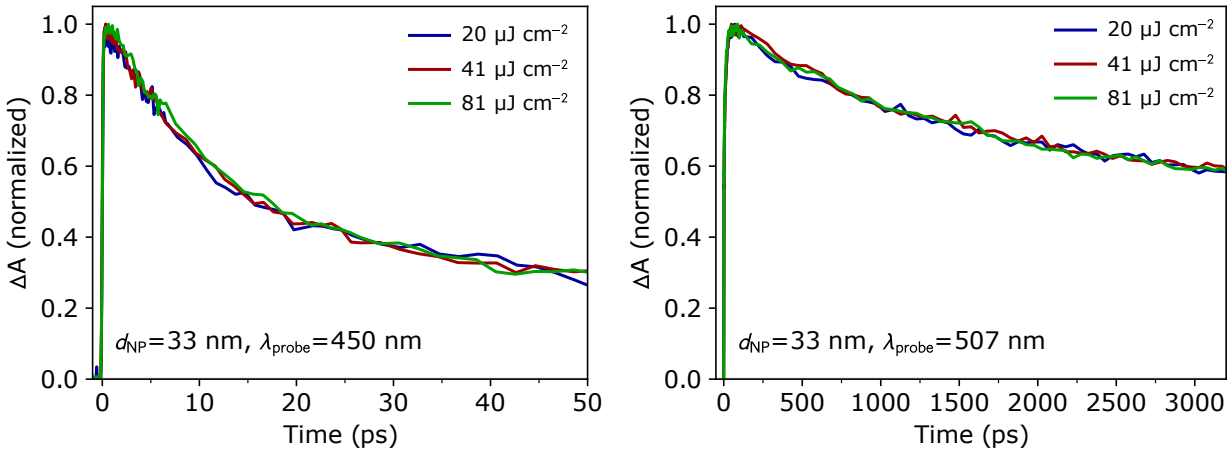

Figure 5.21: Normalized kinetic traces of the (left) S_1 ESA at 450 nm and (right) $T_1/^1(TT)$ ESA at 507 nm for 33-nm amorphous TIPS-Pn NPs, at various excitation densities.

Surface Charge Density-Dependent Experiments

To assess whether interactions with charges at the NP surface influence the exciton dynamics observed here, TA experiments were performed on NPs with differing surface charge densities. Two fractions of 33-nm diameter NPs were made up to a constant ionic strength of 10 µM with NaCl/NaOH solution, with the relative proportion of each salt varied. This NP size was chosen as it has the highest surface area:volume ratio of all NP sizes studied here, and so would likely be the most sensitive to variations in surface charge density. As shown in Table 5.5, addition of NaOH solution to a concentration of only 1 µM resulted in a 3× increase in the zeta potential (ζ) magnitude. As this occurs at a constant ionic strength, this change in ζ must therefore correspond to a change in the surface charge density of the NPs. However, as shown in Figure 5.22, this change

Table 5.5: Zeta potentials of 33-nm NPs with added NaOH/NaCl solution.

Ionic Strength (M)	c_{NaCl} (M)	c_{NaOH} (M)	ζ (mV)
1×10^{-5}	1×10^{-5}	0	-17.5 ± 0.1
1×10^{-5}	9×10^{-6}	1×10^{-6}	-55 ± 7

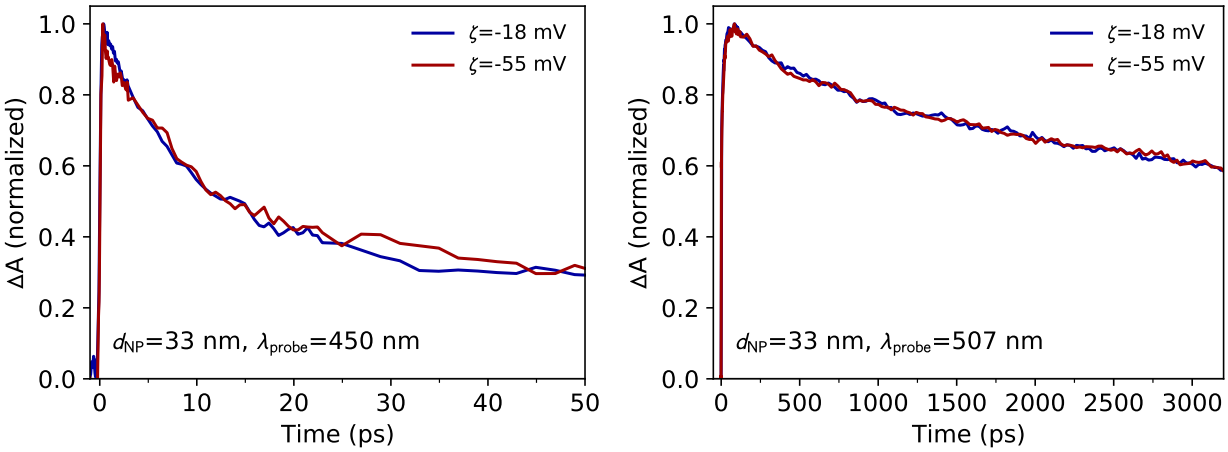

Figure 5.22: Normalized kinetic traces of the (left) S_1 ESA at 450 nm and (right) $T_1/{}^1(TT)$ ESA at 507 nm for 33-nm NPs with differing zeta potentials.

in NP zeta potential results in negligible changes to the decay kinetics of both singlet and triplet excitons in the 33 nm NPs. Therefore, it is unlikely that singlet–charge or triplet–charge annihilation processes contribute significantly to the size-dependent exciton dynamics observed here.

Kinetic Fitting Without Non-Radiative Singlet Decay

As the additional non-radiative decay pathway from the S_1 state discussed in the main text has not previously been identified in amorphous TIPS-Pn, we attempted to fit the experimental data with an alternative kinetic model (described by Figure 5.23) in which no such non-radiative singlet decay can occur. Only one population of singlet excitons is used in this model, for which SF is the only deactivation pathway. All other aspects of this model are identical to that described by Figure 5.6 and Equation 5.5 in the main text. This alternative model is described by following set of coupled differential equations:

$$\begin{aligned}
\frac{\mathrm{d}[S_1]}{\mathrm{d}t} &= -(k_{SF,A} + k_{SF,B})[S_1];\\
\frac{\mathrm{d}[{}^1(TT)_A]}{\mathrm{d}t} &= k_{SF,A}[S_1] - k_{pair}[{}^1(TT)_A];\\
\frac{\mathrm{d}[{}^1(TT)_B]}{\mathrm{d}t} &= k_{SF,B}[S_1] - k_{sep}[{}^1(TT)_B];\\
\frac{\mathrm{d}[T_1]}{\mathrm{d}t} &= 2k_{sep}[{}^1(TT)_B] - k_T[T_1].
\end{aligned} \tag{5.17}$$

Figure 5.24 shows fits by the model described by Figure 5.23 and Equation 5.17 to the TA data for all NP sizes. A relatively good fit is observed for larger particle sizes, but the quality of this fit decreases significantly at smaller sizes. The model fits a ${}^1(TT)$ population almost 2× higher than from the experimental data in the 33-nm NPs, which then decays much too rapidly. A similar trend is also evident for the 45-nm NPs, but to a lesser extent. This is due to the reduced SF yields at these smaller NP sizes (Table 5.2, main text); $\phi'_{SF} \ll 2$ for these smaller particles, but this kinetic model assumes that every singlet exciton formed undergoes SF. This model hence fits too many ${}^1(TT)$

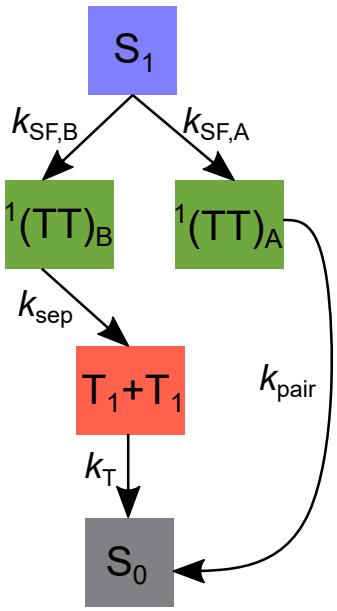

Figure 5.23: Schematic diagram of an alternative kinetic model used to fit the TA data, with SF the only decay pathway for singlet excitons.

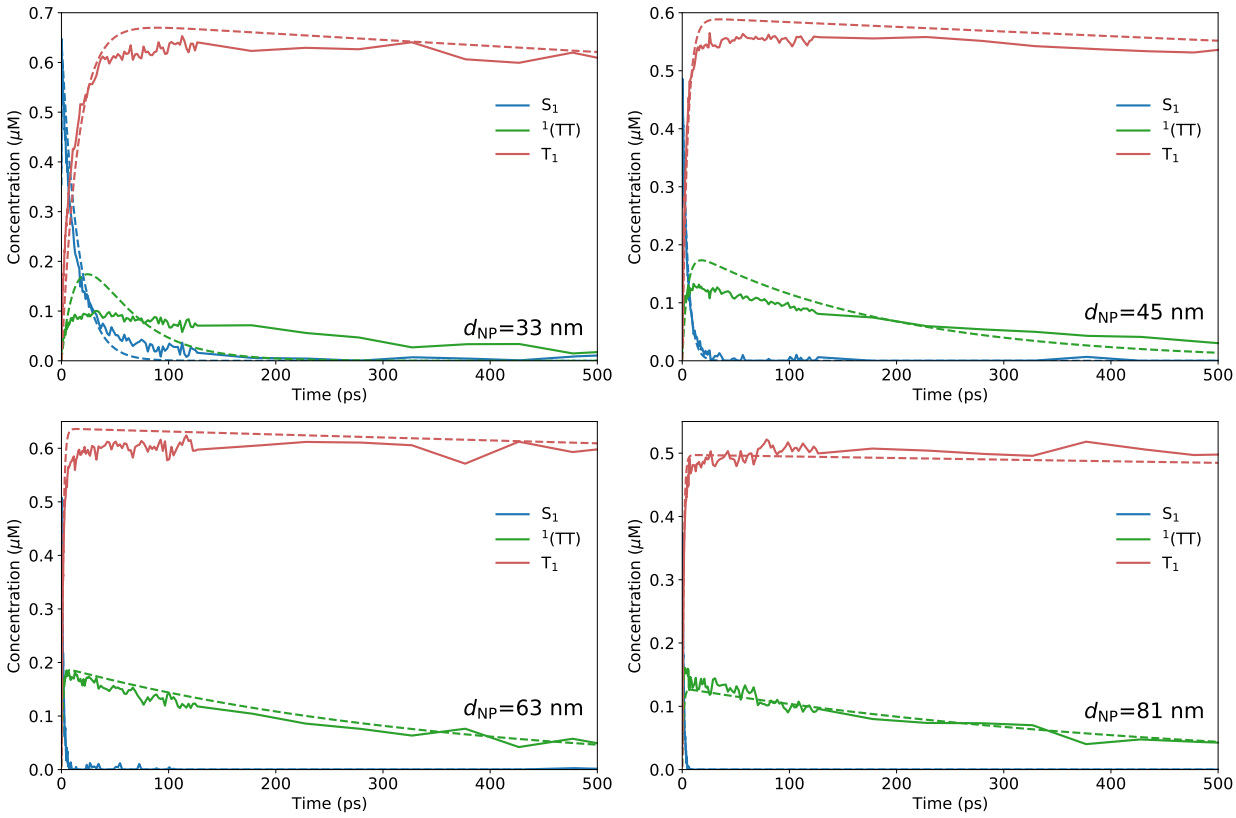

Figure 5.24: Fits of the kinetic model described in Figure 5.23 (dashed lines) to spectrally extracted exciton concentrations (solid lines) for all NP sizes considered here, over the initial 500 ps after excitation. Concentrations were extracted from spectral deconvolution using a ^{1}(TT) basis spectrum determined with $p = 0.1$.

and T_1 excitons for these smaller NPs, and then artificially accelerates ^{1}(TT) decay in an attempt to correct for this. Therefore, the inclusion of non-radiative singlet exciton decay in the kinetic model used in the main text is vital to accurately describing ^{1}(TT) kinetics in the smaller NPs.

Kinetic Fitting Without Non-Radiative Singlet Decay

The fraction of singlet excitons undergoing non-radiative decay fit by the kinetic model used in this work (f_{NR}) scales linearly with inverse NP diameter (Figure 5.25), suggesting a dependence upon the NP surface area:volume ratio (Equation 5.19 below). Therefore, we considered the possibility that this non-radiative S_1 decay occurs only within a layer of finite depth a at the NP surface. If a fraction χ of excitons in this surface layer undergo non-radiative decay, and if singlet excitons are initially homogeneously distributed within a spherical NP, this results in a model of the form

$$f_{NR} = \chi \frac{V_{surf}}{V_{NP}} = \chi \left(1 - \left(\frac{d_{NP} - 2a}{d_{NP}}\right)^3\right) = \chi \left(1 - \left(1 - \frac{2a}{d_{NP}}\right)^3\right), \tag{5.18}$$

where V_{surf} and V_{NP} are the volumes of the surface layer and of the entire NP, respectively. In the limiting case of $a \ll d_{NP}$, Equation 5.18 may be further simplified, expanding in a Taylor series up to first order in $\frac{d_{NP}}{a}$, to

$$f_{NR} \approx \frac{6\chi a}{d_{NP}} \equiv \frac{6a'}{d_{NP}}, \tag{5.19}$$

where a' is an effective surface thickness defined by

$$a' \equiv \chi a. \tag{5.20}$$

In the limit of $a \ll d_{NP}$ the thickness of this surface layer becomes negligible, and V_{surf} reduces to the NP surface area. Therefore, Equation 5.19 is proportional to the NP surface area:volume ratio, yielding the ${d_{NP}}^{-1}$ scaling of this ratio described above.

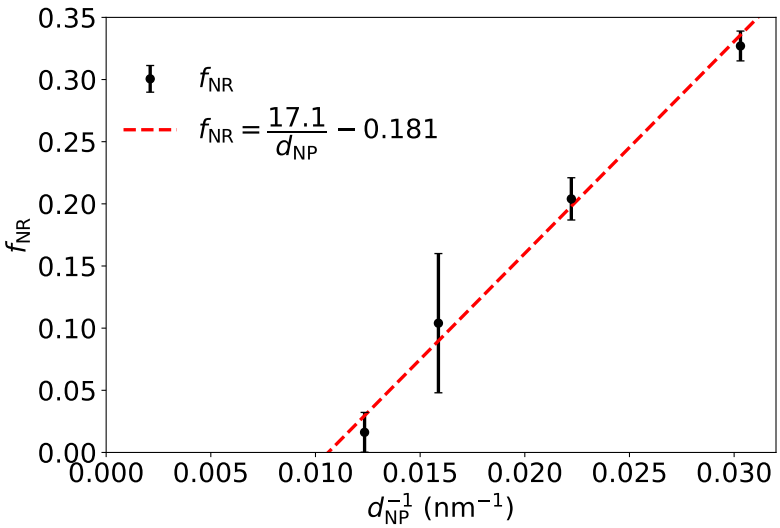

Figure 5.25: Fraction of singlet excitons undergoing non-radiative decay fit by the kinetic model (f_{NR}, black dataset) as a function of inverse NP diameter. The red line shows a linear best-fit to this data.

Figure 5.26 shows fits of Equation 5.19 to f_{NR} determined from kinetic modelling. This surface model fits poorly when using a constant value of a' across all NP sizes. However, if a' is allowed to vary with NP size, a significantly improved fit to the data is observed. Best-fit values of a' for each NP size are shown in Table 5.6, with a clear trend of a' decreasing at larger particle sizes. Due to the coupled nature of a and χ in Equation 5.20, it cannot be determined from this modelling if the scaling of a' arises from changes in a, χ or both of these parameters with NP size. The range of NP sizes studies is also not sufficiently wide to enable sensitive independent fits of a and χ using Equation 5.18. However, if it assumed that a cannot be less than the width of one TIPS-Pn molecule (1.0–1.5 nm, depending upon molecular orientation), then the very small value of $a' = 0.22$ nm fit to the 81-nm NPs must correspond to $\chi \lesssim 0.2$. If χ remained constant across all NP sizes then $a' = 1.80$ nm for the 33-nm NPs would correspond to $a \approx 10$ nm, resulting in this surface layer constituting almost 95% of the 33-nm NPs by volume. This is unlikely, and so it can be inferred that the scaling a' with d_{NP} observed here is at least in part due to χ decreasing at larger particle sizes. This could be explained by increased curvature at the surface of smaller NPs constraining the intermolecular packing of a greater number of molecules (relative to larger NPs), increasing the proportion of surface molecules with morphologies favorable for this non-radiative decay.

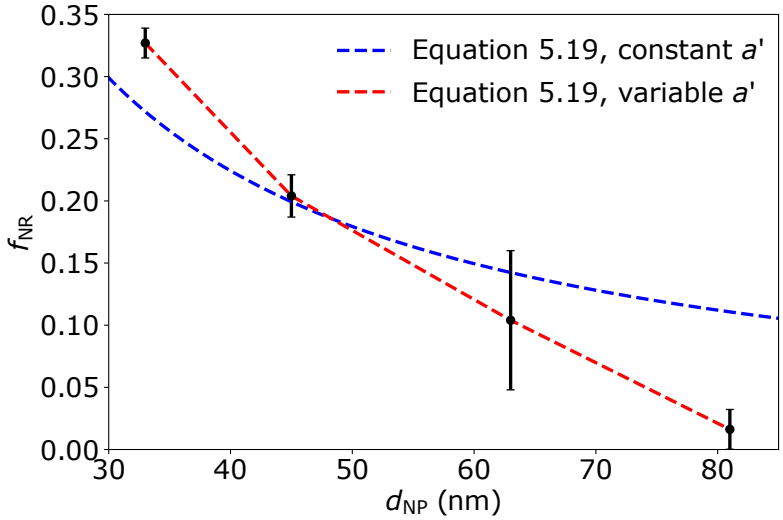

Figure 5.26: Fits of Equation 5.19 to f_{NR} fit from the kinetic model described in Figure 5.6, using a constant value of a' across all NP sizes (blue curve; $a' = 1.5 \pm 0.6$ nm) and allowing a' to fit separately for each NP size (red curve; best-fit values shown in Table 5.6).

Table 5.6: Best-fit values of a' from Equation 5.19 for all NP sizes.

d_{NP} (nm)	a' (nm)
33	1.80
45	1.53
63	1.09
81	0.22

CHAPTER 6
Confinement Effects Upon Triplet Exciton Dynamics in Crystalline TIPS-Pentacene Nanoparticles

Statement of Authorship

Title of Paper	Confinement Effects Upon Triplet Exciton Dynamics in Crystalline TIPS-Pentacene Nanoparticles
Publication Status	Unpublished and Unsubmitted Work Written in Manuscript Style
Publication Details	Hudson, R. J.; Huang, D. M.; Kee, T. W. **2021**, Manuscript in Preparation

Principal Author

Principal Author	R.J. Hudson		
Contribution to the Paper	Experimental work, development of kinetic Monte Carlo model, data analysis, construction of figures, writing of manuscript.		
Overall Percentage	85%		
Certification	This paper reports on original research I conducted during the period of my Higher Degree by Research candidature and is not subject to any obligations or contractual agreements with a third party that would constrain its inclusion in this thesis. I am the primary author of this paper.		
Signature		Date	25/11/21

Co-Author Contributions

By signing the Statement of Authorship, each author certifies that the stated contributions to the following publication are accurate and that permission is granted for the publication to be included in this thesis.

Co-Author	D.M. Huang		
Contribution to the Paper	Supervision of computational work, assisted with data analysis and writing and editing of manuscript.		
Signature		Date	22/11/21

Co-Author	T.W. Kee		
Contribution to the Paper	Supervision of project, assisted with writing and editing of manuscript, corresponding author.		
Signature		Date	22/11/2021

6.1 Abstract

Nanoparticle (NP) dispersions are a popular and convenient medium for the spectroscopic study of ultrafast exciton dynamics within organic semiconductor materials. However, size-dependent morphology changes and exciton kinetics have been reported for many organic semiconducting NPs, limiting their applicability as model systems for bulk materials. In this study, we use time-resolved spectroscopy and kinetic Monte Carlo simulations to assess the potential for size-dependent exciton behaviour in NPs of crystalline 6,13-(triisopropylsilylethynyl)pentacene (TIPS-Pn), a prototypical material for singlet fission. Femtosecond transient absorption experiments show negligible size-dependence in the kinetics of singlet fission and triplet–triplet annihilation (TTA) over a range of particle sizes, suggesting that minimal morphological changes occur with NP size. The simulations predict that triplet decay dominated by geminate recombination exhibits size-dependent kinetics, but decay becomes size-independent for sufficiently large domains, in which decay is dominated by bimolecular TTA. A stochastic model is presented to quantify the timescale of TTA and the NP size at which size-dependent behavior becomes significant, with good agreement observed between the theory and simulation. However, this model indicates that such size-dependent triplet dynamics can only occur at either extremely small NP sizes ($< 30\,\mathrm{nm}$) or low excitation densities ($< 8\times10^{-4}\,\mathrm{nm}^{-3}$), which are not achieved under standard experimental conditions. This work therefore demonstrates that NPs $\gtrsim 30\,\mathrm{nm}$ in diameter are excellent model systems for bulk crystalline TIPS-Pn, as negligible particle size effects will be observable under most experimental conditions. The theory developed here also provides a framework for estimating the range of particle sizes for which exciton confinement effects will be relevant in other materials.

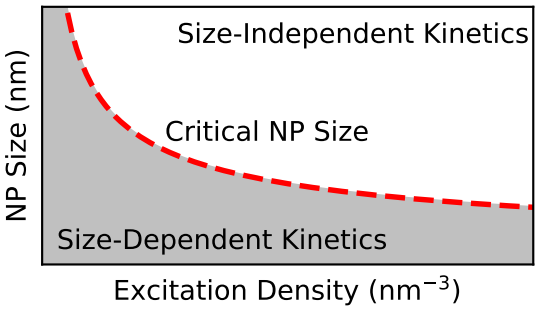

6.2 Introduction

The photophysical process of singlet fission (SF) converts one high energy singlet exciton into two lower energy triplet excitons via a spin-correlated triplet-pair intermediate, through the process[19,20,37]

$$S_1 + S_0 \rightarrow {}^1(TT) \rightarrow T_1 + T_1. \tag{6.1}$$

Research interest in SF has risen substantially over the last decade, as it has been identified as a potential mechanism for improving the performance of single-junction photovoltaic (PV) devices beyond their theoretical efficiency limit.[18,22,23] However, effective improvement of PV device efficiencies by SF-sensitization requires a 200% triplet yield (two triplets formed from every singlet exciton) and quantitative transfer of excitation energy into a harvesting layer,[25] which has so far proved elusive in practical implementations.[27,28,30,32] Therefore, significant research effort is currently focused upon developing a deeper understanding of the fundamental processes associated with triplet formation, separation and dissociation in SF-capable materials, such that the harvestable triplet yield in SF-sensitized PV devices may be improved.[60,259–263]

Pentacene and its derivatives are one of the most widely-studied classes of SF chromophores, as SF in pentacene is slightly exoergic and so occurs very rapidly and with relatively high triplet yield.[19,116] In particular, 6,13-(triisopropylsilylethynyl)pentacene (TIPS-Pn) has attracted significant interest, as its bulky TIPS substituents constrain its intermolecular packing to an extended, two-dimensional pi-stacked motif thought to be highly favorable for SF.[125,264] Crystalline TIPS-Pn has been shown to undergo rapid (sub-picosecond) SF with an estimated 200% triplet yield,[47,119] and possesses characteristic singlet and triplet signals that are easily resolvable through experimental techniques such as transient absorption (TA) or spin resonance spectroscopies.[102,129,131] Therefore, crystalline TIPS-Pn is widely regarded as a model system for intermolecular SF, and so is commonly used as a benchmark in the characterization of new SF chromophores[130,187,265] or as a model to assess the effect of modulating parameters such as crystal packing distance or polymorphism upon SF kinetics.[109,127,128]

Recently, several studies have used aqueous dispersions of nanoparticles (NPs) to spectroscopically quantify exciton dynamics within crystalline TIPS-Pn.[1,2,119,133] Colloidal NP dispersions are convenient for spectroscopic characterization of SF chromophores, as they allow for examination of solid-state excitonic processes while avoiding the effects of photo-bleaching, localized heating, sample opacity and other issues associated with solid films.[35,144] However, small NPs of organic semiconducting materials may exhibit size-dependent photophysical properties that differ markedly from the bulk material.[41,145] In our previous study, we demonstrated that the SF yield and the kinetics of both singlet and triplet excitons in amorphous TIPS-Pn NPs varied dramatically with particle size, which we ascribed to small NP sizes constraining the intermolecular packing in these systems.[3] Additionally, recent reports have noted that size-dependent exciton–exciton annihilation (EEA) kinetics can arise from confinement of highly mobile excitons within small domains.[266,267] Therefore, crystalline TIPS-Pn NPs have potential to exhibit size-dependent exciton kinetics, through either morphological changes with NP size or exciton confinement influencing triplet–triplet annihilation (TTA) kinetics. However, the extent to which either of these factors influence exciton behaviour in small NPs of crystalline TIPS-Pn has not yet been established.

This work presents a combined experimental and computational investigation into the influence of particle size upon exciton dynamics within NPs of crystalline TIPS-Pn. Time-resolved spectroscopic measurements show that the kinetics of SF and TTA are identical for NP sizes ranging from 38 nm to 62 nm, suggesting that these particle sizes possess largely equivalent intermolecular packings. Kinetic Monte Carlo (KMC) simulations of triplet exciton dynamics indicate that geminate recombination of triplet exciton pairs exhibits kinetics that are strongly size-dependent due to confinement of the exciton pair within small crystalline domains, with accelerated triplet recombination occurring at smaller particle sizes. However, this size-dependence disappears at large particle sizes, where decay is dominated by bimolecular TTA and excitons are much more likely to encounter one another than a domain boundary. The crossover from size-independent to size-dependent triplet decay kinetics occurs only at either very low excitation densities or small particle sizes, neither of which are readily accessible experimentally. Size-dependent exciton dynamics are therefore highly unlikely to be experimentally observable in crystalline TIPS-Pn NPs, and so this work highlights that NP dispersions are reasonable model systems for studying excitonic processes within bulk crystalline TIPS-Pn.

6.3 Experimental Methods

Materials

TIPS-Pn was used as-purchased from Ossila. Milli-Q purity water was purified by an 18.2-MΩ cm Millipak Milli-Q IQ-7000 fitted with a 0.22-µm filter. Poly(vinyl alcohol) (PVA; Merck, average molecular weight 46 kg/mol) was sourced as a solid powder, and dissolved to a stock concentration of 10 mg/mL by heating at 90 °C in water for 1 hour. HPLC-grade tetrahydrofuran (THF; RCI Labscan) was freshly distilled before use.

Nanoparticle Preparation

Aqueous dispersions of TIPS-Pn NPs were prepared by re-precipitation from THF into water, a procedure well established as yielding relatively monodisperse NP suspensions with good colloidal stability.[1,35,72,134] 3 mL of TIPS-Pn/THF solution was rapidly injected into 15 mL of water upon vigorous stirring (using a 0.55-µm diameter syringe needle), and stirred for a further 5 minutes. This process was repeated to prepare n independent fractions, which were then combined and concentrated under reduced pressure to a final TIPS-Pn concentration of 100 ppm. Resulting NP suspensions were filtered using a 0.2-µm syringe filter (Sartorius Minisart NML). Variations in NP size were achieved by adjustment of the injection stock concentration ([TIPS-Pn]), and Table 6.1 lists the preparation conditions and resulting sizes of all NP samples. Re-precipitation from THF solution into water is well known to prepare TIPS-Pn NPs with amorphous morphologies,[72,134] but recent work has demonstrated that reorganization to a crystalline packing can be facilitated by a periodic interaction with PVA.[1,119] Therefore, crystallinity in these NPs was induced by addition of PVA solution to a final concentration of 50 ppm, and confirmed by steady-state spectrophotometric characterization (see below).

Steady-State Nanoparticle Characterization

Particle sizes were quantified here by dynamic light scattering (DLS), using a Malvern Zetasizer Nano ZSP with a 633-nm laser source and a backscattering angle of 173 ° (size distributions are shown in the Supporting Information). NP samples throughout this work are hereafter referred to by their Z-average diameters as measured by DLS (d_{NP}), shown in the final column of Table 6.1. Steady-state absorption spectra of NP

Table 6.1: Injection stock concentrations ([TIPS-Pn]) for the preparation of different-sized TIPS-Pn NPs by re-precipitation of THF solution into water, with NP Z-average diameters (d_{NP}) as measured by DLS.

[TIPS-Pn] (ppm)	Fractions (n)	d_{NP} (nm)[a]
20	5	37.8 ± 0.3
50	2	50.8 ± 0.7
100	1	61.6 ± 0.1

[a] Uncertainties are twice the standard error in the mean calculated from triplicate measurements of each sample.

samples were collected using a Cary Varian 1E UV-visible spectrophotometer in a 1-cm path length quartz cuvette (Starna Cells 21-Q-2).

Time-Resolved Spectroscopic Characterization

Time-resolved spectroscopic measurements were made on a transient absorption (TA) spectrometer (Ultrafast Systems, Helios). The primary light source was the output of a Ti:sapphire regenerative amplifier (Spectra Physics, Spitfire Pro XP 100F), producing 800-nm, 100-fs laser pulses at a 1-kHz repetition rate. 590-nm pump pulses were generated using an optical parametric amplifier (Light Conversion, TOPAS-C) from the second harmonic of the signal. The pump beam had a spot size of 561 µm at the sample position, and pump fluences ranged from $40\,\mu J\,cm^{-2}$ to $400\,\mu J\,cm^{-2}$. White-light probe pulses with a spectral range of 450–750 nm were generated by focusing the 800-nm amplifier output onto a 3.2-mm sapphire crystal, with a spot size of 130 µm at the sample position. Pump and probe were polarized at the magic angle of 54.7° relative to one another, in order to minimize polarization biases in the measurements. NP dispersions were held in 2-mm path length quartz cuvettes (Starna Cells 21-Q-2) and stirred continuously during spectroscopic measurements. Negligible photo-degradation or photo-bleaching of NP samples was observed during the course of these experiments.

6.4 Computational Methods

Crystalline Nanoparticle Model

TTA simulations in this work used NP models constructed from the TIPS-Pn crystal packing reported by Anthony and co-workers,[125] with the position of each molecule represented by its center-of-mass. This crystal packing (shown in Figure 6.1) consisted of a two-dimensional slip-stacked packing motif, with layers of these slip-stacked molecules separated through insulating TIPS groups. The crystallographic *a*-axis corresponded to the direction of closest molecular slip-stacking, and the *c*-axis to the direction of separation through TIPS groups. The *b*-axis did not correspond to a nearest-neighbour crystalline separation, and so here we instead considered the direction of next-nearest-neighbour slip-stacking, denoting it the "*b*-packing direction" to avoid confusion with the crystallographic *b*-axis. As will be discussed below, triplet exciton hopping in the *c*-direction is known to be effectively negligible on the timescales considered here,[2] and as such was ignored. The NP models used here therefore consisted of a series of independent *ab*-planes, between which excitons could not transfer or interact. Excitons within each NP *ab*-plane hence evolved in time entirely independently of those in other planes, and so by symmetry only one-half of the NP required explicit modelling. Two independent simulations of the same NP hemisphere were equivalent to one simulation of the full NP, provided that no *ab*-plane passed through the exact center of the NP. To ensure that this condition was met, the NP center was selected as lying halfway between two molecules along the *c*-axis. A hemisphere of radius r_{NP} was then drawn from this origin, with the base of the hemisphere perpendicular to the *c*-axis. All molecules with centers-of-mass lying inside this hemisphere were cleaved from the bulk crystal, to yield a half-nanoparticle of crystalline TIPS-Pn. This construction of a NP model from the TIPS-Pn crystal structure is illustrated in Figure 6.1.

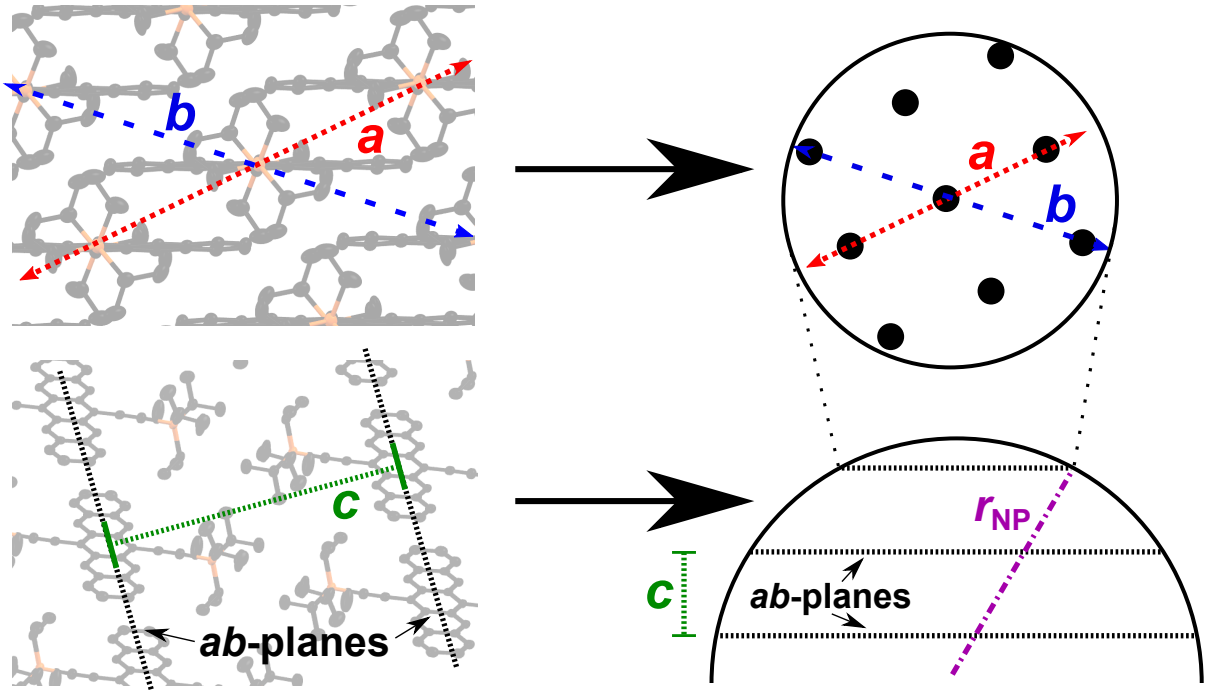

Figure 6.1: Illustration of how the TIPS-Pn crystal structure is mapped onto the crystalline NP model used for kinetic Monte Carlo simulations of triplet–triplet annihilation. a, b and c denote the crystal packing directions of TIPS-Pn (taken from ref. 125), and r_{NP} indicates the NP radius.

Exciton Hopping and Annihilation

In our recent study,[2] rate coefficients of triplet exciton hopping in each crystallographic packing direction of TIPS-Pn were calculated using constrained density functional theory (CDFT) and Marcus theory. This work demonstrated that triplet hopping in the *ab*-plane occurred on a picosecond timescale, but triplet transfer along the *c*-axis was over four orders of magnitude slower than the natural triplet lifetime within TIPS-Pn. Therefore, in the present model we neglected triplet hopping along the *c*-axis, and considered only two-dimensional (2D) mobility within the *ab*-plane. Rate coefficients for hopping in the *a*- and *b*-directions were taken from our previous study, and are listed in Table 6.2.

According to conventional spin-statistical theory, two encountering triplet excitons may form any one of nine (TT) encounter states of singlet, triplet or quintet multiplicity.[65] TTA may then occur through subsequent relaxation of ^{3}(TT) or ^{1}(TT) encounter states (removing one or both triplets, respectively), while ^{5}(TT) states generally dissociate back into free triplet excitons due to very high energies of localized quintet pair states, as indicated in the reaction scheme[93]

$$\mathrm{T_1 + T_1} \rightarrow \begin{cases} {}^1(\mathrm{TT}) \rightarrow \mathrm{S_1 + S_0} \\ {}^3(\mathrm{TT}) \rightarrow \mathrm{T}_n + \mathrm{S_0} \rightarrow \mathrm{T_1 + S_0} \\ {}^5(\mathrm{TT}) \rightarrow \mathrm{T_1 + T_1}. \end{cases} \tag{6.2}$$

However, annihilation through the triplet channel is only possible if a high-lying triplet state T_n is energetically accessible from ^{3}(TT). The $\mathrm{T_1 + T_1} \rightarrow \mathrm{T_2 + S_0}$ process is endoergic by almost 0.4 eV in crystalline TIPS-Pn, which is effectively inaccessible under ambient conditions.[2] Therefore, the singlet channel is expected to dominate TTA in

crystalline TIPS-Pn, and so in the present model we considered TTA only from pair states with singlet character.

The effective annihilation rate coefficient through the singlet channel from pair state l is calculated as

$$k_{\text{ann}} = k_2 |C_{\text{S}}^l|^2, \tag{6.3}$$

where k_2 is the unimolecular rate coefficient of crossing from the triplet manifold to the singlet state and C_{S}^l is the projection of the pure singlet state onto pair state l.[94] $|C_{\text{S}}^l|^2$ for each state was calculated here by explicit diagonalization of the spin Hamiltonian matrix, using the method from ref. 95 (details of these calculations are shown in the Supporting Information). For crystalline TIPS-Pn dimer pairs along both the a- and b-stacking directions, only 3 encounter states exhibited significant singlet character. k_2 has not been previously reported for crystalline TIPS-Pn, but a recent experimental study determined a SF rate coefficient of $10\,\text{ps}^{-1}$, facilitated by coherent mixing of the S_1 and ^{1}(TT) states.[47] Due to this resonance, it is reasonable to assume that the reverse process may occur on a similar timescale, and so we estimated k_2 to be $10\,\text{ps}^{-1}$. Therefore, Equation 6.3 yields $k_{\text{ann}} = 3.3$–$3.6\,\text{ps}^{-1}$ for the three pair states with significant singlet character. This is an order of magnitude larger than the fastest rate coefficient of triplet hopping (Table 6.2), indicating that annihilation is effectively instantaneous compared with exciton hopping within crystalline TIPS-Pn. This is unsurprising, as a number of experimental studies of crystalline acenes have reported TTA to be diffusion-limited.[2,63,110,117]

In the present model, an encounter of two triplet excitons formed one of the nine possible (TT) states, chosen at random. Due to the significant spatial localization of triplet excitons within TIPS-Pn,[102] triplet excitons were considered to "encounter" one another if one exciton attempted to hop to a site already occupied by the other. If the formed pair state was one of the three states with singlet character, mutual annihilation of both excitons occurred instantaneously. If a pair state with no singlet character was formed, the encounter state dissociated back into separate triplet excitons on adjacent sites.

Table 6.2: Summary of parameters used for modelling TTA in crystalline TIPS-Pn NPs.

Parameter	Symbol	Value
a-axis molecular packing [a]	l_{a}	7.565 Å
b-direction molecular packing [a]	l_{b}	10.21 Å
c-axis molecular packing [a]	l_{c}	16.84 Å
Triplet hopping rate coefficient along a-axis [b]	k_a	$3.70 \times 10^{-1}\,\text{ps}^{-1}$
Triplet hopping rate coefficient along b-direction [b]	k_b	$7.94 \times 10^{-3}\,\text{ps}^{-1}$
Natural triplet exciton decay rate coefficient [c]	k_1	$4.76 \times 10^{-7}\,\text{ps}^{-1}$

[a] Taken from ref. 125
[b] Taken from ref. 2
[c] Taken from ref. 110

Triplet–Triplet Annihilation Simulations

For a TTA simulation with a specified NP radius (r_{NP}) and excitation density (ρ_{ex}), the expected number of initial excitations per simulation was given by

$$\langle n_{\mathrm{ex}} \rangle = \rho_{\mathrm{ex}} V_{\mathrm{NP}} = \frac{2}{3} \pi \rho_{\mathrm{ex}} {r_{\mathrm{NP}}}^3, \tag{6.4}$$

as the NP volume being explicitly modelled was one hemisphere. For each simulation trajectory, the number of singlet excitons n_{ex} was drawn from a Poisson distribution centered at $\langle n_{\mathrm{ex}} \rangle$. These excitons were then randomly assigned to sites within the NP model, to emulate a pulsed laser excitation. SF in crystalline TIPS-Pn is known to occur on a sub-picosecond timescale and with quantitative yield,[47,119,129,130] and so every singlet exciton in this model was converted into a pair of triplet excitons. Recent experimental work has indicated that separation of the correlated ^{1}(TT) pair state in crystalline TIPS-Pn occurs by hopping of one triplet exciton away from the SF site.[59] Therefore, every geminate exciton pair in the present model was placed at an initial next-nearest-neighbour separation, with one triplet exciton residing at the initially chosen singlet site and the other randomly placed on a next-nearest-neighbour site in the *ab*-plane. Other experimental studies have suggested that the resulting pair of triplets initially retain some level of spin correlation before dephasing to independent triplets.[62,64,142] However, the timescale over which triplet decorrelation occurs is not well characterized, and so this model did not attempt to emulate this initial spin correlation.

After placing all triplet excitons, the system was then allowed to evolve in time as per the first reaction method KMC algorithm.[172,175,268] Time intervals Δt_i were calculated for all possible processes for all excitons by

$$\Delta t_i = -\frac{\ln x_i}{k_i}, \tag{6.5}$$

where k_i the rate coefficient of process i and $x_i \in (0, 1]$ is a random uniform variate. Allowed processes included hopping to neighbouring sites in the *ab*-plane within the NP and natural triplet decay with a first-order rate coefficient of $4.76 \times 10^{-7}\,\mathrm{ps}^{-1}$ as measured by Grieco and co-workers.[110] The process with the smallest Δt_i was then chosen and acted upon, with the trajectory time advanced by this value. This was then repeated, with Δt_i recalculated for every allowed process after each step, until either all excitons were removed from the system or the simulation reached a trajectory time of 10 ns. Successive trajectories were undertaken until each simulation reached a cumulative total of 10^4 triplet excitons sampled. In the event of either TTA or intrinsic triplet decay, histogram bins corresponding to the time at which the decay event occurred were populated. The normalized triplet population over time was then calculated as

$$P_{\mathrm{T}}(t) = \frac{N(t)}{N_{\mathrm{ex}}}, \tag{6.6}$$

where N_{ex} is the total number of triplet excitons sampled during the simulation and $N(t)$ is the number of excitons surviving at time t. To quantify the triplet population decay, $P_{\mathrm{T}}(t)$ was fit by a stretched exponential function of the form

$$P_{\mathrm{T}}(t) = \exp\left[-\left(\frac{t}{\tau}\right)^{\beta}\right], \tag{6.7}$$

for fit parameters τ and β. Examples of these fits are shown in the Supporting Information. The time scale of the decay of $P_{\mathrm{T}}(t)$ can hence be described by the stretched exponential mean relaxation time $\langle\tau\rangle$, defined as

$$\langle\tau\rangle \equiv \frac{\tau}{\beta}\Gamma\left(\frac{1}{\beta}\right), \tag{6.8}$$

where Γ is the gamma function.

6.5 Results and Discussion

6.5.1 Steady-State Spectrophotometric Characterization

Steady-state absorption spectra of all crystalline TIPS-Pn NPs studied here are shown in Figure 6.2. All NP sizes possess very similar spectra, exhibiting a broad progression of visible absorption peaks and lowest energy absorption at 700 nm characteristic of crystalline TIPS-Pn.[129,131,205] We therefore assign these NPs as possessing predominantly crystalline morphologies, agreeing with several previous reports of PVA inducing large-scale crystallinity in TIPS-Pn NPs.[1,2,119,141] A raised baseline is observed at shorter wavelengths upon increasing particle size, attributable to increased Rayleigh scattering from these larger particles. A weak red-shift in the lowest energy absorption peak also occurs with increasing NP size (inset of Figure 6.2), shifting by 1 nm across the particle sizes considered here. The exact vibronic/phononic nature of the absorption peaks in crystalline TIPS-Pn is not currently well understood, and so it is difficult to assign the cause of this minor spectral shift. However, other authors have hypothesized that the position of the lowest energy absorption band in solid-phase polyacene materials is influenced by delocalization of the lowest-energy singlet exciton.[134] The spectral shift observed here could therefore indicate a minor change in the

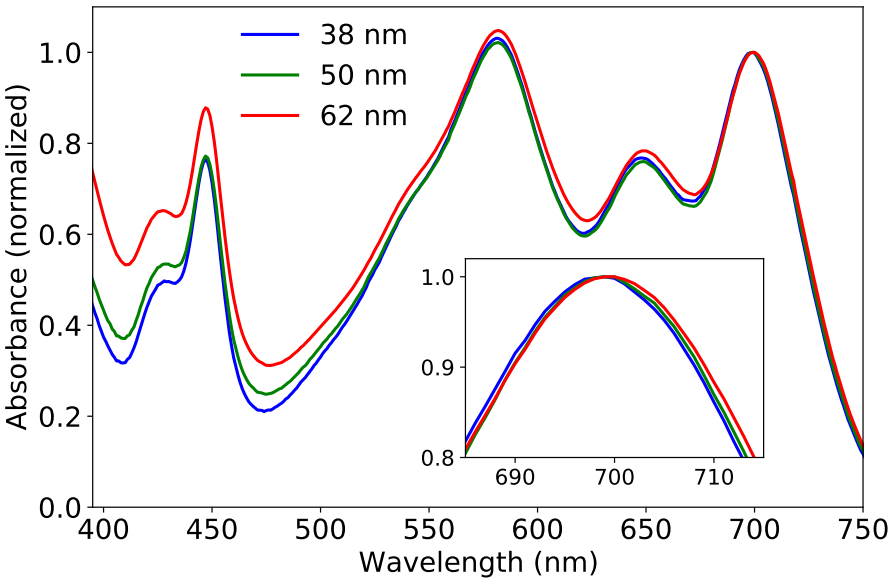

Figure 6.2: Steady-state absorption spectra of crystalline TIPS-Pn NPs of various sizes, normalized to the lowest energy absorption peak around 700 nm. NP samples are labelled by diameter. Inset shows the shift in the lowest-energy absorption peak with NP size.

delocalization length (and hence the local intermolecular packing) with NP size. We recently reported a similar bathochromic shift with increasing diameter for amorphous TIPS-Pn NPs, which was attributed to decreased morphological disorder at larger particle sizes.[3] However, the peak shift observed here for crystalline NPs is much smaller than for the previously reported amorphous NPs, and so any size-dependent changes in the intermolecular packing within these crystalline NPs are likely to be relatively minimal. To assess whether this weak spectral shift corresponded to any changes in exciton behaviour with NP size, we used femtosecond TA spectroscopy to characterize the kinetics of SF and subsequent triplet decay within these crystalline TIPS-Pn NPs.

6.5.2 Time-Resolved Spectrophotometric Characterization

As shown in Figure 6.3a, TA spectra of all NP sizes considered here are nearly indentical. A broad excited-state absorption (ESA) centered at 523 nm is the most dominant spectral feature, with a weaker ESA overlapping ground-state bleach (GSB) features from 550 nm to 750 nm. A subtle restructuring of the 700-nm GSB is evident with increasing NP size, reflecting the weak shift in the corresponding absorption band shown in Figure 6.2. Apart from this GSB shift, however, the TA spectra are effectively identical across all NP sizes. The strong ESA band at 523 nm is well known to arise from a $T_n \leftarrow T_1$ transition within crystalline TIPS-Pn,[2,119,129] and its presence is hence indicative of triplet excitons arising from SF within these NPs. All NP sizes exhibit the same instrument-limited rise in this spectral feature followed by a slow further growth in intensity (Figure 6.3b), corresponding to formation of ^{1}(TT) excitons and subsequent separation to independent triplets, respectively.[142] These kinetic traces are effectively coincident for all NP sizes studied here, indicating that particle size has a minimal effect upon SF dynamics in these NPs. It appears that the origin of the minor steady-state spectral red-shift with size noted above has a negligible effect upon the SF kinetics within these NPs. However, SF in bulk crystalline TIPS-Pn is known to occur on a timescale of 80–100 fs,[47] which is shorter than the 150-fs instrument response function of the TA spectrometer used here, and so small variations in the SF rate with particle size may not be resolvable from these data. Kinetics of the 523-nm triplet ESA over the full 3.2-ns experimental time window are shown in Figure 6.3(c-f), at four different excitation densities. The decay of this feature is accelerated at higher pump fluences, agreeing with previous reports of bimolecular TTA being the predominant triplet decay pathway in crystalline TIPS-Pn.[2,119] At all excitation densities, the kinetics of triplet decay are largely equivalent across all particle sizes studied here. Subtle variations in kinetics between NP sizes may occur at 40 µJ cm^{-2} and 400 µJ cm^{-2}, but these changes lie within the noise level of this data and therefore cannot be confidently assigned.

From the data presented in Figure 6.3, NP size evidently has a negligible effect upon the dynamics of TTA and SF within the range of particle sizes considered here. This result contrasts significantly with our recent study of amorphous TIPS-Pn NPs, in which order-of-magnitude changes in SF and triplet decay kinetics were observed across a range of particle sizes similar to those considered here.[3] This size dependence in amorphous NPs was ascribed to the internal NP morphologies becoming more constrained and disordered at smaller particle sizes. The lack of size-dependent exciton kinetics here hence suggests that such a morphological change with particle size is absent in crystalline TIPS-Pn NPs. This may be a result of the method used to induce NP crystallinity, whereby a spatially periodic interaction with PVA at the NP surface

templates the TIPS-Pn crystal structure.[1] This interaction is likely independent of NP size, and so crystallization with PVA may template equivalent intermolecular packings across a range of particle sizes.

However, different-sized particles with identical morphologies may still exhibit size-dependent exciton dynamics. Recent studies of small crystalline materials have demonstrated that exciton confinement effects can strongly influence the kinetics of EEA when exciton diffusion lengths are similar to or larger than crystal domain sizes.[266,267] We previously estimated triplet exciton diffusion lengths in crystalline TIPS-Pn to be on the order of 100–500 nm (depending on crystallographic orientation),[2] which are considerably larger than the particle sizes studied here or other reports of crystalline TIPS-Pn NPs.[119,133] Exciton confinement effects may therefore be relevant for TTA

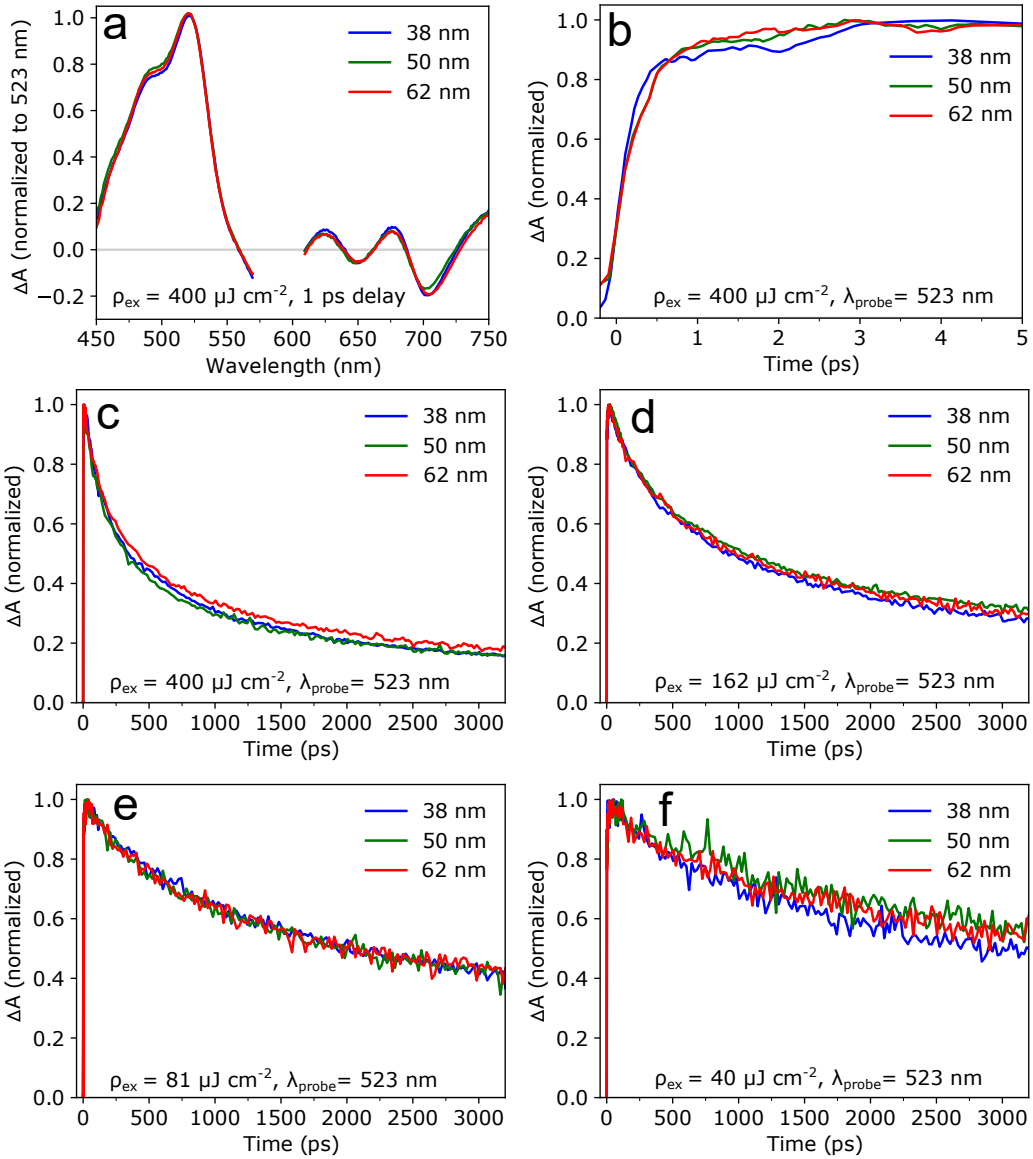

Figure 6.3: (a) Transient absorption spectra at 1 ps delay of different-sized crystalline TIPS-Pn NPs, normalized to the 523 nm ESA. (b) Early-time normalized kinetics of the 523 nm ESA, known to arise from triplet excitons in crystalline TIPS-Pn. (c–f) Long-time normalized kinetics of the 523 nm ESA, at pump fluences of (c) 400 μJ cm^{-2}, (d) 162 μJ cm^{-2}, (e) 81 μJ cm^{-2} and (f) 40 μJ cm^{-2}. NP samples are labelled by diameter.

in crystalline TIPS-Pn, and hence have the potential to induce size-dependent triplet exciton dynamics. While no size-dependent behavior was observed in the data presented in Figure 6.3, only a relatively limited combination of NP sizes and excitation densities were considered in these experiments. To comprehensively study all possible combinations of NP size and excitation density would be experimentally implausible, and so we instead used higher throughput KMC simulations to explore this parameter space for possible exciton confinement effects in crystalline TIPS-Pn NPs.

6.5.3 Triplet–Triplet Annihilation Simulations

6.5.3.1 Geminate Recombination

Figure 6.4a shows normalized triplet population kinetics from KMC simulations containing only a single pair of triplet excitons per NP model. Under such conditions, geminate recombination of the exciton pair is expected to dominate the decay of triplet excitons on the ps–ns timescale. The triplet decay kinetics obtained here exhibit a marked dependence upon NP size, with the rate of triplet decay decreasing significantly at larger particle sizes. This is reflected in the mean relaxation times fit to these decay profiles: as shown in Figure 6.4b, $\langle\tau\rangle$ increases by 3 orders of magnitude upon increasing d_{NP} from 6 nm to 100 nm. This dependence of decay kinetics upon d_{NP} can be rationalized as an exciton confinement effect: excitons in a smaller NP have fewer

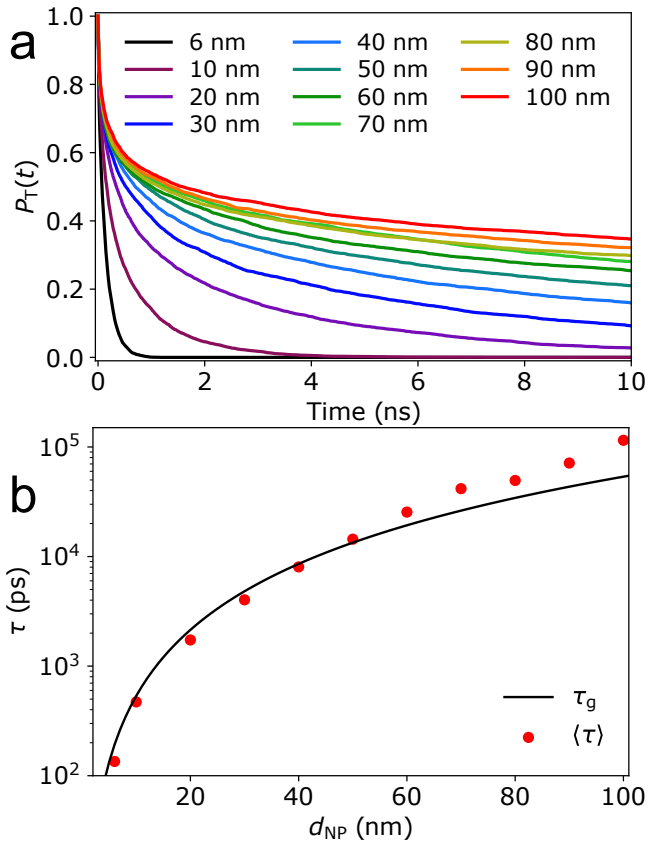

Figure 6.4: (a) Normalized triplet population kinetics from simulations of a geminate pair of triplet excitons in crystalline TIPS-Pn NPs of varying size. (b) Mean relaxation times ($\langle\tau\rangle$) fit from the traces shown in (a), with the first-passage time (τ_g) shown for reference. Traces in (a) are labelled by NP diameter.

sites which they can occupy relative to a larger NP. Therefore, the probability of the exciton pair re-encountering one another is higher in smaller NPs than in larger particles, and so the rate of geminate decay is faster at smaller particle sizes. To quantify this dependence of geminate recombination kinetics upon NP size, we considered the average time taken for the exciton pair to recombine through diffusion-limited motion. This is known as the "first-passage time" or "first-hitting time" (denoted τ_g),[269,270] and for the case here of a geminate pair of triplet excitons undergoing 2D diffusion within a circular domain may be estimated as[270]

$$\tau_g \approx \frac{3\pi^2}{128D} {d_{NP}}^2, \tag{6.9}$$

for D the effective triplet exciton diffusion coefficient (derivation shown in the Supporting Information). Triplet exciton hopping in the model here is limited to the *ab*-plane, and so $D = D_{2D} = 4.32 \times 10^{-4}\,\mathrm{cm^2 s^{-1}}$ (calculation in Supporting Information). This model describes the average time taken for a geminate pair of triplet excitons to encounter and recombine through diffusion-limited TTA when confined within an average-size *ab*-domain for a given NP diameter. Equation 6.9 makes a number of approximations; it assumes that one exciton starts in the exact center of the domain, that excitons in this system diffuse isotropically in two dimensions, and that both the initial pair separation and annihilation radius of TTA are negligible in comparison to the domain size. Despite this, τ_g agrees reasonably with mean relaxation times fit from geminate KMC simulations across all NP sizes considered here (Figure 6.4b). Slight disagreement between $\langle\tau\rangle$ and τ_g occurs for $\tau > 10^4$ ps; however these lifetimes are longer than the simulation time window and so cannot be fit to a high degree of accuracy. The first passage time therefore provides a quantitative estimate of how exciton confinement effects influence the kinetics of geminate triplet recombination in crystalline TIPS-Pn NPs.

6.5.3.2 Bimolecular Annihilation

Under most experimentally relevant conditions, NPs will contain many pairs of excitons arising from SF. We therefore extended our KMC modelling to consider NP systems with multiple geminate pairs of triplet excitons. For each simulation, the number of exciton pairs within the NP was determined from the input excitation density ρ_{ex} and the NP volume (as per Equation 6.4). Resulting triplet population kinetics and fitted relaxation times are shown in Figure 6.5, at three different values of ρ_{ex}. The triplet kinetics show some dependence on NP size at all excitation densities considered, with faster decay again occurring at smaller particle sizes. Unlike the kinetics of geminate TTA discussed above, however, in these many-exciton simulations the triplet decay kinetics eventually reach a plateau with increasing d_{NP}. The NP size at which triplet decay kinetics become size-independent appears to vary inversely with excitation density, occurring at smaller NP sizes upon increasing ρ_{ex}. To both quantify the time scale of bimolecular TTA and understand this transition from size-dependent to size-independent triplet exciton kinetics, we considered a simple model of diffusion-limited TTA. In the limit of triplet decay occurring only through diffusion-limited bimolecular TTA, the rate-limiting step of exciton decay is the diffusive encounter of any two triplet excitons. For a 2D system containing many excitons, the average time taken for two triplets to encounter one another through diffusive motion ("mean encounter time",

denoted τ_b) can be estimated as

$$\tau_b \approx \frac{R^2}{2D}\left[\ln\left(\frac{R}{a}\right) + \frac{9}{4}\right], \tag{6.10}$$

where $R = (\pi l_c \rho_{ex})^{-1/2}$ and a is the annihilation radius, set here to the average nearest-neighbour crystallographic separation in the ab-plane. The derivation of Equation 6.10 is shown in the Supporting Information. Notably, τ_b is entirely independent of NP size

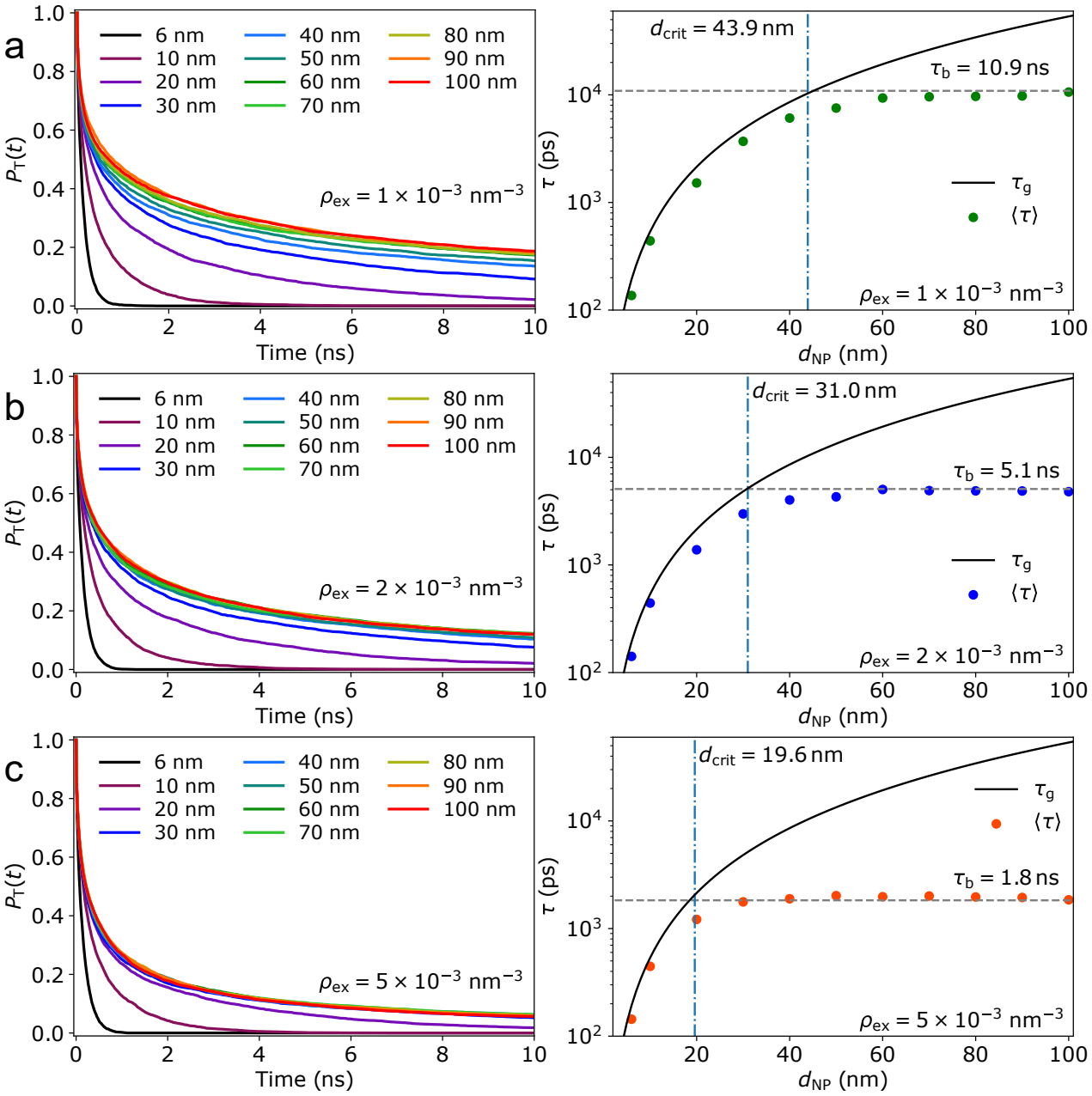

Figure 6.5: (Left) Normalized triplet population kinetics and (right) fitted mean relaxation times for crystalline NPs of varying size, from KMC simulations of TTA at excitation densities of (a) 1×10^{-3} nm^{-3}, (b) 2×10^{-3} nm^{-3} and (c) (a) 5×10^{-3} nm^{-3}. Kinetic traces are labelled by NP diameter. Horizontal dashed lines correspond to mean encounter times as per Equation 6.10, vertical dash-dot lines correspond to critical NP sizes as per Equation 6.12, and solid black curves show the geminate first-passage time for triplet exciton pairs as per Equation 6.9.

(unlike τ_g for geminate recombination), as this model assumes an infinite 2D domain containing a homogeneous exciton distribution. Despite this assumption, Equation 6.10 is expected to be a reasonable description of the TTA timescale for large NPs, as the inter-exciton separation in such systems will be considerably smaller than the average domain size. Therefore, for sufficiently large NP size an exciton will be much more likely to encounter another exciton and annihilate than to reach the domain boundary, and so the triplet decay dynamics would resemble those of the bulk material. As shown in Figure 6.5, $\langle\tau\rangle$ fit from the KMC simulations plateau at values very close to the corresponding mean encounter time predicted by Equation 6.10 at all excitation densities considered here. The mean encounter time is therefore a reasonable estimate of the triplet relaxation time through bimolecular TTA at large particle sizes.

The transition in these simulations from size-dependent decay kinetics at small particle sizes to size-independent dynamics at larger NP sizes thus corresponds to a shift in the dominant mode of exciton decay. Geminate recombination dominates triplet decay at smaller NP sizes and exhibits size-dependent kinetics, while bimolecular TTA is the major exciton decay pathway at larger particle sizes and is size-independent for sufficiently large NPs. To quantify the threshold size at which crossover from geminate recombination to bimolecular annihilation occurs, we considered the minimum NP size required for an exciton to encounter another triplet exciton before reaching a domain boundary. The average radius of a 2D *ab*-domain (denoted $\langle r_{2D}\rangle$) is significantly smaller than the NP diameter in the crystalline models used here, and is equal to $(\pi/8)d_{NP}$ (calculation in Supporting Information). The average 2D inter-exciton distance (denoted r_{ex}) can be calculated from the average 2D triplet density $\rho_{T,2D}$ as

$$\begin{aligned} r_{ex} =& \frac{1}{\sqrt{\rho_{T,2D}}} \\ =& (2l_c\rho_{ex})^{-1/2}, \end{aligned} \tag{6.11}$$

(assuming quantitative SF) where l_c is the crystallographic *c*-axis spacing. The NP size at which triplet decay begins to switch from size-dependent geminate recombination to size-independent bimolecular TTA (termed the "critical size" here, denoted d_{crit}) is expected to occur when the average inter-exciton separation is on the order of the average domain size, i.e. $r_{ex} = \langle r_{2D}\rangle$. Using Equation 6.11, this critical NP size can therefore be estimated as

$$d_{crit} = \frac{8}{\pi}\left(2l_c\rho_{ex}\right)^{-1/2}. \tag{6.12}$$

Critical NP sizes calculated by Equation 6.12 are shown as vertical dash-dotted lines in the right panels of Figure 6.5. For every excitation density considered, d_{crit} predicts with reasonable accuracy the particle size at which the size-dependent triplet kinetics begin to plateau. For $d_{NP} < d_{crit}$ each crystalline domain contains very few excitons, and so a given exciton is more likely to encounter the domain boundary than an exciton from a different geminate pair. The decay kinetics in this region are hence governed by geminate recombination and are strongly size-dependent, following the expected first-passage time for geminate recombination. However, for $d_{NP} > d_{crit}$ domains may contain multiple exciton pairs, and the mean inter-exciton separation is smaller than the average distance from any exciton to the domain boundary. Bimolecular TTA therefore becomes significant in this size region, and so the time scale of triplet decay in this region begin to converge to τ_b. Note that Equations 6.11 and 6.12 refer to the *average* 2D domain size, but each NP possesses domains larger or smaller than

this size. Therefore, NPs slightly larger than d_{crit} will still contain some domains which are sufficiently small that only geminate recombination can occur. Despite this, the agreement between theory and simulation shown in Figure 6.5 indicates that d_{crit} provides a reasonable, quantitative estimate of NP sizes at which size-dependent triplet decay kinetics become significant for NPs of crystalline TIPS-Pn.

6.5.4 Size-Dependent Region of Triplet Kinetics

Figure 6.6 shows the parameter spaces predicted by Equation 6.12 to give strongly size-dependent and size-independent triplet decay kinetics on a plot of d_{crit} versus ρ_{ex}, along with the experimental conditions corresponding to the data presented in Figure 6.3. All experimental data here lie within the size-independent regime of triplet exciton kinetics, which agrees with the lack of size-dependent exciton dynamics observed in Figure 6.3. To observe size-dependent geminate recombination kinetics due to exciton confinement, experiments would have to be performed either at lower excitation densities or with significantly smaller NPs. Ultra-small particle sizes for aqueously-dispersed acene NPs are not impossible: a previous study of diphenyltetracene NPs prepared by re-precipitation reported particle diameters as low as 11 nm.[35] However, the smallest reported particle sizes for TIPS-Pn NPs were 33 nm in diameter,[3,141] only slightly smaller than the 38-nm NPs studied experimentally here. It is unclear whether particle sizes smaller than 33 nm are experimentally achievable for TIPS-Pn NPs; to the best of our knowledge, no attempts have been made at preparing NPs smaller than this. Therefore, while we cannot rule out the possibility of TIPS-Pn NPs smaller than 33 nm being achievable through re-precipitation, such small particle sizes are certainly not relevant within the existing body of literature on crystalline TIPS-Pn NPs.

Additionally, excitation densities cannot be made arbitrarily small for ultrafast

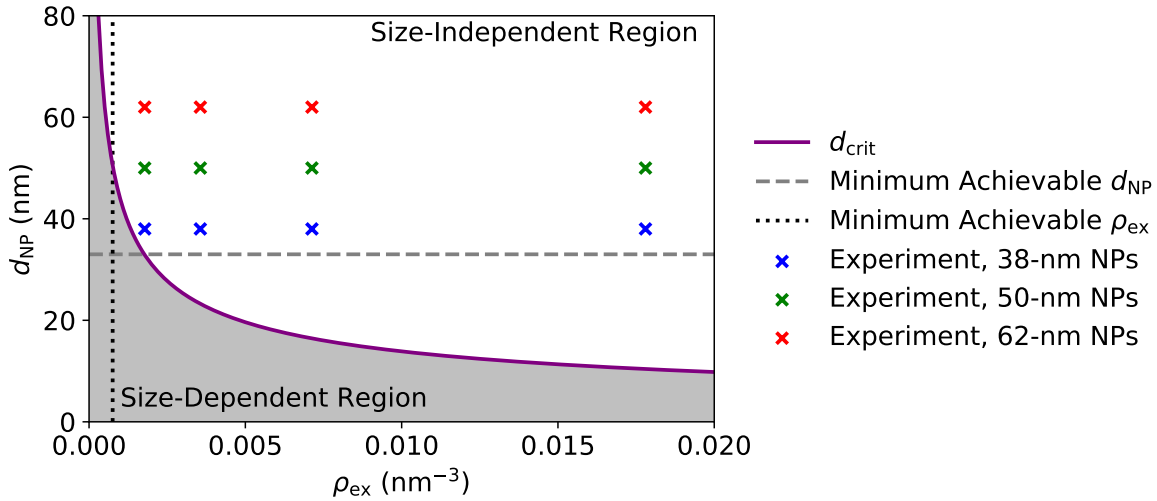

Figure 6.6: Critical NP size (d_{crit}; solid curve) as a function of excitation density (ρ_{ex}), separating regions of size-dependent (shaded region) and size-independent (unshaded region) triplet decay kinetics in crystalline TIPS-Pn NPs. Minimum NP size experimentally achievable to date for crystalline TIPS-Pn[3,141] (33 nm; horizontal dashed line) and lowest excitation density experimentally achievable here (8×10^{-4} nm^{-3}; vertical dotted line) are shown for reference. Experimental conditions corresponding to data shown in Figure 6.3 are shown as coloured crosses.

spectroscopy measurements, as the signal intensity is directly proportional to ρ_{ex}. This is evident in the data presented in Figure 6.3: the signal-to-noise ratio of the data collected at the two lowest excitation densities is significantly poorer than at higher pump fluences. Further reduction of ρ_{ex} would decrease the data quality even more, likely to a point where any size-dependent triplet kinetics would not be resolvable. For the apparatus used here, we estimate the minimum excitation density required for a resolvable triplet signal from these NPs to be approximately $8 \times 10^{-4}\,\mathrm{nm}^{-3}$ (calculation in the Supporting Information), corresponding to a pump fluence of 15–20 $\mu\mathrm{J\,cm}^{-2}$ in the experiments undertaken here. Pump fluences as low as 5–10 $\mu\mathrm{J\,cm}^{-2}$ have previously been reported in other studies of crystalline TIPS-Pn,[73,110,119] but after accounting for excitation wavelength and sample absorbance these are equivalent to the lowest excitation density used here. Therefore, excitation densities below $8 \times 10^{-4}\,\mathrm{nm}^{-3}$ are unlikely to be experimentally accessible for most ultrafast spectroscopic investigations of crystalline TIPS-Pn NPs.

The region of experimentally relevant conditions hence corresponds to the upper-right section of Figure 6.6, bounded by $d_{NP} = 33\,\mathrm{nm}$ (horizontal dashed line) and $\rho_{ex} = 8 \times 10^{-4}\,\mathrm{nm}^{-3}$ (vertical dotted line). As is clearly evident, this parameter space sits almost entirely within the domain of size-independent triplet exciton kinetics. Therefore, it is highly unlikely that any size-dependent exciton dynamics due to confined geminate recombination will be relevant in experimental studies of crystalline TIPS-Pn NPs. This is not to say that such effects *cannot* be observed; higher sensitivity TA apparatus may be able to resolve triplet signals at sufficiently low excitation densities, or preparation of very small TIPS-Pn NPs may prove experimentally possible. Rather, size-dependent triplet dynamics due to confined geminate recombination will be largely negligible in crystalline TIPS-Pn NPs *under typical experimental conditions*. The results presented here therefore indicate that relatively small (d_{NP} = 30–50 nm) NPs are appropriate model systems for studying the bulk exciton dynamics of crystalline TIPS-Pn, as minimal size-dependent kinetic effects will occur under typical experimental conditions.

The KMC model and subsequent analysis presented here assumes TIPS-Pn NPs to be perfectly singly crystalline, containing no polycrystallinity or crystal grain boundaries. High levels of polycrystallinity could potentially accelerate geminate recombination of triplets, due to increased spatial confinement of exciton pairs within small crystalline domains. However, non-equilibrium packing geometries at grain boundaries may also enable triplet transfer in the *c*-direction, breaking the 2D confinement of exciton pairs in single-crystal TIPS-Pn. This could facilitate greater separation of triplet exciton pairs and slow their geminate recombination, hence minimizing size-dependent triplet dynamics. It is unclear to what extent each of these effects contribute to triplet decay kinetics in the NPs studied here, as the degree of polycrystallinity and average crystallite size in TIPS-Pn NPs has not previously been quantified. However, previous studies of TIPS-Pn films have observed significant crystalline alignment, with average domain sizes ranging from tens of nanometers to hundreds of microns.[110,120,228] If crystal domain sizes within NPs are similar to these films, then relatively large-scale crystal alignment is likely present within the particles studied here. Additionally, the absence of amorphous TIPS-Pn spectral features in both steady-state and ultrafast measurements indicates that the NPs studied here are almost entirely crystalline, with negligible levels of amorphous TIPS-Pn remaining within the NP interior. We have previously demonstrated that the crystallization of TIPS-Pn NPs with PVA occurs

through an auto-catalytic mechanism, whereby crystallinity nucleated at the NP surface induces a rearrangement of neighbouring molecules, spreading crystallinity into the NP interior.[1] The significant crystallinity within the NPs studied here implies that this auto-catalytic process spreads throughout the entirety of these NPs, which hence necessitates a substantial level of crystalline alignment throughout the particles. Therefore, we anticipate a high level of single-crystal alignment within the NPs studied here, and so the effects of polycrystallinity and crystal grain boundaries are expected to be minimal.

While this study has focused on the specific example of crystalline TIPS-Pn NPs, the theory presented here regarding size-dependent exciton kinetics arising from exciton confinement may be more broadly applicable to any small NPs of crystalline organic materials in which diffusion-limited EEA is the dominant decay process. d_{crit} depends on only the excitation density and average domain size within the NP, and analogous derivations of Equation 6.12 can be made for one- or three-dimensional triplet exciton diffusion by making adjustments for the effective domain size. In general, small crystalline domains will begin to exhibit size-dependent exciton dynamics when each domain contains sufficiently few excitations that an exciton is on average more likely to encounter the domain boundary than another exciton. For SF chromophores, this will result in confined geminate triplet–triplet recombination accelerating the triplet population decay, as demonstrated here for crystalline TIPS-Pn. However, this theory is also relevant for materials which do not undergo SF, as confinement of a sole singlet exciton to a domain will inhibit EEA entirely. In such circumstances, the exciton decay will instead be limited by the natural exciton lifetime or other decay processes such as exciton–charge annihilation. Therefore, the theory developed here may be a powerful tool when designing spectroscopic experiments using NP dispersions. Calculation of the critical NP size for a given material can inform the choice of experimental conditions, to avoid any potential size-dependent exciton dynamics and ensure that the NPs are a reasonable model of the bulk material. Alternatively, it may be desirable to tune conditions into the size-dependent region of kinetics, to study processes such as geminate recombination or natural exciton decay that may be difficult to observe in the bulk due to rapid bimolecular EEA.

We previously estimated the triplet concentration in crystalline TIPS-Pn NPs under solar irradiation to be on the order of 60 µM (Figure 4.13), corresponding to an excitation density of $2 \times 10^{-5}\,\mathrm{nm}^{-3}$.[2] Using Equation 6.12, such a low excitation density would yield a critical NP size greater than 300 nm, which is larger than any previously-reported TIPS-Pn NPs,[119,133] and indeed larger than the thicknesses of many TIPS-Pn thin-film systems.[73,128,142] The confinement-induced exciton behavior identified in this work may therefore be relevant for PV devices using small NPs or thin films to harness solar energy. Accelerated geminate recombination at small domain sizes may compete with triplet dissociation or interfacial charge transfer and hence reduce device performance, and so should be taken into consideration when designing PV devices employing nanoscale sensitization layers.

6.6 Conclusions

This work has demonstrated that particle-size effects have a negligible effect upon exciton kinetics within crystalline TIPS-Pn NPs. Transient absorption characterization of NPs ranging from 38 nm to 62 nm in diameter shows no changes in the dynamics

of SF or TTA with particle size, suggesting that there are negligible morphological differences across these NP sizes. Kinetic Monte Carlo modelling predicts that size-dependent triplet kinetics will emerge when exciton decay becomes dominated by geminate recombination of triplet pairs, due to confinement of exciton pair within crystalline domains. However, such effects are unlikely to be observed experimentally, as they require very small particle sizes or low excitation densities that are either not practical or experimentally irrelevant. These results therefore indicate that small NPs are excellent model systems for studying the exciton dynamics of bulk crystalline TIPS-Pn, as particle size effects within such systems are expected to be negligible.

Acknowledgements

This work was supported by an Australian Government Research Training Program (RTP) scholarship and funding from the Australian Research Council (DP160103797 and LE0989747). The authors also thank Alexandra Stuart, Jessica de la Perrelle and Dr Patrick Tapping for discussions that contributed to this work.

6.7 Supporting Information

Dynamic Light Scattering Characterization of Nanoparticle Size

Figure 6.7 shows intensity-weighted particle size distributions of all NP samples used in this work. A relatively monodisperse distribution is observed for the smallest particles size studied here, with a Z-average diameter of 38 nm. However, the larger particle sizes exhibit progressively broader distributions with higher polydispersity, possibly due to the relatively high injection concentrations used in their preparation (Table 6.1) inducing a wider range of initial nucleation conditions. However, this polydispersity

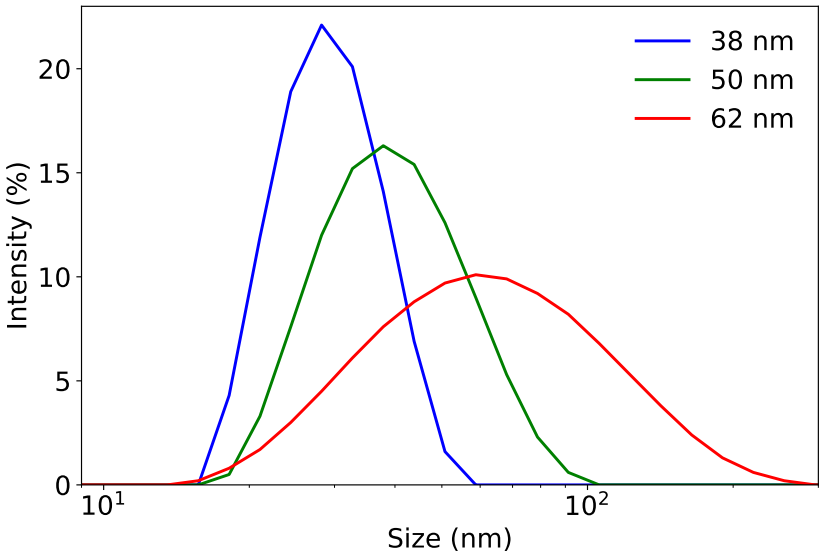

Figure 6.7: Intensity-weighted particle size distributions of TIPS-Pn NPs prepared by re-precipitation from varying injection concentrations. NP samples are labelled by Z-average diameter.

is unlikely to significantly impact the results obtained from experiments undertaken here, as the particle size distributions are centered at different sizes.

It should also be noted that the size distributions shown in Figure 6.7 and Z-average diameters quoted throughout this work correspond to as-prepared NPs, before addition of PVA to induce crystallinity. Previous work by our group suggested that the amorphous-to-crystalline phase transition in TIPS-Pn induced by PVA occurs with a negligible change in particle size, but PVA then coats the NP surface to a depth of tens of nanometers.[1] This coating is measured by DLS as an increase in the NP hydrodynamic diameter, which has potential to complicate interpretation of this data and hinder accurate quantification of particle sizes. Therefore, we consider particle size distributions recorded before addition of PVA to be the most accurate measure of NP size here.

Singlet Projections onto Triplet-Pair Encounter States

The spin Hamiltonian for an interacting pair of triplet excitons localized on molecules A and B may be approximated as[95]

$$\hat{H}_{\text{total}} = \hat{H}_{\text{magnetic}} + \hat{H}_{\text{SS}_\text{A}} + \hat{H}_{\text{SS}_\text{B}} + \hat{H}_{\text{AB}}, \tag{6.13}$$

where $\hat{H}_{\text{magnetic}}$ denotes the Zeeman magnetic field effect on the triplets, $\hat{H}_{\text{AB}}$ the intermolecular coupling between triplets and $\hat{H}_{\text{SS}_i}$ the intramolecular spin–spin interaction on molecule i. $\hat{H}_{\text{magnetic}}$ was set to zero here, as TTA considered in this work occurs under no external magnetic field. $\hat{H}_{\text{SS}_i}$ was calculated as

$$\hat{H}_{\text{SS}_i} = D\left(\hat{S}_{z_i}^2 - \frac{1}{3}|\hat{\boldsymbol{S}}_i|^2\right) + E\left(\hat{S}_{x_i}^2 - \hat{S}_{y_i}^2\right), \tag{6.14}$$

where D and E are the molecular zero-field splitting parameters for crystalline TIPS-Pn ($0.0383\,\text{cm}^{-1}$ and $0.0056\,\text{cm}^{-1}$, respectively[102]) and $\hat{\boldsymbol{S}}_i = \left(\hat{S}_{x_i}, \hat{S}_{y_i}, \hat{S}_{z_i}\right)$ is the two-electron spin operator on molecule i. $\hat{H}_{\text{AB}}$ was assumed to be a dipole–dipole interaction of the form

$$\hat{H}_{\text{AB}} = -X\left[3(\hat{\boldsymbol{S}}_\text{A}\cdot\hat{\boldsymbol{r}})(\hat{\boldsymbol{S}}_\text{B}\cdot\hat{\boldsymbol{r}}) - \hat{\boldsymbol{S}}_\text{A}\cdot\hat{\boldsymbol{S}}_\text{B}\right], \tag{6.15}$$

for $\hat{\boldsymbol{r}}$ the unit vector joining molecules A and B, and X a constant describing the spin-spin coupling strength (assumed to be equal to $D/100$ here; the specific form of this intermolecular coupling term is not important so this term is relatively weak). The Schrödinger equation with Hamiltonian in Equation 6.13 can be solved to give nine eigenvectors for the triplet-pair states (denoted ψ_l, l = 1–9), and the projection of each of these onto the pure singlet state of the system (C_S^l) is given by

$$C_\text{S}^l = 3^{-1/2}(\langle x|_\text{A}\langle x|_\text{B} + \langle y|_\text{A}\langle y|_\text{B} + \langle z|_\text{A}\langle z|_\text{B})|\psi_l\rangle, \tag{6.16}$$

where $\langle x|_i, \langle y|_i, \langle z|_i$ are two-electron spin states on molecule i defined with respect to the molecular symmetry axes of one of the molecules such that $\hat{S}_j\,|k\rangle = i\hbar\epsilon_{jkl}\,|l\rangle$, where ϵ_{jkl} is the permutation symbol and $j, k, l = x, y$ or z.[94,95] Equation 6.16 was evaluated for triplet pair states in crystalline TIPS-Pn by diagonalizing $\hat{H}_{\text{total}}$ in the zero-field basis (using the method from ref. 95) for pair geometries taken from the TIPS-Pn crystal structure.[125] Resulting values of $|C_\text{S}^l|^2$ for each state are listed in Table 6.3.

Table 6.3: Singlet projections onto triplet-pair states for crystalline TIPS-Pn dimer pairs.

State (l)	$\lvert C_{\mathrm{S}}^{l}\rvert^2$	
	a-pair	b-pair
1	0.330	0.329
2	1.73×10^{-6}	1.45×10^{-6}
3	1.99×10^{-33}	1.10×10^{-35}
4	2.84×10^{-32}	1.12×10^{-32}
5	7.21×10^{-4}	3.65×10^{-4}
6	0.346	0.355
7	9.34×10^{-34}	7.15×10^{-33}
8	8.52×10^{-6}	1.29×10^{-5}
9	0.323	0.317

Stretched Exponential Fits to Simulated Triplet Decays

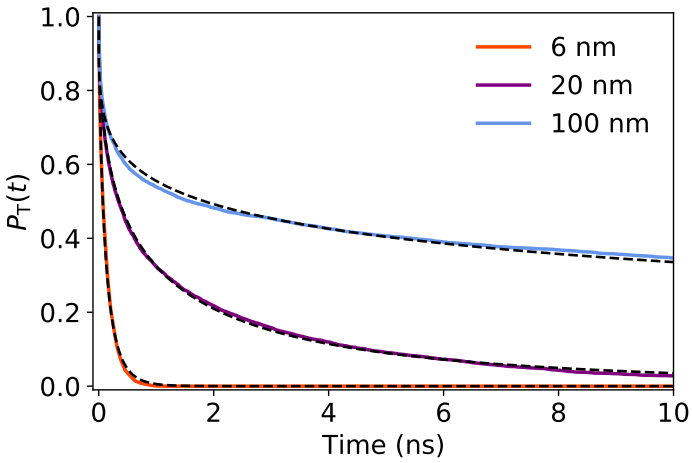

Figure 6.8: Triplet population kinetics from KMC simulations of a single pair of triplet excitons (solid curves), and fits to these traces by stretched exponential functions (dashed curves). Traces are labelled by NP diameter. Best-fit parameters are: $\tau = 113.9 \pm 0.1$ ps, $\beta = 0.755 \pm 0.001$ ($\langle\tau\rangle = 134.9 \pm 0.2$ ps) for the 6-nm NP; $\tau = 779.4 \pm 0.7$ ps, $\beta = 0.474 \pm 0.001$ ($\langle\tau\rangle = 1733 \pm 2$ ps) for the 20-nm NP; and $\tau = 7210 \pm 20$ ps, $\beta = 0.269 \pm 0.001$ ($\langle\tau\rangle = 115\,000 \pm 400$ ps) for the 100-nm NP.

Average Radius of a 2D Plane Within a Hemisphere

The crystalline TIPS-Pn NP model used in KMC modelling here consists of a series of stacked, parallel 2D domains in a hemisphere. As shown in Figure 6.9, for a plane of radius $r_{2\mathrm{D}}$ at height h above the hemisphere base, $r_{2\mathrm{D}}$ and h form two sides of a right-angled triangle, with the hemisphere radius r_{NP} as the hypotenuse. The plane radius may hence be written as

$$r_{2\mathrm{D}} = \sqrt{{r_{\mathrm{NP}}}^2 - h^2}. \tag{6.17}$$

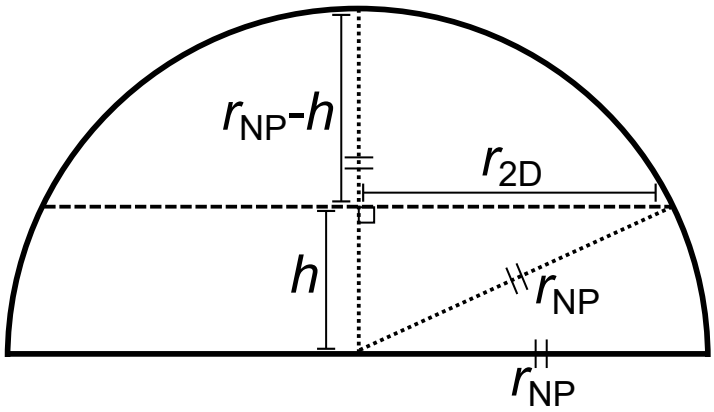

Figure 6.9: Diagram of a 2D plane of radius r_{2D} within a hemisphere of radius r_{NP}, at a height h above the hemisphere base.

The average radius of planes within the NP model $\langle r_{2D} \rangle$ is therefore given by

$$\langle r_{2D} \rangle = \frac{\sum_i \left({r_{NP}}^2 - {h_i}^2 \right)^{1/2}}{\sum_i i}, \tag{6.18}$$

for i planes of height h_i within the NP hemisphere. In the limit of the inter-plane spacing becoming infinitesimally small, Equation 6.18 may be rewritten as

$$\langle r_{2D} \rangle = \frac{\int_0^{r_{NP}} \sqrt{{r_{NP}}^2 - h^2} \mathrm{d}h}{\int_0^{r_{NP}} \mathrm{d}h} = \frac{1}{r_{NP}} \int_0^{r_{NP}} \sqrt{{r_{NP}}^2 - h^2} \mathrm{d}h, \tag{6.19}$$

which has solution

$$\langle r_{2D} \rangle = \frac{\pi}{4} r_{NP} = \frac{\pi}{8} d_{NP}. \tag{6.20}$$

It is worth noting that the inter-plane spacing in crystalline TIPS-Pn ($l_c = 1.684\,\mathrm{nm}$) is finite and not insignificant when considering some of the smaller NPs modelled here. Therefore, to verify the accuracy of the analytical solution shown in Equation 6.20, $\langle r_{2D} \rangle$ was also computed through numerical evaluation of Equation 6.18 for all NP sizes considered here. As shown in Figure 6.10, values of $\langle r_{2D} \rangle$ determined from both the analytical solution and numerical evaluation agree closely across the entire range of NP diameters considered in this work. Equation 6.20 is therefore valid for determining the average size of *ab*-planes within the crystalline TIPS-Pn NP models considered here.

First-Passage Time for Geminate Triplet Recombination

The "first-passage time" τ_g for diffusion-controlled recombination of a neutral geminate pair within a circular 2D domain (with one exciton initially residing at the domain center) has the form[270]

$$\tau_g = \frac{{r_d}^2}{2D} \ln\left(\frac{r_0}{a}\right) - \frac{1}{4D}({r_0}^2 - a^2) + \frac{1}{2a\kappa}({r_d}^2 - a^2), \tag{6.21}$$

for domain radius r_d, annihilation radius a, initial pair separation r_0 and effective diffusion coefficient D. κ is the "association constant" which describes the rate of

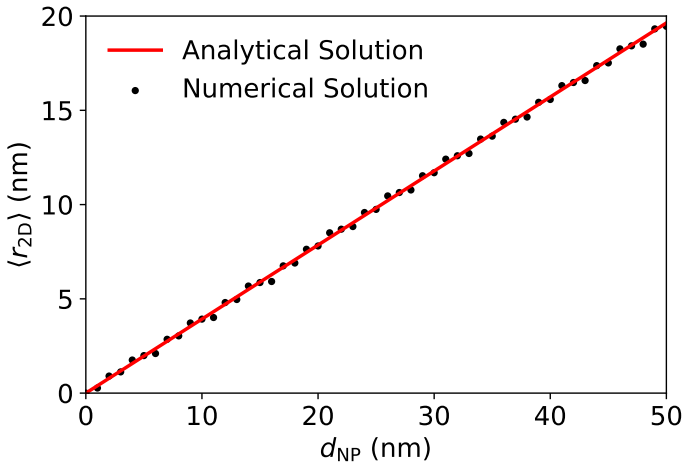

Figure 6.10: Analytical solution (Equation 6.20) and numerical evaluation (Equation 6.18) of $\langle r_{2D} \rangle$ for the range of NP diameters considered here.

exciton recombination at $r = a$, defined by the reactive boundary condition

$$D\left(\frac{\partial p}{\partial r}\right)_{r=a} = \kappa p(a,t), \tag{6.22}$$

for $p(r,t)$ the exciton probability distribution. Here, we assume[244]

$$\kappa \approx \frac{DP(a)}{a}, \tag{6.23}$$

for $P(a)$ the reaction probability at $r = a$, which we take to be 1/3 as only 3/9 encounter states may undergo TTA in the present model. Therefore, Equation 6.21 may be rewritten as

$$\tau_g = \frac{{r_d}^2}{2D}\ln\left(\frac{r_0}{a}\right) - \frac{1}{4D}({r_0}^2 - a^2) + \frac{3}{2D}({r_d}^2 - a^2). \tag{6.24}$$

In the limit of $a \approx r_0 \ll r_d$ (as is the case here for geminate triplet pairs within crystalline TIPS-Pn NPs), Equation 6.24 simplifies to

$$\tau_g \approx \frac{3{r_d}^2}{2D}. \tag{6.25}$$

As shown in the previous section, the average radius of a 2D plane within the NPs considered here is given by $\langle r_{NP} \rangle = \pi d_{NP}/8$. Therefore, the first passage time for a geminate triplet pair within an average-sized NP domain may be written as

$$\tau_g \approx \frac{3\langle r_{NP}\rangle^2}{2D} = \frac{3\pi^2}{128D}{d_{NP}}^2. \tag{6.26}$$

It should be noted that these equations for geminate first-passage times are derived from a model which assumes 2D diffusion of a geminate pair with a circular domain centered at the initial position of one exciton.[270] The KMC simulations here allowed for initial exciton placement at any site within a NP, not just at the center of a 2D domain. Therefore, Equation 6.26 is only an approximation of the geminate first-passage time for the systems considered in this work.

Calculation of the Triplet Exciton Diffusion Coefficient

One-dimensional diffusion coefficients D_i can be determined from exciton hopping coefficients k_i and intermolecular separations l_i by[238]

$$D_i = \frac{1}{2} k_i l_i^2. \tag{6.27}$$

For anisotropic diffusion in two dimensions, the effective two-dimensional diffusion coefficient is given by the geometric mean of the relevant one-dimensional coefficients:[271]

$$D_{2D} = \sqrt{D_a D_b}. \tag{6.28}$$

Using the TIPS-Pn lattice spacings and triplet hopping rate coefficients listed in Table 6.2, the effective two-dimensional diffusion coefficient of a single triplet exciton in the model used here can hence be calculated as $D_{ab} = 2.16 \times 10^{-4}\,\mathrm{cm^2 s^{-1}}$. The effective diffusion coefficient for the relative motion of two equivalent particles is equal to twice the individual diffusion coefficient, and so the effective diffusion coefficient for triplet annihilation and recombination here is $D_{\mathrm{eff}} = 4.32 \times 10^{-4}\,\mathrm{cm^2 s^{-1}}$.

Mean Encounter Time for Bimolecular Annihilation

To estimate the mean encounter time for triplet decay through diffusion-limited bimolecular TTA, we considered the annihilation of two triplet excitons undergoing 2D diffusion relative to one another, with the distance between the excitons restricted to lie between $r = a$ and $r = R$ for $R \geq a$, where a is again the annihilation radius and the outer radius R is defined such that the two excitons in this domain is consistent with the average number of excitons in a domain of this size for the specified triplet exciton density. Assuming that the initial exciton distribution is homogeneous, the mean passage time for the two excitons to encounter and annihilate through diffusion-limited TTA in such a model is given by[272,273]

$$\tau_{\mathrm{b}} = \frac{R^2}{2D}\left[\frac{1}{4R^2}\left(a^2 - 3R^2\right) + \frac{R^2}{R^2 - a^2}\ln\left(\frac{R}{a}\right) + \frac{D}{a\kappa R^2}\left(R^2 - a^2\right)\right], \tag{6.29}$$

where κ is the association constant defined in Equation 6.23. Assuming again that $P(a) = 1/3$, Equation 6.29 may be rewritten as

$$\tau_{\mathrm{b}} = \frac{R^2}{2D}\left[\frac{1}{4R^2}\left(9R^2 - 11a^2\right) + \frac{R^2}{R^2 - a^2}\ln\left(\frac{R}{a}\right)\right], \tag{6.30}$$

which in the limit of $R \gg a$ reduces to

$$\tau_{\mathrm{b}} \approx \frac{R^2}{2D}\left[\ln\left(\frac{R}{a}\right) + \frac{9}{4}\right]. \tag{6.31}$$

Defining R such that the average number of excitons within a circle of this radius is equal to 2 gives

$$\rho_{\mathrm{T,2D}} \pi R^2 = 2, \tag{6.32}$$

where $\rho_{\mathrm{T,2D}}$ is the 2D triplet exciton density given by $\rho_{\mathrm{T,2D}} = 2 l_{\mathrm{c}} \rho_{\mathrm{ex}}$. This may hence be rearranged to give

$$R = (\pi l_{\mathrm{c}} \rho_{\mathrm{ex}})^{-1/2}. \tag{6.33}$$

Lowest Experimentally Achievable Excitation Density

For the experimental apparatus used in this work, the minimum signal required to resolve a TA spectrum is approximately $\Delta A \approx 0.001$. By the Beer-Lambert law, the minimum resolvable triplet concentration in this apparatus is hence given by

$$[T] = \frac{\Delta A(\lambda)}{\epsilon_T(\lambda) l}, \tag{6.34}$$

for path length l and molar extinction coefficient $\epsilon_T(\lambda)$ at wavelength λ. Previous work by our group determined that $\epsilon_T(523\,\text{nm}) = 22\,000\,\text{L}\,\text{mol}^{-1}\text{dm}^{-3}$ for aqueously-dispersed crystalline TIPS-Pn NPs.[2] Therefore, Equation 6.34 yields a minimum observable triplet concentration of $2.27 \times 10^{-7}\,\text{mol}\,\text{dm}^{-3}$. However, this value corresponds to the triplet concentration across the entire aqueous dispersion ($[T]_{sus}$), and does not consider that these excitons are localized only inside the solid NPs contained within this suspension. As shown previously, this may be corrected for by

$$[T]_{NP} = \frac{\rho_{TIPS-Pn}}{c_{NP}} [T]_{sus}, \tag{6.35}$$

where $\rho_{TIPS-Pn} = 1.104\,\text{g}\,\text{cm}^{-3}$ is the density of crystalline TIPS-Pn and c_{NP} is the mass concentration of TIPS-Pn in suspension.[2,125] Assuming $c_{NP} = 100\,\text{ppm}$, the lowest detectable triplet concentration within the NPs is therefore equal to $2.51 \times 10^{-3}\,\text{mol}\,\text{dm}^{-3}$. For quantitative SF (as has been shown to be the case in crystalline TIPS-Pn[119]) the excitation density is equal to half of this. Therefore, the lowest excitation density at which triplet excitons will be experimentally observable is equal to

$$\begin{aligned} \rho_{ex} =& \frac{1}{2} \times 2.51 \times 10^{-3}\,\text{mol}\,\text{dm}^{-3} \\ =& 1.25 \times 10^{-3}\,\text{mol}\,\text{dm}^{-3} \\ =& 7.55 \times 10^{20}\ \text{dm}^{-3} \\ =& 7.55 \times 10^{-4}\ \text{nm}^{-3}. \end{aligned} \tag{6.36}$$

CHAPTER 7
Conclusions and Future Directions

This thesis presented a series of investigations into the how the morphology and intermolecular packing within 6,13-(triisopropylsilylethynyl)pentacene (TIPS-Pn) influences the exciton dynamics associated with singlet fission (SF). These studies focused specifically upon aqueous dispersions of TIPS-Pn nanoparticles (NPs), but many of the key findings may be generalized to bulk TIPS-Pn or other small-molecule SF chromophores.

Chapter 3 studied a novel process of morphological control for TIPS-Pn NPs, whereby poly(vinyl alcohol) (PVA) induced an amorphous-to-crystalline structural reorganization throughout these particles. X-ray diffraction experiments confirmed that the resulting NPs possessed significant long-range crystalline order, and steady-state spectroscopic characterization demonstrated that this molecular rearrangement occurred on a timescale of seconds under ambient conditions. Dynamic light scattering (DLS) studies indicated that this morphological transformation was preceded by adsorption of PVA at the NP surface, suggesting that some form of surface-mediated interaction was responsible for templating crystallinity within TIPS-Pn. This effect was found to be highly specific to TIPS-Pn and PVA: using other water-soluble polymers in place of PVA did not reproduce this phase transition, nor did PVA induce crystallinity in any other substituted acenes. Density functional theory (DFT) modelling suggested that this structural reorganization may be facilitated by a periodic interaction between TIPS groups and PVA hydroxyl groups at the NP surface. Transient absorption (TA) spectroscopy experiments then demonstrated that this PVA-induced phase transition accelerated SF within TIPS-Pn NPs by over an order of magnitude. This work therefore provides a framework for understanding the mechanism by which PVA induces crystallinity in amorphous TIPS-Pn, which had been previously reported in the literature but not well understood.

This study appears to be the first report of such a spatially periodic interaction between polymer and organic material inducing a solid-state structural reorganization. It is currently unknown how widely applicable this effect may be, and future work should investigate other polymer:substrate combinations which exhibit spatially periodic alignment for their potential to influence substrate morphology. For such a structural templating effect to be observed, the substrate material should have amorphous and crystalline phases which are both metastable under ambient conditions and readily distinguishable from one another through techniques such as steady-state spectroscopy. The polymer should contain side-chains or some structural motif capable of undergoing localized intermolecular interactions (such as the hydroxyl groups on PVA) spaced periodically along the backbone, and be readily soluble in the medium used to suspend the substrate. To search for possible combinations of polymer and substrate material which satisfy these conditions, computational screening of structural databases would likely be the most effective starting point. A recent study reported an algorithm for high-throughput screening of epitaxial alignment between metal-organic framework materials and crystalline substrates,[274] and a similar approach may be suitable here.

Further experiments could also investigate the nature of this surface-mediated interaction, and test the level of periodic matching required to induce crystallinity in TIPS-Pn. Testing PVA analogues such as poly(vinyl thiol) or poly(vinyl amine) for their ability to crystallize TIPS-Pn would shed light on how the sterics and electron density of the polymer side chains influence this structural templating effect. Additionally, experiments using small vinyl alcohol oligomers in place of extended PVA chains could be used to determine the minimum interaction length required for this periodic interaction to induce crystallinity. Similarly, extending the spacing between hydroxyl groups upon the polymer chain (i.e. using propenol or butenol monomers in place of vinyl alcohol) or varying PVA tacticity would yield information regarding the length scale and sensitivity of the periodic interaction. Finally, it would be instructive to extend these experiments from small NPs to thin films, to ascertain whether this structural reorganization is also applicable to bulk TIPS-Pn.

Chapter 4 quantified the kinetics of triplet exciton diffusion in crystalline TIPS-Pn, revealing that triplet mobility is highly anisotropic throughout this crystal structure. TA spectroscopy of crystalline TIPS-Pn NPs observed highly fluence-dependent decay kinetics of triplet excitons, indicative of exciton decay occurring primarily through diffusion-limited triplet–triplet annihilation (TTA). Kinetic models allowing for either isotropic or anisotropic three-dimensional (3D) triplet diffusion fit these triplet dynamics equally well, but only the latter yielded best-fit parameters that were physically reasonable. This equivalence in model fits arose from both models having the same mathematical form despite representing very different physical systems, thus highlighting that goodness of fit is not always a reliable indicator of model suitability. Other experimental studies have used this isotropic model to describe triplet diffusion in crystalline pentacene[117] and TIPS-Pn,[110] but this work demonstrated that best-fit parameters arising from this model are not physically representative of materials with anisotropic crystal packing, and may therefore give misleading predictions regarding exciton mobility. Fits of the TA data here with anisotropic 3D or one-dimensional (1D) diffusion models indicated that triplet exciton diffusion is highly anisotropic within crystalline TIPS-Pn. Triplet hopping rates calculated by constrained DFT and Marcus theory agreed with this, predicting triplet mobilities that differed by over 7 orders of magnitude along the three crystallographic axes of TIPS-Pn. These results hence suggest that triplet exciton mobility in device-relevant TIPS-Pn films is highly sensitive to crystallographic orientation, and favorable crystalline alignment may facilitate rapid and long-range exciton transport in single-crystal device films.

Poor triplet exciton mobility is often cited as a significant source of efficiency losses in SF-sensitized PV devices with pentacene or TIPS-Pn active layers.[27–29] However, the impact of anisotropic exciton diffusion and crystal orientation upon triplet mobility within PV devices has not yet been explicitly considered. Estimated triplet diffusion lengths from this work suggested that exciton transport of up to 0.5 µm may be possible along the crystallographic *a*-axis, but that negligible transfer occurs along the *c*-axis within the triplet lifetime. Techniques exist for the large-scale alignment of single-crystal TIPS-Pn films, with one study reporting millimeter-scale crystalline alignment by using a specialized solution coating method.[228] Future attempts to construct SF-sensitized PV devices with crystalline TIPS-Pn as the sensitising layer should therefore focus upon ensuring large-scale crystallographic alignment within the film, with the *a*-axis aligned perpendicular to the device interface. This architecture would maximize the transport of triplet excitons to any harvesting layer, and may hence improve the

efficiencies of SF-sensitized PV devices.

Triplet exciton diffusion coefficients within crystalline TIPS-Pn were quantified here by kinetic modelling of experimental data and from constrained DFT configuration-interaction (CDFT-CI) calculations. While these methods likely give reasonable order-of-magnitude estimates, both of these techniques rely upon significant assumptions that likely introduce some level of error into the computed diffusion coefficients. Further experiments should therefore aim to quantify the anisotropic triplet exciton diffusion coefficients in crystalline TIPS-Pn to a higher level of accuracy. Transient absorption microscopy or similar techniques would be well suited for this, as such experiments spatially map the evolution of exciton distributions over time and may hence allow for direct imaging of the anisotropy in triplet exciton diffusion within crystalline TIPS-Pn.

The kinetic modelling presented in Chapter 4 assumed that TTA in crystalline TIPS-Pn occurred only through the singlet channel, but no spectroscopic evidence was observed for the re-formation of singlet excitons following TTA. It was inferred that these singlets relaxed to the ground state very rapidly and were hence undetectable within the experimental resolution here. However, a recent study of crystalline pentacene demonstrated that TTA formed a ^{1}(TT) pair state capable of radiative decay via a Herzberg-Teller mechanism.[76] This possibility was not considered in the present work, but may explain the lack of observable singlet excitons arising from TTA. Additionally, the data presented here observed a spectral red-shift in the negative TA signal between 700 nm and 750 nm over time, which was attributed to a shift in the TIPS-Pn ground-state bleach (GSB) due to trapping of triplet excitons at low-energy sites. However, emission from the pentacene ^{1}(TT) state also occurs in this spectral range,[76] and so this shift may instead be due to stimulated emission (SE) from radiative ^{1}(TT) excitons formed from TTA. Future experiments could hence investigate the possibility of TTA in TIPS-Pn forming emissive ^{1}(TT) excitons, using time-resolved photoluminescence methods to probe for delayed fluorescence in the red or near-infrared spectral regions.

Chapter 5 investigated the effect of particle size on the photophysical properties of amorphous TIPS-Pn NPs, and observed significant size-dependencies in both SF yield and exciton dynamics. Time-resolved fluorescence experiments demonstrated that the singlet exciton lifetime increased by over an order of magnitude upon decreasing NP diameter from 81 nm to 33 nm. TA spectroscopy measurements showed that this longer singlet lifetime was concurrent with a slower formation of triplet excitons in amorphous TIPS-Pn, indicating that this change in singlet lifetime arose from a slower SF rate at smaller particle sizes. Faster decay of both triplet and triplet-pair excitons was also observed for smaller NPs, attributed to accelerated geminate triplet recombination and faster non-radiative ^{1}(TT) relaxation. Spectral deconvolution and kinetic modelling of this TA data identified that SF yield decreased for smaller NPs, attributed to an additional non-radiative singlet decay pathway becoming significant at small particle sizes. This alternative relaxation channel for singlet excitons within amorphous TIPS-Pn had not previously been identified, and may represent a significant efficiency loss mechanism for SF in disordered acene materials. The size-dependent exciton dynamics and SF yields observed here were ascribed to the NP morphologies becoming more disordered at smaller sizes, possibly due to intermolecular packing constraints imposed by the curvature at the NP surface. This study was the first identification of size-dependent exciton behaviour in amorphous TIPS-Pn NPs, which rationalized quantitative disagreements in the literature regarding exciton dynamics in amorphous TIPS-Pn and therefore highlighted that size-dependent properties must be accounted

for when using small NPs as model systems for bulk materials. However, the exciton kinetics of 81-nm NPs studied here agreed with those previously reported for TIPS-Pn films, indicating that NPs of this size or larger are likely reasonable models for bulk amorphous TIPS-Pn.

A key result of this study was that while all NP sizes studied here exhibited steady-state spectral features that were characteristic of amorphous TIPS-Pn, their size-dependent exciton behavior indicated that they actually possessed significantly different morphologies. Therefore, TIPS-Pn morphologies that are classed as "amorphous" may exhibit significant heterogeneity, as they may contain varying degrees of disorder within their intermolecular packing. A similar effect was recently observed in thin films of disordered rubrene, with SF kinetics that varied dramatically with film thickness.[111] This was attributed to the chromophore morphology changing with film thickness, despite all film thicknesses exhibiting steady-state spectral features highly characteristic of amorphous rubrene. Such morphological variation with rubrene film thickness is presumably similar to the size-dependent morphology changes observed here for TIPS-Pn NPs, with small thicknesses or particle sizes constraining the intermolecular packing. Future experiments should attempt to verify this by testing for both film-thickness and particle-size effects in the same material, either TIPS-Pn or rubrene. Any such correlation of film-thickness and particle-size effects could help to develop a deeper understanding of the exact morphological changes occurring, as films are more suitable than NP dispersions for characterization through imaging methods such as electron microscopy (EM) or atomic force microscopy (AFM). Additionally, if size-dependent NP properties are found to correspond to similar film-thickness effects, small NPs such as those studied here may prove useful in modelling the exciton dynamics within thin films.

Further work could also explore the nature of the non-radiative, non-SF decay pathway for singlet excitons identified here in small TIPS-Pn NPs. The exact mechanism of this singlet quenching was unclear from the data presented here, but the most likely cause is internal conversion through nuclear motions enabled by morphologies formed at small NP sizes. Identification of any vibrational modes associated with this non-radiative exciton decay may be possible through two-dimensional electronic spectroscopy (2DES) or other multidimensional spectroscopic techniques. 2DES has previously been used to identify the nuclear motions associated with rapid exciton decay in polymer blends,[275] and a recent study used this technique to characterize the vibronic couplings associated with the lowest-energy singlet excitons in solvated TIPS-Pn molecules.[276] Understanding the exact role of molecular vibrations in singlet deactivation may have implications beyond the study of TIPS-Pn NPs, as it could influence the design of future SF chromophores to minimize such undesirable efficiency-loss pathways.

Chapter 6 extended this examination of particle-size effects to include crystalline TIPS-Pn NPs, presenting the first systematic investigation into size-dependent NP properties due to both morphological changes and exciton confinement effects. No changes in the kinetics of either SF or TTA were observed for NPs ranging in diameter from 38 nm to 62 nm, despite the previous chapter demonstrating considerable size-dependent behaviour in amorphous TIPS-Pn NPs over this size range. These results therefore indicated that negligible morphological changes occur over this range of particle sizes in crystalline TIPS-Pn. Kinetic Monte Carlo (KMC) simulations were used to model triplet exciton dynamics over a wide range of NP sizes and excitation densi-

ties, and predicted that geminate recombination of triplet pairs would exhibit strongly size-dependent kinetics in crystalline TIPS-Pn NPs due to exciton confinement effects. However, these simulations also indicated that these triplet decay kinetics would become size-independent at sufficiently large particle sizes, at which excitons are much more likely to encounter one another than a domain boundary and so bimolecular TTA dominates triplet decay, with kinetics that resemble those of bulk crystalline TIPS-Pn. A stochastic theory was constructed to predict the critical NP size at which size-dependent geminate recombination kinetics converged to size-independent bimolecular TTA dynamics in crystalline TIPS-Pn NPs, with good agreement observed between theory and KMC models. However, this theory indicated that size-dependent triplet dynamics due to exciton confinement occurred only at very low excitation densities or extremely small NP sizes, neither of which were experimentally achievable here. This region of size-dependent triplet kinetics is therefore largely irrelevant for experimental studies of crystalline TIPS-Pn NPs and so minimal size-dependent exciton behavior can complicate the interpretation of results from such systems, therefore demonstrating that NP suspensions are good models for bulk crystalline TIPS-Pn. The theory developed here can also be generalized to other organic semiconducting materials, and may therefore inform the design of future experiments by predicting NP sizes at which confinement effects are relevant.

No size-dependent triplet exciton dynamics due to exciton confinement were experimentally observable in this work, due to the limited range of excitation densities accessible with the TA spectrometer used here. Future work should aim to conduct similar experiments at significantly lower laser fluences, to access this size-dependent region dominated by geminate triplet recombination and hence probe for these exciton confinement effects. TA spectrometers with higher sensitivity and signal-to-noise than the apparatus employed here do exist, and so careful experimentation should be able to record TA spectra of crystalline TIPS-Pn NPs in the region of size-dependent kinetics.

It would also be informative to extend this study of exciton confinement effects to materials permitting triplet mobility in a different number of dimensions. The results obtained here are strongly influenced by the two-dimensional (2D) restriction of triplet excitons within crystalline TIPS-Pn, but other SF chromophores possess crystallographic packings that allow for triplet mobility in one or three dimensions. As an example, 6,13-(triethylsilylethynyl)pentacene (TES-Pn) contains the same pentacene core as TIPS-Pn, but its smaller TES-substituents constrain its crystal structure to a 1D slip-stacked geometry.[124,209] 1D triplet mobility within crystalline TES-Pn would hence be expected, which may yield more pronounced exciton confinement effects than for 2D diffusion. Future experiments could therefore be designed to test for size-dependent exciton behavior in crystalline TES-Pn NPs, which may be easier to observe under standard experimental conditions than the studies here with TIPS-Pn. Exciton confinement may also be influenced by varying the NP shape, using anisotropic architectures such as nanorods or nanoplatelets. Preparation of high-aspect-ratio structures could increase the level of domain confinement relative to the spherical NPs used here, resulting in more pronounced size-dependent exciton behavior. To the best of our knowledge there are currently no reports of non-spherical TIPS-Pn nanostructures, but nanorod morphologies have been previously described for pentacene and other pentacene derivatives,[277–279] and so preparation of analogous TIPS-Pn materials may be possible.

It is worth noting that the materials considered in this thesis are model systems for

studying intermolecular SF, and are unlikely to be incorporated into any commercial photovoltaic (PV) devices. The T_1 state of TIPS-Pn (0.86 eV; Figure 4.14) is lower in energy than the silicon band-gap (1.1 eV[23]), and so TIPS-Pn triplets formed through SF cannot transfer into the conduction band of any silicon-based PV device. However, many of the conclusions presented in this thesis may have significant implications for the design of PV devices sensitized with other SF chromophores. The findings presented in Chapter 4 regarding anisotropic triplet exciton diffusion will likely be applicable to any organic chromophore, and may hence guide the alignment of SF sensitizer layers. Similarly, the size-dependent exciton dynamics uncovered in Chapters 5 & 6 may be relevant for films of other chromophores, and so understanding these effects could hence inform decisions regarding layer thickness in SF-sensitized PV devices. Finally, the periodicity-induced crystallization investigated in Chapter 3 presents a novel means of morphological control for small organic molecules, which may prove useful in constructing chromophore layers with a desired morphology or crystal alignment for SF-sensitized PV devices.

References

[1] Hudson, R. J.; de la Perrelle, J. M.; Pensack, R. D.; Kudisch, B.; Scholes, G. D.; Huang, D. M.; Kee, T. W. Organizing Crystalline Functionalized Pentacene Using Periodicity of Poly(Vinyl Alcohol). *J. Phys. Chem. Lett.* **2020**, *11*, 516–523.

[2] Hudson, R. J.; Huang, D. M.; Kee, T. W. Anisotropic Triplet Exciton Diffusion in Crystalline Functionalized Pentacene. *J. Phys. Chem. C* **2020**, *124*, 23541–23550.

[3] Hudson, R. J.; Stuart, A. N.; de la Perrelle, J. M.; Huang, D. M.; Kee, T. W. Nanoparticle Size–Dependent Singlet Fission and Exciton Dynamics in Amorphous TIPS-Pentacene. *J. Phys. Chem. C* **2021**, *125*, 21559–21570.

[4] Hudson, R. J.; Huang, D. M.; Kee, T. W. Confinement Effects Upon Triplet Exciton Dynamics in Crystalline TIPS-Pentacene Nanoparticles. **2022**, manuscript in preparation.

[5] Hudson, R. J.; Stuart, A. N.; Huang, D. M.; Kee, T. W. What Next for Singlet Fission in Photovoltaics? The Fate of Triplet and Triplet-Pair Excitons. *J. Phys. Chem. C* **2022**, accepted for publication. DOI: 10.1021/acs.jpcc.2c00273.

[6] International Energy Agency, Key World Energy Statistics 2020. 2020; https://www.iea.org/reports/key-world-energy-statistics-2020.

[7] Lee, J. Y.; Marotzke, J.; Bala, G.; Cao, L.; Corti, S.; Dunne, J. P.; Engelbrecht, F.; Fischer, E.; Fyfe, J. C.; Jones, C.; Maycock, A.; Mutemi, J.; Ndiaye, O.; Panickal, S.; Zhou, T. In *Climate Change 2021: The Physical Science Basis. Contribution of Working Group I to the Sixth Assessment Report of the Intergovernmental Panel on Climate Change*; Masson-Delmotte, V. et al. , Eds.; Cambridge University Press, 2021; Chapter 4: Future Global Climate: Scenario-Based Projections and Near-Term Information.

[8] Gratzel, M. Photoelectrochemical Cells. *Nature* **2001**, *414*, 338–344.

[9] Department of Industry, Science, Energy and Resources, Australian Energy Statistics, Table O: Electricity Generation by Fuel Type 2019-20 and 2020. 2021; https://www.energy.gov.au/publications/australian-energy-statistics-table-o-electricity-generation-fuel-type-2019-20-and-2020.

[10] Shockley, W.; Queisser, H. J. Detailed Balance Limit of Efficiency of p-n Junction Solar Cells. *J. Appl. Phys.* **1961**, *32*, 510–519.

[11] Archer, M. D.; Bolton, J. R. Requirements for Ideal Performance of Photochemical and Photovoltaic Solar Energy Converters. *J. Phys. Chem.* **1990**, *94*, 8028–8036.

[12] Tiedje, T.; Yablonovitch, E.; Cody, G. D.; Brooks, B. G. Limiting Efficiency of Silicon Solar Cells. *IEEE Trans. Electron. Devices* **1984**, *31*, 711–716.

[13] Turro, N. J.; Ramamurthy, V.; Scaiano, J. *Principles of Molecular Photochemistry*; University Science Books: Sausalito, California, USA, 2009.

[14] Yoshikawa, K.; Kawasaki, H.; Yoshida, W.; Irie, T.; Konishi, K.; Nakano, K.; Uto, T.; Adachi, D.; Kanematsu, M.; Uzu, H.; Yamamoto, K. Silicon Heterojunction Solar Cell with Interdigitated Back Contacts for a Photoconversion Efficiency over 26%. *Nat. Energy* **2017**, *2*, 17032.

[15] Green, M. A.; Dunlop, E. D.; Hohl-Ebinger, J.; Yoshita, M.; Kopidakis, N.; Hao, X. Solar Cell Efficiency Tables (Version 58). *Prog. Photovolt. Res. Appl.* **2021**, *29*, 657–667.

[16] De Vos, A. Detailed Balance Limit of the Efficiency of Tandem Solar Cells. *J. Phys. D: Appl. Phys.* **1980**, *13*, 839–846.

[17] Beery, D.; Schmidt, T. W.; Hanson, K. Harnessing Sunlight via Molecular Photon Upconversion. *ACS Appl. Mater. Interfaces* **2021**, *13*, 32601–32605.

[18] Hanna, M. C.; Nozik, A. J. Solar Conversion Efficiency of Photovoltaic and Photoelectrolysis Cells with Carrier Multiplication Absorbers. *J. Appl. Phys.* **2006**, *100*, 074510.

[19] Smith, M. B.; Michl, J. Recent Advances in Singlet Fission. *Annu. Rev. Phys. Chem.* **2013**, *64*, 361–386.

[20] Miyata, K.; Conrad-Burton, F. S.; Geyer, F. L.; Zhu, X.-Y. Triplet Pair States in Singlet Fission. *Chem. Rev.* **2019**, *119*, 4261–4292.

[21] Futscher, M.; Rao, A.; Ehrler, B. The Potential of Singlet Fission Photon Multipliers as an Alternative to Silicon-Based Tandem Solar Cells. *ACS Energy Lett.* **2018**, *3*, 2587–2592.

[22] Tayebjee, M. J. Y.; Gray-Weale, A. A.; Schmidt, T. W. Thermodynamic Limit of Exciton Fission Solar Cell Efficiency. *J. Phys. Chem. Lett.* **2012**, *3*, 2749–2754.

[23] Tayebjee, M. J. Y.; McCamey, D. R.; Schmidt, T. W. Beyond Shockley–Queisser: Molecular Approaches to High-Efficiency Photovoltaics. *J. Phys. Chem. Lett.* **2015**, *6*, 2367–2378.

[24] Tayebjee, M. J. Y.; Mahboubi Soufiani, A.; Conibeer, G. J. Semi-Empirical Limiting Efficiency of Singlet-Fission-Capable Polyacene/Inorganic Hybrid Solar Cells. *J. Phys. Chem. C* **2014**, *118*, 2298–2305.

[25] Daiber, B.; van den Hoven, K.; Futscher, M. H.; Ehrler, B. Realistic Efficiency Limits for Singlet-Fission Silicon Solar Cells. *ACS Energy Lett.* **2021**, *6*, 2800–2808.

[26] Lloyd, M.; Mayer, A.; Tayi, A.; Bowen, A.; Kasen, T.; Herman, D.; Mourey, D.; Anthony, J.; Malliaras, G. Photovoltaic Cells from a Soluble Pentacene Derivative. *Org. Electron.* **2006**, *7*, 243–248.

[27] Yang, L.; Tabachnyk, M.; Bayliss, S. L.; Böhm, M. L.; Broch, K.; Greenham, N. C.; Friend, R. H.; Ehrler, B. Solution-Processable Singlet Fission Photovoltaic Devices. *Nano Lett.* **2015**, *15*, 354–358.

[28] Congreve, D. N.; Lee, J.; Thompson, N. J.; Hontz, E.; Yost, S. R.; Reusswig, P. D.; Bahlke, M. E.; Reineke, S.; Van Voorhis, T.; Baldo, M. A. External Quantum Efficiency Above 100% in a Singlet-Exciton-Fission–Based Organic Photovoltaic Cell. *Science* **2013**, *340*, 334–337.

[29] Jadhav, P. J.; Brown, P. R.; Thompson, N.; Wunsch, B.; Mohanty, A.; Yost, S. R.; Hontz, E.; Van Voorhis, T.; Bawendi, M. G.; Bulović, V.; Baldo, M. A. Triplet Exciton Dissociation in Singlet Exciton Fission Photovoltaics. *Adv. Mater.* **2012**, *24*, 6169–6174.

[30] Pazos-Outón, L. M.; Lee, J. M.; Futscher, M. H.; Kirch, A.; Tabachnyk, M.; Friend, R. H.; Ehrler, B. A Silicon-Singlet Fission Tandem Solar Cell Exceeding 100% External Quantum Efficiency with High Spectral Stability. *ACS Energy Lett.* **2017**, *2*, 476–480.

[31] Kunzmann, A.; Gruber, M.; Casillas, R.; Zirzlmeier, J.; Stanzel, M.; Peukert, W.; Tykwinski, R. R.; Guldi, D. M. Singlet Fission for Photovoltaics with 130 % Injection Efficiency. *Angew. Chem. Int. Ed.* **2018**, *57*, 10742–10747.

[32] Einzinger, M.; Wu, T.; Kompalla, J. F.; Smith, H. L.; Perkinson, C. F.; Nienhaus, L.; Wieghold, S.; Congreve, D. N.; Kahn, A.; Bawendi, M. G.; Baldo, M. A. Sensitization of Silicon by Singlet Exciton Fission in Tetracene. *Nature* **2019**, *571*, 90–94.

[33] Ullrich, T.; Munz, D.; Guldi, D. M. Unconventional Singlet Fission Materials. *Chem. Soc. Rev.* **2021**, *50*, 3485–3518.

[34] Bhattacharyya, K.; Datta, A. Polymorphism Controlled Singlet Fission in TIPS-Anthracene: Role of Stacking Orientation. *J. Phys. Chem. C* **2017**, *121*, 1412–1420.

[35] Mastron, J. N.; Roberts, S. T.; McAnally, R. E.; Thompson, M. E.; Bradforth, S. E. Aqueous Colloidal Acene Nanoparticles: A New Platform for Studying Singlet Fission. *J. Phys. Chem. B* **2013**, *117*, 15519–15526.

[36] Monahan, N.; Zhu, X.-Y. Charge Transfer-Mediated Singlet Fission. *Annu. Rev. Phys. Chem.* **2015**, *66*, 601–618.

[37] Felter, K.; Grozema, F. C. Singlet Fission in Crystalline Organic Materials: Recent Insights and Future Directions. *J. Phys. Chem. Lett.* **2019**, *10*, 7208–7214.

[38] Teichen, P. E.; Eaves, J. D. A Microscopic Model of Singlet Fission. *J. Phys. Chem. B* **2012**, *116*, 11473–11481.

[39] Havenith, R. W.; de Gier, H. D.; Broer, R. Explorative Computational Study of the Singlet Fission Process. *Mol. Phys.* **2012**, *110*, 2445–2454.

[40] Berkelbach, T. C.; Hybertsen, M. S.; Reichman, D. R. Microscopic Theory of Singlet Exciton Fission. II. Application to Pentacene Dimers and the Role of Superexchange. *J. Chem. Phys.* **2013**, *138*, 114103.

[41] Mauck, C. M.; Hartnett, P. E.; Wu, Y.-L.; Miller, C. E.; Marks, T. J.; Wasielewski, M. R. Singlet Fission within Diketopyrrolopyrrole Nanoparticles in Water. *Chem. Mater.* **2017**, *29*, 6810–6817.

[42] Zirzlmeier, J.; Casillas, R.; Reddy, R.; Coto, P. B.; Lehnherr, D.; Chernick, E. T.; Papadopoulos, I.; Thoss, M.; Tykwinski, R. R.; Guldi, D. M. Solution-Based Intramolecular Singlet Fission in Cross-Conjugated Pentacene Dimers. *Nanoscale* **2016**, *8*, 10113–10123.

[43] Basel, B. S.; Zirzlmeier, J.; Hetzer, C.; Reddy, S. R.; Phelan, B. T.; Krzyaniak, M. D.; Volland, M. K.; Coto, P. B.; Young, R. M.; Clark, T.; Thoss, M.;

Tykwinski, R. R.; Wasielewski, M. R.; Guldi, D. M. Evidence for Charge-Transfer Mediation in the Primary Events of Singlet Fission in a Weakly Coupled Pentacene Dimer. *Chem* **2018**, *4*, 1092–1111.

[44] Margulies, E. A.; Miller, C. E.; Wu, Y.; Ma, L.; Schatz, G. C.; Young, R. M.; Wasielewski, M. R. Enabling Singlet Fission by Controlling Intramolecular Charge Transfer in Pi-Stacked Covalent Terrylenediimide Dimers. *Nat. Chem.* **2016**, *8*, 1120–1125.

[45] Lukman, S.; Musser, A. J.; Chen, K.; Athanasopoulos, S.; Yong, C. K.; Zeng, Z.; Ye, Q.; Chi, C.; Hodgkiss, J. M.; Wu, J.; Friend, R. H.; Greenham, N. C. Tuneable Singlet Exciton Fission and Triplet–Triplet Annihilation in an Orthogonal Pentacene Dimer. *Adv. Funct. Mater.* **2015**, *25*, 5452–5461.

[46] Chan, W.-L.; Ligges, M.; Jailaubekov, A.; Kaake, L.; Miaja-Avila, L.; Zhu, X.-Y. Observing the Multiexciton State in Singlet Fission and Ensuing Ultrafast Multielectron Transfer. *Science* **2011**, *334*, 1541.

[47] Bakulin, A. A.; Morgan, S. E.; Kehoe, T. B.; Wilson, M. W. B.; Chin, A. W.; Zigmantas, D.; Egorova, D.; Rao, A. Real-Time Observation of Multiexcitonic States in Ultrafast Singlet Fission Using Coherent 2D Electronic Spectroscopy. *Nat. Chem.* **2016**, *8*, 16–23.

[48] Miyata, K.; Kurashige, Y.; Watanabe, K.; Sugimoto, T.; Takahashi, S.; Tanaka, S.; Takeya, J.; Yanai, T.; Matsumoto, Y. Coherent Singlet Fission Activated by Symmetry Breaking. *Nat. Chem.* **2017**, *9*, 983–989.

[49] Mandal, A.; Chen, M.; Foszcz, E. D.; Schultz, J. D.; Kearns, N. M.; Young, R. M.; Zanni, M. T.; Wasielewski, M. R. Two-Dimensional Electronic Spectroscopy Reveals Excitation Energy-Dependent State Mixing during Singlet Fission in a Terrylenediimide Dimer. *J. Am. Chem. Soc.* **2018**, *140*, 17907–17914.

[50] Chan, W.-L.; Ligges, M.; Zhu, X.-Y. The Energy Barrier in Singlet Fission can be Overcome Through Coherent Coupling and Entropic Gain. *Nat. Chem.* **2012**, *4*, 840–845.

[51] Stern, H. L.; Cheminal, A.; Yost, S. R.; Broch, K.; Bayliss, S. L.; Chen, K.; Tabachnyk, M.; Thorley, K.; Greenham, N.; Hodgkiss, J. M.; Anthony, J.; Head-Gordon, M.; Musser, A. J.; Rao, A.; Friend, R. H. Vibronically Coherent Ultrafast Triplet-Pair Formation and Subsequent Thermally Activated Dissociation Control Efficient Endothermic Singlet Fission. *Nat. Chem.* **2017**, *9*, 1205–1212.

[52] Musser, A. J.; Liebel, M.; Schnedermann, C.; Wende, T.; Kehoe, T. B.; Rao, A.; Kukura, P. Evidence for Conical Intersection Dynamics Mediating Ultrafast Singlet Exciton Fission. *Nat. Phys.* **2015**, *11*, 352–357.

[53] Deng, G.-H.; Qian, Y.; Li, X.; Zhang, T.; Jiang, W.; Harutyunyan, A. R.; Chen, G.; Chen, H.; Rao, Y. Singlet Fission Driven by Anisotropic Vibronic Coupling in Single-Crystalline Pentacene. *J. Phys. Chem. Lett.* **2021**, *12*, 3142–3150.

[54] Schultz, J. D.; Shin, J. Y.; Chen, M.; O'Connor, J. P.; Young, R. M.; Ratner, M. A.; Wasielewski, M. R. Influence of Vibronic Coupling on Ultrafast Singlet Fission in a Linear Terrylenediimide Dimer. *J. Am. Chem. Soc.* **2021**, *143*, 2049–2058.

[55] Zeiser, C.; Cruz, C.; Reichman, D. R.; Seitz, M.; Hagenlocher, J.; Chronister, E. L.; Bardeen, C. J.; Tempelaar, R.; Broch, K. Vacancy Control in Acene Blends Links Exothermic Singlet Fission to Coherence. *Nat. Commun.* **2021**, *12*, 5149.

[56] Monahan, N. R.; Sun, D.; Tamura, H.; Williams, K. W.; Xu, B.; Zhong, Y.; Kumar, B.; Nuckolls, C.; Harutyunyan, A. R.; Chen, G.; Dai, H.-L.; Beljonne, D.; Rao, Y.; Zhu, X.-Y. Dynamics of the Triplet-Pair State Reveals the Likely Coexistence of Coherent and Incoherent Singlet Fission in Crystalline Hexacene. *Nat. Chem.* **2017**, *9*, 341–346.

[57] Folie, B. D.; Haber, J. B.; Refaely-Abramson, S.; Neaton, J. B.; Ginsberg, N. S. Long-Lived Correlated Triplet Pairs in a π-Stacked Crystalline Pentacene Derivative. *J. Am. Chem. Soc.* **2018**, *140*, 2326–2335.

[58] Yong, C. K. et al. The Entangled Triplet Pair State in Acene and Heteroacene Materials. *Nat. Commun.* **2017**, *8*, 15953.

[59] Lee, T. S.; Lin, Y. L.; Kim, H.; Pensack, R. D.; Rand, B. P.; Scholes, G. D. Triplet Energy Transfer Governs the Dissociation of the Correlated Triplet Pair in Exothermic Singlet Fission. *J. Phys. Chem. Lett.* **2018**, *9*, 4087–4095.

[60] Korovina, N. V.; Chang, C. H.; Johnson, J. C. Spatial Separation of Triplet Excitons Drives Endothermic Singlet Fission. *Nat. Chem.* **2020**, *12*, 391–398.

[61] Pun, A. B.; Asadpoordarvish, A.; Kumarasamy, E.; Tayebjee, M. J. Y.; Niesner, D.; McCamey, D. R.; Sanders, S. N.; Campos, L. M.; Sfeir, M. Y. Ultra-Fast Intramolecular Singlet Fission to Persistent Multiexcitons by Molecular Design. *Nat. Chem.* **2019**, *11*, 821–828.

[62] Pensack, R. D.; Ostroumov, E. E.; Tilley, A. J.; Mazza, S.; Grieco, C.; Thorley, K. J.; Asbury, J. B.; Seferos, D. S.; Anthony, J. E.; Scholes, G. D. Observation of Two Triplet-Pair Intermediates in Singlet Exciton Fission. *J. Phys. Chem. Lett.* **2016**, *7*, 2370–2375.

[63] Grieco, C.; Doucette, G. S.; Munro, J. M.; Kennehan, E. R.; Lee, Y.; Rimshaw, A.; Payne, M. M.; Wonderling, N.; Anthony, J. E.; Dabo, I.; Gomez, E. D.; Asbury, J. B. Triplet Transfer Mediates Triplet Pair Separation during Singlet Fission in 6,13-Bis(triisopropylsilylethynyl)-Pentacene. *Adv. Funct. Mater.* **2017**, *27*, 1703929.

[64] Scholes, G. D. Correlated Pair States Formed by Singlet Fission and Exciton-Exciton Annihilation. *J. Phys. Chem. A* **2015**, *119*, 12699–12705.

[65] Merrifield, R. E. Magnetic Effects on Triplet Exciton Interactions. *Pure Appl. Chem.* **1971**, *27*, 481–498.

[66] Kim, H.; Zimmerman, P. M. Coupled Double Triplet State in Singlet Fission. *Phys. Chem. Chem. Phys.* **2018**, *20*, 30083–30094.

[67] Burdett, J. J.; Bardeen, C. J. Quantum Beats in Crystalline Tetracene Delayed Fluorescence Due to Triplet Pair Coherences Produced by Direct Singlet Fission. *J. Am. Chem. Soc.* **2012**, *134*, 8597–8607.

[68] Wang, R.; Zhang, C.; Zhang, B.; Liu, Y.; Wang, X.; Xiao, M. Magnetic Dipolar Interaction Between Correlated Triplets Sreated by Singlet Fission in Tetracene

Crystals. *Nat. Commun.* **2015**, *6*, 8602.

[69] Tayebjee, M. J. Y.; Sanders, S. N.; Kumarasamy, E.; Campos, L. M.; Sfeir, M. Y.; McCamey, D. R. Quintet Multiexciton Dynamics in Singlet Fission. *Nat. Phys.* **2016**, *13*, 182–188.

[70] Sakai, H.; Inaya, R.; Nagashima, H.; Nakamura, S.; Kobori, Y.; Tkachenko, N. V.; Hasobe, T. Multiexciton Dynamics Depending on Intramolecular Orientations in Pentacene Dimers: Recombination and Dissociation of Correlated Triplet Pairs. *J. Phys. Chem. Lett.* **2018**, *9*, 3354–3360.

[71] Lubert-Perquel, D.; Szumska, A. A.; Azzouzi, M.; Salvadori, E.; Ruloff, S.; Kay, C. M. W.; Nelson, J.; Heutz, S. Structure Dependence of Kinetic and Thermodynamic Parameters in Singlet Fission Processes. *J. Phys. Chem. Lett.* **2020**, *11*, 9557–9565.

[72] Stuart, A. N.; Tapping, P. C.; Schrefl, E.; Huang, D. M.; Kee, T. W. Controlling the Efficiency of Singlet Fission in TIPS-Pentacene/Polymer Composite Nanoparticles. *J. Phys. Chem. C* **2019**, *123*, 5813–5825.

[73] Zhou, Z.; Ma, L.; Guo, D.; Zhao, X.; Wang, C.; Lin, D.; Zhang, F.; Zhang, J.; Nie, Z. Ultrafast Dynamics of Long-Lived Bound Triplet Pair Generated by Singlet Fission in 6,13-Bis(triisopropylsilylethynyl) Pentacene. *J. Phys. Chem. C* **2020**, *124*, 14503–14509.

[74] Sanders, S. N.; Kumarasamy, E.; Pun, A. B.; Steigerwald, M. L.; Sfeir, M. Y.; Campos, L. M. Intramolecular Singlet Fission in Oligoacene Heterodimers. *Angew. Chem., Int. Ed.* **2016**, *128*, 3434.

[75] Pensack, R. D.; Tilley, A. J.; Grieco, C.; Purdum, G. E.; Ostroumov, E. E.; Granger, D. B.; Oblinsky, D. G.; Dean, J. C.; Doucette, G. S.; Asbury, J. B.; Loo, Y.-L.; Seferos, D. S.; Anthony, J. E.; Scholes, G. D. Striking the Right Balance of Intermolecular Coupling for High-Efficiency Singlet Fission. *Chem. Sci.* **2018**, *9*, 6240–6259.

[76] Bossanyi, D. G.; Matthiesen, M.; Wang, S.; Smith, J. A.; Kilbride, R. C.; Shipp, J. D.; Chekulaev, D.; Holland, E.; Anthony, J. E.; Zaumseil, J.; Musser, A. J.; Clark, J. Emissive Spin-0 Triplet-Pairs are a Direct Product of Triplet-Triplet Annihilation in Pentacene Single Crystals and Anthradithiophene Films. *Nat. Chem.* **2021**, *13*, 163–171.

[77] Förster, T. 10th Spiers Memorial Lecture. Transfer Mechanisms of Electronic Excitation. *Discuss. Faraday Soc.* **1959**, *27*, 7–17.

[78] Hofkens, J.; Cotlet, M.; Vosch, T.; Tinnefeld, P.; Weston, K. D.; Ego, C.; Grimsdale, A.; Müllen, K.; Beljonne, D.; Brédas, J. L.; Jordens, S.; Schweitzer, G.; Sauer, M.; Schryver, F. D. Revealing Competitive Förster-Type Resonance Energy-Transfer Pathways in Single Bichromophoric Molecules. *Proc. Natl. Acad. Sci.* **2003**, *100*, 13146–13151.

[79] Dexter, D. L. A Theory of Sensitized Luminescence in Solids. *J. Chem. Phys.* **1953**, *21*, 836–850.

[80] Yost, S. R.; Hontz, E.; Yeganeh, S.; Van Voorhis, T. Triplet vs Singlet Energy Transfer in Organic Semiconductors: The Tortoise and the Hare. *J. Phys. Chem.*

C **2012**, *116*, 17369–17377.

[81] Mikhnenko, O. V.; Blom, P. W. M.; Nguyen, T.-Q. Exciton Diffusion in Organic Semiconductors. *Energy Environ. Sci.* **2015**, *8*, 1867–1888.

[82] Turner, D. B.; Wilk, K. E.; Curmi, P. M. G.; Scholes, G. D. Comparison of Electronic and Vibrational Coherence Measured by Two-Dimensional Electronic Spectroscopy. *J. Phys. Chem. Lett.* **2011**, *2*, 1904–1911.

[83] Collini, E.; Scholes, G. D. Coherent Intrachain Energy Migration in a Conjugated Polymer at Room Temperature. *Science* **2009**, *323*, 369–373.

[84] Cassette, E.; Pensack, R. D.; Mahler, B.; Scholes, G. D. Room-Temperature Exciton Coherence and Dephasing in Two-Dimensional Nanostructures. *Nat. Commun.* **2015**, *6*, 6086.

[85] Collini, E.; Wong, C. Y.; Wilk, K. E.; Curmi, P. M. G.; Brumer, P.; Scholes, G. D. Coherently Wired Light-Harvesting in Photosynthetic Marine Algae at Ambient Temperature. *Nature* **2010**, *463*, 644–648.

[86] Turner, D. B.; Dinshaw, R.; Lee, K.-K.; Belsley, M. S.; Wilk, K. E.; Curmi, P. M. G.; Scholes, G. D. Quantitative Investigations of Quantum Coherence for a Light-harvesting Protein at Conditions Simulating Photosynthesis. *Phys. Chem. Chem. Phys.* **2012**, *14*, 4857–4874.

[87] Engel, G. S.; Calhoun, T. R.; Read, E. L.; Ahn, T.-K.; Mancal, T.; Cheng, Y.-C.; Blankenship, R. E.; Fleming, G. R. Evidence for Wavelike Energy Transfer Through Quantum Coherence in Photosynthetic Systems. *Nature* **2007**, *446*, 782–786.

[88] Kassal, I.; Yuen-Zhou, J.; Rahimi-Keshari, S. Does Coherence Enhance Transport in Photosynthesis? *J. Phys. Chem. Lett.* **2013**, *4*, 362–367, PMID: 26281724.

[89] Brumer, P. Shedding (Incoherent) Light on Quantum Effects in Light-Induced Biological Processes. *J. Phys. Chem. Lett.* **2018**, *9*, 2946–2955.

[90] Wilkins, D. M.; Dattani, N. S. Why Quantum Coherence Is Not Important in the Fenna-Matthews-Olsen Complex. *J. Chem. Theory Comput.* **2015**, *11*, 3411–3419.

[91] May, V. Kinetic Theory of Exciton-Exciton Annihilation. *J. Chem. Phys.* **2014**, *140*, 054103.

[92] Suna, A. Kinematics of Exciton-Exciton Annihilation in Molecular Crystals. *Phys. Rev. B* **1970**, *1*, 1716–1739.

[93] Dick, B.; Nickel, B. Accessibility of the Lowest Quintet State of Organic Molecules Through Triplet–Triplet Annihilation; An Indo CI Study. *Chem. Phys.* **1983**, *78*, 1–16.

[94] Piland, G. B.; Burdett, J. J.; Kurunthu, D.; Bardeen, C. J. Magnetic Field Effects on Singlet Fission and Fluorescence Decay Dynamics in Amorphous Rubrene. *J. Phys. Chem. C* **2013**, *117*, 1224–1236.

[95] Tapping, P. C.; Huang, D. M. Comment on "Magnetic Field Effects on Singlet Fission and Fluorescence Decay Dynamics in Amorphous Rubrene". *J. Phys. Chem. C* **2016**, *120*, 25151–25157.

[96] Kondakov, D. Y.; Pawlik, T. D.; Hatwar, T. K.; Spindler, J. P. Triplet Annihilation Exceeding Spin Statistical Limit in Highly Efficient Fluorescent Organic Light-Emitting Diodes. *J. Appl. Phys.* **2009**, *106*, 124510.

[97] Cheng, Y. Y.; Fückel, B.; Khoury, T.; Clady, R. G. C. R.; Tayebjee, M. J. Y.; Ekins-Daukes, N. J.; Crossley, M. J.; Schmidt, T. W. Kinetic Analysis of Photochemical Upconversion by Triplet Triplet Annihilation: Beyond Any Spin Statistical Limit. *J. Phys. Chem. Lett.* **2010**, *1*, 1795–1799.

[98] Auckett, J. E.; Chen, Y. Y.; Khoury, T.; Clady, R. G. C. R.; Ekins-Daukes, N. J.; Crossley, M. J.; Schmidt, T. W. Efficient Up-Conversion by Triplet-Triplet Annihilation. *J. Phys. Conf. Ser.* **2009**, *185*, 012002.

[99] Bayliss, S. L.; Chepelianskii, A. D.; Sepe, A.; Walker, B. J.; Ehrler, B.; Bruzek, M. J.; Anthony, J. E.; Greenham, N. C. Geminate and Nongeminate Recombination of Triplet Excitons Formed by Singlet Fission. *Phys. Rev. Lett.* **2014**, *112*, 238701.

[100] Mozumder, A.; Pimblott, S. M. The Influence of the Diffusional Anisotropy on Bimolecular Reaction Rate of Neutrals in Molecular Crystals: Triplet–Triplet Annihilation in Anthracene. *Chem. Phys. Lett.* **1990**, *167*, 542–546.

[101] Grieco, C.; Kennehan, E. R.; Kim, H.; Pensack, R. D.; Brigeman, A. N.; Rimshaw, A.; Payne, M. M.; Anthony, J. E.; Giebink, N. C.; Scholes, G. D.; Asbury, J. B. Direct Observation of Correlated Triplet Pair Dynamics during Singlet Fission Using Ultrafast Mid-IR Spectroscopy. *J. Phys. Chem. C* **2018**, *122*, 2012–2022.

[102] Bayliss, S. L.; Thorley, K. J.; Anthony, J. E.; Bouchiat, H.; Greenham, N. C.; Chepelianskii, A. D. Localization Length Scales of Triplet Excitons in Singlet Fission Materials. *Phys. Rev. B* **2015**, *92*, 115432.

[103] Gösele, U.; Seeger, A. Theory of Bimolecular Reaction Rates Limited by Anisotropic Diffusion. *Phil. Mag.* **1976**, *34*, 177–193.

[104] Hsu, C.-P. The Electronic Couplings in Electron Transfer and Excitation Energy Transfer. *Acc. Chem. Res.* **2009**, *42*, 509–518.

[105] Schmidt, T. W. A Marcus-Hush Perspective on Adiabatic Singlet Fission. *J. Chem. Phys.* **2019**, *151*, 054305.

[106] Yang, C.-H.; Hsu, C.-P. First-Principle Characterization for Singlet Fission Couplings. *J. Phys. Chem. Lett.* **2015**, *6*, 1925–1929.

[107] Tamura, H.; Huix-Rotllant, M.; Burghardt, I.; Olivier, Y.; Beljonne, D. First-Principles Quantum Dynamics of Singlet Fission: Coherent versus Thermally Activated Mechanisms Governed by Molecular π Stacking. *Phys. Rev. Lett.* **2015**, *115*, 107401.

[108] Sanders, S. N.; Kumarasamy, E.; Pun, A. B.; Trinh, M. T.; Choi, B.; Xia, J.; Taffet, E. J.; Low, J. Z.; Miller, J. R.; Roy, X.; Zhu, X.-Y.; Steigerwald, M. L.; Sfeir, M. Y.; Campos, L. M. Quantitative Intramolecular Singlet Fission in Bipentacenes. *J. Am. Chem. Soc.* **2015**, *137*, 8965–8972.

[109] Doucette, G. S.; Huang, H.-T.; Munro, J. M.; Munson, K. T.; Park, C.; Anthony, J. E.; Strobel, T.; Dabo, I.; Badding, J. V.; Asbury, J. B. Tuning Triplet-

Pair Separation versus Relaxation Using a Diamond Anvil Cell. *Cell Rep. Phys. Sci.* **2020**, *1*, 100005.

[110] Grieco, C.; Doucette, G. S.; Pensack, R. D.; Payne, M. M.; Rimshaw, A.; Scholes, G. D.; Anthony, J. E.; Asbury, J. B. Dynamic Exchange During Triplet Transport in Nanocrystalline TIPS-Pentacene Films. *J. Am. Chem. Soc.* **2016**, *138*, 16069–16080.

[111] Chen, C.-H.; Sher, P.-H.; Chen, C.-P.; Choi, W.-K.; Bardeen, C. J.; Chiu, T.-L.; Wang, J.-K.; Lee, J.-H. Thickness-Dependent Exciton Dynamics in Thermally Evaporated Rubrene Thin Films. *J. Phys. Chem. C* **2020**, *124*, 25729–25737.

[112] Piland, G. B.; Bardeen, C. J. How Morphology Affects Singlet Fission in Crystalline Tetracene. *J. Phys. Chem. Lett.* **2015**, *6*, 1841–1846.

[113] Arias, D. H.; Ryerson, J. L.; Cook, J. D.; Damrauer, N. H.; Johnson, J. C. Polymorphism Influences Singlet Fission Rates in Tetracene Thin Films. *Chem. Sci.* **2016**, *7*, 1185–1191.

[114] Zhu, T.; Wan, Y.; Guo, Z.; Johnson, J.; Huang, L. Two Birds with One Stone: Tailoring Singlet Fission for Both Triplet Yield and Exciton Diffusion Length. *Adv. Mater.* **2016**, *28*, 7539–7547.

[115] Han, J.; Xie, Q.; Luo, J.; Deng, G.-H.; Qian, Y.; Sun, D.; Harutyunyan, A. R.; Chen, G.; Rao, Y. Anisotropic Geminate and Non-Geminate Recombination of Triplet Excitons in Singlet Fission of Single Crystalline Hexacene. *J. Phys. Chem. Lett.* **2020**, *11*, 1261–1267.

[116] Marciniak, H.; Pugliesi, I.; Nickel, B.; Lochbrunner, S. Ultrafast Singlet and Triplet Dynamics in Microcrystalline Pentacene Films. *Phys. Rev. B* **2009**, *79*, 235318.

[117] Poletayev, A. D.; Clark, J.; Wilson, M. W. B.; Rao, A.; Makino, Y.; Hotta, S.; Friend, R. H. Triplet Dynamics in Pentacene Crystals: Applications to Fission-Sensitized Photovoltaics. *Adv. Mater.* **2014**, *26*, 919–924.

[118] Berghuis, A. M.; Raziman, T. V.; Halpin, A.; Wang, S.; Curto, A. G.; Rivas, J. G. Effective Negative Diffusion of Singlet Excitons in Organic Semiconductors. *J. Phys. Chem. Lett.* **2021**, *12*, 1360–1366.

[119] Pensack, R. D.; Grieco, C.; Purdum, G. E.; Mazza, S. M.; Tilley, A. J.; Ostroumov, E. E.; Seferos, D. S.; Loo, Y.-L.; Asbury, J. B.; Anthony, J. E.; Scholes, G. D. Solution-Processable, Crystalline Material for Quantitative Singlet Fission. *Mater. Horiz.* **2017**, *4*, 915–923.

[120] Diao, Y.; Lenn, K. M.; Lee, W.-Y.; Blood-Forsythe, M. A.; Xu, J.; Mao, Y.; Kim, Y.; Reinspach, J. A.; Park, S.; Aspuru-Guzik, A.; Xue, G.; Clancy, P.; Bao, Z.; Mannsfeld, S. C. B. Understanding Polymorphism in Organic Semiconductor Thin Films through Nanoconfinement. *J. Am. Chem. Soc.* **2014**, *136*, 17046–17057.

[121] Boehm, B. J.; Nguyen, H. T. L.; Huang, D. M. The Interplay of Interfaces, Supramolecular Assembly, and Electronics in Organic Semiconductors. *J. Phys. Condens. Matter* **2019**, *31*, 423001.

[122] Nagano, M.; Hasegawa, T.; Myoujin, N.; Yamaguchi, J.; Itaka, K.; Fukumoto, H.;

Yamamoto, T.; Koinuma, H. The First Observation of ^{1}H-NMR Spectrum of Pentacene. *Jpn. J. Appl. Phys.* **2004**, *43*, L315–L316.

[123] Campbell, R. B.; Robertson, J. M.; Trotter, J. The Crystal and Molecular Structure of Pentacene. *Acta Crystallogr.* **1961**, *14*, 705–711.

[124] Anthony, J. E.; Eaton, D. L.; Parkin, S. R. A Road Map to Stable, Soluble, Easily Crystallized Pentacene Derivatives. *Org. Lett.* **2002**, *4*, 15–18.

[125] Anthony, J. E.; Brooks, J. S.; Eaton, D. L.; Parkin, S. R. Functionalized Pentacene: Improved Electronic Properties from Control of Solid-State Order. *J. Am. Chem. Soc.* **2001**, *123*, 9482–9483.

[126] Eaton, S. W.; Shoer, L. E.; Karlen, S. D.; Dyar, S. M.; Margulies, E. A.; Veldkamp, B. S.; Ramanan, C.; Hartzler, D. A.; Savikhin, S.; Marks, T. J.; Wasielewski, M. R. Singlet Exciton Fission in Polycrystalline Thin Films of a Slip-Stacked Perylenediimide. *J. Am. Chem. Soc.* **2013**, *135*, 14701–14712.

[127] Jones, A. C.; Kearns, N. M.; Ho, J.-J.; Flach, J. T.; Zanni, M. T. Impact of Non-Equilibrium Molecular Packings on Singlet Fission in Microcrystals Observed using 2D White-Light Microscopy. *Nat. Chem.* **2020**, *12*, 40–47.

[128] Armstrong, Z. T.; Kunz, M. B.; Jones, A. C.; Zanni, M. T. Thermal Annealing of Singlet Fission Microcrystals Reveals the Benefits of Charge Transfer Couplings and Slip-Stacked Packing. *J. Phys. Chem. C* **2020**, *124*, 15123–15131.

[129] Ramanan, C.; Smeigh, A. L.; Anthony, J. E.; Marks, T. J.; Wasielewski, M. R. Competition between Singlet Fission and Charge Separation in Solution-Processed Blend Films of 6,13-Bis(triisopropylsilylethynyl)pentacene with Sterically-Encumbered Perylene-3,4:9,10-bis(dicarboximide)s. *J. Am. Chem. Soc.* **2012**, *134*, 386–397.

[130] Wu, Y.; Liu, K.; Liu, H.; Zhang, Y.; Zhang, H.; Yao, J.; Fu, H. Impact of Intermolecular Distance on Singlet Fission in a Series of TIPS Pentacene Compounds. *J. Phys. Chem. Lett.* **2014**, *5*, 3451–3455.

[131] Ostroverkhova, O.; Shcherbyna, S.; Cooke, D. G.; Egerton, R. F.; Hegmann, F. A.; Tykwinski, R. R.; Parkin, S. R.; Anthony, J. E. Optical and Transient Photoconductive Properties of Pentacene and Functionalized Pentacene Thin Films: Dependence on Film Morphology. *J. Appl. Phys.* **2005**, *98*, 033701.

[132] Chen, J.; Anthony, J.; Martin, D. C. Thermally Induced Solid-State Phase Transition of Bis(triisopropylsilylethynyl) Pentacene Crystals. *J. Phys. Chem. B* **2006**, *110*, 16397–16403.

[133] Tayebjee, M. J. Y.; Schwarz, K. N.; MacQueen, R. W.; Dvořák, M.; Lam, A. W. C.; Ghiggino, K. P.; McCamey, D. R.; Schmidt, T. W.; Conibeer, G. J. Morphological Evolution and Singlet Fission in Aqueous Suspensions of TIPS-Pentacene Nanoparticles. *J. Phys. Chem. C* **2016**, *120*, 157–165.

[134] Pensack, R. D.; Tilley, A. J.; Parkin, S. R.; Lee, T. S.; Payne, M. M.; Gao, D.; Jahnke, A. A.; Oblinsky, D. G.; Li, P.-F.; Anthony, J. E.; Seferos, D. S.; Scholes, G. D. Exciton Delocalization Drives Rapid Singlet Fission in Nanoparticles of Acene Derivatives. *J. Am. Chem. Soc.* **2015**, *137*, 6790–6803.

[135] Walker, B. J.; Musser, A. J.; Beljonne, D.; Friend, R. H. Singlet Exciton Fission in Solution. *Nat. Chem.* **2013**, *5*, 1019–1024.

[136] Grieco, C.; Doucette, G. S.; Munson, K. T.; Swartzfager, J. R.; Munro, J. M.; Anthony, J. E.; Dabo, I.; Asbury, J. B. Vibrational Probe of the Origin of Singlet Exciton Fission in TIPS-pentacene Solutions. *J. Chem. Phys.* **2019**, *151*, 154701.

[137] Dvořák, M.; Prasad, S. K. K.; Dover, C. B.; Forest, C. R.; Kaleem, A.; MacQueen, R. W.; Petty, A. J.; Forecast, R.; Beves, J. E.; Anthony, J. E.; Tayebjee, M. J. Y.; Widmer-Cooper, A.; Thordarson, P.; Schmidt, T. W. Singlet Fission in Concentrated TIPS-Pentacene Solutions: The Role of Excimers and Aggregates. *J. Am. Chem. Soc.* **2021**, *143*, 13749–13758.

[138] Jiang, Y.; McNeill, J. Light-Harvesting and Amplified Energy Transfer in Conjugated Polymer Nanoparticles. *Chem. Rev.* **2017**, *117*, 838–859.

[139] Tuncel, D.; Demir, H. V. Conjugated Polymer Nanoparticles. *Nanoscale* **2010**, *2*, 484–494.

[140] Wang, C.; Tauber, M. J. High-Yield Singlet Fission in a Zeaxanthin Aggregate Observed by Picosecond Resonance Raman Spectroscopy. *J. Am. Chem. Soc.* **2010**, *132*, 13988–13991.

[141] de la Perrelle, J. M. Coherence and Singlet Fission of TIPS-Pentacene Probed by Two-dimensional Electronic Spectroscopy. M.Sc. thesis, Department of Chemistry, The University of Adelaide, Adelaide, SA, 2021.

[142] Munson, K. T.; Gan, J.; Grieco, C.; Doucette, G. S.; Anthony, J. E.; Asbury, J. B. Ultrafast Triplet Pair Separation and Triplet Trapping following Singlet Fission in Amorphous Pentacene Films. *J. Phys. Chem. C* **2020**, *124*, 23567–23578.

[143] Fu, H.-B.; Yao, J.-N. Size Effects on the Optical Properties of Organic Nanoparticles. *J. Am. Chem. Soc.* **2001**, *123*, 1434–1439.

[144] Kasai, H.; Nalwa, H. S.; Oikawa, H.; Okada, S.; Matsuda, H.; Minami, N.; Kakuta, A.; Ono, K.; Mukoh, A.; Nakanishi, H. A Novel Preparation Method of Organic Microcrystals. *Jpn. J. Appl. Phys.* **1992**, *31*, L1132.

[145] Kasai, H.; Kamatani, H.; Okada, S.; Oikawa, H.; Matsuda, H.; Nakanishi, H. Size-Dependent Colors and Luminescences of Organic Microcrystals. *Jpn. J. Appl. Phys.* **1996**, *35*, L221–L223.

[146] Chung, H.-R.; Kwon, E.; Oikawa, H.; Kasai, H.; Nakanishi, H. Effect of Solvent on Organic Nanocrystal Growth using the Reprecipitation Method. *J. Cryst. Growth* **2006**, *294*, 459–463.

[147] Mori, J.; Miyashita, Y.; Oliveira, D.; Kasai, H.; Oikawa, H.; Nakanishi, H. Stopped-Flow Analysis on the Mechanism of Perylene Nanoparticle Formation by the Reprecipitation Method. *J. Cryst. Growth* **2009**, *311*, 553–555.

[148] Chaplin, M. Theory vs Experiment: What is the Surface Charge of Water? *Water* **2009**, *1*, 1–28.

[149] Nagai, M.; Huang, J.; Cui, D.; Wang, Z.; Huang, W. Two-Step Reprecipitation Method with Size and Zeta Potential Controllability for Synthesizing Semiconducting Polymer Nanoparticles. *Colloid. Polym. Sci.* **2017**, *295*, 1153–1164.

[150] Gray-Weale, A.; Beattie, J. K. An Explanation for the Charge on Water's Surface. *Phys. Chem. Chem. Phys.* **2009**, *11*, 10994–11005.

[151] Buch, V.; Milet, A.; Vácha, R.; Jungwirth, P.; Devlin, J. P. Water Surface is Acidic. *Proc. Natl. Acad. Sci.* **2007**, *104*, 7342–7347.

[152] Vácha, R.; Marsalek, O.; Willard, A. P.; Bonthuis, D. J.; Netz, R. R.; Jungwirth, P. Charge Transfer between Water Molecules As the Possible Origin of the Observed Charging at the Surface of Pure Water. *J. Phys. Chem. Lett.* **2012**, *3*, 107–111.

[153] Lee, V. E.; Scott, D. M.; Prud'homme, R. K.; Priestley, R. D. In *Polymer Colloids: Formation, Characterization and Applications*; Priestley, R. D., Prud'homme, R. K., Eds.; Royal Society of Chemistry, 2019; Vol. 9; Chapter Flash Nano-Precipitation and -Complexation to Produce Polymer Colloids, pp 61–99.

[154] Fudickar, W.; Linker, T. Why Triple Bonds Protect Acenes from Oxidation and Decomposition. *J. Am. Chem. Soc.* **2012**, *134*, 15071–15082.

[155] Lopez, R.; Feldman, L. C.; Haglund, R. F. Size-Dependent Optical Properties of VO_2 Nanoparticle Arrays. *Phys. Rev. Lett.* **2004**, *93*, 177403.

[156] Hoo, C. M.; Starostin, N.; West, P.; Mecartney, M. L. A Comparison of Atomic Force Microscopy (AFM) and Dynamic Light Scattering (DLS) Methods to Characterize Nanoparticle Size Distributions. *J. Nanopart. Res.* **2008**, *10*, 89–96.

[157] Pappas, I.; Fitzgerald, M.; Huang, X.-Y.; Li, J.; Pan, L. Thermally Resolved in Situ Dynamic Light Scattering Studies of Zirconium(IV) Complex Formation. *Cryst. Growth Des.* **2009**, *9*, 5213–5219.

[158] Kaszuba, M.; McKnight, D.; Connah, M. T.; McNeil-Watson, F. K.; Nobbmann, U. Measuring Sub Nanometre Sizes Using Dynamic Light Scattering. *J. Nanopart. Res.* **2008**, *10*, 823–829.

[159] Cao, A. Light Scattering. Recent Applications. *Anal. Lett.* **2003**, *36*, 3185–3225.

[160] Einstein, A. Über die von der molekularkinetischen Theorie der Wärme geforderte Bewegung von in ruhenden Flüssigkeiten suspendierten Teilchen. *Ann. Phys.* **1905**, *322*, 549–560.

[161] Finsy, R.; De Jaeger, N. Particle Sizing by Photon Correlation Spectroscopy. Part II: Average values. *Part. Part. Syst. Charact.* **1991**, *8*, 187–193.

[162] Koppel, D. E. Analysis of Macromolecular Polydispersity in Intensity Correlation Spectroscopy: The Method of Cumulants. *J. Chem. Phys.* **1972**, *57*, 4814–4820.

[163] Schrödinger, E. An Undulatory Theory of the Mechanics of Atoms and Molecules. *Phys. Rev.* **1926**, *28*, 1049–1070.

[164] Born, M.; Oppenheimer, R. Zur Quantentheorie der Molekeln. *Ann. Phys.* **1927**, *389*, 457–484.

[165] Hohenberg, P.; Kohn, W. Inhomogeneous Electron Gas. *Phys. Rev.* **1964**, *136*, B864–B871.

[166] Kohn, W.; Sham, L. J. Self-Consistent Equations Including Exchange and Correlation Effects. *Phys. Rev.* **1965**, *140*, A1133–A1138.

[167] Frisch, M. J. et al. Gaussian 16 Revision C.01. 2016; Gaussian Inc. Wallingford CT.

[168] Shao, Y. et al. Advances in Molecular Quantum Chemistry Contained in the Q-Chem 4 Program Package. *Mol. Phys.* **2015**, *113*, 184–215.

[169] Dederichs, P. H.; Blügel, S.; Zeller, R.; Akai, H. Ground States of Constrained Systems: Application to Cerium Impurities. *Phys. Rev. Lett.* **1984**, *53*, 2512–2515.

[170] Wu, Q.; Van Voorhis, T. Direct Optimization Method to Study Constrained Systems Within Density-Functional Theory. *Phys. Rev. A* **2005**, *72*, 024502.

[171] Yeganeh, S.; Van Voorhis, T. Triplet Excitation Energy Transfer with Constrained Density Functional Theory. *J. Phys. Chem. C* **2010**, *114*, 20756–20763.

[172] Tapping, P. C.; Clafton, S. N.; Schwarz, K. N.; Kee, T. W.; Huang, D. M. Molecular-Level Details of Morphology-Dependent Exciton Migration in Poly(3-hexylthiophene) Nanostructures. *J. Phys. Chem. C* **2015**, *119*, 7047–7059.

[173] Kroeze, J. E.; Savenije, T. J.; Candeias, L. P.; Warman, J. M.; Siebbeles, L. D. Triplet Exciton Diffusion and Delayed Interfacial Charge Separation in a TiO_2/PdTPPC Bilayer: Monte Carlo Simulations. *Sol. Energ. Mat. Sol.* **2005**, *85*, 189–203.

[174] Daniel, C.; Westenhoff, S.; Makereel, F.; Friend, R. H.; Beljonne, D.; Herz, L. M.; Silva, C. Monte Carlo Simulation of Exciton Bimolecular Annihilation Dynamics in Supramolecular Semiconductor Architectures. *J. Phys. Chem. C* **2007**, *111*, 19111–19119.

[175] Barford, W.; Bittner, E. R.; Ward, A. Exciton Dynamics in Disordered Poly(p-phenylenevinylene). 2. Exciton Diffusion. *J. Phys. Chem. A* **2012**, *116*, 10319–10327.

[176] Athanasopoulos, S.; Hennebicq, E.; Beljonne, D.; Walker, A. B. Trap Limited Exciton Transport in Conjugated Polymers. *J. Phys. Chem. C* **2008**, *112*, 11532–11538.

[177] Lee, J.; Jadhav, P.; Reusswig, P. D.; Yost, S. R.; Thompson, N. J.; Congreve, D. N.; Hontz, E.; Van Voorhis, T.; Baldo, M. A. Singlet Exciton Fission Photovoltaics. *Acc. Chem. Res.* **2013**, *46*, 1300–1311.

[178] Le, A. K.; Bender, J. A.; Arias, D. H.; Cotton, D. E.; Johnson, J. C.; Roberts, S. T. Singlet Fission Involves an Interplay between Energetic Driving Force and Electronic Coupling in Perylenediimide Films. *J. Am. Chem. Soc.* **2018**, *140*, 814–826.

[179] Masoomi-Godarzi, S.; Liu, M.; Tachibana, T.; Goerigk, L.; Ghiggino, K. P.; Smith, T. A.; Jones, D. J. Solution-Processable, Solid State Donor–Acceptor Materials for Singlet Fission. *Adv. Energy Mater.* **2018**, *8*, 1801720.

[180] Hetzer, C.; Guldi, D. M.; Tykwinski, R. R. Pentacene Dimers as a Critical Tool for the Investigation of Intramolecular Singlet Fission. *Chem. Eur. J.* **2018**, *24*, 8245–8257.

[181] Wilson, M. W. B.; Rao, A.; Ehrler, B.; Friend, R. H. Singlet Exciton Fission in Polycrystalline Pentacene: From Photophysics toward Devices. *Acc. Chem. Res.*

2013, *46*, 1330–1338.

[182] Pun, J. K. H.; Gallaher, J. K.; Frazer, L.; Prasad, S. K. K.; Dover, C. B.; MacQueen, R. W.; Schmidt, T. W. TIPS-Anthracene: A Singlet Fission or Triplet Fusion Material? *J. Photonics Energy* **2018**, *8*, 022006.

[183] Dover, C. B.; Gallaher, J. K.; Frazer, L.; Tapping, P. C.; Petty II, A. J.; Crossley, M. J.; Anthony, J. E.; Kee, T. W.; Schmidt, T. W. Endothermic Singlet Fission is Hindered by Excimer Formation. *Nat. Chem.* **2018**, *10*, 305–310.

[184] Pace, N. A.; Arias, D. H.; Granger, D. B.; Christensen, S.; Anthony, J. E.; Johnson, J. C. Dynamics of Singlet Fission and Electron Injection in Self-Assembled Acene Monolayers on Titanium Dioxide. *Chem. Sci.* **2018**, *9*, 3004–3013.

[185] Thampi, A.; Stern, H. L.; Cheminal, A.; Tayebjee, M. J. Y.; Petty, A. J.; Anthony, J. E.; Rao, A. Elucidation of Excitation Energy Dependent Correlated Triplet Pair Formation Pathways in an Endothermic Singlet Fission System. *J. Am. Chem. Soc.* **2018**, *140*, 4613–4622.

[186] Lee, J.; Bruzek, M. J.; Thompson, N. J.; Sfeir, M. Y.; Anthony, J. E.; Baldo, M. A. Singlet Exciton Fission in a Hexacene Derivative. *Adv. Mater.* **2013**, *25*, 1445–1448.

[187] Herz, J.; Buckup, T.; Paulus, F.; Engelhart, J. U.; Bunz, U. H. F.; Motzkus, M. Unveiling Singlet Fission Mediating States in TIPS-pentacene and its Aza Derivatives. *J. Phys. Chem. A* **2015**, *119*, 6602–6610.

[188] Sharifzadeh, S.; Wong, C. Y.; Wu, H.; Cotts, B. L.; Kronik, L.; Ginsberg, N. S.; Neaton, J. B. Relating the Physical Structure and Optoelectronic Function of Crystalline TIPS-Pentacene. *Adv. Funct. Mater.* **2015**, *25*, 2038–2046.

[189] Doan, S. C.; Kuzmanich, G.; Gard, M. N.; Garcia-Garibay, M. A.; Schwartz, B. J. Ultrafast Spectroscopic Observation of a Quantum Chain Reaction: The Photodecarbonylation of Nanocrystalline Diphenylcyclopropenone. *J. Phys. Chem. Lett.* **2012**, *3*, 81–86.

[190] Manna, B.; Ghosh, R.; Palit, D. K. Exciton Dynamics in Anthracene Nanoaggregates. *J. Phys. Chem. C* **2015**, *119*, 10641–10652.

[191] Manna, B.; Nandi, A.; Ghosh, R. Ultrafast Singlet Exciton Fission Dynamics in 9,10-Bis(phenylethynyl)anthracene Nanoaggregates and Thin Films. *J. Phys. Chem. C* **2018**, *122*, 21047–21055.

[192] Patra, A.; Hebalkar, N.; Sreedhar, B.; Radhakrishnan, T. P. Formation and Growth of Molecular Nanocrystals Probed by their Optical Properties. *J. Phys. Chem. C* **2007**, *111*, 16184–16191.

[193] Pensack, R. D.; Ashmore, R. J.; Paoletta, A. L.; Scholes, G. D. The Nature of Excimer Formation in Crystalline Pyrene Nanoparticles. *J. Phys. Chem. C* **2018**, *122*, 21004–21017.

[194] Manna, B.; Ghosh, R.; Palit, D. K. Ultrafast Energy Transfer Process in Doped-Anthracene Nanoaggregates is Controlled by Exciton Diffusion: Multiple Doping Leads to Efficient White Light Emission. *J. Phys. Chem. C* **2016**, *120*, 7299–7312.

[195] Manna, B. Temperature Dependence of Resonance Energy Transfer in DCM

Doped Anthracene Nanoaggregates. *J. Lumin.* **2019**, *209*, 379–386.

[196] Nandi, A.; Manna, B.; Ghosh, R. Interplay of Exciton–Excimer Dynamics in 9,10-Diphenylanthracene Nanoaggregates and Thin Films Revealed by Time-Resolved Spectroscopic Studies. *Phys. Chem. Chem. Phys.* **2019**, *21*, 11193–11202.

[197] Gesquiere, A. J.; Uwada, T.; Asahi, T.; Masuhara, H.; Barbara, P. F. Single Molecule Spectroscopy of Organic Dye Nanoparticles. *Nano Lett.* **2005**, *5*, 1321–1325.

[198] Jalalian, M.; Mirkazemi, S.; Alamolhoda, S. The Effect of Poly Vinyl Alcohol (PVA) Surfactant on Phase Formation and Magnetic Properties of Hydrothermally Synthesized $CoFe_2O_4$ Nanoparticles. *J. Magn. Magn. Mater.* **2016**, *419*, 363–367.

[199] Kakade, S.; Ghosh, R.; Palit, D. K. Excited State Dynamics of Zinc-Phthalocyanine Nanoaggregates in Strong Hydrogen Bonding Solvents. *J. Phys. Chem. C* **2012**, *116*, 15155–15166.

[200] Zhou, F.; Zhou, R.; Hao, X.; Wu, X.; Rao, W.; Chen, Y.; Gao, D. Influences of Surfactant (PVA) Concentration and pH on the Preparation of Copper Nanoparticles by Electron Beam Irradiation. *Radiat. Phys. Chem.* **2008**, *77*, 169–173.

[201] Xie, R.; Xiao, D.; Fu, H.; Ji, X.; Yang, W.; Yao, J. Effect of PVA on the Growth and the Optical Properties of Perylene Nanocrystals. *New J. Chem.* **2001**, *25*, 1362–1364.

[202] Latterini, L.; Roscini, C.; Carlotti, B.; Aloisi, G. G.; Elisei, F. Synthesis and Characterization of Perylene Nanoparticles. *Phys. Status Solidi A* **2006**, *203*, 1470–1475.

[203] Galindo-Rodriguez, S.; Allémann, E.; Fessi, H.; Doelker, E. Physicochemical Parameters Associated with Nanoparticle Formation in the Salting-Out, Emulsification-Diffusion, and Nanoprecipitation Methods. *Pharm. Res.* **2004**, *21*, 1428–1439.

[204] Aragó, J.; Viruela, P. M.; Ortí, E.; Malavé Osuna, R.; Hernández, V.; López Navarrete, J. T.; Swartz, C. R.; Anthony, J. E. Functionalized Pentacenes: A Combined Theoretical, Raman and UV–Vis Spectroscopic Study. *Theor. Chem. Acc.* **2011**, *128*, 521–530.

[205] Hwang, D. K.; Fuentes-Hernandez, C.; Berrigan, J. D.; Fang, Y.; Kim, J.; Potscavage, W. J.; Cheun, H.; Sandhage, K. H.; Kippelen, B. Solvent and Polymer Matrix Effects on TIPS-Pentacene/Polymer Blend Organic Field-Effect Transistors. *J. Mater. Chem.* **2012**, *22*, 5531–5537.

[206] Kyrychenko, A.; Pasko, D. A.; Kalugin, O. N. Poly(Vinyl Alcohol) as a Water Protecting Agent for Silver Nanoparticles: the Role of Polymer Size and Structure. *Phys. Chem. Chem. Phys.* **2017**, *19*, 8742–8756.

[207] Bunn, C. W. Crystal Structure of Polyvinyl Alcohol. *Nature* **1948**, *161*, 929–930.

[208] Chai, J.-D.; Head-Gordon, M. Long-Range Corrected Hybrid Density Functionals with Damped Atom–Atom Dispersion Corrections. *Phys. Chem. Chem. Phys.* **2008**, *10*, 6615–6620.

[209] Thorley, K. J.; Finn, T. W.; Jarolimek, K.; Anthony, J. E.; Risko, C. Theory-

Driven Insight into the Crystal Packing of Trialkylsilylethynyl Pentacenes. *Chem. Mater.* **2017**, *29*, 2502–2512.

[210] Ullah Khan, H.; Li, R.; Ren, Y.; Chen, L.; Payne, M. M.; Bhansali, U. S.; Smilgies, D.-M.; Anthony, J. E.; Amassian, A. Solvent Vapor Annealing in the Molecular Regime Drastically Improves Carrier Transport in Small-Molecule Thin-Film Transistors. *ACS Appl. Mater. Interfaces* **2013**, *5*, 2325–2330.

[211] Geißler, D.; Gollwitzer, C.; Sikora, A.; Minelli, C.; Krumrey, M.; Resch-Genger, U. Effect of Fluorescent Staining on Size Measurements of Polymeric Nanoparticles Using DLS and SAXS. *Anal. Methods* **2015**, *7*, 9785–9790.

[212] Dapprich, S.; Komáromi, I.; Byun, K.; Morokuma, K.; Frisch, M. J. A New ONIOM Implementation in Gaussian98. Part I. The Calculation of Energies, Gradients, Vibrational Frequencies and Electric Field Derivatives. *J. Mol. Struc. (Theochem)* **1999**, *461-462*, 1–21.

[213] Vreven, T.; Byun, K. S.; Komáromi, I.; Dapprich, S.; Montgomery, J. A.; Morokuma, K.; Frisch, M. J. Combining Quantum Mechanics Methods with Molecular Mechanics Methods in ONIOM. *J. Chem. Theory Comput.* **2006**, *2*, 815–826.

[214] Chai, J.-D.; Head-Gordon, M. Systematic Optimization of Long-Range Corrected Hybrid Density Functionals. *J. Chem. Phys.* **2008**, *128*, 084106.

[215] Dunning, T. H. Gaussian Basis Sets for use in Correlated Molecular Calculations. I. The Atoms Boron Through Neon and Hydrogen. *J. Chem. Phys.* **1989**, *90*, 1007–1023.

[216] Woon, D. E.; Dunning, T. H. Gaussian Basis Sets for use in Correlated Molecular Calculations. III. The Atoms Aluminum Through Argon. *J. Chem. Phys.* **1993**, *98*, 1358–1371.

[217] Dewar, M. J. S.; Zoebisch, E. G.; Healy, E. F.; Stewart, J. J. P. Development and Use of Quantum Mechanical Molecular Models. 76. AM1: A New General Purpose Quantum Mechanical Molecular Model. *J. Am. Chem. Soc.* **1985**, *107*, 3902–3909.

[218] Bentea, L.; Watzky, M. A.; Finke, R. G. Sigmoidal Nucleation and Growth Curves Across Nature Fit by the Finke–Watzky Model of Slow Continuous Nucleation and Autocatalytic Growth: Explicit Formulas for the Lag and Growth Times Plus Other Key Insights. *J. Phys. Chem. C* **2017**, *121*, 5302–5312.

[219] Finney, E. E.; Finke, R. G. Fitting and Interpreting Transition-Metal Nanocluster Formation and Other Sigmoidal-Appearing Kinetic Data: A More Thorough Testing of Dispersive Kinetic vs Chemical-Mechanism-Based Equations and Treatments for 4-Step Type Kinetic Data. *Chem. Mater.* **2009**, *21*, 4468–4479.

[220] Morris, A. M.; Watzky, M. A.; Agar, J. N.; Finke, R. G. Fitting Neurological Protein Aggregation Kinetic Data via a 2-Step, Minimal "Ockham's Razor" Model: The Finke-Watzky Mechanism of Nucleation Followed by Autocatalytic Surface Growth. *Biochemistry* **2008**, *47*, 2413–2427.

[221] Watzky, M. A.; Finke, R. G. Transition Metal Nanocluster Formation Kinetic and Mechanistic Studies. A New Mechanism When Hydrogen Is the Reductant: Slow, Continuous Nucleation and Fast Autocatalytic Surface Growth. *J. Am.*

Chem. Soc. **1997**, *119*, 10382–10400.

[222] Watzky, M. A.; Morris, A. M.; Ross, E. D.; Finke, R. G. Fitting Yeast and Mammalian Prion Aggregation Kinetic Data with the Finke Watzky Two-Step Model of Nucleation and Autocatalytic Growth. *Biochemistry* **2008**, *47*, 10790–10800.

[223] Lue, S. J.; Chen, J.; Yang, J. M. Crystallinity and Stability of Poly(vinyl alcohol)-Fumed Silica Mixed Matrix Membranes. *J. Macromol. Sci. B* **2007**, *47*, 39–51.

[224] Moneghini, M.; Kikic, I.; Voinovich, D.; Perissutti, B.; Filipović-Grčić, J. Processing of Carbamazepine–PEG 4000 Solid Dispersions with Supercritical Carbon Dioxide: Preparation, Characterisation, and in vitro Dissolution. *Int. J. Pharm.* **2001**, *222*, 129–138.

[225] Borowicz, B.; Nickel, B. Application of High-Accuracy Time-Resolved Laser Spectroscopy to the Study of Diffusion-Controlled Triplet-Triplet Annihilation. *Opto-Electron. Rev.* **2004**, *12*, 325–332.

[226] Smoluchowski, M. v. Drei Vortrage uber Diffusion. Brownsche Bewegung und Koagulation von Kolloidteilchen. *Z. Phys.* **1916**, *17*, 557–585.

[227] Chandrasekhar, S. Stochastic Problems in Physics and Astronomy. *Rev. Mod. Phys.* **1943**, *15*, 1–89.

[228] Diao, Y.; Tee, B. C. K.; Giri, G.; Xu, J.; Kim, D. H.; Becerril, H. A.; Stoltenberg, R. M.; Lee, T. H.; Xue, G.; Mannsfeld, S. C. B.; Bao, Z. Solution Coating of Large-Area Organic Semiconductor Thin Films with Aligned Single-Crystalline Domains. *Nat. Mater.* **2013**, *12*, 665–671.

[229] Xiao, C.; Kan, X.; Liu, C.; Jiang, W.; Zhao, G.; Zhao, Q.; Zhang, L.; Hu, W.; Wang, Z.; Jiang, L. Controlled Formation of Large-Area Single-Crystalline TIPS-pentacene Arrays Through Superhydrophobic Micropillar Flow-Coating. *J. Mater. Chem. C* **2017**, *5*, 2702–2707.

[230] Perdew, J. P.; Burke, K.; Ernzerhof, M. Generalized Gradient Approximation Made Simple. *Phys. Rev. Lett.* **1996**, *77*, 3865–3868.

[231] Hehre, W. J.; Ditchfield, R.; Pople, J. A. Self–Consistent Molecular Orbital Methods. XII. Further Extensions of Gaussian–Type Basis Sets for Use in Molecular Orbital Studies of Organic Molecules. *J. Chem. Phys.* **1972**, *56*, 2257–2261.

[232] Jortner, J.; Rice, S. A.; Katz, J. L.; Choi, S. Triplet Excitons in Crystals of Aromatic Molecules. *J. Chem. Phys.* **1965**, *42*, 309–323.

[233] Lebental, M.; Choukri, H.; Chénais, S.; Forget, S.; Siove, A.; Geffroy, B.; Tutiš, E. Diffusion of Triplet Excitons in an Operational Organic Light-Emitting Diode. *Phys. Rev. B* **2009**, *79*, 165318.

[234] Hertel, D.; Meerholz, K. Triplet-Polaron Quenching in Conjugated Polymers. *J. Phys. Chem. B* **2007**, *111*, 12075–12080.

[235] Olaya-Castro, A.; Scholes, G. D. Energy Transfer from Förster–Dexter Theory to Quantum Coherent Light-Harvesting. *Int. Rev. Phys. Chem.* **2011**, *30*, 49–77.

[236] Engel, E.; Leo, K.; Hoffmann, M. Ultrafast Relaxation and Exciton–Exciton Annihilation in PTCDA Thin Films at High Excitation Densities. *Chem. Phys.*

2006, *325*, 170–177.

[237] Marcus, R. A. On the Theory of Oxidation-Reduction Reactions Involving Electron Transfer. I. *J. Chem. Phys.* **1956**, *24*, 966–978.

[238] Voter, A. F.; Doll, J. D. Transition State Theory Description of Surface Self-Diffusion: Comparison with Classical Trajectory Results. *J. Chem. Phys.* **1984**, *80*, 5832–5838.

[239] Wan, Y.; Guo, Z.; Zhu, T.; Yan, S.; Johnson, J.; Huang, L. Cooperative Singlet and Triplet Exciton Transport in Tetracene Crystals Visualized by Ultrafast Microscopy. *Nat. Chem.* **2015**, *7*, 785–792.

[240] Yang, F.; Wang, X.; Fan, H.; Tang, Y.; Yang, J.; Yu, J. Effect of In Situ Annealing Treatment on the Mobility and Morphology of TIPS-Pentacene-Based Organic Field-Effect Transistors. *Nanoscale Res. Lett.* **2017**, *12*, 503.

[241] Swenberg, C. E. Theory of Triplet Exciton Annihilation in Polyacene Crystals. *J. Chem. Phys.* **1969**, *51*, 1753–1764.

[242] Bachilo, S. M.; Weisman, R. B. Determination of Triplet Quantum Yields from Triplet Triplet Annihilation Fluorescence. *J. Phys. Chem. A* **2000**, *104*, 7711–7714.

[243] Pustulka, K. M.; Wohl, A. R.; Lee, H. S.; Michel, A. R.; Han, J.; Hoye, T. R.; McCormick, A. V.; Panyam, J.; Macosko, C. W. Flash Nanoprecipitation: Particle Structure and Stability. *Mol. Pharmaceutics* **2013**, *10*, 4367–4377.

[244] Erban, R.; Chapman, S. J. Reactive Boundary Conditions for Stochastic Simulations of Reaction-Diffusion Processes. *Phys. Biol.* **2007**, *4*, 16–28.

[245] Crank, J. *The Mathematics of Diffusion*, 2nd ed.; Oxford University Press, 1979.

[246] Probstein, R. F. *Physicochemical Hydrodynamics: An Introduction*; John Wiley & Sons, 2005.

[247] Dexter, D. L. Two Ideas on Energy Transfer Phenomena: Ion-Pair Effects Involving the OH Stretching Mode, and Sensitization of Photovoltaic Cells. *J. Lumin.* **1979**, *18-19*, 779–784.

[248] Rao, A.; Friend, R. H. Harnessing Singlet Exciton Fission to Break the Shockley-Queisser Limit. *Nat. Rev. Mater.* **2017**, *2*, 17063.

[249] Gish, M. K.; Pace, N. A.; Rumbles, G.; Johnson, J. C. Emerging Design Principles for Enhanced Solar Energy Utilization with Singlet Fission. *J. Phys. Chem. C* **2019**, *123*, 3923–3934.

[250] Kurokawa, N.; Yoshikawa, H.; Hirota, N.; Hyodo, K.; Masuhara, H. Size-Dependent Spectroscopic Properties and Thermochromic Behavior in Poly(substitutedthiophene) Nanoparticles. *ChemPhysChem* **2004**, *5*, 1609–1615.

[251] van Stokkum, I. H. M.; Larsen, D. S.; van Grondelle, R. Global and Target Analysis of Time-Resolved Spectra. *Biochim. Biophys. Acta Bioenerg.* **2004**, *1657*, 82–104.

[252] Prasad, J.; Kopelman, R. A New Technique to Differentiate Between Geminate and Nongeminate Recombination of Triplet Excitons. *J. Lumin.* **1990**, *45*, 258–259.

[253] Tilley, A.; Pensack, R. D.; Kynaston, E. L.; Scholes, G. D.; Seferos, D. S. Singlet Fission in Core-Shell Micelles of End-Functionalized Polymers. *Chem. Mater.* **2018**, *30*, 4409–4421.

[254] Kosco, J. et al. Enhanced Photocatalytic Hydrogen Evolution from Organic Semiconductor Heterojunction Nanoparticles. *Nat. Mater.* **2020**, *19*, 559–565.

[255] Schweitzer, C.; Schmidt, R. Physical Mechanisms of Generation and Deactivation of Singlet Oxygen. *Chem. Rev.* **2003**, *103*, 1685–1758.

[256] Wollscheid, N.; Pérez Lustres, J. L.; Kefer, O.; Hahn, S.; Brosius, V.; Bunz, U. H. F.; Motzkus, M.; Buckup, T. Oxygen-Catalysed Sequential Singlet Fission. *Nat. Commun.* **2019**, *10*, 5202.

[257] Ishibashi, Y.; Arinishi, M.; Katayama, T.; Miyasaka, H.; Asahi, T. Excited-State Dynamics of Fullerene Nanoparticles Dispersed in Pure Water. *Chem. Lett.* **2012**, *41*, 1104–1106.

[258] Roberts, S. T.; McAnally, R. E.; Mastron, J. N.; Webber, D. H.; Whited, M. T.; Brutchey, R. L.; Thompson, M. E.; Bradforth, S. E. Efficient Singlet Fission Discovered in a Disordered Acene Film. *J. Am. Chem. Soc.* **2012**, *134*, 6388–6400.

[259] Pace, N. A.; Korovina, N. V.; Clikeman, T. T.; Holliday, S.; Granger, D. B.; Carroll, G. M.; Nanayakkara, S. U.; Anthony, J. E.; McCulloch, I.; Strauss, S. H.; Boltalina, O. V.; Johnson, J. C.; Rumbles, G.; Reid, O. G. Slow Charge Transfer from Pentacene Triplet States at the Marcus Optimum. *Nat. Chem.* **2020**, *12*, 63–70.

[260] Pace, N. A.; Rugg, B. K.; Chang, C. H.; Reid, O. G.; Thorley, K. J.; Parkin, S.; Anthony, J. E.; Johnson, J. C. Conversion Between Triplet Pair States is Controlled by Molecular Coupling in Pentadithiophene Thin Films. *Chem. Sci.* **2020**, *11*, 7226–7238.

[261] Pace, N. A.; Clikeman, T. T.; Strauss, S. H.; Boltalina, O. V.; Johnson, J. C.; Rumbles, G.; Reid, O. G. Triplet Excitons in Pentacene Are Intrinsically Difficult to Dissociate via Charge Transfer. *J. Phys. Chem. C* **2020**, *124*, 26153–26164.

[262] Huang, Y.; Buyanova, I. A.; Phansa, C.; Sandoval-Salinas, M. E.; Casanova, D.; Myers, W. K.; Greenham, N. C.; Rao, A.; Chen, W. M.; Puttisong, Y. Competition Between Triplet Pair Formation and Excimer-Like Recombination Controls Singlet Fission Yield. *Cell Rep. Phys. Sci.* **2021**, *2*, 100339.

[263] Seiler, H.; Krynski, M.; Zahn, D.; Hammer, S.; Windsor, Y. W.; Vasileiadis, T.; Pflaum, J.; Ernstorfer, R.; Rossi, M.; Schwoerer, H. Nuclear Dynamics of Singlet Exciton Fission in Pentacene Single Crystals. *Sci. Adv.* **2021**, *7*, eabg0869.

[264] Wang, L.; Olivier, Y.; Prezhdo, O. V.; Beljonne, D. Maximizing Singlet Fission by Intermolecular Packing. *J. Phys. Chem. Lett.* **2014**, *5*, 3345–3353.

[265] Herz, J.; Buckup, T.; Paulus, F.; Engelhart, J.; Bunz, U. H. F.; Motzkus, M. Acceleration of Singlet Fission in an Aza-Derivative of TIPS-Pentacene. *J. Phys. Chem. Lett.* **2014**, *5*, 2425–2430.

[266] Flanders, N. C.; Kirschner, M. S.; Kim, P.; Fauvell, T. J.; Evans, A. M.; Helweh, W.; Spencer, A. P.; Schaller, R. D.; Dichtel, W. R.; Chen, L. X. Large Ex-

citon Diffusion Coefficients in Two-Dimensional Covalent Organic Frameworks with Different Domain Sizes Revealed by Ultrafast Exciton Dynamics. *J. Am. Chem. Soc.* **2020**, *142*, 14957–14965.

[267] Gramlich, M.; Bohn, B. J.; Tong, Y.; Polavarapu, L.; Feldmann, J.; Urban, A. S. Thickness-Dependence of Exciton-Exciton Annihilation in Halide Perovskite Nanoplatelets. *J. Phys. Chem. Lett.* **2020**, *11*, 5361–5366.

[268] Jansen, A. P. J. *An Introduction to Kinetic Monte Carlo Simulations of Surface Reactions*; Springer, 2012; Vol. 856.

[269] Mozumder, A. Mean Recombination Time of Diffusion Controlled Geminate Reactions. *J. Chem. Phys.* **1982**, *76*, 5107–5111.

[270] Prüstel, T.; Tachiya, M. Reversible Diffusion-Influenced Reactions of an Isolated Pair on Some Two Dimensional Surfaces. *J. Chem. Phys.* **2013**, *139*, 194103.

[271] Arkhincheev, V. E. The Calculation of Effective Three-Dimensional Diffusion Coefficient from Survival Probability Asymptotic at Anisotropic Diffusion in Medium with Absorbing Traps. *Physica A* **2019**, *518*, 343–348.

[272] Szabo, A.; Schulten, K.; Schulten, Z. First Passage Time Approach to Diffusion Controlled Reactions. *J. Chem. Phys.* **1980**, *72*, 4350–4357.

[273] Deutch, J. A Simple Method for Determining the Mean Passage Time for Diffusion Controlled Processes. *J. Chem. Phys.* **1980**, *73*, 4700.

[274] Tarzia, A.; Takahashi, M.; Falcaro, P.; Thornton, A. W.; Doonan, C. J.; Huang, D. M. High-Throughput Screening of Metal-Organic Frameworks for Macroscale Heteroepitaxial Alignment. *ACS Appl. Mater. Interfaces* **2018**, *10*, 40938–40950.

[275] De Sio, A.; Camargo, F. V. d. A.; Winte, K.; Sommer, E.; Branchi, F.; Cerullo, G.; Lienau, C. Ultrafast Relaxation Dynamics in a Polymer: Fullerene Blend for Organic Photovoltaics Probed by Two-Dimensional Electronic Spectroscopy. *Eur. Phys. J. B* **2018**, *91*, 236.

[276] Le, D. V.; de la Perrelle, J. M.; Do, T. N.; Leng, X.; Tapping, P. C.; Scholes, G. D.; Kee, T. W.; Tan, H.-S. Characterization of the Ultrafast Spectral Diffusion and Vibronic Coherence of TIPS-Pentacene using 2D Electronic Spectroscopy. *J. Chem. Phys.* **2021**, *155*, 014302.

[277] Zhang, R.; Guan, Y.; Zhu, Z.; Lv, H.; Li, F.; Sun, S.; Li, J. Multifunctional Tetracene/Pentacene Host/Guest Nanorods for Enhanced Upconversion Photodynamic Tumor Therapy. *ACS Appl. Mater. Interfaces* **2019**, *11*, 37479–37490.

[278] Savu, S.-A.; Casu, M. B.; Schundelmeier, S.; Abb, S.; Tönshoff, C.; Bettinger, H. F.; Chassé, T. Nanoscale Assembly, Morphology and Screening Effects in Nanorods of Newly Synthesized Substituted Pentacenes. *RSC Adv.* **2012**, *2*, 5112–5118.

[279] Akai-Kasaya, M.; Ohmori, C.; Kawanishi, T.; Nashiki, M.; Saito, A.; Aono, M.; Kuwahara, Y. Formation and Electrical Transport Properties of Pentacene Nanorod Crystal. *Nanotechnology* **2010**, *21*, 365601.